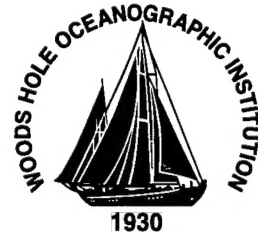


MIT/WHOI 97-20

**Massachusetts Institute of Technology  
Woods Hole Oceanographic Institution**



**Joint Program  
in Oceanography/  
Applied Ocean Science  
and Engineering**



---

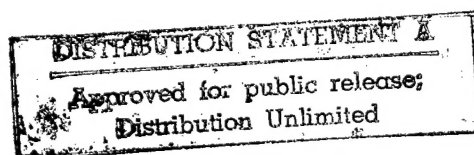
**DOCTORAL DISSERTATION**

*Development of the BASS Rake Acoustic Current Sensor:  
Measuring Velocity in the Continental Shelf Wave  
Bottom Boundary Layer*

by

Archie Todd Morrison III

June 1997



DTIC QUALITY INSPECTED 6

19971229 240

**MIT/WHOI**

**97-20**

**Development of the BASS Rake Acoustic Current Sensor:  
Measuring Velocity in the Continental Shelf Wave Bottom Boundary Layer**

by

Archie Todd Morrison III

Massachusetts Institute of Technology  
Cambridge, Massachusetts 02139

and

Woods Hole Oceanographic Institution  
Woods Hole, Massachusetts 02543

June 1997

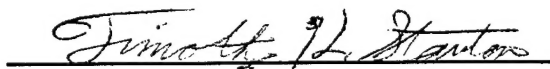
**DOCTORAL DISSERTATION**

Funding was provided by the Office of Naval Research through AASERT under Grant N00014-93-1-1140 and the National Science Foundation under Grant OCE-9314357.

Reproduction in whole or in part is permitted for any purpose of the United States Government. This thesis should be cited as: Archie Todd Morrison III, 1997. Development of the BASS Rake Acoustic Current Sensor: Measuring Velocity in the Continental Shelf Wave Bottom Boundary Layer. Ph.D. Thesis. MIT/WHOI, 97-20.

Approved for publication; distribution unlimited.

**Approved for Distribution:**

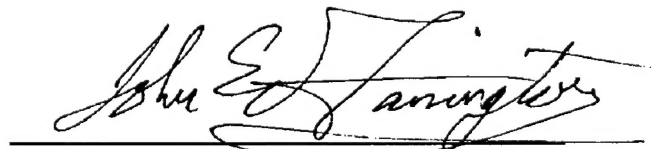


**Timothy K. Stanton, Chair**

Department of Applied Ocean Physics and Engineering



**Marcia K. McNutt**  
MIT Director of Joint Program



**John W. Farrington**  
WHOI Dean of Graduate Studies



Development of the BASS Rake Acoustic Current Sensor:  
Measuring Velocity in the  
Continental Shelf Wave Bottom Boundary Layer

By

Archie Todd Morrison III

B. A., Engineering and Applied Science, Harvard University (1981)

M. S., Ocean Engineering, Massachusetts Institute of Technology (1994)

O. E., Oceanographic Engineering, Massachusetts Institute of Technology and  
Woods Hole Oceanographic Institution (1994)

Submitted in partial fulfillment of the  
requirements for the degree of

DOCTOR OF PHILOSOPHY

at the

MASSACHUSETTS INSTITUTE OF TECHNOLOGY

and the

WOODS HOLE OCEANOGRAPHIC INSTITUTION

June 1997

© 1997 Archie Todd Morrison III

All rights reserved.

The author hereby grants to MIT and WHOI permission to reproduce  
and distribute copies of this thesis document in whole or in part.

Signature of Author Archie T. Morrison III  
Joint Program in Applied Ocean Science and Engineering  
Massachusetts Institute of Technology/  
Woods Hole Oceanographic Institution

Certified by Albert J. Williams 3rd  
Dr. Albert J. Williams 3rd  
Thesis Supervisor  
Woods Hole Oceanographic Institution

Accepted by Henrik Schmidt  
Professor Henrik Schmidt  
Joint Committee for Applied Ocean Science and Engineering, Acting Chair  
Massachusetts Institute of Technology/  
Woods Hole Oceanographic Institution

# Development of the BASS Rake Acoustic Current Sensor: Measuring Velocity in the Continental Shelf Wave Bottom Boundary Layer

By

Archie Todd Morrison III

Submitted to the Massachusetts Institute of Technology/  
Woods Hole Oceanographic Institution  
Joint Program in Applied Ocean Science and Engineering  
in partial fulfillment of the requirements for the degree of

DOCTOR OF PHILOSOPHY

## Abstract

Surface swell over the continental shelf generates a sheet of oscillatory shear flow at the base of the water column, the continental shelf wave bottom boundary layer. The short periods of surface swell sharply limit the thickness of the wave boundary layer, confining it to a thin region below an oscillatory, but essentially irrotational, core. For a wide range of shelf conditions, the vertical extent of the wave boundary layer does not exceed 2.5 *cm* and is commonly less. The extreme narrowness of this boundary layer is responsible for high levels of bottom stress and turbulent dissipation. Even in relatively mild sea states, the wave induced bottom shear stress can be sufficient to initiate sediment motion. The wave bottom boundary layer plays an important role in the processes of sediment entrainment and transport on the continental margins.

This thesis documents the development, testing, and field use of a new instrument, the BASS Rake, designed to measure velocity profiles in the wave boundary layer. The mechanical design supports multiple measurement levels with millimeter vertical spacing. The mechanical design is integrated with an electronic interface designed to permit flexible acquisition of a suite of horizontal and vertical velocity measurements without sacrificing the electronic characteristics necessary for high measurement accuracy. The effects of velocity averaging over the sample volume are calculated with a model of acoustic propagation in a scattering medium appropriate to the scales of a single differential travel time axis. A simpler parametric model of the averaging process is then developed and used to specify the transducer characteristics necessary to image the wave boundary layer on the continental shelf.

A flow distortion model for the sensor head is developed and the empirical determinations of the Reynolds number, Keulegan-Carpenter number, and angular dependencies of the sensor response for the laboratory and field prototypes is presented. The calibrated sensor response of the laboratory prototype is tested against concurrent LDV measurements over a natural sand bed in a flume. The single measurement accuracy of the BASS Rake is higher than that of the LDV and the multiple sample

volumes confer other advantages. For example, the ability of the BASS Rake to image vertically coherent turbulent instabilities, invisible to the LDV, is demonstrated. Selected data from a twenty-four day field deployment outside the surf zone of a local beach are presented and analyzed. The data reveal regular reworking of the sand bed, the generation and modification of sand ripples, and strong tidal modulation of the current and wave velocities on semi-diurnal, diurnal, and spring/neap time scales. The data set is unique in containing concurrent velocity time series, of several weeks duration, with coverage from 1 *cm* to 20 *cm* above the bottom.

Thesis Committee:

Dr. Albert J. Williams 3rd, Chair

Dr. John H. Trowbridge

Prof. Michael S. Triantafyllou

Chair of the Defense:

Dr. Eugene A. Terray

## Acknowledgements

First, I would like to extend my sincere thanks to the members of my doctoral committee, Dr. Albert J. Williams 3rd, Dr. John H. Trowbridge, and Prof. Michael S. Triantafyllou, and to the chairman of my defense, Dr. Eugene A. Terray. They have been supportive and invaluable resources throughout this process. I would like to add a special thanks to Sandy Williams who has been and continues to be both a mentor and a friend.

My thanks to Dr. Joseph Kravitz of the Office of Naval Research. ONR has contributed substantial financial support to this research and to my graduate education through AASERT funding under ONR Grant N00014-93-1-1140. Thanks also to Mr. Lawrence Clark of the National Science Foundation. NSF supported the purchase of hardware and services under NSF Grant OCE-9314357.

I consider myself fortunate to have been taught by Sue Cloutier, Rod Spurr, Gordon Ivanosky, Ed Yarosh, Ed Herlin, Al Palumbo, Roland Marandino, Al Pandiscio, James Williams, Clay Thompson, Mike Triantafyllou, Paul Sclavounos, John Trowbridge, Jim Irish, and Sandy Williams. They all stand out in my mind as teachers of note. Their instruction has made significant contributions to the sum of my knowledge and they have left lasting impressions on the way I approach problems.

I would also like to extend my sincere and heartfelt thanks to those at Woods Hole, MIT, and other locales who have willingly offered their time and knowledge through discussion, instruction, advice, and, in many cases, actual work. Jake Peirson and Ronni Schwartz have always been ready to provide a safe haven in any storm. Penny Chisholm's kind words in support of my endeavors teaching elementary school students were greatly appreciated. On several occasions Mark Grosenbaugh has willingly and successfully gone to bat for me. I have every confidence we will someday understand each other's jokes. Judy White, Anita Norton, Sue Oliver, and Shirley Barkley are ever helpful and always know what I have forgotten to sign or submit. Judy, in particular, always lets me know exactly where I stand and exactly where to go. Ann Martin, Cindy Sellers, Eric Cunningham, and Art Newhall have all happily provided aid and assistance when asked. Dick Koehler, Neil Brown, Al Bradley, Al

Duester, and Karlen Wannop have been invaluable sources of ideas and advice for circuit design. Ned Forrester contributed an enormous amount of time and expertise during the great noise hunt. The Fresnel problem was recognized, just in time, by Tim Duda, and Gene Terray taught me how to solve it. The support frames for the two prototypes were well designed by Don Peters and Glenn McDonald and well built by Martin Woodward, Charles Clemishaw, and Geoff Ekblaw. Great jobs everyone and I'm really sorry about the scratches and that bent leg. Anyway, everything worked terrifically well and I'll need those slider blocks with the hand wheels by yesterday. Without the help and expertise of Janet Fredericks, I would still be unpacking the field data. Tom Kleindinst did a great job photographing the equipment and laboratory tests. Tom and Dave Gray put up with my kibitzing with grace and aplomb while scanning and skillfully processing the images. The DocuTech debacle wouldn't have been nearly as much fun without the company and hard work of Mark Hickey and Steve Allsop. Gary Stanborough patiently showed me how to pot polyurethane the right way. During the flume tests the LDV was skillfully coaxed along by Jay Sisson. Ole Madsen introduced me to the mysteries of the continental shelf wave bottom boundary layer and the wonders of sediment transport. Alex Hay and Jim Ledwell have provided advice and timely words of encouragement on several occasions. Scott McIntyre, the UberGeek, without whom all computer related activity everywhere would come to a crashing halt, provided unique assistance on many occasions.

Several groups of people provided special services that I would like to recognize here. First, thanks to all the regulars at C&D for all the questions, answers, and sea stories over the years. Most of you know who you are. See you at the next chain flogging. I'll bring the donuts.

Sandy Williams, Glenn McDonald, Alan Hinton, Fred Thwaites, Larry Connor, and Terry Rioux repeatedly, willingly, and often gleefully, even during the snow storms, flung themselves into the November and December surf with me to deploy, inspect, and recover the field prototype. Thanks also to Don Peters who suffered alone on the beach and kept the truck warm for some of the rest of us. Terry, I'm almost certain you were mistaken about the location of my bubbles. Everyone, I'm

still really sorry about that switch. Thanks for your help and an extra thanks to Fred who wore the leaky drysuit and only grumped about it a little.

The Stockroom Dudes, Rich Lovering, Sam Lomba, Glenn Enos, and Ellen Moriarty, happily gave me access to the component drawers during the dark development days of 1996 and were uncomplaining when it came to my many, many midnight requisitions. Thanks for the moral and material support and I hope I got everything logged correctly and back where it belonged. If you need any help with the resistors, just let me know.

Those midnight requisitions were aided and abetted by the people who really run the Institution. WHOI After Dark, Dave McDonald, Jim Dunn, Bob Wilson, Bill Sparks, Bill Cruwys, Steve Rossetti, Bob Bossardt, and Bob Hendricks, had the things I needed to carry on, keys, coffee, and conversation, at all hours of all the days, nights, and weekends. The ribbing was endless and so was the encouragement and support. Thanks from "Stockroom" Morrison.

These acknowledgements would be grievously incomplete without special mention of some people who have provided me with particularly valued support while this research was in progress. For knowledge shared, services rendered, and especially friendship I would like to thank Hanumant Singh, Fred Thwaites, Naomi Fraenkel, Maria Hood, and Diane DiMassa.

Thank you to my loving, supportive, understanding, and wonderful family. I couldn't have done it without you. My much better half, Hilary, has made many perceptive contributions, but my favorite is the working title of the first BASS Rake paper: "A Theoretical Analysis of the Predicted Performance of a Hypothetical Instrument: Thought Experiments in the Virtual Reality Ocean Boundary Layer". My daughter, Abigail, always has a hug and a smile for me and recently offered some very timely advice, which I have tried to take to heart: "Go finish writing your book". Here it is, Abby. My son, Daniel, has mastered the art of smiling and wiggling with joy. "The Happy Guy" provides a full share of support and good cheer.

Finally, I would like to thank my parents, Archie and Beverly, for first teaching me the things I really needed to know.



## Author's Biographical Note

Archie Todd Morrison III graduated from Harvard University in 1981 with a Bachelor of Arts degree, *cum laude*, in Engineering and Applied Science / Electrical Engineering. At Harvard he also maintained a minor subject in Early and Oral Literatures. From 1981 until 1986 he was employed as a Senior Field Engineer by Raytheon, servicing missile fire control radars operated by the United States and foreign navies.

After leaving Raytheon in 1986, the author studied mathematics as a special student at Yale University. He also took a field course in underwater archaeology at the Isles of Shoals Marine Laboratory, administered by Cornell University and the University of New Hampshire.

In 1987 Todd married Hilary Ann Gonzalez and moved to Atlanta so that she could accept a postdoctoral fellowship in the Special Pathogens Branch of the Centers for Disease Control. He spent the two subsequent years operating a soup kitchen and maintaining a secure mailing address for thirty-five hundred homeless residents of that city. In 1989 they returned to New England where Todd began graduate work in the Massachusetts Institute of Technology / Woods Hole Oceanographic Institution Joint Program in Oceanographic Engineering.

Their first child, Abigail Michelle, was born in January of 1992, in time to witness the development of full ocean depth jello for instrument calibration. In 1994 Todd earned Master of Science and Ocean Engineer degrees for his thesis, "System Identification and State Reconstruction for Autonomous Navigation of an Underwater Vehicle in an Acoustic Net". He then turned to the development of instrumentation for the study of the continental shelf wave bottom boundary layer, the subject of this thesis.

Their second child, Daniel Gareth, was born in September of 1996, in time to witness the first field deployments of the BASS Rake. Todd, Hilary, Abigail, and Daniel currently live in East Falmouth, Massachusetts. Hilary is a molecular biologist at the Marine Biological Laboratory in Woods Hole. Todd will be continuing the development of the BASS Rake at the Woods Hole Oceanographic Institution. Abigail and Daniel help them focus on the things of real importance.





For  
Hilary  
and  
Abigail  
and  
Daniel

who make getting home  
the best part of any day.



# Contents

<b>1</b>	<b>Introduction</b>	<b>27</b>
1.1	The Continental Shelf Wave Bottom Boundary Layer . . . . .	27
1.2	Research Contributions . . . . .	31
1.3	Development Chronology and Thesis Outline . . . . .	33
<b>2</b>	<b>Boundary Layer Scales and the Mechanical Design of the Sensor Head</b>	<b>37</b>
2.1	Introduction and Background . . . . .	37
2.2	Characteristic Scales of the WBBL . . . . .	42
2.3	Previous Work with Existing Instruments and Techniques . . . . .	51
2.3.1	Models of the Wave-Current Boundary Layer . . . . .	51
2.3.2	An Assessment of Existing Instrumentation . . . . .	55
2.4	The BASS Rake Sensor Head . . . . .	81
2.4.1	Preliminary Error Analysis . . . . .	93
2.5	Summary . . . . .	97
<b>3</b>	<b>The Interface to the Acoustic Transducer Array</b>	<b>99</b>
3.1	Introduction . . . . .	99
3.2	System Background and Interface Requirements . . . . .	101
3.3	Interface Design . . . . .	111
3.3.1	Switching Element Selection . . . . .	111
3.3.2	Development of the L-Section . . . . .	114
3.3.3	The Layered Multiplexer . . . . .	118

3.3.4	Addressing the Array . . . . .	125
3.4	Circuit Modifications for the P3 Transducers . . . . .	132
3.4.1	Modification of the L-Section for Small Transducer Operation . . . . .	133
3.4.2	The COSAC Receiver Amplifier . . . . .	140
3.5	Conclusions . . . . .	147
<b>4</b>	<b>The Single Axis Sample Volume . . . . .</b>	<b>151</b>
4.1	Introduction . . . . .	151
4.2	Formal Description and Solution . . . . .	153
4.2.1	Diffraction and Wave Propagation Between Two Transducers . . . . .	153
4.2.2	Defining the Scattering Mechanism . . . . .	157
4.2.3	The Fresnel Integral in a Scattering Medium . . . . .	160
4.2.4	Calculating the BASS Rake Sample Volume . . . . .	164
4.3	A Simplified Parametric Model of the Sample Volume . . . . .	186
4.4	The Effect of Fresnel Averaging On Continental Shelf Wave Bottom Boundary Layer Measurements . . . . .	190
4.5	Summary . . . . .	198
<b>5</b>	<b>Tow Tank and Flume Evaluation of the Laboratory Prototype . . . . .</b>	<b>203</b>
5.1	Introduction . . . . .	203
5.2	The Laboratory Prototype . . . . .	204
5.3	Modeling the Flow Distortion . . . . .	208
5.4	Tow Tank Calibration . . . . .	214
5.4.1	Steady Flow . . . . .	214
5.4.2	Oscillatory Flow . . . . .	223
5.5	Flume Measurements Over a Sand Bed . . . . .	226
5.5.1	Test Conditions and Equipment . . . . .	226
5.5.2	Zero Calibration . . . . .	231
5.5.3	Test Results and Analysis . . . . .	234
5.6	Conclusions . . . . .	245

<b>6</b>	<b>Calibration and Deployment of the Field Prototype</b>	<b>247</b>
6.1	Introduction . . . . .	247
6.2	The Field Prototype . . . . .	249
6.3	Harbor Deployment . . . . .	257
6.4	Tow Tank Calibration . . . . .	262
6.5	Near-Shore Field Deployments . . . . .	269
6.5.1	Bottom Observations During the First Deployment . . . . .	269
6.5.2	Near-Bottom Velocity Measurements During the Second Deployment . . . . .	276
6.6	Conclusions . . . . .	300
<b>7</b>	<b>Conclusion</b>	<b>303</b>
7.1	General Summary . . . . .	303
7.2	Directions for Future Development . . . . .	305
<b>A</b>	<b>Derivation and Solution of the Equation of Motion for a Wall Boundary Layer</b>	<b>309</b>
A.1	Derivation of the Governing Equation . . . . .	310
A.2	Solutions of the Governing Equation . . . . .	315
A.2.1	The Eddy Viscosity . . . . .	315
A.2.2	Solution for a Steady Current . . . . .	318
A.2.3	The Hydrodynamic Roughness . . . . .	318
A.2.4	Solution for a Laminar Wave Boundary Layer . . . . .	321
A.2.5	Solution for a Turbulent Wave Boundary Layer . . . . .	323
<b>B</b>	<b>Schematic Wiring Diagrams for the BASS Rake Laboratory Prototype</b>	<b>331</b>



# List of Figures

2.1	BASS Rake Acoustic Transducer Geometry . . . . .	82
2.2	P2 and P3 Transducer Arrays . . . . .	83
2.3	Transducer Array for the Wave Bottom Boundary Layer . . . . .	86
2.4	P2 Tine Cross-Section and Transducer Mount . . . . .	88
2.5	P3 Tine Cross-Section and Transducer Mount . . . . .	89
2.6	Estimated BASS Rake Error Surfaces . . . . .	96
3.1	Equivalent Model of the BASS Transmit/Receive Process . . . . .	106
3.2	Equivalent Model of the Transmit/Receive Process with the Multiplexer . . . . .	110
3.3	VN3205 N-Channel Enhancement Mode Vertical DMOS FET . . . . .	113
3.4	Removing Capacitive Feedthrough Coupling with an FET Shunt Switch . . . . .	115
3.5	Quad FET L-Section . . . . .	116
3.6	Two Layer Multiplexer . . . . .	119
3.7	Schematic Diagram of the Completed L-Section . . . . .	125
3.8	Address Structure for the MUX . . . . .	127
3.9	Extended L-Section for P3 Operation . . . . .	136
3.10	Equivalent Model of the Transmit/Receive Process with an Extended P3 L-Section . . . . .	137
3.11	COSAC Schematic . . . . .	144
3.12	Bessel Bandpass Filter Frequency Response - Magnitude . . . . .	148
3.13	Bessel Bandpass Filter Frequency Response - Phase . . . . .	149



4.1	Definition Sketch for the Fresnel-Kirchoff Formula . . . . .	154
4.2	Construction of the Ellipsoidal Sample Volume . . . . .	156
4.3	BASS Rake Acoustic Axis Geometry for the Fresnel Integral in a Scattering Medium . . . . .	165
4.4	Acoustic Axis Beam Width and Timing Window . . . . .	169
4.5	Acoustic Axis Beam Width and Timing Window Mapped to the NIS . . . . .	173
4.6	Real and Imaginary NIS Integrand Surfaces for a Logarithmic Velocity Profile - Top View . . . . .	178
4.7	Real and Imaginary NIS Integrand Surfaces for a Logarithmic Velocity Profile - End View . . . . .	179
4.8	Calculated Fresnel Zone Averages Along a Logarithmic Velocity Profile - Linear Axes . . . . .	180
4.9	Calculated Fresnel Zone Averages Along a Logarithmic Velocity Profile - Semilog Axes . . . . .	181
4.10	Real and Imaginary Parts of the Eikonal Normalized to Velocity Space . . . . .	182
4.11	Real and Imaginary Parts of the Eikonal Normalized to Velocity Space and Corrected for Systematic Bias . . . . .	183
4.12	Real and Imaginary Parts of the P2 Eikonal Normalized to Velocity Space and Corrected for Systematic Bias . . . . .	185
4.13	Beam Pattern Approximations for a P2 Transducer Acoustic Axis . .	188
4.14	Comparison of the Eikonal and Parametric Models of Fresnel Zone Averaging . . . . .	189
4.15	Beam Pattern Approximations for an Acoustic Axis Using 5 MHz, 2.5 mm Transducers . . . . .	192
4.16	Real and Imaginary Parts of the 5 MHz Eikonal Normalized to Velocity Space and Corrected for Systematic Bias . . . . .	193
4.17	Further Comparison of the Eikonal and Parametric Models of Fresnel Zone Averaging . . . . .	194

4.18 Imaging a Laminar Wave Boundary Layer with P2 Transducers . . .	196
4.19 Imaging a Laminar Wave Boundary Layer with 5 <i>MHz</i> , 2.5 <i>mm</i> Transducers . . . . .	197
4.20 Hypothetically Imaging a Laminar Wave Boundary Layer with P3 Transducers . . . . .	198
4.21 Imaging a Turbulent Wave Boundary Layer with P2 Transducers . . .	199
4.22 Imaging a Turbulent Wave Boundary Layer with 5 <i>MHz</i> , 2.5 <i>mm</i> Transducers . . . . .	200
5.1 P2 Tine Showing Transducers . . . . .	206
5.2 BASS Rake Laboratory Prototype . . . . .	207
5.3 Distortion of a Uniform Potential Flow by Two Round Tines . . . . .	209
5.4 Steady Flow Disturbed by Two Halfround Tines . . . . .	211
5.5 WHOI Tow Tank and Carriage with the BASS Rake Laboratory Prototype . . . . .	215
5.6 Surface Deformation During Tow Tank Calibration of the Laboratory Prototype . . . . .	216
5.7 Measured Velocity During 30 <i>cm</i> · <i>s</i> <sup>-1</sup> Forward and Reverse Tows . .	217
5.8 Gain Correction as a Function of Reynolds Number . . . . .	219
5.9 Single-Valued Mapping from <i>u<sub>meas</sub></i> to <i>u<sub>gc</sub></i> . . . . .	221
5.10 Calibrated Measurement Accuracy of the Laboratory Prototype . . .	222
5.11 Calibrated Response in Oscillatory Flow at <i>KC</i> = 8 . . . . .	225
5.12 Calibrated Response in Oscillatory Flow at <i>KC</i> = 20 . . . . .	226
5.13 Calibrated Response in Oscillatory Flow at <i>KC</i> = 100 . . . . .	227
5.14 The 17 <i>m</i> Flume with the BASS Rake Prototype and LDV In Position . . . . .	230
5.15 BASS Rake Tines Positioned Over a Flat Sand Bed . . . . .	231
5.16 Along-Flume View of Laboratory Prototype and the Downstream Field of Bedforms . . . . .	232
5.17 Bedform Field Under BASS Rake Sample Volumes . . . . .	233

5.18	Bedform Field Under LDV Sample Volume . . . . .	234
5.19	Velocity Records from the Zero Offsets Calibration . . . . .	235
5.20	Measurement of a $1\text{ mm} \cdot \text{s}^{-1}$ Current Driven by Thermal Convection . . . . .	236
5.21	6 Minute BASS Rake and LDV Averages at Six Nominal Velocities .	237
5.22	BASS Rake and LDV Disagreement as a Function of Height for Each Trial . . . . .	238
5.23	BASS Rake and LDV Measurements of Turbulent Fluctuations . . . .	240
5.24	Bedform Propagation Past the BASS Rake Sample Volumes, Part 1 .	241
5.25	Bedform Propagation Past the BASS Rake Sample Volumes, Part 2 .	242
5.26	Flume Speed Fluctuations at a Nominal Velocity of $8\text{ cm} \cdot \text{s}^{-1}$ . . . .	243
5.27	Detail from $8\text{ cm} \cdot \text{s}^{-1}$ Velocity Records . . . . .	244
6.1	The Assembled BASS Rake Field Prototype . . . . .	250
6.2	Zero Calibration of the Field Prototype . . . . .	251
6.3	Field Prototype Transducer Array . . . . .	253
6.4	Definition Sketch for the Instrument Coordinate System . . . . .	255
6.5	Bottom Velocity Measurements in Great Harbor . . . . .	259
6.6	Spectra of the Velocity Measured $1\text{ cmab}$ . . . . .	260
6.7	Velocity Profiles Over a Single Wave Cycle . . . . .	261
6.8	Gain Correction Surface as a Function of Tow Speed and Rotation Angle . . . . .	265
6.9	Polar Presentation of the Gain Correction Surface . . . . .	266
6.10	Calibrated Measurement Accuracy of the Field Prototype . . . . .	268
6.11	Coastal Chart and Bathymetry for the Woods Hole Area . . . . .	270
6.12	Coastal Chart and Bathymetry for Nobska Beach . . . . .	271
6.13	Anchor and Anchor Line Securing the Field Prototype to the Bottom . . . . .	272
6.14	Nobska Beach and the Deployment Area . . . . .	273
6.15	Ripple Geometry Near the Tines . . . . .	274

6.16 Sand Ripples Near the Tines . . . . .	275
6.17 Regular Sand Ripples at Site 2 . . . . .	277
6.18 Velocity Measurements at Level 3 for December 11, 1996 . . . . .	280
6.19 Running Averages of the Level 3 Velocity Components for December 11, 1996 . . . . .	281
6.20 20 Minute Standard Deviations and Means for December 11, 1996 . .	282
6.21 20 Minute Standard Deviations and Means for December 7, 1996 . . .	283
6.22 Wave Spectra for December 7, 1996 . . . . .	284
6.23 3 Minute Time Series, 1600 hours on December 7, 1996 . . . . .	290
6.24 3 Minute Time Series, 1900 hours on December 7, 1996 . . . . .	291
6.25 3 Minute Time Series, 2200 hours on December 7, 1996 . . . . .	292
6.26 A Single Wave Cycle from the December 7 Storm . . . . .	294
6.27 Velocity Profiles for the December 7 Storm Wave . . . . .	295
6.28 A Single Wave Cycle from the December 7 Flood Tide . . . . .	296
6.29 Velocity Profiles for the December 7 Flood Tide Wave . . . . .	297
6.30 Wave Spectra for December 11, 1996 . . . . .	298
6.31 3 Minute Time Series, 1400 hours on December 11, 1996 . . . . .	299
6.32 3 Minute Time Series, 0445 hours on December 11, 1996 . . . . .	300
6.33 Velocity Profiles During the December 11 Ebb Tide . . . . .	301
6.34 Velocity Profiles During the December 11 Flood Tide . . . . .	302
A.1 Definition of Terms for the Governing Equations . . . . .	311
A.2 Velocity and Stress Profiles for a Laminar Wave Boundary Layer . . .	324
A.3 Magnitude and Phase of Velocity and Stress for a Laminar Wave Boundary Layer . . . . .	325
A.4 Velocity and Stress Profiles for a Turbulent Wave Boundary Layer . .	327
A.5 Turbulent Stress Profiles Over an Extended Vertical Range . . . . .	328
A.6 Magnitude and Phase of Velocity and Stress for a Turbulent Wave Boundary Layer . . . . .	329

B.1	Backplane . . . . .	334
B.2	P2 {4,6} Multiplexer Board . . . . .	335
B.3	MUX Sequencer Board . . . . .	336
B.4	Dummy Load . . . . .	337
B.5	Tine Board . . . . .	338
B.6	P3 {4,6} Multiplexer Board . . . . .	339
B.7	P3 Cascode Output Signal Amplifier Circuit (COSAC) . . . . .	340
B.8	BASS Transmit/Receive Board . . . . .	341

# List of Tables

3.1	Allowed LLMUX Pairs . . . . .	130
3.2	ULMUX Codes for LLMUX Pairs . . . . .	130
3.3	OR Gate I/O Assignments . . . . .	130
5.1	Keulegan-Carpenter Numbers for Oscillatory Tow Cart Motions . . .	224
6.1	Gain Correction as a Function of Tow Speed and Rotation Angle . . .	264
6.2	Wave Boundary Layer Characteristics on December 7, 1996 . . . . .	293
A.1	Wave Conditions for Laminar and Turbulent Wave Boundary Layers . . . . .	323



In a turbulent boundary layer, kinetic energy from the free-stream flow is converted into turbulent fluctuations and then dissipated into internal energy by viscous action. This process is continual, such that the turbulent boundary layer is self-sustaining in the absence of strong stabilizing effects.

For as long as these facts have been known, fluid dynamicists have sought to understand just how boundary-layer turbulence is generated at the expense of the mean motion, and just how it is dissipated. These are the objectives of studying the internal "structure" of turbulence. Since boundary-layer flows are the technical driver for so many engineering applications, immense human and financial resources have been brought to bear on the problem over many decades of study. The progress made, however, has not been commensurate with the effort expended, reflecting the fundamental complexity of turbulence phenomena.

*Stephen K. Robinson, 1991*





# Chapter 1

## Introduction

### 1.1 The Continental Shelf Wave Bottom Boundary Layer

Conceptually, flow in the continental shelf bottom boundary layer can be decomposed into mean and fluctuating components. It is common practice, in modeling the boundary layer, to solve the two cases separately and assemble the solution from the results. The mean flow is associated with tidal and other quasi-steady motions, with horizontal length scales from one to several tens of kilometers. Temporal scales are also large, typically no less than several hours and extending up to days and, occasionally, to longer periods. On the continental shelf, with depths no greater than 150 *m* to 200 *m*, the orbital velocities of wind driven surface waves penetrate to the bottom and give rise to the fluctuating component of the bottom boundary layer flow. The horizontal length scales of the oscillatory flow are only tens to hundreds of meters and temporal scales are only seconds to minutes. It is the wide difference in the temporal scales that permits the decomposition of the flow and that gives rise to the continental shelf wave bottom boundary layer.

The long time and horizontal length scales of the mean flow permit the current boundary layer to extend to the surface over the shelf unless the thickness is limited by stratification or Coriolis effects. In contrast, the short periods of wave motion

confine the wave bottom boundary layer (WBBL) to a thin sheet of sheared flow below an oscillatory, but essentially irrotational, core. The shear of the mean current remains important above the WBBL, but the oscillatory flow above the WBBL is well described by potential flow and linear wave theory. The vertical extent of the wave boundary layer is scaled by the period and strength of the near-bottom orbital velocity and by the interaction of this flow with the mean current and the bottom. For a wide range of shelf conditions, the wave bottom boundary layer does not exceed 2.5 cm in thickness. Its depth is commonly no more than a centimeter.

The existence of the wave boundary layer has a number of important consequences. Because of the difference in vertical scale, the bottom shear stress associated with the wave flow can be up to an order of magnitude larger than the bottom stress caused by the mean current for comparable flow speeds. Even in relatively mild sea states, the wave induced bottom stress can be sufficient to initiate sediment motion. The wave boundary layer thus plays a central role in the entrainment of sediment into the water column. The strong shear in the narrow boundary layer increases the turbulent dissipation of flow energy so that the apparent roughness of the bottom, as seen by the mean flow, is much larger than would be expected for the scale of the physical roughness elements. The increased turbulence acts to keep entrained sediment in suspension. The mean current, which could not have entrained the sediment, then produces a net advective transport, potentially over the long horizontal scales of the steady flow.

Sediment transport is an area of active experimental and theoretical research. The movement of sediment in the nearshore environment has obvious links to coastal erosion, the maintenance of navigable harbors and channels, and the stability and longevity of shelf based structures. Accurate interpretation of the geological record on the shelf is dependent on knowledge of erosional and depositional processes. Equally important is the movement of contaminated sediments introduced by dumping or dredging operations. The resulting degradation of water quality is a public safety issue both for its effect on recreational use of the sea shore and its effect on commercial fisheries. Less obvious are the implications of down slope transport of sediment on

atmospheric CO<sub>2</sub> levels. Briefly, the hypothesized removal of carbonaceous sediment from the bottom of the shelf based oceanic carbon cycle casts the ocean as a long term sink for carbon re-introduced into the global carbon cycle by the mining and burning of fossil fuels.

Our understanding of these processes is limited by the absence of any high resolution field observations. Many laboratory studies have been conducted, but sediment beds in wave tanks and flumes have demonstrably different behavior than sediment beds on the shelf. Further, these studies were conducted with mechanically scanned, single measurement volume instruments and the measured vertical structure is necessarily an ensemble average over many wave periods. Stochastic stationarity is required over the period of measurement. It might be argued that this is sufficient for the mean flow or for monochromatic waves, the controlled conditions of the laboratory. However, resolution of the vertical structure of the spectral waves typical of the shelf or of the vertical coherence of the turbulent fluctuations at the heart of boundary layer behavior is impossible. Critical aspects of boundary layer flow, in or out of the laboratory, are simply invisible to a sensor with a single measurement volume. Finally, it is difficult to combine waves and currents in the laboratory, particularly at the high crossing angles common on the inner shelf. Field studies of the WBBL have been rare and have been conducted with equipment that is not well suited to the task. In addition to the deficiencies associated with single measurement volume instrumentation, the sensors used have been too sensitive to variations in environmental conditions and have lacked the mechanical robustness necessary for reliable, autonomous operation on the shelf.

Analytical, semi-empirical and numerical models of the wave-current boundary layer have been used to supplement and guide these studies. Field observations are required to establish or constrain the parameters of the models. For example, the hydrodynamic roughness, the roughness of the bottom as perceived by the flow, is a required input to most boundary layer models. Typically, this quantity is not modified as the model converges. The hydrodynamic roughness depends on grain size, bedform shape and scale, and sediment movement. The dependence is complex,

non-linear, and poorly characterized. No field measurements have made a spatially dense velocity profile through the WBBL from which the bottom roughness could be determined. Thus there is no well defined empirical relationship between the hydrodynamic roughness and the physical bottom roughness, a quantity that could be measured directly, as the other initialization parameters are, and used to start the model. Like the laboratory experiments, the models often focus on fairly simple cases, with monochromatic, bi-directional waves, co-directional currents, and relatively simple, non-erodable bottom geometries. Conditions on the shelf are significantly more complicated than those that can commonly be created in the laboratory or in a model. The wave field is neither monochromatic nor bi-directional in general, the angle of the current changes on several time scales and is often large, and the sediment is highly variable spatially and temporally over a range of characteristics.

Resolving the dynamic structure of the wave boundary layer requires a sensor with multiple sample volumes and fine vertical resolution. The sensor must be physically robust and the measurement must be insensitive to the wide range of environmental conditions found on the continental shelf, particularly the near-shore zone. Such an instrument would be able to image wave boundary layer flow, producing profiles from fully concurrent velocity measurements as well as averaged ensembles. Vertically coherent turbulent structures could be investigated and a better empirical relationship between the physical and the hydrodynamic roughness could be established. An instrument with multiple sample volumes could also directly measure the velocity immediately above the wave boundary layer, the forcing function of the linearized governing equation for boundary layer flow. A surrogate measurement of pressure, surface wave height, or the velocity well above the boundary layer could be avoided.

This thesis documents the development, evaluation, and successful field deployment of an instrument, the BASS Rake, specifically designed to support the requirements outlined above. The BASS Rake uses the differential acoustic travel time technique of BASS, the Benthic Acoustic Stress Sensor, applied to a geometry suitable for the narrow confines of the continental shelf wave bottom boundary layer. The instrument uses many sample volumes and the measurement technique has an

established record of accuracy and reliability on the continental margin. The BASS Rake makes it possible to profile a thin boundary layer, in the field, under essentially arbitrary conditions. The method and equipment are robust to fouling, sediment transport through the sample volume, and physical loading by the flow. Steady, monochromatic, and broadband spectral flows can all be meaningfully profiled. Stationary conditions are not necessary. These abilities are currently unique to the BASS Rake.

## 1.2 Research Contributions

The success of this project rests on several technical innovations and intellectual contributions. Each plays an important role in the production of a functional and proven instrument from the elementary conceptual design. The first of these is the integrated mechanical design of the BASS Rake sensor head. Four times support the acoustic transducers and the transmission lines in a geometry dictated by the nature and scale of flow in a wave boundary layer and by the use of the BASS differential travel time technique. The design balances the number and spacing of transducers available to image the flow against minimum wire diameters, electrical and acoustic cross-channel interference, flow disturbance by the sensor, ease of manufacture, and mechanical strength. To achieve that balance, most of the physical elements of the sensor head serve in several roles, often acting in the electrical design as well as the mechanical one.

The accuracy and stability of the BASS measurement depends critically on the electrical characteristics of the transmit/receive circuit and the transmission lines connecting that circuit to a pair of transducers. Full utilization of the BASS Rake transducer array requires a multiplexing interface between the transmit/receive circuit and the transducers. No commercially available interface approaches the characteristics and performance necessary to preserve the quality of the BASS measurement. The second contribution is a flexible interface with extremely low through resistance and an innovative structure that optimizes signal loading, provides significant noise

and cross-channel isolation, and preserves the electrical characteristics of the transmit/receive circuit and the transmission lines. It should be emphasized that the mechanical and electrical designs did not evolve independently. By intent, many features of each design address and solve the identified deficiencies of the other. The operation of the sensor depends on this integrated approach.

Characterizing and understanding the response of a sensor is critical to the development of any instrument. In the case of the BASS Rake, two processes affect the response. The first is velocity averaging over the Fresnel zone, the effective sample volume of an acoustic path. To understand and predict the effects of the averaging process, it was necessary to develop and solve a complex model describing acoustic propagation in a scattering medium on the scale of a BASS Rake acoustic axis. Because the proposed measurement required a close approach to the bottom, it was also necessary for the model to include the interaction of the sample volume and the boundary. It appears that this problem has not previously been solved for these conditions. The complex model was used to predict the circumstances under which Fresnel averaging would produce errors in velocity measurements and those results were confirmed empirically during flume and laboratory testing. A simpler parametric model of the averaging process was also developed and shown to produce substantially the same results with considerably reduced computational overhead. The faster parametric model is now an important tool in the design of the BASS Rake transducer array.

The second, and far more significant process affecting the response of the BASS Rake, is the flow disturbance caused by the tines. The disturbance and the effect on the measurement were predicted, estimated, and bounded using a simple model. The Reynolds number and angular dependencies for both steady and oscillatory flow were determined in a tow tank, confirming the predictions of the model. The results and the explanation based on the model are consistent with the literature for flow around bluff bodies. This is the first time a Reynolds number dependence has been explicitly demonstrated and quantified for any BASS instrument. Once the effect had been determined, a mapping was developed from the measured velocity to the undisturbed

velocity and incorporated in the calibration and accuracy estimate of the instrument. The calibration was then verified in a flume over a sand bottom.

After laboratory evaluation was completed, a field prototype was constructed and deployed outside the surf zone of a local beach. Velocity profiles beginning within millimeters of the bottom were measured inside a 6 *ms* window at one second intervals for a period of several weeks. The instrument proved reliable, recording through several storms and revealing an asymmetric tidal dependence for both the waves and the mean flow. Regular reworking of the bed was observed and the velocity profiles showed clear evidence of the advection of turbulent eddies through the sample volumes. The data set is unique in that it contains concurrent velocity time series, of several weeks duration, with coverage from 1 *cm* to 20 *cm* above the bottom. The demonstrated reliability of the instrument and the return of a field data set were the final, important steps in the development of a functional and now proven instrument design.

### 1.3 Development Chronology and Thesis Outline

The possibility of applying the BASS differential travel time measurement to the wave bottom boundary layer was first raised in early 1993, but not pursued until the middle of 1994. At that time the integrated mechanical design of the sensor head began to evolve. A functioning prototype of that portion of the design underwent very preliminary tests in January of 1995. Those tests demonstrated that a BASS acoustic axis could operate in close proximity to a natural bottom, validating the most basic requirement of the proposed design.

The characteristics of the electrical interface required for full function of the transducer array were specified in the spring of 1995. The constraints were too tight to be met by commercially available circuits and, over several months, specialty components with promising characteristics were identified and a design that could support the requirements was developed. Circuit cards, a chassis and backplane, new versions of the sensor head, and operating software were fabricated and written during the



fall. Most of these activities competed for time with a tight cruise and instrument rescue schedule. The laboratory prototype was assembled and ready for evaluation in January of 1996. Many difficulties, mostly related to the small transducers, were encountered and solved over the course of the spring. Once functional, the flow distortion of the laboratory prototype was mapped in the tow tank. The evaluation of the Fresnel averaged sample volume was also undertaken at this time. Late in the summer these corrections were applied during a comprehensive set of flume tests. Working over a sand bottom, the operation and accuracy of the laboratory prototype were proven.

The BASS Rake field prototype was designed and built during the fall of 1996 and successfully deployed outside the surf zone of a local beach in both November and December. Twenty-four days of field data, velocity profiles recorded at 1 Hz, were extracted from the logger in January. Processing and analysis took place at various times over the winter. The data set shows regular reworking of the sand bed and the growth and evolution of ripples during storm and tide induced bedload transport is apparent. Tidal modulation of both the quasi-steady current and the waves on semi-diurnal, diurnal, and spring/neap time scales is pronounced. The flow was shown to exhibit several asymmetries which could lead to the net advective transport of sediment.

The details associated with the events of this brief summary are documented in the chapters that follow. Chapter 2 focuses on the mechanical design of the BASS Rake. It begins with general background information about some of the major influences guiding the underlying design philosophy. The time and length scales of the wave boundary layer are detailed and the constraints these impose on the mechanical design are identified. The discussion of boundary layer scales is based on information that can be found in the literature. Some of the most important aspects of these studies are summarized and discussed in Appendix A. The discussion in Chapter 2 then turns to models of the continental shelf boundary layer and a lengthy assessment of existing instrumentation. Finally, the mechanical design of the BASS Rake sensor head is described and a preliminary error analysis is presented.

The electrical design, specifically the multiplexing interface between the transmit/receive circuit and the transducer array, is the subject of Chapter 3. The interface specification is presented through a discussion of the characteristics of the existing BASS circuitry and the mechanical design that provide the primary constraints. The interface design is then laid out, beginning at the component level and proceeding to larger circuit blocks. The design includes both the signal path and the more conventional hardware, firmware, and software needed to control operation. A complete set of schematic diagrams is provided in Appendix B. The chapter concludes with a description of the modifications to the basic circuit that are required when measurements are made with particularly small piezoelectric transducers.

The sample volume of a single acoustic axis is determined in Chapter 4. The discussion begins with the classical theories of wave propagation and progresses to the more complex case of propagation through a scattering medium. A mathematical form, a Fresnel integral, describing a BASS differential travel time axis is derived and solved analytically for two canonical cases. A numerical solution for flow in a logarithmic boundary layer is presented and then used to assess a simple parametric model of the averaging process. The effects of Fresnel averaging in the continental shelf wave bottom boundary layer are determined using the parametric model. The simple model is also used to specify the necessary characteristics of the transducer array for accurate imaging within a few millimeters of the bottom.

Chapter 5 documents the implementation and evaluation of the mechanical and electrical designs in the laboratory prototype. Details of the prototype's construction are presented, followed by a qualitative model of the flow distortion associated with the tines. The model accurately bounds the effects of the distortion on the measurement. Tow tank tests used to characterize the Reynolds number dependence of the response in steady flow and Keulegan-Carpenter number dependence in oscillatory flow are described. These results are incorporated in a non-linear sensor calibration mapping and applied to profile measurements made in a flume over a sand bottom. The calibrated measurements are presented and shown to match concurrent measurements made using a laser Doppler velocimeter to a high degree of precision.

The BASS Rake field prototype is described in Chapter 6. The important features of the support frame and the sensor are summarized and the results of a brief immersion in Great Harbor are presented. The tow tank calibration is then detailed. The response of the field prototype is more complex than that of the laboratory prototype because it depends on both the magnitude and the angle of the flow. A description of the near-shore field deployments at Nobska Beach, including visual observations of the bottom at both sites, follows. Selections from the returned field data, several weeks of  $1\text{ Hz}$  velocity profiles, are analyzed and discussed at length to conclude the chapter. A general summary with suggestions for future development and research is presented in Chapter 7.

Finally, a few thoughts on the material selected for inclusion seem appropriate to close this chapter. Research is the work of detectives. It begins with a question. As the question is explored and knowledge deepens, it may be refined or changed. Different avenues appear and decisions are made to explore or postpone their investigation. Some alleys are dead ends, yet they may return considerable information. It is only in hindsight and after reflection that the path behind may appear less ill defined and cluttered. The detective story often reaches a sense of closure, of understanding, at the end. In science that closure is, happily, a transitory experience. A successful development raises new and deeper questions and provides an improved ability to address them. I have tried, in the chapters that follow, to describe not just the instrument that worked, but some of the more important developments and variations that were tried along the way. It would be wrong to regard these as failures. Several will be indispensable to future versions of the BASS Rake. Throughout the development it has been the work done to understand and resolve the difficulties and setbacks that has reliably produced the greatest improvements in performance. This is the nature, and part of the pleasure, of research.

## Chapter 2

# Boundary Layer Scales and the Mechanical Design of the Sensor Head<sup>†</sup>

### 2.1 Introduction and Background

This chapter describes the development of the mechanical design of the BASS Rake sensor head. The characteristic scales of flow in the wave bottom boundary layer (WBBL) on the continental shelf and an evolving understanding of the capabilities of the BASS measurement technique have guided the design process. BASS Rake measurements are made using the BASS differential travel time (DTT) technique developed in and used by this laboratory [90]. This method was chosen because of its high accuracy and linearity and because of its extreme robustness to environmental conditions. These are necessary characteristics for any boundary layer instrument, particularly one intended for field use. The established electronic noise floor of the BASS measurement is  $0.3 \text{ mm} \cdot \text{s}^{-1}$  [53, 90, 92]. Measurements are accurate to 1 %, inclusive of flow disturbance, and linear over the range  $\pm 240 \text{ cm} \cdot \text{s}^{-1}$  [90, 92]. Flow disturbance is a more serious issue for the BASS Rake and will be discussed briefly in

---

<sup>†</sup>Some of the material presented in this chapter was originally published in *Proceedings of the IEEE Fifth Working Conference on Current Measurement* [55].

this chapter and at greater length in Chapters 5 and 6. Extensive field use has shown that BASS performance is not sensitive to the concentration of sediment in the water column. The measurement is influenced by biofouling, but only to the extent that marine growth may increase the flow disturbance. For example, the acoustic signal is not blocked by barnacles or seaweed attached to the transducer face, but flow noise may increase or the turbulent spectrum may change for smaller eddy scales. In one extreme case, the instrument continued to function while an octopus occupied the acoustic volume. Measured velocities were near zero. For storms, other high current and wave events, and use in or near the surf zone, failures are functions of the strength and stability of the support structure. Accurate measurements generally continue in these cases as long as power is maintained. However, rotation to a global Cartesian frame may be compromised by environmental modifications to the support structure. This has also been true of the occasional interaction with fishing trawlers [93].

A BASS DTT measurement is made by a pair of disk shaped, piezoelectric ceramic transducers, facing each other along an acoustic measurement axis. The differential arrival time of signals started simultaneously and traversing the axis in opposite directions is proportional to the average velocity along the axis [90]. The nominal relationship is

$$\Delta t = \frac{2L\bar{u}_{axis}}{c^2} \quad (2.1)$$

where  $t$  is time,  $\bar{u}_{axis}$  is the average along-axis fluid velocity and  $c$  is the local speed of sound, assumed to be constant over the path length,  $L$ . Equation 2.1 involves several simplifications which will be explored more fully in Chapter 4. The relationship, as given and assuming the accuracy of the simplifications, is correct to approximately 1 part in  $10^6$  for oceanic fluid velocities and a BASS sensor as commonly arranged and deployed. Transducer separation is normally 15 cm with a 10  $\mu$ s signal pulse at 1.75 MHz. The 0.3 mm  $\cdot$  s<sup>-1</sup> single measurement accuracy is achieved by running each measurement with both forward and reversed receiver connections to remove bias. A single measurement cycle, inclusive of propagation and processing time, requires 320  $\mu$ s. This allows a wide operational bandwidth and the use of multiple

sample volumes with nearly simultaneous measurements. For example, 100 acoustic axes forming an array could be polled inside a 35 ms window. The reader is referred to Williams, *et al.* [90] for additional information about the BASS DTT measurement.

The primary focus of the mechanical design is the arrangement of these acoustic measurement axes. The geometry of the axes must be tailored to sample the velocity structure of the continental shelf WBBL. That structure is confined to a thin sheet of oscillatory shear flow overlying the sediment bed. For a broad range of shelf conditions, the vertical extent of the WBBL is less than 2.5 cm. A more detailed discussion of wave boundary layer structure can be found in Appendix A. Suitable references, listed in the bibliography, include Kajiura [38], Smith [73], Davies, Soulsby, and King [13], Grant and Madsen [24, 27] and Madsen [46]. This chapter assumes working familiarity with wave-current boundary layer flow and terminology on the part of the reader.

Imaging the velocity structure in such a narrow region requires very high vertical resolution. Observing the dynamic structure, particularly of wave flow during non-stationary conditions, requires multiple sample volumes. No existing field capable instruments meet these requirements. Detailed resolution is available in the laboratory with some instruments or by constraining the flow to produce artificially thick wave boundary layers. However, most of these techniques employ only one sample volume. Profiles are built up over time by mechanically scanning across the boundary layer. This is legitimate in the laboratory where the flow can be controlled and conditions are relatively stationary, but those are not the conditions found on the shelf. The inability to dynamically image boundary layer structure on the shelf, and often in the laboratory, limits further study and understanding of boundary layer processes and their effects.

Multiple sample volumes, spanning the WBBL and also sensing the irrotational oscillatory core immediately above it, have the added advantage of providing a direct, correlated measurement of  $u_\infty$ , the forcing input to the linearized governing equation for the boundary layer.

$$\frac{\partial u}{\partial t} = \frac{\partial u_\infty}{\partial t} + \frac{\partial \tau / \rho}{\partial z} \quad (\text{A.21})$$

The derivation and solution of Equation A.21 are the subjects of Appendix A. A direct measurement would also contribute to greater understanding of boundary layer structure and behavior. Previous measurements have used indirect measures as surrogates for the forcing term. One common practice has been to measure pressure, generally well above the boundary layer. Alternatively,  $u_\infty$  has been determined by applying linear wave theory to surface wave measurements or to velocity measurements. In either case the measurement is made well above the boundary layer.

For the BASS Rake, resolution depends on both the geometry of the acoustic axes and on the resolution of an individual axis. Consideration of the individual sample volume and its effects on the response of an acoustic axis will be postponed until Chapter 4. This is a complex process that has not previously been examined in detail for a BASS sensor. Here it is noted that the extent of the sample volume is largely determined by the acoustic frequency. A conscious decision was made early in this development not to treat the acoustic frequency as a design parameter. This was done for two reasons. First, it was recognized that significant changes to an already tightly constrained transmit/receive (T/R) circuit would be necessary to support the large number of channels and the flexible acoustic axis selection of the proposed BASS Rake transducer array. These changes are the subject of Chapter 3. Other components currently used in BASS have effective operational bandwidth limits less than an order of magnitude above the signal frequency. It was therefore desirable to avoid any additional changes to the underlying BASS circuitry made necessary by large changes in the operating frequency.

Second, the piezoelectric transducers are driven at their resonant frequency. This is fixed during production because it depends on the material properties and physical dimensions of the disk. Therefore, any change in operating frequency requires new transducers. Neither the production delay nor the financial cost are inconsequential. These concerns were particularly cogent during the time and budget limited prototyping phase of the BASS Rake development documented by this thesis. There are, however, potential benefits to a change in frequency that, because of this work, can now be understood and predicted with some confidence. These are explored with a

parametric model in Chapter 4. There it will be shown that a relatively small increase in the frequency of the acoustic signal can significantly improve vertical resolution. Changes to the operating frequency will be undertaken in the future as part of the continuing development of the Rake.

In consequence, the mechanical design discussed in this chapter tries to optimize resolution as a function of the axes geometry defined by the transducer array. The diameter and spacing of the transducers are the primary design variables. Constraints are provided by the magnitude of the flow disturbance caused by the transducers and the structure supporting the array. The electronics, particularly the transducer signal lines, impose a number of constraints that require mechanical as well as electrical solutions. For example, the volume of the transducer wiring harness must be minimized without sacrificing environmental and cross-channel signal isolation. Dynamic flexure of the lines must be eliminated to preserve the zero offset calibration [53]. Ohmic transmission line terminations must be made to both faces of each transducer, yet the T/R face should remain unobstructed to maintain a clean beam pattern and to reduce transmission loss. Mechanical alignment of the transducers and stiffness of the structure should be assured by the design. Issues related to the ease and cost of manufacture should not be ignored. These examples do not constitute an exhaustive list. All of the design variables and constraints are interrelated and each change requires trade-offs to maintain a balanced design.

One of the principal contributions of this research is the integrated design of the support structure and transducer mounting. The transducer support tines of the BASS Rake, which will be described in Section 2.4, successfully addressed the design requirements, resolving many of the conflicting imperatives. The remaining problems were solved by integrating the development of the new electronic interface (Chapter 3) into the overall design process. The success of the design depends on balanced trade-offs between resolution and flow disturbance and on innovations which eliminate many of the electro-mechanical difficulties. The result is a high resolution, multiple sample volume instrument that is robust to field conditions.

This introductory section has presented some of the background information in-



fluencing the design of the BASS Rake. The characteristic scales of the continental shelf WBBL, which this new instrument is tailored to sample, are discussed in Section 2.2. More detailed information about the structure of the wave boundary layer can be found in Appendix A and in several of the references [45, 46, 80, 81]. The motivation to design and construct this instrument arose from the inability to make accurate, detailed structural measurements of the continental shelf WBBL with existing instrumentation. Previous laboratory and field studies have used a variety of techniques to make near-bottom velocity measurements. Section 2.3 examines several of these investigations with regard to the strengths and the limitations of the instruments used, and their suitability for dynamic profiling in the field. The design of the BASS Rake specifically targets several of those limitations. The design of the sensor head is presented in Section 2.4. That section also includes a preliminary analysis of measurement errors caused by flow distortion. Comparisons between the various techniques are made throughout the chapter with a short summary of the principal strengths and weaknesses of the BASS Rake presented in Section 2.5.

## 2.2 Characteristic Scales of the WBBL

Resolving the dynamic structure of the wave bottom boundary layer, as with any process, requires accurate measurements with spatial and temporal spacings that are small compared with the characteristic scales of flow in the layer. A reasonable working target is measurement granularity an order of magnitude smaller than the flow scales to be resolved. It should be recognized, however, that this level of detail may not be possible or that it may be insufficient to prevent aliasing of still smaller features. Flexibility and caution are required in applying any design rule.

Several of the characteristic scales of the WBBL have been estimated here based on the Grant and Madsen (GM) wave-current boundary layer model [24, 27, 45, 46]. [24] and [27] describe early versions of the model. The most recent and complete definitions are found in [45] and [46]. Some features of the GM model are discussed in Section 2.3.1. Additional details can be found in Appendix A. Nominal values

of  $10 \text{ cm} \cdot \text{s}^{-1}$  for the characteristic boundary layer fluid velocity and  $1 \text{ cm} \cdot \text{s}^{-1}$  for the shear velocity have been assumed for the order of magnitude estimates given below. The target resolutions will be used in the assessment of other techniques in Section 2.3.2 and in the design of the BASS Rake sensor head in Section 2.4.

To begin with, the characteristic time scale of the wave boundary layer is the wave period,  $T$ . Surface swell with periods from 5 s to 20 s is ubiquitous on the continental shelf. Sample rates of several Hertz adequately sample the wave motion. Time scales for the turbulent component of the flow range to considerably smaller values and will be discussed later in this section. It should be recognized that the characteristic time and length scales derived from GM, like the velocity profiles, are fundamentally time and phase averaged descriptions of the WBBL flow. This is true of all the semi-empirical models. A model of the turbulence is used in the formulation of the model, but that component of the flow is not part of the final description.

The characteristic vertical length scale is the thickness of the wave bottom boundary layer. Following GM and assuming a laminar flow, the thickness,  $\delta_w$ , is scaled with the kinematic viscosity,  $\nu$ , and the radian wave frequency,  $\omega$ .

$$\delta_w = \sqrt{\frac{2\nu}{\omega}} \quad (2.2)$$

The laminar scale height can range to approximately half a centimeter on the shelf, but is more typically in the range 1 mm to 3 mm. Velocity variations about  $u_b$ , the velocity of the irrotational flow above the wave boundary layer, occur up to three scale heights above the bottom. The layer of laminar shear flow is commonly 4 mm to 8 mm thick. Other investigators have defined the scale height as  $\delta_w = 4\sqrt{\frac{\nu}{\omega}}$  to reflect this [39].

An assumption of turbulent flow in the wave boundary layer would scale the thickness with the shear velocity and the wave frequency.

$$\delta_w = \frac{\kappa u_{*m}}{\omega} \quad (2.3)$$

$\kappa = 0.4$  is von Karman's constant,  $u_{*m} = \sqrt{\tau_m/\rho}$  is the maximum shear velocity,  $\tau_m$  is the maximum bottom shear stress, and  $\rho$  is the density of sea water. On the shelf the turbulent scale height is on the order of a centimeter, typically falling between 0.5 cm and 2.5 cm. There is very little velocity variation about  $u_b$  above  $\delta_w$  in the turbulent case.

The work of Jensen, Sumer, and Fredsøe has shown that the WBBL is laminar, transitional, or turbulent as a function of the wave Reynolds number,  $RE = \frac{u_{bm}^2}{\omega \nu}$  [35].  $u_{bm}$  is the maximum near-bottom wave orbital velocity, the amplitude of  $u_b = \Re \{u_{bm} e^{i\omega t}\}$ . Conley and Inman have argued that, under near breaking waves, the wave bottom boundary layer can alternate between laminar and turbulent flow inside a transitional range of  $RE$  [10]. Below or above that range the layer is purely laminar or purely turbulent. Grant and Madsen [27] (early GM) and Trowbridge and Agrawal [83] expect that the wave boundary layer on the shelf will generally be turbulent. Jonsson [36] and Jonsson and Carlsen [37] maintain that oscillatory flow near the bed under waves in the coastal zone is always rough turbulent. The more recent definition of GM [46] employs both smooth and rough turbulent regimes, which are a reasonable match to the observations of Conley and Inman. The GM model in [46] was also used to calculate the canonical laminar and turbulent wave boundary layer profiles used in Chapter 4 and Appendix A. Given the variability of bottom conditions on the shelf, it is not unreasonable to expect both laminar and turbulent wave boundary layers. Vertical spacing of sample volumes at millimeter or finer intervals is necessary in either case.

On a flat bed there are two horizontal length scales of interest, the wavelength and the orbital excursion amplitude. The wavelength,  $\lambda_w$ , scales the distance over which wave velocities change. Wavelengths on the shelf are typically tens to hundreds of meters. This does not seriously constrain the horizontal extent of the sample volume. The orbital excursion amplitude at the bottom,  $A_{bm}$ , can be calculated from linear wave theory,

$$A_{bm} = \frac{u_{bm}}{\omega} = \frac{a\omega}{\sinh(k_w h)} \frac{1}{\omega} \quad (2.4)$$

where  $k_w$  is the wave number, and  $h$  is the water depth. On the shelf the excursion amplitude can range up to one or two meters, however, values from 10 cm to 50 cm are typical. The field of turbulent fluctuations advected through the sample volume is determined by  $A_{bm}$ . Measurements of turbulent spectra may be biased if the horizontal extent of the sample volume is not kept small compared to the excursion amplitude. To illustrate this, consider the extreme case of a sample volume much longer than  $A_{bm}$ . Each measurement would be sampling essentially the same field of turbulence, frozen in the sense of Taylor's hypothesis and advecting back and forth. However, it should be noted that DTT measurements appear to resolve scales of turbulence much smaller than the path length [29, 75, 84]. This topic is explored in greater detail in Chapter 4. While the turbulent response of these sensors is not fully understood, the path length of a single volume does not appear to be a constraint in the sense discussed here.

The wave excursion amplitude also has some influence on the length scales of bedforms. These structures are produced under waves and currents when the bed is erodible and the bottom stress is sufficient to induce sediment motion. The mechanisms involved are nonlinear and neither fully modeled nor understood [46]. Reworking of the bed on the continental shelf may be largely an episodic process, with the bedforms seen by the flow normally those organized by earlier conditions. Sediment beds are also commonly reworked by biological activity. For the case of wave generated ripples in equilibrium with the flow, Wiberg and Harris have argued that bedform scales are roughly determined by the ratio  $\frac{A_{bm}}{d_g}$ , where  $d_g$  is a representative grain diameter for the bottom sediment [87]. For  $\frac{A_{bm}}{d_g} < \approx 5 \times 10^3$ , the ripple wavelength,  $\lambda_b$ , and the ripple height,  $\eta_b$ , are scaled by  $A_{bm}$ . Examination of the data suggests their conclusion is valid for laboratory ripples with

$$\lambda_b \approx 0.65 A_{bm} \quad (2.5)$$

and

$$\eta_b \approx 0.1 A_{bm} \quad (2.6)$$

The ripple height was generally larger than  $\delta_w$  for the laboratory observations and a well defined wave boundary layer could not form. The field data presented by Wiberg and Harris, for  $\frac{A_{bm}}{d_g} > \approx 2 \times 10^3$ , shows a considerable degree of scatter, particularly for  $\eta_b$ . The mappings from  $\frac{A_{bm}}{d_g}$  to  $\frac{\lambda_b}{d_g}$  and  $\frac{\eta_b}{d_g}$  are steep and do not appear to be single-valued. In the field, many values of the ripple wavelength and height are observed for the same value of  $\frac{A_{bm}}{d_g}$ . The contention that these quantities scale with  $d_g$  for large values of  $\frac{A_{bm}}{d_g}$  is only an order of magnitude approximation for the ripple wavelength ( $\lambda_b \sim 500d_g$ ) and has no validity for the ripple height. The ripple heights observed in the field were reported to be generally smaller than  $\delta_w$  so that a wave boundary layer could form. It should also be noted that there is little agreement between the laboratory and field observations for the transitional range of  $\frac{A_{bm}}{d_g}$  and the two data sets trend differently outside that range. Neither data set could be used to characterize or predict the other. Differences in bed response between the laboratory and the field for flows which otherwise achieve hydrodynamic similitude have been observed by other investigators (e.g., Conley and Inman [10]). The issue of a simple predictive model for ripple geometry on the shelf remains open.

My own observations of ripple geometry, made while diving on instruments at many shelf locations, include ripple wavelengths from 5 *cm* to 50 *cm* and ripple heights from 0.5 *cm* to 15 *cm*. Shapes have varied from sharp crests with shallow, flat troughs to rounded, relatively symmetrical crests and troughs. The latter apparently were produced by earlier, more vigorous flow conditions, followed by slow erosion and spreading of the sharper features. Ripple fields vary from well organized, regular patterns to relatively chaotic, bifurcating assemblages with no uniform orientation. Size, shape, and orientation can change dramatically on very short ( $O(1\text{ m})$ ) spatial scales. Observations of the shelf have also included areas that are relatively featureless on these scales or that exhibit disorganized, distributed roughness due to biological activity or cobbles. Seaweed appears to have a low pass effect, inhibiting the penetration of short period waves to the bottom in some instances. The shelf is dynamic and the topography changes over time at any given site. These observations indicate that bottom features can be a more severe constraint on sample volume size than the

excursion amplitude. The flow near the roughness elements is not, in general, well described by models. Making measurements among bedforms is difficult and requires resolution of both horizontal and vertical velocities on fine spatial scales. The relationship of physical roughness elements to the hydrodynamic roughness, the roughness experienced by the flow, is also poorly characterized. As discussed at greater length in Section 2.3.1 and in Appendix A, that area of investigation would benefit greatly from an ability to measure near-bed velocity profiles simply and reliably on the shelf (and in the laboratory). This is one of the principal tasks for which the BASS Rake is designed.

Other boundary layer phenomena of interest include turbulence, bursting and sweeping, streaming, and the viscous sublayer. It can be shown, on observational and dimensional grounds, that the dissipation rate,  $\varepsilon$ , depends on  $l$  and  $u'$ , the characteristic length and velocity scales of the largest eddies [39]. The largest turbulent eddies scale with the boundary layer thickness and the shear velocity [39, 46] so the dissipation scales as

$$\varepsilon \sim \frac{u'^3}{l} \sim \frac{u_{*m}^3}{\delta_w} \quad (2.7)$$

For typical shelf values the dissipation rate is on the order of  $1 \text{ cm}^2 \cdot \text{s}^{-3}$ . Based on a continuation of the dimensional argument, Kolmogorov's microscale for viscous dissipation is

$$\eta = \left( \frac{\nu^3}{\varepsilon} \right)^{\frac{1}{4}} \quad (2.8)$$

This is the length scale at which turbulent kinetic energy, which has cascaded down from larger to smaller eddies, is dissipated by viscous forces. For the dissipation rate given above, the viscous microscale is a few tenths of a millimeter. Measurement intervals would need to be smaller than  $\frac{\eta}{2}$  to resolve the full extent of the inertial and dissipating subranges of the turbulent spectrum. The dissipation scale is not resolvable by the existing techniques discussed in Section 2.3.2. In the inertial subrange lower values of  $k\eta$  will be accessible to the extent that  $\delta_w$  and  $u_{*m}$  are well resolved. Some additional comments on this topic, particularly as it applies to the BASS Rake, are warranted.

The desirability of multiple sensing volumes was established in Section 2.1. However, the circuit complexity, transducer size, and wiring harness bulk associated with submillimeter transducer spacing over several centimeters makes vertical spacing finer than millimeter scale doubtful in this situation. In the presence of a net advective flow, however, finer measurement intervals can be achieved temporally as the field of turbulent fluctuations, assumed frozen, is advected past the sensor. This approach will work for the horizontal flow in the wave boundary layer. Therefore, while the turbulent spectrum for  $k_v\eta \rightarrow 1$ , where  $k_v$  is the vertical turbulent wave number, may not be directly accessible from the near simultaneous measurements along a vertical profile, the spectrum for  $k_h\eta \rightarrow 1$ , where  $k_h$  is the horizontal turbulent wave number, should be. Turbulence in a shear layer is expected to be anisotropic only for values of  $k_t\eta \ll 1$  (i.e., for  $k_t z = O(1)$ , where  $k_t$  is the turbulent wave number and  $z$  is height above the bottom). The turbulence should be isotropic for larger values of  $k_t\eta$  in the inertial subrange. It will be the noise level of the velocity measurement and the effective size of the sample volume that limit the measurement of the spectra. As noted, the electronic noise floor of BASS is  $0.3 \text{ mm} \cdot \text{s}^{-1}$  and the DTT measurement accurately records turbulent scales on the order of  $1 \text{ mm}$ . However, the intrusive geometry of the BASS Rake distorts the flow and raises the noise floor to  $O(3 \text{ mm} \cdot \text{s}^{-1})$  (see Chapter 5). If the microscale depends only on  $\varepsilon$  and  $\nu$ , then dimensional analysis suggests a time scale

$$t_\eta \sim \left(\frac{\nu}{\varepsilon}\right)^{\frac{1}{2}} \quad (2.9)$$

which is on the order of  $10^{-1} \text{ s}$  and thus a velocity scale

$$u_\eta = \frac{\eta}{t_\eta} = (\nu\varepsilon)^{\frac{1}{4}} \quad (2.10)$$

which is on the order of  $1 \text{ mm} \cdot \text{s}^{-1}$ . Relatively high sampling rates,  $20 \text{ Hz}$  to  $30 \text{ Hz}$  would resolve  $t_\eta$ , are possible in bursts, with data written directly to RAM. Slower serial transfers and storage to disk could be postponed. Velocity resolution on the order of  $10^{-1} \text{ mm} \cdot \text{s}^{-1}$  is indicated. Those sample rates are realistic, but the finest scales of velocity resolution are not. The sample rates and velocity accuracy are

sufficient to resolve the primary wave flow where periods range from 5 s to 20 s and discrimination of velocity differences on the order of  $1 \text{ mm} \cdot \text{s}^{-1}$  may be required. However, the measurement volume is not easily reduced to the scale of  $\eta$ . Resolution of the inertial subrange will be limited by the effective dimensions of the DTT sample volume for turbulence.

Bursting and sweeping are phenomena arising from the complex evolution of the three dimensional vortical structures observed by flow visualization methods in turbulent wall boundary layers. Detailed reviews have been written by Head and Bandyopadhyay [32] and by Robinson [65]. A summary discussion can be found in Kundu [39]. McLean, *et al.* [44] and Nikolaides, *et al.* [60], among others, have contributed detailed observations. Briefly, vortices oriented parallel to the boundary and perpendicular to the flow are distorted and stretched away from, bursting, or towards, sweeping, the boundary. The phenomena are quasi-periodic and increase the vertical exchange of horizontal momentum, the Reynolds stress. The sweeping of higher speed water closer to the boundary has been observationally linked with the initiation of sediment motion in a wave boundary layer [10]. Semi-empirical relationships predicting the period and the cross-stream and streamwise spacing are given by Conley and Inman [10].

$$\frac{T_s u_{bm}}{\delta_w} \approx 5 \quad (2.11)$$

$$s^+ \sim \frac{s u_{*m}}{\nu} \approx 100 \quad (2.12)$$

$$l_s = T_s u_{bm} = 5 \delta_w \quad (2.13)$$

$T_s$  is the period,  $s^+$  and  $s$  are the dimensionless and dimensional cross-stream spacing, and  $l_s$  is the streamwise spacing. These expressions were originally derived for unidirectional, turbulent flow, but they are in reasonable agreement with wave boundary layer observations made in near breaking waves [10]. For shelf conditions, assuming these relationships are valid, bursting and sweeping occur at a frequency of approximately 3 Hz with spacing of 1 cm cross-stream and 5 cm along stream. Sampling rates near 10 Hz and sample volumes smaller than 1 cm are indicated.



Streaming is a second order steady flow that occurs in oscillatory boundary layers where asymmetries exist. The horizontal variation of the horizontal velocity over a wavelength causes a small, periodic vertical velocity because of continuity. If the two velocities are not precisely in quadrature, due to dissipation for example, net vertical transfer of horizontal momentum occurs. The result is a steady horizontal flow. Batchelor suggests that the streaming velocity,  $u_s$ , is scaled by the irrotational oscillation velocity, the wave frequency, and the wavelength [5].

$$u_s \sim \frac{u_b^2}{\omega \lambda_w} \quad (2.14)$$

Equivalently, recognize that streaming is a function of the convective acceleration terms in the equations of motion. Those terms are on the order of  $\frac{u}{c_p}$  compared to the retained terms in the linearized boundary layer equations. This derivation can be found in Appendix A.  $u$  may be identified as the maximum wave orbital velocity immediately above the boundary layer and  $c_p = \frac{\omega}{k}$  as the phase velocity of the waves. On the shelf  $u_s$  is on the order of  $10^0 \text{ mm} \cdot \text{s}^{-1}$  to  $10^{-1} \text{ mm} \cdot \text{s}^{-1}$  with the larger portion of the range more common in shallow depths. These velocities are up to an order of magnitude below the velocities of the turbulent microscale and would be difficult or impossible to detect.

When the boundary is sufficiently smooth, a viscous sublayer forms beneath the logarithmic layer of a boundary layer flow. Caldwell and Chriss made measurements at 200 *m* in a quasi-steady tidal flow using a heated thermistor [8, 9]. Their analysis of the measurements strongly suggested the existence of a 6 *mm* viscous sublayer in the ocean. However, aspects of that analysis have since been questioned [27] and the discussion of Section 2.3.2 casts some doubt on the accuracy of the measurements. An instrument capable of resolving a laminar wave bottom boundary layer would also be able to resolve a steady viscous sublayer of a few millimeters thickness. However, the thickness of the viscous sublayer scales with the kinematic viscosity and the shear velocity [39].

$$\delta_v \simeq \frac{5\nu}{u_{*m}} \quad (2.15)$$

The viscous sublayer thickness beneath the wave bottom boundary layer on the shelf will be less than a millimeter. As previously discussed, it is doubtful that spatial resolution below millimeter scales can be achieved.

## 2.3 Previous Work with Existing Instruments and Techniques

Research into the structure of the wave boundary layer in the laboratory has primarily focused on monochromatic, bi-directional waves over relatively simple, non-erodable bottom geometries. The comparatively rare field studies have been largely confined to the near-shore region beyond the surf zone. Taken as a whole, the literature in this area is fairly rich and the investigations cited below represent only a fraction of the published record. Additional references can be found through the sources cited here. Particularly notable in this regard are the concise summary listings in Agrawal and Aubrey [2] and in Trowbridge and Agrawal [83]. Several of the data sets that do exist are collected and replotted in Madsen and Wikramanayake [45] and in Madsen [46].

### 2.3.1 Models of the Wave-Current Boundary Layer

The structure and direction of the laboratory and field studies have been guided by a number of analytical, numerical, and semi-empirical descriptions of the wave and wave-current boundary layers. A brief digression to discuss some of these models is appropriate. The models selected for mention were chosen to provide some historical perspective on developments in this field and are not intended as an exhaustive list.

Based on earlier experimental work dating from the mid 1940s to the mid 1960s, Kajiura proposed a three layer eddy viscosity model for a turbulent oscillatory boundary layer in 1968 [38].<sup>1</sup> His earlier (1964) theoretical solution for the turbulent case

---

<sup>1</sup>The eddy viscosity and eddy viscosity models are discussed in Appendix A. In the sense used here, the eddy viscosity is a model expressing the turbulent stress (primarily the vertical flux of momentum known as the Reynolds stress,  $-\overline{u'w'}$ ) in terms of the velocity field in a turbulent boundary layer. In general, a functional relationship between the stress and the flow variable(s) is needed to close the set of equations describing the velocity field in a boundary layer. The kinematic

was featured in the new model. Interestingly, that earlier work apparently represents the first solution to this problem. In the 1968 model, constant values of the eddy viscosity were used in inner and outer layers with a linear variation in a transition region. This was done in analogy to the wall, log, and defect layer structure of a steady turbulent boundary layer with the characteristics of the wave turbulence averaged over a full cycle. The Kajiura model reproduced the gross features of the boundary layer, but could not reproduce the structural details observed in the laboratory. Applicability was limited to monochromatic waves with no current and Kajiura considered the characterization of the bottom roughness unsatisfactory. It should be noted that characterization of the bottom roughness, particularly under waves and combined wave-current flows, is still not a solved problem and remains an area of active research (see, for example Mathisen and Madsen [47, 48], Appendix A, and further comments below). Despite its shortcomings, Kajiura's work had considerable influence on later developments and several of his simplifying assumptions are retained, with modification, in present models of the wave-current boundary layer.

In 1977, Smith proposed a fairly detailed, two layer eddy viscosity model for sediment transport on the continental shelf [73]. The model was semi-empirical, explicitly combining the limited experimental results available with simplified formulations of the physics of the fluid flow and the fluid-sediment interaction. The Smith model was originally limited to co-directional currents and waves, but is otherwise quite similar to the 1979 Grant-Madsen model then under development [24]. The most visible difference between the two models is Smith's use of a continuous, piecewise linear, eddy viscosity as opposed to the discontinuous, piecewise linear, eddy viscosity of the GM model. The Smith model is notable for introducing a "proper basic fluid mechanical input" [73] into a sediment transport model and for its attempt to characterize the interaction of fluid and sediment under the complicated natural conditions of the con-

---

viscosity provides closure in laminar flow where the viscous stress is proportional to the spatial derivative of the velocity across the boundary layer. The eddy viscosity provides an analogous closure for turbulent flow. However, the eddy viscosity is itself a function of the flow, rather than being a material property of the fluid. Thus the governing equation for a turbulent boundary layer is, in general, non-linear.

tinental shelf. However, Smith himself noted several weak points in the model. These were a direct result of both the generally incomplete understanding of the physics of turbulent boundary layer flow and fluid-sediment interaction and the paucity of experimental data. It may reasonably be argued that the general understanding of these phenomena is not significantly greater today, largely for the same reasons. Good experimental data for unsteady turbulent boundary layers, particularly for combined wave-current flows, remains scarce. Field measurements showing some evidence of a wave boundary layer are limited to three recent near-shore experiments, all with relatively coarse vertical resolution [17, 74, 83]. Further discussion of these investigations can be found in Section 2.3.2.

More recently, numerical models have been used to describe the wave-current boundary layer. The eddy viscosity is usually determined as the product of characteristic velocity and length scales. Depending on the complexity of the model, these quantities may be functions of distance from the boundary, wave phase, and the velocity. Typically, the velocity scale is the square root of the turbulent kinetic energy. The length scale may be formulated in the sense of a Prandtl mixing length (see Appendix A). The turbulent energy dissipation often enters into these formulations as part of the closure. One example is the 1988 numerical model of Davies, Soulsby, and King [13]. In this model the system of equations is closed by explicit equations for the turbulent kinetic energy and the characteristic length scale in terms of the flow variables. The boundary conditions on these quantities require that the eddy viscosity vary linearly with distance from the boundary as the bottom is approached. Linear variation of the eddy viscosity across the boundary layer is the form normally assumed by semi-empirical models such as those of Smith and Grant-Madsen. The accuracy of these models is a result of the dominant influence of the flow very near to the bottom on the overall behavior of the boundary layer. As noted, numerical characterization permits temporal variation and greater complexity in the formulation of the eddy viscosity. For these reasons numerically determined velocity profiles are often assumed to be accurate descriptions of the time or phase averaged flow in the boundary layer. As such, numerical models are often used to test the accuracy of

the simpler semi-empirical models [45].

The semi-empirical GM model, which has been followed here, was first developed in the late-1970s [24]. The model has evolved since that time and been evaluated using higher order solutions [80, 81], numerical models [45, 46], and experimental results [26, 47, 48]. The most recent formulation can be found in Madsen [46] and, with some comparison to other models, in Madsen and Wikramanayake [45]. GM is readily applied to field and laboratory data, including spectral waves and waves with a crossing current at an arbitrary angle. Agreement with laboratory measurements is generally good [25, 47, 48] and the model has made reasonably accurate predictions about the current boundary layer above the wave boundary layer on the continental shelf [26]. It enjoys a wide, if not universal, degree of acceptance among the semi-empirical models. However, the physics of turbulent boundary layers is far from fully understood [65]. Madsen has, on several occasions, assessed the accuracy of wave-current boundary layer models, including GM, at no greater than 10 % to 20 % [46, 47, 48]. This assessment should not be neglected when applying these models.

One particularly weak area is the specification of bottom roughness. In common with other boundary layer models, the bottom roughness experienced by the flow is a user input to the GM model. The hydrodynamic roughness is known to depend, sometimes quite strongly, on the geometry, physical scale, and active motion of the roughness elements and bedforms [25, 46, 47, 48]. However, while the equivalent roughness of closely packed, immobile cobbles may simply scale up from that of closely packed, immobile sand grains, the equivalent roughnesses of distributed cobbles, biologically generated sand piles, ripples of various shapes, heights, and wavelengths, and actively moving bedload and bedforms is not well understood. The data base, derived largely from laboratory experiments, remains sparse and the results show considerable scatter. As a result, the equivalent roughness is not well modeled, even in an empirical sense. Estimates of the roughness for typical field conditions are, at this time, only approximations based on experience and intuition. This concern is discussed at greater length in Appendix A. One task of the BASS Rake, with its ability to make vertically detailed, near-bottom velocity profiles, will be to address

this issue.

Several cautionary notes are also in order here. Recall that these models describe the time and phase averaged behavior of the flow. Measurements include a turbulent component of the velocity field that is not part of the model solution. Therefore, measurements must be averaged for legitimate comparison to the models. Averaging has the added benefit of reducing the stochastic measurement errors caused by inherent sensor noise. Fortunately, the electronic noise level and the errors associated with flow distortion by the sensor head are quite small,  $O(0.3 \text{ mm} \cdot \text{s}^{-1})$  and  $O(3 \text{ mm} \cdot \text{s}^{-1})$ . Additionally, measurements along a single line, such as a BASS Rake profile, will not be able to map the complex, changing, three dimensional structure that turbulent flow is generally recognized to exhibit [32, 44, 60, 65]. However, resolution of some statistical properties of turbulence in the WBBL is possible with the BASS Rake. This was discussed in Section 2.2. Further discussion of the structure of the WBBL and the GM model can be found in Appendix A and the references.

### 2.3.2 An Assessment of Existing Instrumentation

The characteristic scales of flow in the continental shelf WBBL were discussed at some length in Section 2.2. For the purposes of this assessment it should be added that conditions on the continental shelf are typically more complicated than those that can commonly be created in the laboratory or in a model. For example, the near-shore wave field is spectral rather than monochromatic. Fortunately, wave energy is often predominantly localized in one or two frequency bands within the broader spectral distribution, permitting some simplifying assumptions in applying models to the data. Examples of near-shore wave spectra can be found in Agrawal and Aubrey [2], Conley and Inman [10], Lukasik and Grosch [42], and the BASS Rake field prototype data presented in Chapter 6. Similarly, while the near-shore wave field is not uniaxial, there is a strong tendency for wave velocities to be shoreward. However, steady and quasi-steady near-shore tidal currents tend to flow along-shore. Farther off-shore the wave field is still spectral and flow directions are generally less constrained. Crossing waves and currents are not readily achieved under most laboratory conditions and

are not featured in many of the semi-empirical models. GM is one of the exceptions.

It is important, particularly when making a profile measurement, to recognize that conditions on the shelf are not generally stationary. One of the limitations inherent in many of the instruments described below is dependence on a single measurement volume which must be mechanically scanned through the boundary layer to obtain a profile. The scan rate is limited by flow disturbance considerations and by the noise level of individual measurements. Many of these devices require averages over several to many measurements to achieve good velocity resolution. It may take several hours to construct even a coarsely resolved profile. Vertical correlations through the boundary layer are not available using these devices and profiles are necessarily ensemble averages over many wave cycles. Clearly such a profile is only meaningful during stationary conditions. Multiple sample volumes spanning the WBBL also permit a direct, correlated measurement of  $u_\infty$ , the forcing velocity above the wave boundary layer. This was discussed in Section 2.1. These are the primary scientific motivations for multiple sample volumes in the design of the BASS Rake. A practical objection to mechanical scanning is the well established propensity of moving parts to foul and jam in the ocean environment. Densely spaced, multiple sample volumes are not necessarily an option with other techniques. Restrictions are commonly due to difficult operational requirements exacerbated by the additional sensors or prohibitive increases in flow distortion. The operational requirements and flow distortion created by the BASS Rake sensor head are largely independent of the number of acoustic axes.

Shelf bottom characteristics are spatially variable over a wide range of length scales and, because sediment is erodable, variations on a range of time scales also occur. As mentioned above, Conley and Inman reported an asymmetry in bed response between wave crest and wave trough observed in the field which is not reproduced in laboratory experiments that otherwise achieve hydrodynamic similitude [10]. Agrawal and Aubrey observed a similar asymmetry in turbulent intensity during the wave cycle [2]. The general conditions outlined here and in previous sections demonstrate the need for detailed and accurate *in situ* measurements and suggest the characteristics

needed to successfully image the WBBL. Fine scale measurement capabilities alone are not sufficient; a sensor must be able to function reliably in the field, not just in the laboratory.

#### 2.3.2.1 Hot Wires, Hot Films, and Heated Thermistors

The first class of sensors to be considered includes hot wires, hot films, and heated thermistors. These devices are sensitive primarily to flow speed and only weakly to flow direction. The lack of directionality requires *a priori* knowledge of flow conditions to resolve. Such knowledge is generally available in the laboratory, but not necessarily in the field. Mildly directional versions can be made using multiple elements in a crossing geometry. Because of the sensor supports, these arrangements will have a strongly preferred principal direction of flow. They will not be omnidirectional and may not be usable in oscillating flow. The crossing geometry also increases the sample volume, which is otherwise determined by the dimensions of the element and the boundary layer that forms around it. Note that the sample volume is a function of the flow. Characteristic dimensions of 0.5 mm and larger are typical. The shape of the volume depends on the geometry of the sensing element and its orientation to the flow. These are necessarily intrusive sensors. The sensing element and its supports always cause some level of flow distortion. The degree of disturbance depends strongly on the geometry of flow, element, and supports.

These sensors function by measuring heat loss to the surrounding fluid. The loss of heat increases with both the relative velocity and the differential temperature between the sensing element and the fluid. Temperature sensitivity is reduced by calibration at expected ambient temperatures and by holding the heated element  $10^{\circ}\text{C}$  to  $20^{\circ}\text{C}$  above expected ambients. The operating temperature is held constant by monitoring the element's electrical resistance,  $R$ , and adjusting the electrical current,  $i$ , to keep  $R$  constant. The heat loss is  $i^2 R$ . Each element must be carefully and individually calibrated to determine the mapping from heat loss to fluid speed for a given ambient temperature range. Ideally, calibrations should be obtained in turbulent or oscillating flows to include the effects of heat transfer through the unsteady boundary layer



around the element in the dynamic frequency response [28]. Changes in the heat transfer properties due to fouling, contamination, and corrosion can be rapid, particularly for smaller elements. Such changes cause the non-linear response to drift, sometimes dramatically, and can quickly invalidate the measurements.

These devices have a number of features and capabilities which have led to widespread use for fluid dynamic measurements. They also have several limitations which do not recommend them for field use on the continental shelf. Hot wires can resolve a few tenths of a millimeter per second in the laboratory by averaging many measurements taken at high sampling rates,  $O(10^2 \text{ Hz})$ . Resolution degrades under less controlled conditions. Their normally small size and wide bandwidth allow broadband measurements of turbulent spectra. However, they are quite fragile physically and can be extremely sensitive to fouling, contamination and corrosion. Calibration can be lost in a few seconds, depending on the concentration and type of suspended material. Fouling is particularly rapid in natural flows where suspended material is commonly filamentous. Ocean water, because of the salt content, enhances contamination and corrosion compared to fresh water use. The delicacy of the wires makes cleaning, especially by the mechanical means that might be employed cyclically in a field instrument, rather dubious. Hot wires have a long history of successful laboratory use, commonly in wind tunnels where the rapidity of fouling is greatly reduced. Some manufacturers suggest that their use be restricted to gaseous flows, however, they have been used in encapsulated form in the ocean by Gust [28]. Gust used coaxial metal tubing to increase strength at the expense of greatly reduced bandwidth. The time constant of the response was estimated to be a significant fraction of a second. Reduction of the bandwidth to a few Hertz is a common result when heated sensing elements are made more rugged for field use. Fouling, contamination, and corrosion remained significant problems for the metal-clad hot wires and *in situ* cleaning repeated at three minute intervals was necessary. Deployments were restricted to a few hours. A large array of these devices would present many operational problems, particularly in the energetic, near-shore zone where concentrations of suspended material are often high. The lack of strong directionality, the need for a principal direction of

flow, and the restriction to very short, often labor intensive, deployments also suggest they are not suitable for dynamically imaging the WBBL.

Hot films are larger and mechanically tougher than hot wires. Bandwidth is reduced, but still amply sufficient for turbulent spectra. Flow speed resolution is typically millimeters per second to centimeters per second, achieved by averaging at high sample rates. As with hot wires, fouling is a critical problem and calibration can be lost in less than a minute. Hot films can be mounted on a substrate, often quartz, to improve ruggedness or fouling characteristics, but the thermal mass and conductivity of the substrate can limit response time or restrict use to a preferred flow direction. For example, fouling can be slowed by mounting the film as a frustrum band on the surface of a conical substrate oriented into the flow. This geometry inhibits entanglement of filamentous suspended material, but it can only be used in unidirectional flow and would have little utility in an oscillatory boundary layer.

Hot films have been used successfully in several field experiments. Hart, Clark, and Jasentuliyana used hot films to construct profiles in the turbulent boundary layer above rocks in a fresh water stream [30]. A single film, mounted on a hand held rod, was oriented into the prevailing flow and manually positioned at each of six heights from 1 mm to 10 mm above the surface of the rock at selected locations. The film was cleaned by hand using a fine, sable hair brush immediately before each data run. Data were collected at 256 Hz for only 4 s in each run because of the rapid loss of calibration due to fouling. Measurements were channeled directly to a PC for bulk storage and processing. After each set of runs the film was cleaned in a 5 % solution of acetic acid. Once or twice each day the film was calibrated in the field by towing it through a still water bath. The films broke frequently during use and handling. These precautions were clearly very labor intensive and were not always effective. The authors report that fouling by "particulate and dissolved contaminants" and bubble formation on the heated film caused a number of variations in the data. Variations were also caused by changes in the discharge rate of the stream during data acquisition. Both effects were controlled for with replicate data sets. Each data point is an average over many realizations and depends, to some extent, on a steady and relatively stationary flow.

Those conditions are not generally found on the shelf. The quality of this data set is due to great care in acquisition and processing by the authors and to the nature of the flow and the field location. Their experiment was successful, but Hart, *et al.* contend, based on their experience, “that hot-film anemometry is unsuitable for field use.” Their procedures are clearly unsuitable for instrument deployments of any duration on the continental shelf. This would be particularly true for the interesting fluid dynamic conditions of a storm and for instruments with many sensing elements.

Conley and Inman used a pair of hot films to measure near bed velocities in a few meters of water under near-breaking waves [10]. The experiment took place adjacent to a pier so that data generated by the 128  $Hz$  sample rate of the sensors could be cabled directly to a shore based computer. The films were attached to a rod that could slide vertically on a light frame. The mounting gave the films 1  $cm$  along-shore and vertical separations and oriented them to measure on-shore and off-shore flow. The frame also supported a pressure sensor and an EM current meter at a height of 50  $cmab$ . Before each run the rod was raised by divers to place the hot films level with the current meter for *in situ* calibration and then lowered so that the bottom film was approximately 1  $cmab$ . Run durations appear to be limited to 60 s. Operation required a number of other adjustments before each run to account for the dynamic nature of the fluid-sediment interface at this site. All adjustments were apparently made by divers. The elevation of the pressure and EM current sensor precluded direct measurement of  $u_{\infty}$  in the absence of a dynamically measured profile.

The films used by Conley and Inman were designed by TSI, Incorporated for use in electrically conductive fluids such as sea water [10]. The manufacturer states that salt water, particularly sea water, tends to be the liquid that most limits lifetime of these sensors. Operating lifetime in water, even in clean water, varies from a few minutes to tens of hours and frequent cleaning is suggested [96]. The failure mode is generally rapid delamination of the protective (quartz) coating. In their reported results, Conley and Inman focus on visual records of the bottom obtained from a video camera mounted on the frame. The discussion of hot film calibration and behavior is abbreviated and readers are referred to an earlier paper by coworkers for

a more detailed assessment. In the referenced paper, Flick and George reported many difficulties with breakage and calibration drift [16]. They only used the films because they felt that no other instrument then available (1990) could be used successfully in the surf zone due to the presence of bubbles and debris. They specifically included laser Doppler velocimeters and acoustic techniques in that assessment, adding that the size of these instruments and the accompanying flow disturbance also precluded their use. One is left with the clear impression that they would happily have dispensed with the hot films forever given some alternative. Their experience seems similar to that of Hart, *et al.* [30].

Quite recently (1994), Foster used a diagonally offset, five element array of hot films to profile from 1 *cmab* to 5 *cmab* with 1 *cm* vertical spacing [17]. Measurements were made in 2 *m* depths under breaking and near-breaking waves close to the crest of a sand bar and adjacent to a pier. All data were cabled to shore for logging and processing. The array was calibrated *in situ* with an EM current meter mounted 14 *cmab* for 10 minutes before each run. The array was then removed from the water to be repositioned vertically on the sensor mount, and redeployed for 34 minutes. The effective sample rate was 256 *Hz*. The films were fabricated by TSI and the manufacturer's evaluation of the Conley and Inman films applies here as well.<sup>2</sup> There is no discussion of sensor cleaning or response drift during the deployment. One 34 minute run was selected by Foster for analysis. Changes in sensor response due to suspended sediment were estimated, based on a theoretical model, to be less than 5 % and therefore ignored. This is not unreasonable given the estimated 10 % to 20 % accuracy of WBBL models [46, 47, 48]. One film exhibited unstable gain, possibly due to fouling, and could not be used. Acceptable data returned by the remaining four films varied from 23 % to 68 %. The EM current meter record from 14 *cmab* was used to derectify the flow speeds registered by the hot films. The results show

---

<sup>2</sup>For the record, the author does not wish to imply by this any criticism of TSI in particular. TSI produces a selection of fine sensors that are widely and successfully used in a variety of situations. TSI should be applauded for their honest evaluation of the performance limitations that are simply inherent with sea water immersion. Heated element sensors, regardless of the manufacturer, have many significant problems associated with their use in the ocean. An alternative technique that avoids those limitations is needed.

some evidence of a wave boundary layer several centimeters thick. However, the measurements are quite noisy, with reported standard deviations on the order of  $10 \text{ cm} \cdot \text{s}^{-1}$  for  $u_{bm} \approx 40 \text{ cm} \cdot \text{s}^{-1}$ . This is larger than the calculated shear velocities. The averages do not achieve a strong match with the models. Of course, the weakness in this case may well be the models. Conditions during the experiment were dynamic and rapidly changing. The operational difficulties associated with hot films are again evident. These near-bed dynamic profile measurements, a first, also demonstrate the difficulty of interpretation inherent in real flows and, therefore, the need for more and better data.

As mentioned above, the accuracy of hot wires and films is, to some extent, achieved by averaging over the many realizations made possible by high sampling rates. The sampling bandwidth is also useful in studies of turbulence. However, the high data rate has a tendency, not insurmountable, but certainly exhibited in the experiments discussed here, to tie the instrument to shore based power and logging facilities. The need may be inescapable for an instrument of this class built with many sampling elements. An infrastructure requirement of this nature, like the labor intensive approach, sharply restricts possible sites of WBBL study. This will also be characteristic of the optical instruments to be discussed below.

BASS instrumentation is not limited in this manner. BASS has very high single measurement accuracy [53, 90, 92] and an established record of multiple sample volume ocean current and turbulence measurements [19, 54, 75, 90]. A typical deployment includes 20 to 28 acoustic axes and the work to be presented in Chapters 3 and 5 demonstrates the feasibility of an increase to approximately 100 paths. The high single measurement accuracy sharply reduces the sample rate and therefore the data storage requirements. Until disk capacities increased, BASS also employed *in situ* processing [19, 54, 91]. Fast electronics allow for very low power operation [90]. Other characteristics of BASS were discussed in Section 2.1. Many long duration, unattended, multiple sample volume deployments have been successfully completed on the shelf in recent years [93]. Chapter 6 describes the unattended, twenty-four day deployment of the BASS Rake field prototype in 3 m of water, 30 m off-shore

from a local beach. Profiles were continuously recorded at 1 Hz for a range of calm and storm conditions for most of December, 1996. The unit was self-contained, inclusive of battery power and data logging. The deployment was terminated only when strong wave forcing during a storm deformed the anchors, pulled them out of the bottom, and rolled the entire quadrapod frame onto its side. Although no longer in the boundary layer, those acoustic axes that were not physically sheared off the tine, during the period of active slamming while the anchors were torn out, continued to function.

The use of heated sensing element devices extremely close to a boundary raises an additional concern. The boundary layer that forms around the heated element contributes significantly to the calibrated response function of the sensor. As the bottom is approached, the sensor boundary layer is deformed, altering the response of the instrument. Sufficiently close to the bottom the calibration can no longer be considered accurate. If the sensing element is in contact with the bottom, a boundary layer no longer surrounds it and calibration is lost. Attendant fouling and contamination from the contact may prevent restoration of the response by simply raising the element. In many cases, the contact by hot wires and films will permanently damage the element [30]. Proximity may be a problem for the two hot film studies described above, nevertheless, the data sets are of interest and clearly demonstrate some of the trade-offs associated with the use of these devices in the field. The concluding remarks on the metal-clad hot wires of Gust, above, are applicable to the work with hot films as well. The performance of a BASS acoustic axis in the immediate vicinity of the bottom is discussed at length in Chapter 4.

Heated thermistors have also been used successfully in the ocean. They operate under some of the restrictions necessary for hot films and wires, however, heated thermistors are commonly encapsulated. In this form they exhibit greater mechanical robustness than films and wires, but much reduced bandwidth. The time constant of the response may be a significant fraction of a second. A correction can be made in the case of a sinusoidal, or nearly sinusoidal, signal [42], but accuracy is affected for more complicated inputs, especially at higher frequencies. Encapsulation can decrease, but

not eliminate, sensitivity to fouling and contamination. Like hot wires and films, heated thermistors are not directional. Accuracy, in the laboratory, is similar to hot films [9]. Sampling rates are typically much lower, often a few Hertz or less, because of the slow response [8, 9, 42].

A widely cited series of experiments was conducted in 1978 and 1979 by Caldwell and Chriss [8, 9]. A heated thermistor was vertically traversed by a crank and piston over a repeated 1 minute cycle. The profiler was attached to a frame sitting on the bottom at a depth of 200 *m*. At the top of the traverse the heated thermistor was approximately 20 *cmab*. At the lower extreme the sensor was 1 *cm* to 2 *cm* below the fluid-sediment interface. The thermistor signal and the piston position were recorded every 1.5 *s*. These values vary somewhat depending on the experiment. In one case, for example, a profile with approximately 1 *cm* vertical resolution from 1 *cmab* to 20 *cmab* and finer resolution below that was constructed by averaging the results of all traverses taken during one hour near peak tidal flow. The averaging was also used to remove the considerable wave signal. The direction of flow was established from a Savonius rotor and vane mounted on the frame approximately 60 *cmab*. A fixed brush was positioned near the top of the traverse with the intent of removing contaminants from the sensor as it passed. The thermistor was calibrated after the experiment by towing in an annular bath chilled to the ambient temperature recorded at the site. No *in situ* calibrations were performed.

Based on the constructed profiles, the authors argued that they had detected a 6 *mm* thick viscous sublayer [8] and evidence for multiple scales of bottom roughness [9]. The conclusions were based on a small portion of the collected data and have since been questioned by Grant and Madsen [27]. Grant and Madsen argued that the method of analysis was flawed and, in particular, did not support the conclusion of multiple roughness scales. The detection of a viscous sublayer is difficult to evaluate. Cleaning and calibration procedures are not described at any length by the authors and there is no mention or discussion of the effects of fouling and contamination due to repeated insertion into the bottom. It would be quite surprising if this was negligible. Realistically the data are a little weak and the conclusion should

be questioned; the evidence for a sublayer depends on the response of the thermistor when the boundary layer around it is maximally distorted and fouling is greatest. It is noted that a linear velocity profile indicating a viscous sublayer was apparently not seen in other parts of the data set and no similar measurements or detections have since been made by other investigators. Although this study appears to be flawed, it is interesting that the thermistors were sufficiently tough to continue functioning despite the rough handling. These devices could, presumably, survive in the surf zone, but their lack of directionality and low bandwidth would still prevent them from dynamically imaging the WBBL.

In 1963, Lukasik and Grosch unequivocally detected the presence of a wave boundary layer beneath ocean swell using a heated thermistor [42]. The measurement was made under swell in 12 *m* of water approximately 400 *m* off-shore of Block Island, Rhode Island. This apparently little known study is the earliest field measurement of a wave boundary layer of which I am aware. The forcing pressure above the boundary layer was sensed by a pressure sensor mounted flush with the bottom. This is consistent with a linear governing equation (Appendix A), which assumes the dynamic pressure is constant across the (thin) bottom boundary layer. Note that, unlike most field experiments, this is a direct measurement of the forcing term in the linearized governing equation for the boundary layer, rather than a surrogate velocity or pressure measured well above the boundary layer. Constant velocity tows in a small tank were used to calibrate the steady state response. The frequency response of the sensor was also determined in the laboratory and a correction for the estimated time constant,  $\tau_{tc} = 0.3\text{ s}$ , was applied to the measurements. Swell periods ranged from 5 *s* to 18 *s* with peaks at 8 *s* and 13 *s*. The thermistor was positioned by divers and data were collected for 30 minutes at each of four heights. Instrument outputs were continuously recorded by stylus on paper tape and manually digitized at 1 *Hz* in post-processing. During digitizing the flow speed sensed by the thermistor was manually mapped to velocity perpendicular to the shoreline. The authors confined themselves to a frequency domain analysis because of the spectral nature of the swell.

The detection was based on the phase difference between the pressure signal and



the derived thermistor velocity. The highest thermistor position was 38 *cmab* and the two signals were shown to have the same phase at that height. This is the expected result. At its lowest position, the thermistor was half buried in the sand bottom. Clearly, because of fouling and element boundary layer distortion, this placement changed the response of the sensor. This is not discussed by the authors and their claim that this measurement uniformly averages the velocity over the exposed height is not supportable. However, it is primarily the magnitude of the response that changes. The phase of the response will be weakly affected as long as the response time,  $\tau_{tc} = 0.3\text{ s}$  away from the boundary, remains small compared with the wave period. Even if this is not the case and  $\tau_{tc}$  is raised significantly by the contact, the detection of the wave boundary layer remains valid. Independent of changes in  $\tau_{tc}$ , the response to flow past the thermistor must show a phase lag,  $\phi_{lag} < 90^\circ$ ; heat loss has a first order transfer function [62]. The bottom velocity measured by Lukasik and Grosch led the forcing velocity, as measured by the pressure sensor, by approximately  $10^\circ$ . A lead of this magnitude could only be caused by the bottom velocity leading the forcing velocity. A phase lead is predicted by models of both laminar and turbulent wave boundary layers and is observed in laboratory studies [35, 46]. The measurement was imprecise for the reasons noted, but the evidence for this early field detection of a wave boundary layer is quite clear.

It is interesting, from the perspective of 1997, to note that Lukasik and Grosch were only aware of the laminar solution for the wave boundary layer when they published in October 1963. The detailed laboratory measurements of Jonsson were published in the proceedings of a conference held in London in September 1963, one month earlier, and were almost certainly not available to Lukasik and Grosch as they wrote their paper [36].<sup>3</sup> Kajiura did not publish his analytical solution for the turbulent WBBL, predicting a  $30^\circ$  phase lead, until the following year, 1964. The

---

<sup>3</sup>Actually, it is unlikely that the Jonsson measurements would have alleviated the confusion had they been available. The wave boundary layer generated by Jonsson in an oscillating water tunnel was intended to be fully turbulent. It should have been, given the value of the wave Reynolds number, but the measured phase lead of the boundary layer velocity was clearly that of a laminar WBBL. The measurements of Jonsson and this curious result are discussed in Section 2.3.2.2

laminar phase lead at the bottom is  $\approx 45^\circ$ , but the turbulent phase lead, predicted by modern models (e.g., GM) and confirmed by experiments (e.g., [35]), is only  $\approx 10^\circ$ . Without that knowledge, Lukasik and Grosch were unable to explain the phase lead of  $10^\circ$  to  $15^\circ$  they observed, a phase lead now known to be characteristic of a turbulent or transitionally turbulent wave boundary layer. Having said this, it should also be noted that the phase lead and flow regime in the WBBL during this experiment cannot be determined with great precision because of the contact with the bottom. The actual lag of the sensor is bounded, but unknown. It may have been larger than the expected value for which the authors corrected and the actual phase lead of the boundary layer may have been larger than the reported  $10^\circ$  to  $15^\circ$ . WBBL phase is discussed in Appendix A. Observing the relative phase of the WBBL is one of the preliminary targets of the BASS Rake field prototype discussed in Chapter 6. Some of the difficulties associated with this target are discussed in Chapter 4.

The discussion of heated element sensors has been lengthy because their popularity and wide usage required a detailed assessment. They possess a number of good qualities for boundary layer measurement and have been used with some success in the field to produce interesting and important results. They also have a number of weaknesses, most notably lack of directionality, fragility, and extreme sensitivity to fouling, which sharply restrict their utility in the field. This is clear from reports, both published and unpublished, of their use. Most of those problems would be greatly increased in an instrument with many simultaneous sample volumes. This should not be interpreted as a general indictment of this class of instruments; heated elements are clearly the right sensor for some situations. However, dynamically imaging the WBBL on the continental shelf is arguably not one of them. Rather, in common with the techniques below, these sensors are a complementary approach, each bringing a particular set of strengths to the problem of understanding the bottom boundary layer.

### 2.3.2.2 Mechanical Techniques

In the late 1960s, Sleath developed an instrument to sense near bed wave speeds in a wave tank [71, 72]. The sensor operated by measuring the tension in a long (7.62 *cm*), thin (.0254 *mm*), glass fiber held parallel to the bed and perpendicular to the direction of flow. In its favor, this approach has a sample volume with a small vertical extent and was robust in laboratory usage. Fairly high accuracy was obtained, primarily by phase averaging over several realizations under the relatively stationary conditions achieved in the laboratory. The response is non-linear and the output was subject to drift. Sleath compensated for the offset in the laboratory by taking the value of lowest tension in monochromatic flow as a new zero. Drift changes in other calibration parameters are not discussed. As with the heated element sensors, the measurement is necessarily intrusive. Some level of flow distortion is always caused by the sensing element and its supports. The fiber senses only speed and must be oriented perpendicular to the flow. Flow direction must be known in advance. The response to oscillating flow was mildly asymmetric.

Sleath made measurements with high vertical resolution within a millimeter of impermeable and deep sand beds in a laminar wave boundary layer. He is apparently among the first to accomplish this. Wave parameters were selected such that no sediment motion occurred [72]. Strikes by grains suspended in the water column or saltating during bed load transport would have corrupted the tension measurement. Clearly fouling would have a similarly detrimental effect. Both are known hazards of near bed measurements in the field. The cantilevered bar and strain gauges used to sense the tension in the fiber would also be subject to loss of calibration through fouling. Multiple wires would compound these problems and increased the flow distortion. In short, objections to the use of heated element sensors in the field apply here as well.

Surprisingly detailed sets of wave boundary layer profiles were made in 1963 by Jonsson [36] and in 1976 by Jonsson and Carlsen [37]. The measurements were made with a micropropeller spinning about a vertical axis in an oscillating water tunnel. The propeller was illuminated from one side by a small lamp and a photodiode on

the other side sensed variations in the intensity of forward scatter from the lamp. The output signal from the diode was counted to derive angular velocity. The sensor had been developed previously by Jonsson. Calibration with known flows defined a mapping to fluid speed. As with all of the devices discussed so far, the propeller was a speed sensor and flow direction had to be determined by other means. The lamp, propeller, and diode were located along a line perpendicular to the oscillating velocity to reduce the flow disturbance. Measurements at each height in the constructed profiles were phase averages over 25 or 50 wave periods. The apparatus did not have sufficient bandwidth to be sensitive to turbulent velocities.

Both studies used large, two dimensional roughness elements to create artificially thick wave boundary layers with vertical extents of several centimeters [36, 37, 46]. The propeller had a vertical extent of 5 mm. The vertical extent of the sample volume over which velocities were averaged with some weighting is presumably at least that large. The results of the parametric model presented in Chapter 4 show that this is too large to make accurate measurements in the thinner wave boundary layers typical for the continental shelf. The closest approach to the bed with this instrument was approximately 5 mm. While it would not be impossible to adapt this technique for use in the field, it would still lack directionality and sensitivity to fouling and contamination would clearly be high. The lamp, propeller, and diode cause a significant distortion of flow even when perpendicularly oriented. Multiple sample volumes could not be closely space because of the physical size of the components and the resulting disturbance of the flow. While modern optical fibers and smaller propellers could reduce the distortion, susceptibility to fouling and widening of the response deadband would increase.

There is a curious aspect to the Jonsson/Jonsson and Carlsen measurements. This was briefly touched on during the discussion of the Lukasik and Grosch experiment in Section 2.3.2.1. Jonsson and Carlsen based their characterization of the wave boundary layer they generated as fully turbulent on a boundary layer Reynolds number,  $\frac{u_{bm}\delta_w}{\nu}$  [36]. In the GM model it is the wave Reynolds number,  $\frac{u_{bm}A_{bm}}{\nu} = \frac{u_{bm}^2}{\omega\nu}$ , that characterizes the transition. The relationship of  $\delta_w$  to  $A_{bm}$  involves other, variable,

parameters of the flow so that the connection between the two Reynolds numbers is not clear. However, the wave Reynolds number can be easily calculated from the reported data and is at least on the order of  $10^6$ . According to the results of Jensen, Sumer, and Fredsøe, *undertaken in the same forced oscillation water tunnel used by Jonsson and Carlsen*, this should indeed be fully turbulent flow with a  $10^\circ$  boundary layer phase lead [35]. The problem, as mentioned in Section 2.3.2.1, is that the measurements of Jonsson and Carlsen show a  $40^\circ$  to  $45^\circ$  boundary layer phase lead [36, 37]. Jonsson actually states that the lead is  $25^\circ$  [36]. The assertion is apparently based on the measured velocity maxima. However, the smoothed velocity curves fitted to the measurements distinctly exhibit the larger,  $40^\circ$  to  $45^\circ$ , lead. The smaller value, even if correct, would not resolve the problem. It should also be noted that the near-bottom velocity measurement was made  $3.5\text{ mm}$  above the theoretical bed. The phase lead there is expected to be less than the maximum value by  $5^\circ$  to  $15^\circ$ .

Appeal can be made to only a few differences between the experiments. Jensen, *et al.* made their measurements using a two axis laser Doppler velocimeter<sup>4</sup> This is an unlikely explanation given the  $8\text{ s}$  to  $10\text{ s}$  wave periods used and the number of wave cycles over which measurements were averaged. Jensen, *et al.* operated the tunnel closer to its natural resonance and were thus able to suppress second and third harmonics to negligible levels. The contribution of the second and third harmonics to the velocity was 10% in the Jonsson and Carlsen experiments. Those components of the velocity were therefore in the laminar range of the wave Reynolds number, but it is unclear how they could have changed the overall phase lead. Maximum wave velocities were similar, although those of Jonsson and Carlsen tended to be larger. The remaining candidate is the roughness elements. Jonsson and Carlsen used two dimensional, triangular, concrete ripples either  $0.6\text{ cm}$  or  $2.4\text{ cm}$  high. Jensen, Sumer, and Fredsøe used both the smooth bottom of the tunnel and sheets of tightly packed sand one grain thick and glued to the bottom. Grain diameters were either  $0.35\text{ mm}$  or  $1.5\text{ mm}$ . Assuming there is not something fundamentally flawed in the measurements reported by Jonsson and Carlsen, this behavioral difference of the flow has

---

<sup>4</sup>The operation and performance of LDVs are described in Section 2.3.2.4.

profound implications for laboratory research where the use of large, two dimensional, roughness elements is common. Many, perhaps most, studies do not make correlated measurements of the forcing and bottom velocities. The phase difference would not be readily apparent. This may, in fact, have some bearing on unresolved discussions in Madsen [46] and in Mathisen and Madsen [47, 48].

In closing this section it is interesting to note that the 1963 measurements by Jonsson were used extensively by Kajiura in the formulation and testing of his model of the turbulent wave boundary layer [38].

### 2.3.2.3 Acoustic Instruments

Acoustic Doppler current profilers (ADCPs), first built in the early 1980s, are widely used from a variety of stationary and moving platforms to measure the velocity profile over a range of spatial distances. Meters to tens or hundreds of meters are typical. The measurement is made by range gating the back scattered acoustic energy from paired beams angled away from the nominal line of the profile. The Doppler frequency shift of the return in each range bin indicates the along beam velocity averaged over the beam width and range gate defined volume. Geometry and an assumption of flow homogeneity for the volume of water spanned by the beams yields the velocity vector. The energy is scattered from suspended material and bubbles. A typical angle of inclination from the profile line for the oppositely tilted beams is  $30^\circ$ . Commercial units with up to 128 range gates, ranges adjustable from 5 m to 200 m, and update rates of 4 Hz to 5 Hz are available. Operating frequencies are generally a few hundred kilohertz. Shorter range, downward looking units have been mounted a few meters above the bottom to profile the bottom boundary layer on numerous occasions. Greatly in their favor, ADCPs sense multiple sample volumes within a small window of time and are relatively non-intrusive. They have proven field capability and ruggedness. However, ADCPs are not well suited to the task of resolving the small scales of the WBBL.

To begin with, the transducers of an ADCP are mounted in a common central housing and the beams diverge as range from the housing increases. The beam sepa-

ration at the bottom for the downward looking installation described is much larger than normal excursion amplitudes. In some cases it may be a significant fraction of a wavelength. The assumption of flow homogeneity needed to derive the velocity is simply not valid. This weakness has actually been addressed and solved by Hay and co-workers [31]. They mounted the transducers separately and oriented them inward to ensconce a common volume above the bottom. Spatial resolution depends, in this case, on the beam width and the range gate.

ADCP measurements depend critically on averaging many realizations to achieve accuracy on the scale of the sample volumes. Acquisition of a sufficient suite of realizations can occupy a significant fraction of a wave cycle. Standard deviations of several tens of centimeters per second are the norm. Range resolution is limited by the operating frequency. A practical determination of the Doppler shift requires many cycles of the returned acoustic signal. The range bins of most ADCPs extend over at least a meter along the beam. For example, Gartner and Cheng report a recent study undertaken in San Francisco Bay using a downward looking, broad band ADCP specifically design for bottom boundary layer work [22]. The standard deviation of the recorded velocities was  $0.7 \text{ cm} \cdot \text{s}^{-1}$ , achieved by averaging the measurements taken over a 2 minute window. Resolution of wave frequencies would greatly increase the measurement error. To achieve better range resolution the operating frequency of this unit is  $1200 \text{ kHz}$ . In the high resolution mode the range bins are  $5 \text{ cm}$  long. Recall that  $\delta_w$  is on the order of  $1 \text{ cm}$  and that the velocity structure contained within that thickness needs to be resolved, potentially with millimeter per second accuracy. Patently this cannot be done with a  $5 \text{ cm}$  range bin.

Even if range resolution were improved, two characteristics would still limit the closest approach of a range gate to the bottom. Because the beam must approach the bottom at an angle to have any sensitivity to horizontal velocities, one edge of the mainlobe wave front scatters off of the bottom first and saturates the receiver. A similar problem is caused by the sidelobes of the beam pattern. For some ranges of the grazing angle, the bottom return of the sidelobe arrives before the near-bottom return of the mainlobe. Empirically, the closest approach to a boundary is one to two

range gates. The ADCP of Gartner and Cheng, with 5 cm range resolution, could make measurements no closer than 9 cm to the bottom.

A similar profiling instrument is the single beam, pulse-to-pulse coherent Doppler sensor described by Veron and Melville [85]. Rather than measure the frequency shift of range gated backscatter, the coherent Doppler measures the pulse to pulse phase change of range gated backscatter caused by the between pulse, along beam, displacement of scatterers. The sensor was designed to measure turbulence in the inertial subrange under waves over short ranges,  $O(1\text{ m})$ . The physical pulse length is 7 mm ( $9.3\text{ }\mu\text{s}$ ) at 1.72 MHz, the range bins are approximately 1 cm long, and the beam is narrow. Reported laboratory and field results show that the instrument is sensitive to eddies as small as 1 cm to 2 cm. This represents a significant improvement on the sample volume of the ADCP, but 1 cm is still too large for the WBBL. As with the ADCP, receiver saturation by sidelobes or the angled mainlobe would preclude measurements within a few centimeters of the bottom.

The acoustic Doppler velocimeter (ADV) is a relatively new instrument, first described for laboratory use in 1993 [7] and subsequently adapted for field use [3]. A 10 MHz signal with a pulse duration of  $4.8\text{ }\mu\text{s}$  is emitted from a centrally placed transmitter. Backscatter from suspended material is received at three locations equally spaced around the transmitter and focused on a common sample volume 5 cm beyond the transmitter. The angle between the transmitted and received beams is  $30^\circ$ . Coherent pulses are repeated at several hundred Hertz and the velocity vector is derived from the pulse to pulse phase change in the backscatter signal at each receiver. These realizations are averaged to reach a reasonable level of accuracy and output as measurements at up to 25 Hz [7, 86]. This is the technique used by Veron and Melville, but applied to a distributed transducer geometry to sense the complete velocity vector rather than the single along beam component. Like the ADCP, the ADV is field capable and relatively non-intrusive. Flows roughly aligned with the longitudinal axis of the pressure housing are strongly distorted and should be avoided. While the ADV depends on the presence of scatterers to operate, it has a wide dynamic range of acceptable concentrations. This is not generally an issue for either laboratory or



field use.

The most immediate drawback is dependence on a single sample volume. The problems associated with constructing a profile under those circumstances have already been discussed. The sample volume itself is an ellipsoid extending 9 *mm* along the transmit axis, commonly perpendicular to the boundary, and 6.5 *mm* across the axis [7, 86]. Measurements are averages of the returns from scatterers throughout this volume. There is no localization within the volume. These dimensions are essentially the same as the wave boundary layer thickness. Intuitively, this is too large a volume to profile the WBBL. This intuition is confirmed by the detailed calculations for volumetric averaging of velocities in Chapter 4. The ADV can sample within 5 *mm* of the boundary as measured from the center of the sample volume. Below that level the bottom is in the sample volume and the strong return swamps the rest of the signal. Voulgaris and Trowbridge have shown that below 2 *cmab* the ADV measurement of Reynolds stress in a steady boundary layer deviates from theoretical predictions, while agreeing with predictions above that level[86]. This may be due to the size of the largest turbulent eddies, a function of distance from the boundary, compared to the size of the averaging volume. Their measurements of the mean flow were unbiased down to 1 *cmab*. Measurement accuracy, as measured by standard deviation, varied with programmable characteristics controlling the number of realizations and the elapsed time averaged into a measurement from 0.5 *cm · s<sup>-1</sup>* to 2.5 *cm · s<sup>-1</sup>* [86]. The ADV is a very capable instrument. It has finer spatial resolution than a standard BASS, though considerably lower single measurement accuracy. It does not, however, appear to be suited to WBBL measurements.

The bistatic coherent Doppler velocity profiler (BCDV) described by Stanton [74] is structurally and functionally similar to the ADV. The ADV is, to some extent, derived from the BCDV design. The description of ADV operation above is applicable here with the important addition that the BCDV is a profiling instrument. Velocity profiles are measured by range gating the back scattered signal at each receiver. The minimum vertical extent of the sample volumes is limited to 1.6 *cm* by the duration of the transmitted pulse. Improvements to this resolution limit are planned. Stanton

reports profiles beginning within 1 *cm* of the bottom and continuing to 40 *cm* in 5 *cm* increments. Notably, this instrument has performed successfully in the field. Like the ADV, the BCDV has a very high sample rate and measurements are averaged to improve accuracy. This is a very promising approach, but improvements in sample volume size, vertical resolution, and closest approach to the bottom are required before the BCDV will be able to image velocity structure in a narrow, 1 *cm* to 2 *cm*, wave boundary layer.

The standard configuration of BASS [90] and the geometrically and operationally similar VDV [79] should be mentioned, briefly, to complete this section on acoustic instruments. It is clear from the size and geometry of the crossing acoustic axes of these sensors that their closest approach to the boundary is, at best, several centimeters, approximately half the path length. Measurements this close to the boundary may be accurate for the average flow, which varies on scales that are large compared to the volume spanned by the axes. However, for measurements of the turbulent component of the flow, the implicit spatial average over the angled axes actually imposes a minimum approach of approximately two path lengths. Closer to the boundary the most energetic turbulent eddies, which scale with distance above the bottom, are small enough to be hidden by the spatial averaging. The near bed deviations from theory of the measured Reynolds stress observed by Voulgaris and Trowbridge with the ADV may be related to this phenomenon.

#### 2.3.2.4 Optical and Flow Visualization Methods

Visualizing the flow by introducing hydrogen bubbles, smoke, dyes, or particles has a long history in the study of fluid dynamics, often simply to allow observers to watch and study the flow by eye. Movie and, more recently, video records could be made of the flow for later review at variable speeds. Still photographs with long exposures to show particle tracks were also common. This work was largely qualitative and focused on understanding the nature and behavior of flow in the laboratory. Quantitative information was occasionally extracted from the movies with considerable labor. Phenomena such as the onset of turbulence in a steady boundary layer and the

separation of flow around a bluff body or a wing section are representative examples. The broadly accepted conceptual model of turbulent structure in boundary layers is due in large part to these investigations. Numerical models of turbulence have also played an important role. The review articles by Head and Bandyopadhyay [32] and by Robinson [65] discuss the observations and results of many of these studies. Still photographs can be found in most textbooks of fluid dynamics (e.g., Batchelor [5], Kundu [39], Lamb [40]).

In the late 1980s and early 1990s, advances in automated techniques for the rapid and reliable analysis of images made quantitative measurement of two dimensional velocity fields in flows seeded with neutrally buoyant particles possible. This approach is commonly referred to as particle image velocimetry (PIV) or particle tracking velocimetry (PTV), depending on the family of algorithms used to process the images. Digital techniques (DPIV and DPTV) using CCD based cameras are now in common use and hybrid techniques are being developed and applied [11, 41, 89]. For example, Veron and Melville used DPIV in the laboratory to evaluate the performance of their pulse-to-pulse coherent Doppler instrument [85]. The process underlying all of these variations is straightforward. To make a measurement a thin, two dimensional sheet of the fluid is illuminated using a pulsed laser and repeatedly imaged. The velocity is determined from the displacement of illuminated particles on sequential images and the elapsed time between images. Sample volumes with a characteristic length of a millimeter or less are possible. Velocity accuracy depends on such factors as the size of the particles and speed of the flow, image timing, the physical extent of the image pixels, and the processing algorithm. Accuracy levels of 1 % of the full scale velocity have been reported [11, 41]. This is a very promising approach for boundary layer measurements, particularly given the information content of a two dimensional measurement.

Despite the potentially high accuracy, the focus with this technique has remained somewhat qualitative. Results are often stated in pixel, rather than physical, coordinates as system development continues. Some emphasis has been placed on the study of vortical patterns in the flow to elucidate turbulent structure in the boundary layer.

A caution is offered by Robinson who has noted that different statistical approaches to the analysis of two dimensional data can infer markedly different three dimensional structures [65]. There is a more significant problem associated with the average flow. Velocity components perpendicular to the plane of illumination can cause severe errors. The errors increase sharply with the percentage of out-of-plane particles. Values above 15 % can cripple some algorithms while others are more robust [11]. This restricts the use of DPIV/DPTV to two dimensional flows and requires fairly precise alignment. This presents little difficulty in the laboratory, but field use would be difficult or impossible under those conditions. DPIV/DPTV is an immature, but actively evolving technology, and new algorithms may alleviate this constraint.

DPIV/DPTV processing benefits from evenly distributed, uniform particles. Some algorithms are optimized for particle size, concentration, and reflectance properties [11]. Ambient particles will tend to degrade performance because of the wide spectrum of characteristics they present [21]. Additionally, natural particles such as sand or bubbles are not neutrally buoyant so they introduce biases in the vertical velocity field. Removing the bias would require determination of the density of each particle in the field. This is a nontrivial task and currently beyond the capabilities of DPIV/DPTV systems [21]. Seeding the continental shelf with uniquely tagged artificial particles is not a realistic option. Other operational difficulties presented by field use are the flow disturbance caused by the physical bulk of the equipment. Increasing the distance from the sample volume is constrained by the optical turbidity of coastal waters. Power and data storage requirements are substantial and a physical connection to shore may be essential. For example, a gigabyte hard disk can store only two minutes of video images. Magnetic tapes can store several hours of video images. Of course, processing even that much data also presents some difficulties. Field deployments of this technology would almost certainly yield interesting results, but a substantial development effort is necessary first.

The laser Doppler velocimeter (LDV) is the instrument of choice for many experiments and measurements. Among studies already cited in this chapter, Jensen, Sumer, and Fredsøe [35], McLean, Nelson, and Wolfe [44], Mathisen and Madsen [47,

48], and Voulgaris and Trowbridge [86] all used LDVs to make their measurements or to evaluate the performance of other instruments. An LDV was also used in testing the BASS Rake laboratory prototype described in Chapter 5. The LDV has high bandwidth and can be used for turbulence measurements. A representative sample rate is  $25\text{ Hz}$ . Like the ADV, high measurement accuracy,  $O(1\text{ mm} \cdot \text{s}^{-1})$ , is achieved by averaging many realizations acquired at a significantly higher rate. As used in the laboratory, often in flumes and wave tanks with optically transparent walls, the instrument is non-intrusive. LDVs typically have only one sample volume. Profile construction requires stationary conditions and vertical correlations across the boundary layer of turbulent and other components of the flow cannot be measured. The problems this presents for field use have already been discussed.

The sample volume is defined by the intersection of two relatively narrow laser beams. An ellipsoid  $1\text{ mm}$  long and  $0.3\text{ mm}$  across is representative. The crossing beams generate an interference pattern and the changing intensity of light scattered from particles as they pass through these fringes is Fourier transformed using an FFT. A component of velocity in the plane of the beams is determined from the Doppler frequency of the changes. Multiple components of the velocity can be measured in the volume using additional, linearly independent, beams. Three beam, two axes, LDVs are common. Either ambient or seeded particles can be used, but the range of allowable concentrations is limited to approximately four orders of magnitude. This is much more narrow than the operational range of the ADV. If the concentration is too low, there is seldom a particle in the small measurement volume. Measurement dropouts are frequent and accuracy becomes unacceptably low. At high concentrations there are two modes of failure. Commonly the beams are so severely attenuated that there is simply no signal. More rarely, the number of particles simultaneously crossing the fringe pattern flattens the intensity fluctuations to such an extent that detection in the transform domain is ambiguous or impossible. Naturally occurring variations in particle size can also cause dropouts.

While they are primarily laboratory instruments, LDVs have been adapted for field use. Two related studies will be discussed here. The link is the common author,

Agrawal, who has worked to develop field capable, laser based sensors over many years. In 1992, Agrawal and Aubrey made wave and steady velocity measurements with a two axes LDV above sand ripples in 2.5 m of water [2]. The instrument housings were bulky and required alignment across the axis of flow to reduce distortion. The distortion was further reduced by using a long, in water transmission path length of 95 cm. Because of the resulting attenuation the instrument could only be used in reasonably clear water. Divers were used to raise and pivot the LDV so that phase averaged profiles could be constructed. Data editing for dropouts and bad data points was a relatively major undertaking. This experiment is part of the ongoing development of the LDV for use in the continental shelf WBBL and several improvements have since been made by Agrawal. However, the data rate necessarily remains high and power requirements are significantly greater than for acoustic instruments. Both characteristics tend to tie the LDV to shore based power and data collection facilities.

In 1995, Trowbridge and Agrawal constructed a four point WBBL profile over a sand bottom well outside the surf zone [83]. They used a two axes, downward looking LDV operated in a backward scattering mode. In this orientation the instrument measured both components of the horizontal velocity. Fiber optics were used so that electronics housings could be placed well away from the single sample volume. Most of the optical path was occupied by a tapered, clear plastic tube filled with clean water to reduce sensitivity to high sediment concentrations. The ambient water path length was only 1 cm. Sampling was controlled through an operator interface to a microprocessor in the electronics package. The sample volume was placed sequentially at each of six heights from 0.5 cmab to 16 cmab. Data were recorded at 25 Hz for 90 s at each height. Thus each profile required 18 minutes to construct. This is clearly an improved design.

Unfortunately, the coastal zone is a difficult environment. The instrument was deployed for two days and eventually returned a few hours of data. Conditions were generally not stationary, and there were continuous problems with attenuation of the beams despite the short path length. Usable data were collected at only four of the six heights and due to a failure in the stepper motor controlling the mechanical scan

the actual heights above bottom are not certain. One axis of the LDV failed. The data return rate for the other axis, largely due to beam attenuation by ambient, suspended material, averaged only 10 % to 20 %. Turbulent spectra could not be computed because of the irregular performance and low effective sample rate [83]. Agrawal maintains that the beam attenuation can be overcome by increasing the transmitted power. This would make shore power essential. Additionally, it is not clear that this expedient alone would sufficiently alleviate the problem. It might, for example, decrease the signal-to-noise (S/N) ratio. In contrast, a standard BASS sensor, mounted on the LDV tripod to act as a velocity reference, operated continuously at 10 *Hz* throughout the deployment. The genesis of the BASS Rake can be traced directly to the profound difficulties observed and experienced by Trowbridge in conducting this experiment.

Veron and Melville have noted that it is only acoustical and optical techniques that permit spatially dense measurements of fluid velocities. It is their opinion, based on laboratory experience with LDV and DPIV/DPTV instrumentation, that "optical techniques, while very attractive, may be less robust than acoustical systems in the active wave zone." [85] Further development of optical techniques should be undertaken, but their statement is an accurate assessment of the current capabilities of these instruments.

The experiments cited here are intended to be representative of the field and laboratory applications of these sensors. The list is by no means exhaustive. The assessments include all of the techniques and instruments, of which I am aware, that might be applied to the task of making velocity measurements within the wave bottom boundary layer on the continental shelf. Criticisms should be viewed in that context. These are, in general, very capable, high performance instruments. They were simply not designed or intended for use in the field or within the narrow wave boundary layer. The BASS Rake was designed from the beginning for that use. Improvements in the capabilities of the other instruments will, no doubt, continue. The optical instruments are particularly promising in this respect. Finally, it should be recognized that the BASS Rake has limitations of its own. It would be incorrect to view these techniques

as competitors. The various sensors form a suite of complementary approaches that can be collectively applied to the dynamic behavior of the ocean on the shelf.

## 2.4 The BASS Rake Sensor Head

The mechanical design described here focuses on the geometry of the acoustic axes, the integrated mount and support structure of the transducers, and the flow distortion created by that structure. The geometry is specifically tailored to investigation of the wave bottom boundary layer and the driving flow immediately above it. Figure 2.1 is a schematic representation of the basic sensor geometry for a full capability field instrument. The transducers are mounted in four slender vertical tines arranged in a square. Two intersecting acoustic DTT paths are used to determine the horizontal velocity vector at each measurement level. The name "BASS Rake" was bestowed on the instrument because of the general appearance of the sensor head.

The development of the BASS Rake has, to date, proceeded incrementally through several prototyping steps. Both the final design and the notable intermediate stages will be described here. Three pairs of tines were actually fabricated for laboratory evaluation. The first pair, designated P1 (Prototype 1), demonstrated that the mechanical design could actually be produced and that the basic concept was valid. It was shown that a BASS acoustic axis could, without great difficulty, make velocity measurements a few millimeters above a natural sand bottom. The P1 transducers were connected to the transmit/receive circuit using enamel coated transformer wire. The flow distortion caused by the sensor head is minimized by making the tine diameter as small as possible. The limiting factors are the cross-tine dimension of the transducer array and the cross-sectional area of the transmission line harness. Those two factors may also be related. Transformer wire is considerably smaller, more robust, and more easily worked with than miniature, shielded wire. Part of the design trade-off here is the signal isolation of shielded conductors versus the desire to place 30 to 50 transducers and their transmission lines in a narrow tine. Using a bread-boarded fragment of the multiplexer (MUX) interface described in Chapter 3, the P1



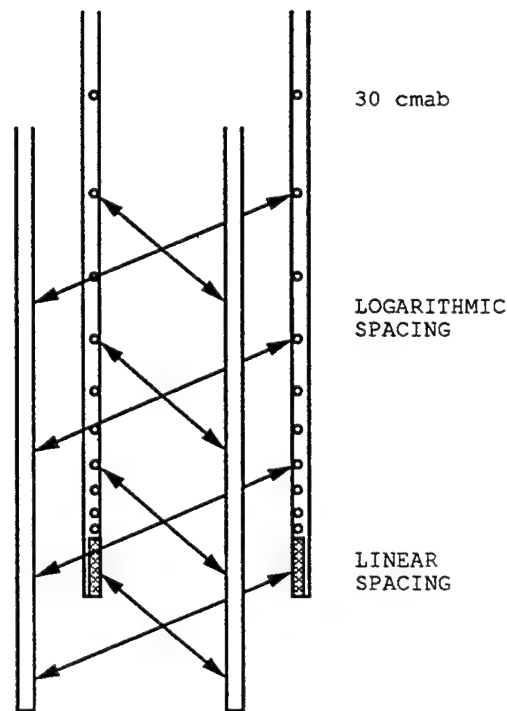


Figure 2.1: BASS RAKE ACOUSTIC TRANSDUCER GEOMETRY - Transducers are mounted in a high density array in the bottom 3.5 cm of each tine. Additional transducers are mounted with logarithmic spacing between 4 cm and 30 cm above the bottom. The tines are  $\approx 1$  cm in diameter. Crossing horizontal acoustic DTT paths are used to determine the horizontal velocity vector at each measurement level. The name “BASS Rake” is descriptive of the general appearance of the sensor head.

tines were used to demonstrate that the interface provided sufficient cross-channel and environmental isolation, even with unshielded conductors in a common harness, to make clean, accurate velocity measurements. Relieving the constraint in this way is a good example of the integrated nature of the overall design.

In the wake of the preliminary tests the P1 tines were cannibalized and then re-assembled to evaluate the robustness and performance of miniature shielded biomedical wire. The shielded wire proved to be quite frail and working with it, while not impossible, was difficult. These tines, designated P2, were eventually used in the tow tank and flume testing of the BASS Rake laboratory prototype described in Chapter 5. That was not the original intent, but the result of unexpected charac-



Figure 2.2: P2 AND P3 TRANSDUCER ARRAYS - The P2 transducers (left) have a  $6\text{ mm}$  diameter and center locations  $0.45\text{ cm}$ ,  $1.2\text{ cm}$ ,  $2.4\text{ cm}$ , and  $4.9\text{ cm}$  from the end of the tine. The diameter of the P2 tine is approximately  $1\text{ cm}$ . The P3 transducers (right) have a  $2.5\text{ mm}$  diameter. They are arranged in three offset columns to achieve  $1\text{ mm}$  vertical separations over a  $1.1\text{ cm}$  array near the end of the tine. The diameter of the P3 tine is approximately  $1\text{ cm}$ . Photographs by Tom Kleindinst, WHOI.

teristics of the third pair of tines, designated P3, which ultimately precluded their use. The P1/P2 tines, henceforth P2, supported only four acoustic axes, sufficient for the preliminary tests, and used transducers with a diameter of  $6\text{ mm}$ . Of the four, one channel worked only intermittently due to a partial failure in one of the shielded wires. The #38 stranded center conductor of these cables is easily fatigued by the movement and circuit changes inherent in the prototyping process. The P2 transducers were arranged in a single column along the bottom  $5\text{ cm}$  of each tine. As discussed in Section 2.2, the target vertical resolution is  $1\text{ mm}$ , which cannot be achieved in a  $1\text{ cm}$  tine with  $6\text{ mm}$  transducers. The P3 tines supported twelve acoustic axes. The  $2.5\text{ mm}$  diameter P3 transducers were arranged in three offset columns in a  $1\text{ cm}$  diameter tine with  $1\text{ mm}$  vertical spacing in the bottom centimeter of each tine, thus achieving the target vertical spacing. Photographs of the P2 and P3 transducer arrays are shown in Figure 2.2.

$2.5\text{ mm}$  is the lower size limit for disk shaped transducers. Smaller, rectangular

transducers can be manufactured, but specifications for size and frequency are less precisely met. The upper frequency limit is roughly  $10\text{ MHz}$  [76]. Several other mechanical and electrical constraints also limit reduction in transducer size below  $2.5\text{ mm}$ . Simply fabricating the tines, particularly the transducer mounting and attachment of the signal wires, would become considerably more difficult. The output voltage of the receiver is proportional to the fourth power of transducer radius for given transmitter voltage and operating frequency. The transmit voltage cannot be increased to make up for this because of constraints imposed by the MUX. Amplification and filtering to recover the received signal is possible with the  $2.5\text{ mm}$  transducers, as discussed in Chapter 3, but would be significantly more difficult with smaller transducers. Experience with the  $2.5\text{ mm}$  transducers has also shown that, as the transducer diameter becomes comparable to its thickness, normally  $1.1\text{ mm}$  for resonant operation at  $1.75\text{ MHz}$ , the operating frequency is no longer simply proportional to the thickness. The P3 transducers are  $1.1\text{ mm}$  thick, but are actually resonant at  $0.85\text{ MHz}$ . They also exhibited significant electrical reactance. Changes to the MUX to balance the reactive component of the transducer load were required to improve acoustic coupling to the water. Again, this is discussed in Chapter 3.

As noted, there were problems which precluded using the P3 transducers. The enamel coated transformer wire was used for the transmission lines and the transducer mounting and tine fabrication techniques were verified. Among 24 transducers on two tines there were no failures through several months of constant use and occasional rough handling. This design is reliable and physically robust. The MUX demonstrated strong signal isolation and RMS noise was reduced to a few tenths of a millimeter per second. In fact, all aspects of the system performed admirably when the transducers were positioned well away from the boundary. Failure occurred on close approach to the sand and was due to the particularly wide mainlobe of the transmit/receive beam pattern, which was enhanced by the unexpectedly low signal frequency, and to the nature of the acoustic interaction with the bottom. This is discussed in Chapter 4. However, the detailed analysis and calculations in that chapter also show that  $2.5\text{ mm}$  diameter transducers operated at  $5\text{ MHz}$  would perform as

well near the bottom as the P2 transducers did. Such transducers would also have a significantly more narrow sample volume so that individual axes would retain high accuracy right down to the fluid-sediment interface in a nonlinear velocity profile. Additionally, the P3 development work has already addressed and solved most of the mechanical and electrical problems associated with using very small transducers. Therefore, a sensor design based on 2.5 mm transducers in three offset columns with 1 mm vertical resolution down to  $\approx 1$  mmab in a 1 cm tine will be assumed in the remainder of this chapter and in Chapter 3. Further discussion of the P2 and P3 transducers and tines will be included where appropriate. Tines with reduced flow distortion, but lower vertical resolution, such as single columns of either 6 mm or 2.5 mm transducers, are retained as options for future development.

The overall distribution of acoustic axes was shown in Figure 2.1. Figure 2.3 provides an enlarged view of the dense, linear portion of the array at the bottom of each tine. Within the linear array there are 38 measurement levels with 1 mm vertical spacing. Transducer centers are located from 0 mm to 37 mm above the nominal bottom. There are 10 additional measurement levels located from 4 cm to 30 cm above the nominal bottom with logarithmic spacing. Above that level a standard BASS sensor can be used. The transducer pattern was chosen to maximize the number of measurements made within the WBBL. Above that level velocity changes more slowly with height and coarser vertical sampling is appropriate. The flow is expected to be strongly horizontal within 30 cm of the bottom and this design emphasizes vertically detailed measurements of horizontal motion. However, measurements of vertical velocity can be made flexibly as circumstances dictate. This is done using the MUX to pair transducers mounted at different levels. The angled acoustic axes created in this way include both horizontal and vertical components which can be identified based on geometry and companion measurements. The physical limitation on this measurement is simply that paired transducers lie within each others' mainlobe. Angled measurements were made successfully with all three tine prototypes. The importance of sensing vertical velocity fluctuations is discussed in Chapter 3.

The phrase "nominal bottom" refers to an idealized relative location of an idealized

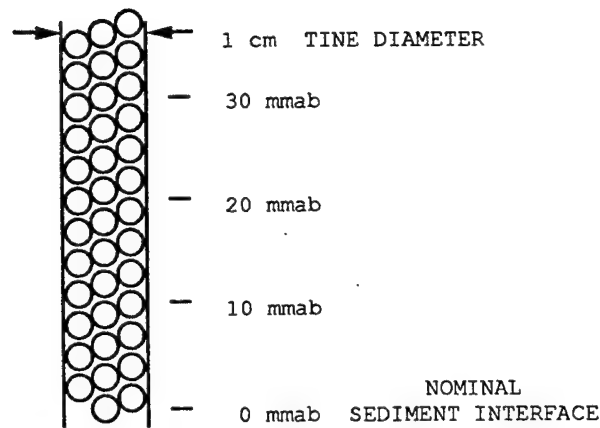


Figure 2.3: TRANSDUCER ARRAY FOR THE WAVE BOTTOM BOUNDARY LAYER - A dense transducer array is used along the bottom 4 cm of the sensor to resolve the behavior of the wave bottom boundary layer. The transducers are 2.5 mm in diameter and arranged to have 1 mm vertical spacing. Vertical velocities are measured by selecting a receiver within the main lobe but at a different height from the transmitting transducer. The MUX allows all transducers to be used for both horizontal and vertical velocity measurements.

fixed, flat fluid-sediment interface. It is employed as a convenience so that particular measurement levels along the tines can be referred to unambiguously. Field conditions are never that simple or that static. This is the reason for the relatively large extent of the linear array compared to the expected thickness of the WBBL. On deployment, the lower most measurement levels can be buried in the sediment. Then subsequent vertical movement of the interface due to erosion or deposition leaves some portion of the dense array spanning the WBBL except for exceedingly severe transport events. The location of the interface is known to millimeter accuracy simply by identifying the axes which do not return valid measurements and which are, therefore, buried. The need for precise vertical placement of relatively heavy equipment by divers is also eliminated. Experience positioning the laboratory prototype in the flume and deploying the field prototype beyond the surf zone has amply demonstrated the utility of this feature. The broad extent of the linear array is also useful in the presence of small ripples.

The duration of the measurement cycle for a single acoustic path is approximately

320  $\mu s$ . Of this, 220  $\mu s$  is the acoustic travel time for a 15 *cm* path length. The remainder is associated with processing and storage. All 96 acoustic axes of the BASS Rake can be sampled within a 31 *ms* window. Angled paths can be added to the list as necessary. Complete profiles could be measured at 20 *Hz* to 30 *Hz*, as discussed in Section 2.2. Such bursts would be limited only by the availability of RAM. Profiling rates of a few Hertz would be limited only by hard disk size and batteries.

Mounting the transducers in the tines and making signal connections presented several challenges. Both faces of a transducer are coated with a metallic film during manufacture and electrical connections must be made to each side to transmit and receive. However, the heat generated during normal soldering depolarizes part of the piezoelectric ceramic so that it is no longer active and the wire attached to the T/R face obscures and distorts the signal. These are not negligible problems for transducers this small. Further, the signal wires must be immobilized to fix the zero offset of each axis so that the offset can be removed during calibration [53]. Shielding to prevent capacitive coupling with the seawater, a conductive fluid, must be provided for the same reason. The cause of the offsets is also discussed in Chapter 3. Resistance to environmental factors like corrosion is desirable. Stiffness and rigidity of the tines during handling and deployment is essential.

Cross-sectional views of P2 and P3 tines are shown in Figures 2.4 and 2.5. Each transducer sits on a narrow shoulder in a mounting well milled into a flat strip of brass. The annular radius of the shoulder is less than 0.1 *mm*. Transducers are mechanically bound to the strip with polyurethane to provide both strength and compliance. The T/R face, oriented to the left in both figures, is electrically connected to the brass by conductive silver epoxy. The epoxy is applied around the edge of the face. This retains the symmetry of the T/R face and leaves it almost completely unobscured. The mounting strip, held at ground potential, provides a common signal return path for all of the transducers and space need only be allotted for a single wire to each transducer. The signal wires are connected to the back faces of the transducers using silver epoxy to prevent depolarization during soldering. A drop of polyurethane is

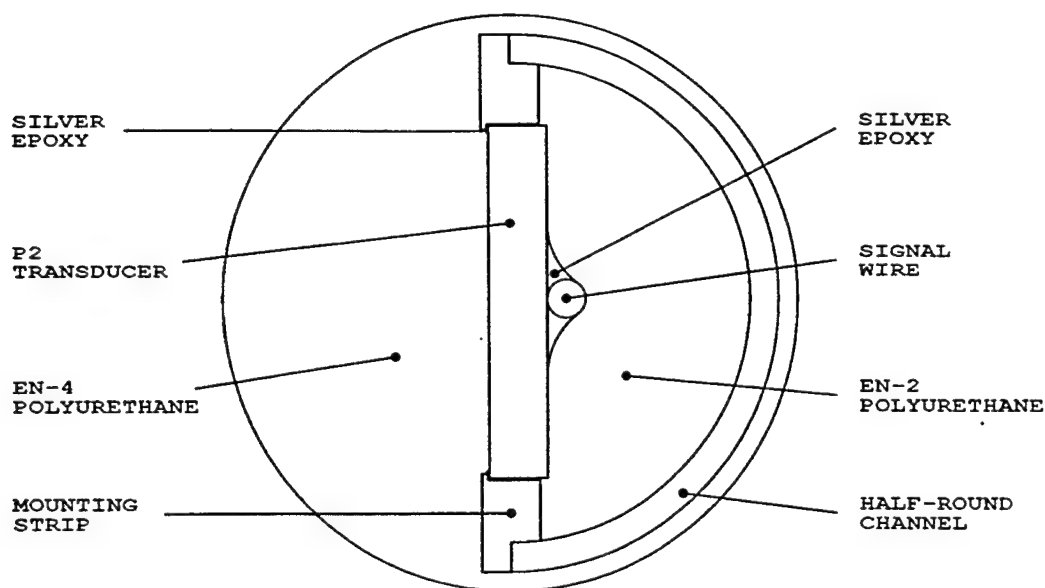


Figure 2.4: TINE CROSS-SECTION AND P2 TRANSDUCER MOUNT - This view along a P2 tine shows one of the 6 mm transducers sitting in a mounting well. The unobscured T/R face is oriented to the left. The front and back electrical connections and signal wire are shown, but the rest of the wiring harness has not been included. The diameter of the completed tine is approximately 1 cm. The various elements in the figure are drawn to a common scale and show a P2 tine as it was built. The overall diameter can be reduced by 2 mm to 3 mm if tines are fabricated using these transducers in the future.

added over the connection, after the epoxy cures, for strength during assembly.

The signal wires are run along the tine. As discussed above, enamel coated, unshielded wire functions admirably in this role. The MUX provides signal isolation and transformer wire is both smaller and stronger than miniature shielded wire. The maximum allowable outside diameter of the signal wires, assuming 48 transducers, the tine dimensions shown in Figure 2.5, and 70 % packing efficiency, is 0.5 mm. If shielded wire is used, anunjacketed version can reduce the outside diameter to this specified maximum. The shields and mounting strip are electrically common so that contact is not a problem. The signal contacts on the backs of the transducers are insulated by the polyurethane coating added when the signal connections were made. A halfround brass channel covers the connections and guides the wires up the tine. The brass strip and channel combine to provide both mechanical stiffness and the necessary electrical shield against capacitive coupling with the sea water. Brass was

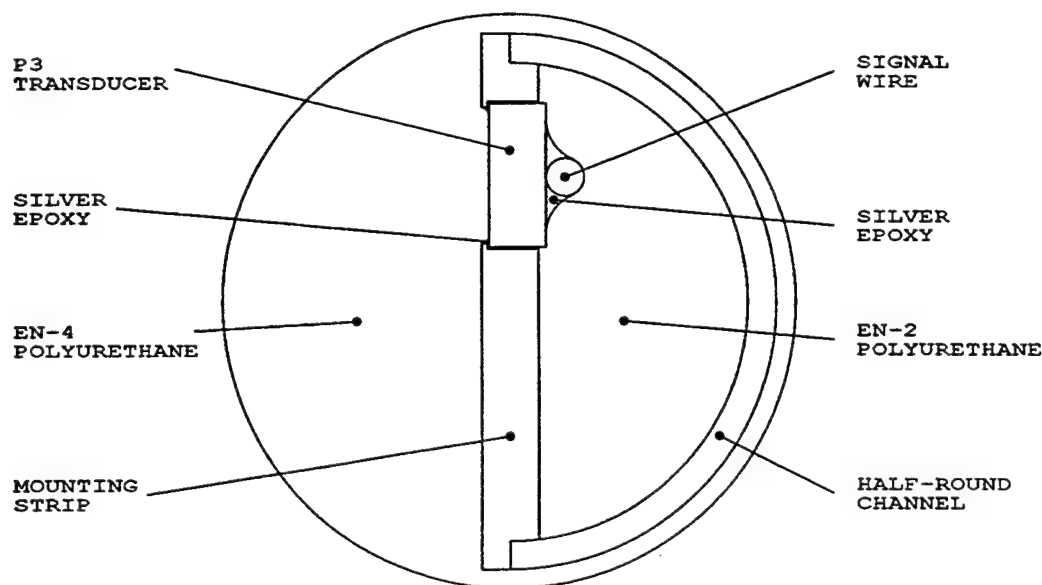


Figure 2.5: TINE CROSS-SECTION AND P3 TRANSDUCER MOUNT - This view along a P3 tine shows one of the 2.5 mm transducers sitting in a mounting well within the dense, linear portion of the array. The unobscured T/R face is oriented to the left. The front and back electrical connections and signal wire are shown, but the rest of the wiring harness is not included. The diameter of the completed tine is approximately 1 cm. The various elements in the figure are drawn to a common scale and show a P3 tine as it was built.

chosen because it is stiffer than aluminum and because soldered connections can be made to it easily.

The volume enclosed by the channel and strip is filled with EN-2 polyurethane. EN-2 was developed for use with transformer windings and has a very low viscosity before setting. The low viscosity makes it relatively easy, during the curing process, to remove air bubbles trapped among the signal wires during injection of the polyurethane. The polyurethane used to bond the transducers to the mounting strip and to strengthen the signal wire connection is also EN-2. The injected polyurethane holds the signal wires firmly in place. This fixes the zero offset and reduces mechanical strains on the electrical connections. The halfround assembly is then filled out to a cylindrical cross-section using EN-4 polyurethane. EN-4 is more difficult to work with than EN-2 and considerable care must be taken during the potting process. However, EN-4 has well described acoustic properties that recommend its use here. Most importantly, the acoustic index of refraction of EN-4 matches the acoustic refraction



index of water fairly closely. The asymmetric covering over the transducers does not strongly deflect the acoustic beams.

A round cross-section was originally chosen so that the wakes shed by the tines would not change with the relative orientation of the sensor head to the flow. However, analysis and observations of the flow disturbance caused by the tines during the laboratory prototype evaluation described in Chapter 5 suggest that halfround tines may be preferable. The P2 tines were carved down in this manner to obtain the results reported in Chapter 5. The half centimeter of polyurethane at either end of the acoustic path provides several  $dB$  of added attenuation. This is not a problem with 2.5  $mm$  transducers because receiver amplification is necessary even without the added attenuation. The greater circuit complexity and the degradation of the S/N ratio that generally accompanies amplification are already present. The 6  $mm$  transducers could function in fully round tines without amplification, but the S/N ratio was weaker than is generally desirable in BASS. Performance was improved in the halfround tines. The DTT velocity measurement described by Equation 2.1 is linearly dependent on the path length,  $L$ . Therefore, filling or not filling 10 % of the acoustic path with unmoving material must be accounted for during sensor calibration. Finally, the gain of the BASS Rake depends on the Reynolds number based on the diameter of the tine and the flow speed. The dependence is explored in detail in Chapters 5 and 6. Here it is sufficient to note that, like the drag coefficient for two dimensional bodies, the dependence is strongly related to the point of flow separation and the spreading angle of the wake. A cylinder would also have a Keulegan-Carpenter (KC) dependence for values of KC that could be found in the ocean for a 1  $cm$  tine. A halfround cross-section also has a KC dependence, but it is flat to much lower values. When tested with halfround tines, the laboratory prototype exhibited no dependence over the oceanic range of KC values. These characteristics of two dimensional bodies are well supported by experiments recorded in the literature (e.g., [6, 15, 23, 66, 67]). For halfround tines the sensor gain depends only on velocity and not on wave frequency. The dependence has been well characterized for the BASS Rake sensor head and can be included seamlessly as part of instrument calibration and postprocessing.

The tines extend 2 *cm* to 3 *cm* beyond the nominal bottom and are attached to a common ring. The ring gives added stiffness and strength to the tine assembly and fixes the relative location of the transducers. The overall length of the tines is on the order of 1 *m* to reduce the near-bottom flow distortion due to the pressure housing containing the electronics. Stiffeners are added to the tines beginning a few centimeters above the uppermost measurement level and extending to the mechanical assembly at the top. The tines are not pressure sealed at either end. The polyurethane transmits the ambient pressure so there is no differential across the transducers, the mounting strip, or the channel. This permits the transducers to function and prevents compression or deflection of the assembly with depth. Either effect could invalidate the calibration. The design also eliminates any significant differential pressure along the tines. This prevents a cold flow of the internal polyurethane that could damage the tines and the electrical connections.

The length and slenderness of the tines requires some caution in handling and during deployment. Once in place wave forcing is unlikely to damage them directly. However, they are certainly vulnerable to impacts from a large, submerged object, either drifting or towed. This is one of the unfortunate realities of instrumenting the continental shelf. Trawler proof designs are not an option here because the heavy matting normally used would interrupt the flow. Damage to the tines can also result if the frame supporting the instrument shifts or rolls and thereby applies shearing and compressive forces. This tendency can be countered by increasing the stability of the frame with heavy footpads or anchors. Seemingly extreme measures may be necessary. Recall, for example, the termination of the field experiment referred to in Section 2.3.2.1. Seven heavy load, screw-in anchors used to secure the field prototype were plastically deformed and pulled free from a sand and cobble bottom during a storm. The instrument rocked an unknown number of times on the footpads and tines before rolling over and coming to rest on its back. The ring secured to the ends of the tines was bent during this process, having been repeatedly slammed into the bottom as the frame rocked. The tines were relatively undamaged, but the field prototype did not use the integrated tine design described here. Rather, as part of the prototyping

process, standard, polyurethane potted, BASS transducers were bolted to a stock rod of stainless steel (see Chapter 6). The solid rod was certainly less susceptible to longitudinal bucking than the thin walled brass support of the integrated tine. Clearly, more secure anchors will be needed in the future, at least in the immediate vicinity of the surf zone. The incident serves as a classic example of the benefits of prototyping.

Because of the locations of the four tines, the azimuthal cosine response of the sensor head is not expected to be flat. Tow tank tests described in Chapter 6 show this is the case and that the BASS Rake benefits from being roughly lined up with the flow. Orientation accuracy within  $\pm 30^\circ$  is sufficient. That figure is based on the field prototype, which, as mentioned above, did not use the slender, constant cross-section tines described here. The actual window may be considerably wider. The pathological case for tines located on the vertices of a square is an orientation of  $\pm 45^\circ$ . At that angle half of the acoustic axes are perpendicular to the flow and measure only cross-wake fluctuations. The other axes fall completely within the wake of one of the tines. This cosine response is repeated in each quadrant. Crossing waves and currents on the shelf can make a workable orientation difficult to identify. Two fairly simple modifications address this problem. The acoustic path length can be increased. This reduces the overall error due to flow distortion and widens the window of allowable angles. Minor changes in software and hardware timing, which have been used before, are necessary to support the longer axis. A second approach is to change the crossing angle of the acoustic axes by locating the tines on the vertices of an appropriately scaled rectangle. Both of these capabilities were built into the mechanical assembly securing the top of the tines in the field prototype described in Chapter 6. A more complex solution will be discussed in Section 2.4.1.

The final aspect of the tine design considered here is passing nearly 200 signal wires through the endcap of a pressure housing so that they can be connected to the MUX. Commercially available connectors cannot provide enough through pins in the area of a standard 6"ID endcap. The solution is a tapered hole for each of the four wire harnesses. Once the harness is in place the hole is filled with UC-32, one

of the harder polyurethanes. Like EN-2, UC-32 has low viscosity before setting so that voids within the harness will be filled. Precoating of the wires and manipulation of harness during potting will insure a good seal. The addition of UC-22, a softer polyurethane, on either end of the UC-32 plug will reduce bending strains in the wires. The strength of this method is sufficient for differential pressures on the continental shelf. For tines that are fixed in place, the electrical pass-through and the assembly holding the top of the tines can be combined in a double endcap. One plate holds the top of the tines firmly in place and allows the harnesses to pass through. Both sides of this plate are exposed to ambient pressure to prevent cold flow along the tine as previously discussed. A second plate contains the polyurethane harness seals and mates to the pressure housing as a standard endcap with O-ring seals. The plates are joined by four to six short posts for mechanical strength. The volume between them is filled with polyurethane to transmit ambient pressure to the top of the tines and to prevent movement of the harnesses. Capacitive coupling with the seawater will be prevented by passing the harness through a braided ground strap between the top of the tines and the pressure housing. This design will be incorporated in the final field instrument.

### **2.4.1 Preliminary Error Analysis**

To begin with, it should be emphasized that all instruments create some flow distortion in field use. The existence of the distortion is significant because it requires that the response of the sensor depend, in a general sense, on the relative velocity and the relative angle of the flow. Of course, the strength of these effects varies considerably from sensor to sensor and may or may not affect the quantity being sensed. The dependence is often incorporated in the calibration constants of an instrument or is implicit in the calibration procedure. In Chapters 5 and 6, the flow dependence of the BASS Rake, discussed briefly in this section, is modeled and empirically determined. This is done explicitly and in detail because the BASS Rake, in common with all velocity sensors, distorts the quantity it is intended to measure. The development of the instrument would be grievously incomplete without the detailed analysis.

The preliminary analysis presented here is concerned with errors related to the distortion of flow by the sensor head. The approach employs several simplifying assumptions and is only intended to bound the error for flows well aligned with the tines. As noted, this topic will be revisited in greater depth in Chapters 5 and 6. The flow obstruction presented by the tines can completely compromise a measurement when the flow is parallel to one set of the crossing acoustic paths. The best performance will be obtained when the velocity field is oriented at approximately  $45^\circ$  to both sets of acoustic paths. This presents no difficulty in most laboratory settings. On the shelf, where currents and waves commonly cross and prevailing motions often change direction, a flexible solution is required. As discussed above, longer path lengths and different crossing angles for the axes can alleviate the problem in some circumstances. A more dynamic solution may be achieved by deploying multiple BASS Rakes with different orientations. Given the relatively broad angular window of acceptable relative angles, no more than three sensor heads would be required. Two would probably be sufficient. The sensor heads could be deployed from a central structure and the measurements of a standard BASS sensor could be used to select uncompromised data from the multiple records. This is, admittedly, a mildly complicated solution, but the shelf is not a simple place.

Even with a fairly ideal orientation, the tines still create some flow distortion. The total disturbance is, roughly, comprised of potential flow distortions and wake effects. The induced errors depend on the flow speed,  $u$ , the tine diameter,  $d_t$ , and the path length,  $L$ . The error due to potential flow distortion by a single tine,  $\Delta u_{PF}$ , can be obtained by integrating the velocity distortion along an acoustic path [39].

$$\frac{\Delta u_{PF}}{u} = \frac{d_t^2}{4L} \left[ \frac{1}{L} - \frac{1}{d_t/2} \right] \cos \theta \approx 0.7 \frac{d_t}{L} \quad (2.16)$$

There is some cancellation of the contributions of the four tines in the center because of symmetry. At other points along the path of the integral the potential fields interfere constructively. To be conservative, the four tines are treated as independent contributors to the total error in the calculation below.

Following Trivett, Terray, and Williams [78], wake induced errors can be attributed to the velocity defect and vortex shedding.

$$\frac{\Delta u_{VD}}{u} = 0.66 C_D \frac{d_t}{L} \quad (2.17)$$

$$\frac{\Delta u_{VS}}{u} = 0.02 \frac{d_t}{L} \quad (2.18)$$

$\Delta u_{VD}$  is the velocity defect error and  $\Delta u_{VS}$  is the velocity error caused by vortex shedding. The drag coefficient,  $C_D$ , is approximately 1. It will be taken as a constant in the calculation below. The actual dependence of  $C_D$  on the Reynolds and Keulegan-Carpenter numbers will be incorporated in the analysis of Chapter 5. The constant in Equation 2.18 is scaled up from that given by Trivett, *et al.* assuming the relationship is linear in  $\frac{d_t}{L}$ . The original constant was empirically derived from spectral data for a particular strut diameter and path length [78]. Equation 2.17 is a far field solution being applied in the near field of the wake. Further simplifying assumptions are implicit in all three formulas, but it is only a rough bound on the error that is sought. Arguably, these formulas overpredict the error for uniform flow. However, the oscillatory nature of the flow being investigated causes complicated wake interactions with an effect on the error that is difficult to anticipate.

Error surfaces calculated as functions of velocity and path length assuming 1 cm tines are shown in Figure 2.6. The surface in the top panel is the error as a percentage of the velocity. The lower panel shows the actual velocity error. The calculation assumes independent contributions from four potential flow distortions and two wakes crossing the acoustic axes.

The percentage error is flat for a given path length and the error is always reduced by increasing the tine separation. However, the error surface suggests further reductions will be small beyond  $L = 15 \text{ cm}$  to  $20 \text{ cm}$ . Velocity resolution, as shown by Equation 2.1, is also improved with tine separation, but the sample volume is both longer and wider. The latter characteristics degrade vertical resolution and are therefore undesirable. Other design requirements, such as the strength of the received signal, are also affected. Selection of the path length necessarily requires some de-

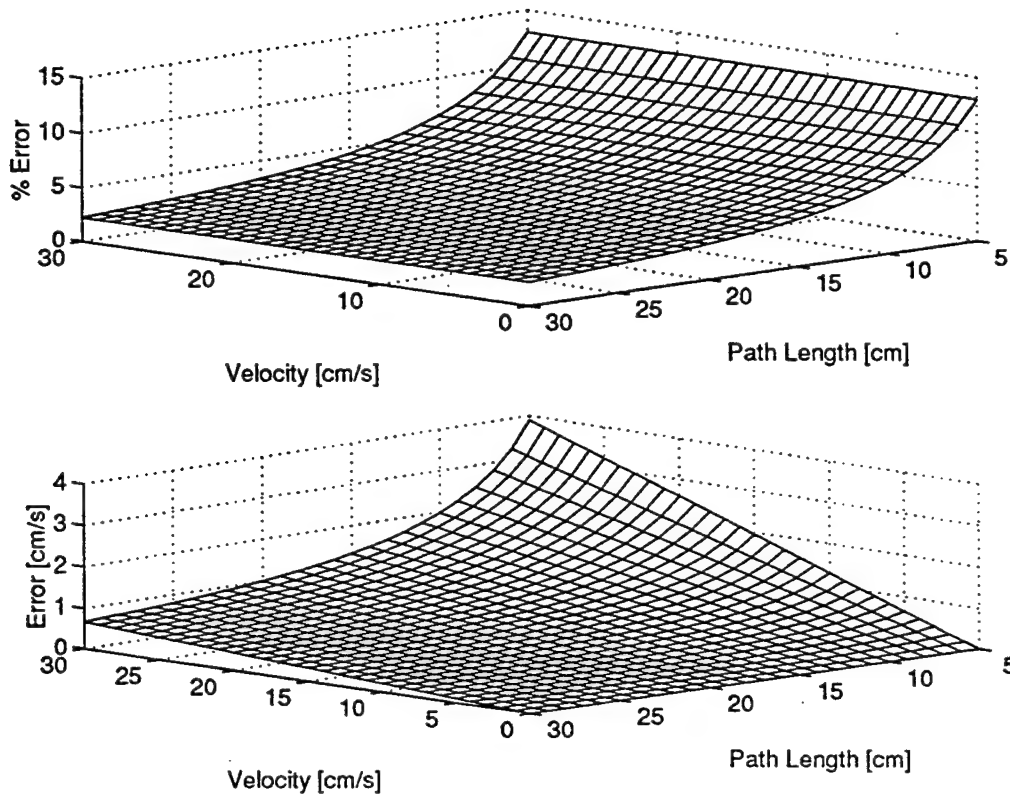


Figure 2.6: ESTIMATED BASS RAKE ERROR SURFACES - The surfaces estimate the error in BASS Rake measurements as functions of the actual velocity and the path length assuming 1 cm tines. The top panel shows the error as a percentage of the velocity. The lower panel shows the actual velocity error. The calculation assumes independent contributions from four potential flow distortions and two wakes crossing the acoustic axes. This is a conservative formulation and arguably bounds the error.

sign trade-offs. A reasonable balance is achieved for  $L = 15 \text{ cm}$ , which appears to hold the error below 5 % for four tines well oriented to the flow. It will be shown in Chapters 5 and 6 that this is an accurate estimate. It is also interesting to compare the potential measurement error to Madsen's estimate of 10 % to 20 % accuracy for WBBL models [46, 47, 48]. Finally, the results described in Chapters 5 and 6 demonstrate that the average flow induced error of the BASS Rake is systematic. It can be removed accurately and easily through calibration and postprocessing.

## 2.5 Summary

The notable weakness of the BASS Rake, as with many of the other techniques discussed in Section 2.3.2, is strong, localized variation in the azimuthal cosine response. This is of particular concern on the shelf. Several possible solutions were suggested in Section 2.4. It should be noted that, outside the narrow range of pathological angles where the flow lines up with one set of acoustic axes, the effects of flow distortion can be very accurately characterized and removed in calibration and postprocessing. Unlike most of the other approaches, additional sample volumes can generally be added to a tine without adding to the flow disturbance.

The distinctive characteristic and strength of the BASS Rake is its ability to accurately and reliably measure spatially dense, temporally coherent, velocity profiles in the field. Measurements can be made within two millimeters of the bottom and continued through the WBBL and into the forcing flow above it. The spatial qualities of the profile are achieved with densely spaced, multiple sample volumes and fine cross-axis resolution. Temporal coherence and high profiling rates result from the short duration and high accuracy of each individual measurement. The acoustic DTT measurement and the hardware are extremely robust when deployed in the energetic environment of the continental shelf. However, significant emphasis must be placed on support frame stability and anchoring during deployment. The importance of these abilities for the study of the wave boundary layer, both in the field and in the laboratory, has been discussed throughout this chapter.

The strengths and weaknesses of other boundary layer velocity sensors have also been discussed at some length. The BASS Rake has the obvious advantages of multiple sample volumes and field capability. However, existing techniques are not without significant abilities and the BASS Rake is not without failings. Instrument selection depends on many aspects of the environment and the quantities to be measured. No single sensor can be the best choice in all situations. The BASS Rake is both a capable and a complementary development. The study of the wave bottom boundary layer can benefit from the enhanced selection of tools.





## Chapter 3

# The Interface to the Acoustic Transducer Array<sup>†</sup>

### 3.1 Introduction

This chapter documents the design of the layered, low impedance, multiplexer (MUX) interface between the BASS Rake transducer array and the existing BASS transmit/receive (T/R) circuit. The transducer array described in Chapter 2 will be assumed here. The scientific and technical motivations for a multiplexing interface are discussed in Section 3.2, as are the performance requirements imposed on the interface by the system. In particular, the relevant characteristics of the T/R circuit, originally described by Williams, *et al.* [90], will be presented. The design of the interface is developed at length in Section 3.3. The discussion includes selection of the switching elements, assembly of basic component blocks, layering of the blocks to reduce transmission line loading, and addressing the array. The multiplexer will be shown to provide a 20 % increase in the efficiency of current delivery to the receiver load compared to a standard BASS. Conclusions about the performance of the MUX are summarized in Section 3.5.

Several references were made in Chapter 2 to the difficulties associated with the

---

<sup>†</sup>Some of the material presented in this chapter was originally published in *Proceedings OCEANS '95* [56] and in *Sea Technology* [57]

2.5 mm P3 transducers. Some of the P3 characteristics are associated with the relatively small diameter to thickness ratio of the transducer and may be alleviated by the planned thinner, higher frequency, transducers described in Chapter 4. Others are associated with the small diameter alone. Early experiments with the laboratory prototype demonstrated that transducers of this size cannot be used with an unmodified BASS T/R circuit to make DTT measurements. This failure is independent of the wide beam angle that ultimately precluded the use of these transducers. Circuit modifications were developed in the course of this investigation that produced reliable P3 DTT measurements with a noise floor of  $0.5 \text{ mm} \cdot \text{s}^{-1}$ .  $0.3 \text{ mm} \cdot \text{s}^{-1}$  is the nominal noise floor of the BASS measurement.  $0.5 \text{ mm} \cdot \text{s}^{-1}$  is well below the noise level produced by the wake of the BASS Rake sensor head for most flows (see Chapter 5). The circuit solutions used for the P3 transducers are directly applicable to 2.5 mm transducers with higher operating frequencies. The layered multiplexer provides both improved efficiency in the delivery of current to loads and an insertion point for the modifications. No changes to existing circuit cards are necessary. The layered MUX is thus an integral part of successful small transducer operation. The P3 circuit changes used in the laboratory prototype are described in Section 3.4.

The schematic wiring diagrams presented in this chapter are largely circuit fragments or simplified functional blocks. A complete set of schematics describing the laboratory prototype are included in Appendix B for reference. In this chapter, and the appendix, an understanding of and familiarity with the characteristics and terminology of passive and active electronic components, circuit networks, and operational amplifiers is assumed on the part of the reader. If this background is lacking, or simply requires some review, the texts by Horowitz and Hill [34] and by Skilling [69] are notable both as references and for the quality of their presentations.

## 3.2 System Background and Interface Requirements

The sensor array consists of 192 acoustic transducers mounted on four tines. Pairs of transducers on opposing tines define 96 horizontal measurement axes crossing to form 48 measurement levels. A standard BASS instrument uses dedicated T/R circuits hardwired to each axis. It is an absolute requirement of the differential travel time (DTT) measurement that the two transducers defining an acoustic path are connected to the same T/R circuit. The velocity measurement has no basis without the common time reference that connection provides to the two transmitted signals simultaneously traversing the acoustic axis in opposite directions [90, 92]. A single T/R circuit card holds four independently selectable T/R circuits connected to the four axes of a single BASS measurement volume. Five measurement volumes, twenty acoustic axes, is the normal complement for a BASS tripod. Hardwiring the BASS Rake in this manner is undesirable for a number of reasons. First, the BASS Rake transducer array would require 24 T/R boards and 75 *cm* of space on the backplane. A longer pressure housing, and possibly a separate housing for batteries and data logging, would also be necessary. The flow disturbance around the housing(s) would increase and mounting the electronics package on the support frame would become more difficult. Recall from Chapter 2 that the tines are to extend from the endcap of the vertically mounted electronics housing. This has important benefits for the quality of zero offset calibration. The assembly must be able to slide vertically on the frame as a unit to position the transducer array relative to the fluid-sediment interface while preserving the zero calibration. The overall length of the housing can become a critical limit in the design of the support frame.

Second, the current six bit axis address would need to be extended to eight bits to choose among 96 hardwired acoustic axes.<sup>1</sup> Actually, since the size of the address

---

<sup>1</sup>Two bits select one of four axes on a T/R card. Three bits select one of eight possible cards, although five is the normal number because of penetrator allocation on the endcap of the pressure housing. One bit selects the normal or reverse (N/R) measurement direction. The paired N/R measurements are used to eliminate offsets and drift in the receiver and significantly enhance the

space is not strictly a function of the interface design, but of the number of transducers or pairs of transducers, a larger address space is an unavoidable necessity. As such it presents two problems. First, all of the digital input/output (I/O) lines on the controlling microprocessor are already in use. An address scheme using only three of the current six I/O pins to select two of 192 transducers will be presented in Section 3.3.4. Of more significance to the current argument against hardwiring the BASS Rake, there are two vacant pins on the edge connector of the T/R card, but additional circuitry to decode the longer address would be required. Available space is limited on that board. Further, changing the existing card and modifying existing backplanes or maintaining two versions of the same card are highly undesirable options.

Finally, and most importantly, hardwiring would constrain the scientific potential of the BASS Rake by limiting the measurements that can be made. Pairing transducers at different heights permits the measurement of vertical velocity fluctuations in the turbulent component of the flow. For example, a direct measurement of the Reynolds stress,  $-\overline{u'w'}$ , would be possible. This is a well established capability of the BASS DTT measurement [19, 26, 54, 84, 90]. The vertical flux of buoyancy,  $\overline{T'_t w'}$ , where  $T'_t$  is turbulent fluctuation of temperature, can also be measured directly, using a technique that was originally described by Trivett [77] and that is now being developed and used by Shaw, Williams, and Trowbridge [68]. Additionally, the diagonal measurements would increase the utility of the instrument among bedforms. Obviously, fixed diagonal measurements could be hardwired, but each one requires the sacrifice of two horizontal measurement levels. The angled paths cannot be used to replace the lost horizontal measurements because they lack the necessary vertical resolution and cannot approach the bottom as closely. Recall, from the discussion of the "nominal bottom" in Chapter 2, that the location of the fluid-sediment interface relative to the tines is not fixed. Hardwiring the angled axes would require prior knowledge, a fixed reference, and precise placement in the field. None of these

---

accuracy of the velocity measurement. Two additional bits would be required to select one of the 24 required T/R cards. As many as 32 cards could be supported.

conditions can be met.

A multiplexer interface that could select the useful transducer pairs from opposing tines and connect any selected pair to the same T/R circuit would make a full suite of velocity measurements possible. Additionally, with a multiplexer, changing the selection of measurement axes can be accomplished in software or firmware. Alteration of the wiring harness, backplane, and circuit cards is unnecessary. A flexible response to different deployment scenarios becomes possible. Flexibility in pairing makes the measurement objectives outlined above possible. For example, a parallel set of angled paths would return a full profile of vertical velocity fluctuations despite movement of the fluid-sediment interface and without sacrificing any horizontal measurements. The interface can also be constructed so that no changes to the existing, standard, circuit cards are necessary.

Backplane space savings depend on the number of cards needed to hold the multiplexer and the number of hardwired T/R cards eliminated by the interface. Potentially the transducer array could be driven from a single T/R circuit. However, anticipating for a moment the development in Section 3.3, this will depend on the nature of the switching elements in the interface. Using a single T/R circuit to drive the entire array might present a prohibitive capacitive shunt load to the transmission line because of the number of involved switching elements. That shunt load on the signal could be reduced, at the expense of some measurement flexibility, if, for example, each of the 4 T/R circuits on a single T/R board was multiplexed to the 24 odd or even transducer pairs on opposing tines.

To make this division less obscure, a short digression to define tine and transducer identification is in order. The tines are designated "A", "B", "C", and "D" arranged in a clockwise square. The transducers in tines A and C communicate with each other. The crossing axes are defined by the transducers in tines B and D. Transducers in each tine are denoted by a two digit numeric label from "00" to "47" in height order from bottom to top. Axes A00-C00 and B00-D00 form the lowest measurement level, defined to be at the "nominal bottom" (see Chapter 2). Similarly, axes A22-C22 and B22-D22 form the measurement level 22 *mm* above the nominal bottom. The

proposed division of the load would assign two T/R circuits to the AC tine pair. One T/R circuit is multiplexed to transducers with odd number designations and the other T/R circuit is multiplexed to transducers with even number designations. The remaining two T/R circuits on the T/R board are assigned to the BD tine pair with the same transducer distribution. In this scheme, angled connections between even and odd levels are not possible because they do not share a common T/R circuit. Some flexibility is lost, but transmission line loading is reduced.

The number of T/R circuits and boards actually used therefore reflects a balance between signal loading and measurement flexibility. Similarly, multiplexing to the T/R circuits as well as the transducers would trade an increase in shunt load for restored flexibility. Multiplexing has the potential to reduce the number of T/R boards from 24, required to hardwire the transducers, to perhaps one or two. This represents a considerable savings in backplane space that could be applied to the multiplexer. A flexible interface to 96 axes and the necessary T/R cards can reasonably be expected to fit in the 15 *cm* of backplane normally occupied by the five T/R cards supporting the normal complement of 20 axes. This estimate is based on the MUX breadboards fabricated for the laboratory prototype described in Chapter 5.

The ability to satisfy the measurement objectives makes the multiplexer an attractive approach, but some properties of the differential travel time measurement and the design of the BASS Rake sensor head impose significant constraints on the electrical characteristics of any interface between the T/R circuit and the transducer. The first of these is switching speed. Each normal or reverse measurement over a 15 *cm* path length has a duration of 160  $\mu s$ . The acoustic propagation time is 110  $\mu s$  and the remaining 50  $\mu s$  is used for switching overhead and measurement processing [90]. Transducer connections are necessarily fixed during the propagation time. Small extensions of the overhead period can cause significant decreases in the maximum profiling rate because of the large number of acoustic axes. Therefore the MUX must be able to change state well within the 50  $\mu s$  overhead period. A design constraint on the switching time of 10  $\mu s$  or less is necessary.

It is also necessary for the interface to provide signal isolation between the chan-

nels. BASS channels are well isolated by separate T/R circuits, a coaxial harness, and the geometry of the acoustic paths [90]. The multiplexer intentionally shares T/R circuits between many channels. The small cross-sectional area of the tines, the large number of signal lines needed, and the established frailty of the miniature biomedical wire, make the use of shielded transmission lines problematic. The close proximity of signal wires within the tines enhances capacitive coupling between channels. The geometry of the BASS Rake sensor head encourages acoustic coupling between channels. Intentional cross-channel linkages in the form of angled measurements are, in fact, part of the design. Capacitive and acoustic coupling can contaminate the velocity measurement along the selected path with velocities from other axes within the array. Each measurement would actually be a weighted average of the velocities along all of the axes in the array and the fine vertical resolution needed to profile the WBBL would be lost. A rough estimate suggests that a measurement accuracy of 5% to 10% requires 30 dB to 40 dB of isolation between channels.

The most severe constraint on the interface is the need for extremely low through resistance. A value on the order of an ohm or less is necessary. The requirement is due to the sensitivity of the BASS DTT velocity measurement to variations in the equivalent capacitance of the interface, the transmission lines, and the transducer electrodes. The nature of the sensitivity can be demonstrated with the simple model of the transmit/receive process shown in Figure 3.1. The various components are electrically equivalent circuits in the Thévenin sense [69]. The argument and observations presented here follow those given by Morrison, *et al.* [53], Williams, *et al.* [90], and Williams [92].

The transmitter is modeled as a voltage source,  $v_S$ , with source resistance,  $R_S$ . The shunt capacitance,  $C_{T1}$ , represents the capacitances of the transmission line and the transducer electrodes. In a standard BASS instrument the transmission line is 6 m of coaxial cable with an equivalent capacitance of approximately 1000 pF. The electrodes are thin, metallic films plated over the two faces of the transducer during fabrication. The equivalent capacitance of the standard 1 cm transducer, essentially the parallel plate capacitance, is also approximately 1000 pF. For 1 m of enamel



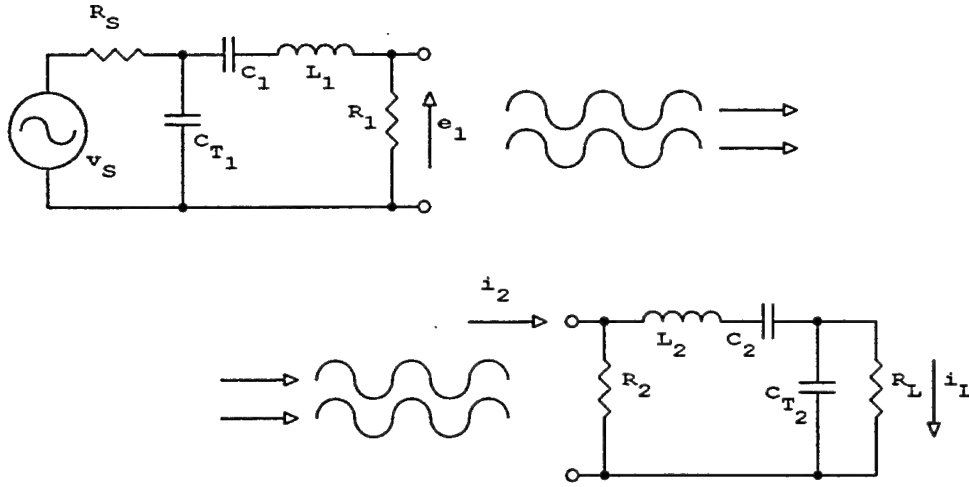


Figure 3.1: EQUIVALENT MODEL OF THE BASS TRANSMIT/RECEIVE PROCESS - A model for the transmitter and transmitting transducer is shown in the upper portion of the figure. A similar model for the receiving transducer and receiver is shown in the lower portion. The models are electrically equivalent circuits in the Thévenin sense [69]. It is the transfer function from  $v_S$ , the transmitter voltage, to  $i_L$ , the receiver current, that is of interest. Variations in  $C_{T1}$  and  $C_{T2}$ , the equivalent capacitances of the transmission lines and the transducer electrodes, change the phase of the transfer function and degrade the accuracy and stability of the velocity measurement. The effect can be sharply limited by keeping  $R_S$  and  $R_L$ , the source and load resistances, small. Redrawn from Williams, *et al.* [90] with the permission of the first author.

coated wire in a harness and a 2.5 mm transducer, as in a BASS Rake tine, the equivalent shunt capacitance is approximately 130 pF. The series impedance of  $C_1$ ,  $L_1$ , and  $R_1$  is  $Z_1 = R_1 + X_{C_1} + X_{L_1}$ , where  $X$  is the electrical reactance of the component in the subscript.<sup>2</sup>  $Z_1$  models the behavior of the piezoelectric ceramic. The transducer has a  $Q$  of approximately 5 near resonance, but this can vary depending on material, resonant frequency, and transducer size. The receiving transducer and transmission line are modeled in the same way with the notational difference of a 2 in the subscript.  $R_L$  is the receiver load.

The voltage applied by the transmitter,  $v_S$ , induces a voltage,  $e_1$ , across the equivalent resistance of the transducer. Resistors are dissipative elements, typically radiating energy away in the form of heat. In the case of a piezoelectric transducer,

<sup>2</sup>Capacitive reactance is defined by  $X_C = \frac{-j}{\omega C}$  and inductive reactance is defined by  $X_L = j\omega L$ . The symbol,  $j$ , is the imaginary unit value defined by the equation  $j^2 = -1$ . Reactances are pure imaginary values.

$R_1$  dissipates the electrical energy by radiating acoustic energy into the water. This concept will be important in understanding the interface modifications made for the P3 transducers. This model will be revisited for that purpose in Section 3.4. At the receiver the reciprocal process occurs. The radiated energy induces a current,  $i_2$ , in the piezoelectric transducer and the current in the transducer induces a current,  $i_L$ , through the receiver load,  $R_L$ .<sup>3</sup>

For simplicity, let the radiation transfer function from  $e_1$  to  $i_2$  be given by

$$i_2(t) = e_1(t - \Delta)G \quad (3.1)$$

where  $t$  is time,  $G$  is the transconductance gain, and  $\Delta$  is the time needed for the acoustic signal to propagate from the transmitter to the receiver. There is no need for a more complicated propagation model here. The balance of the transfer function relating the receiver load current to the transmitter source voltage is determined by applying voltage and current divider equations [34, 69].

$$i_L(t) = \frac{v_S(t - \Delta)GR_1R_2}{\left[R_S \left(\frac{Z_1}{X_{CT_1}} + 1\right) + Z_1\right] \left[R_L \left(\frac{Z_2}{X_{CT_2}} + 1\right) + Z_2\right]} \quad (3.2)$$

Only the reactive elements can change the phase of the received signal. These elements are confined to the denominator in Equation 3.2. If the reactive elements are fixed for the duration of the normal/reverse measurement cycle, the model is symmetric when the source and load resistance are equal. While these values can be closely matched, they cannot be kept precisely equal. The inequality produces a differential change in phase for the two directions. The phase shifts differentially move the zero crossings of the received signals to which the DTT measurement is referenced. This causes an offset in the measured velocity at zero flow. The offset can be removed during calibration if two conditions are met. First, the reactances

---

<sup>3</sup>It is strictly equivalent to use a voltage,  $e_2$ , as the quantity induced by the radiated energy and to proceed with the derivation from there. However, the receiver is a cascode circuit [34, 90], which is best understood as a transresistance amplifier taking a current input and producing a voltage output. Therefore, it is conceptually easier to work with  $i_L$  and, because the output variable is  $i_L$ , it is algebraically easier to use  $i_2$ .

must be unchanging for the duration of the experiment. Unfortunately, while  $Z_1$  and  $Z_2$  are, for practical purposes, constants,  $C_{T1}$  and  $C_{T2}$  are highly variable. In particular, they change with flexure and pressure compression of the normal, coaxial, transmission lines. There is also a significant effect for flexure of enamel coated wire in a harness. There is a pressure effect for the coated wire only if the relative position of the wires is changed. The change in capacitance can be understood on physical grounds and the model demonstrates its importance to the accuracy and stability of the measurement.

Dynamic flexure can be limited to the extent that the harness can be immobilized. It is now standard procedure with BASS to securely lash the 6 m coaxial cables of the harness to the tripod frame. A thousand or more "tie-wraps" are commonly used for this purpose. However, several meters of each signal cable run along guy wires and are, therefore, not entirely immobilized. Static pressure effects are removed by performing the calibration *in situ*. However, the offsets can still be a significant fraction of the  $\pm 240 \text{ cm} \cdot \text{s}^{-1}$  dynamic range of the instrument and the dynamic variations can produce a large and limiting noise floor. Thus, reducing the sensitivity of the measurement to variations in the shunt capacitances is also a necessary condition for accurate calibration and measurement with BASS. In contrast, the design of the BASS Rake confers considerably more immunity to the dynamic variations. This will prove important given the modifications that are necessary for P3 operation. The BASS Rake transmission lines are only 1 m in length and are, compared to a BASS harness, completely immobilized in the polyurethane of the tine and endcap. Empirically, noise due to flexure is entirely negligible for both the P2 and the P3 transducers. The pressure effect on a harness of unshielded wires embedded in polyurethane that is not supporting a pressure differential is also entirely negligible for shelf depths. This is a second argument for enamel coated wire rather than miniature, shielded, biomedical specialty wire. The BASS Rake will still experience large offsets if the sensitivity to shunt capacitive variation is not reduced and this will limit the dynamic range of the measurement. However, the dynamic variations will be too small to produce a large, limiting noise floor even if the sensitivity is not strongly reduced.

To reduce the sensitivity of the measurement to variations in the shunt capacitances, observe that the shunt reactances only appear in the transfer function inside quantities multiplied by the source and load resistances. The sensitivity of the velocity measurement to shunt capacitive variation can be sharply limited if  $R_S$  and  $R_L$  are kept small. The source and load resistances in BASS are both approximately  $10\ \Omega$ . This generally limits BASS zero offsets to less than  $\pm 1\text{ cm} \cdot \text{s}^{-1}$ . There is no significant loss of dynamic range for offsets of this magnitude. Static pressure effects are too small to measure for shelf depths and the noise from an immobilized harness is negligible. By keeping the source and load resistances this small, BASS actually achieves an accuracy limited by Johnson (thermal) noise in the receiver circuit. The resolution limit in differential travel time is  $40\text{ ps}$ . This represents  $0.3\text{ mm} \cdot \text{s}^{-1}$  in velocity. Distortion by the supports is the real limit on accuracy for most flows. To maintain this level of performance, any increase in the source and load resistances must be negligibly small. Any increase should be limited to 10 %, approximately  $1\ \Omega$ . It will be necessary to violate this stricture, in a controlled way, for P3 operation (see Section 3.4).

The equivalent circuit for the MUX is a through resistance,  $R_M$ , and a shunt capacitance,  $C_M$ . MUX equivalents are shown installed in the transmitter and receiver transmission lines in Figure 3.2. It should be clear from the schematic representation in the figure that the interface and transmission line shunt capacitances are additive.  $C_{M_1}$  and  $C_{M_2}$  contribute to signal loading and, if variable, to measurement noise. Therefore, the shunt capacitance of the MUX must be kept within reasonable limits. In particular, it must present an impedance at the operating frequency that is large compared to  $R_L$ . Most of the current produced by the receiving transducer will then flow through the receiver.

It should be equally clear that the through resistance adds to the source and load resistances. The BASS measurement is notable for a very high level of single measurement accuracy. This is one of the reasons the BASS DTT technique was selected. Exceedingly small source and load resistances in a carefully balanced design are integral to that level of performance. Increasing those values by any significant

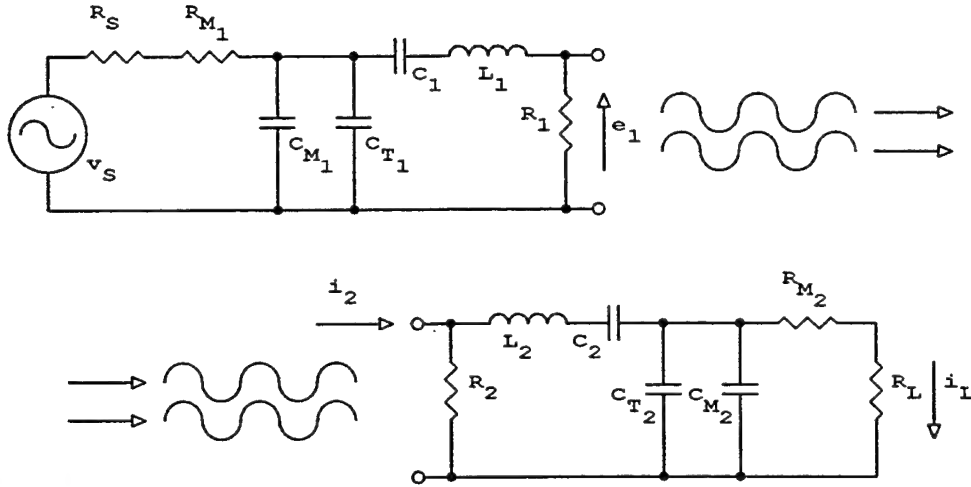


Figure 3.2: EQUIVALENT MODEL OF THE TRANSMIT/RECEIVE PROCESS WITH THE MULTIPLEXER - The equivalent model of the MUX is a through resistance,  $R_M$ , and a shunt capacitance,  $C_M$ . MUX equivalents are shown here installed in the transmitter and receiver transmission lines. The through resistance adds to the source and load resistances. Therefore,  $R_{M1}$  and  $R_{M2}$  must be kept negligibly small compared to  $R_S$  and  $R_L$  so that the effects of the variable shunt capacitances remain small. Similarly,  $C_{M1}$  and  $C_{M2}$  add to  $C_{T1}$  and  $C_{T2}$ , contributing to signal loading and, if variable, to measurement noise.

amount would alter the existing balance and cause an unacceptable degradation in measurement accuracy and performance. Thus, the strict requirement that  $R_M$  be no more than approximately  $1\Omega$ . The severity of this constraint is evident in the observation that  $1\Omega$  is one to two orders of magnitude smaller than the through resistance of any commercially available, *low impedance*, multiplexer. A new design, using specialty components and an optimized structure, was needed to meet the requirements of the BASS Rake WBBL sensor.

In summary, the necessary characteristics of an interface satisfying the constraints imposed by the BASS T/R circuit and the BASS Rake sensor design are extremely low through resistance,  $\leq O(1\Omega)$ , rapid switching,  $\leq O(10\mu s)$ , flexible cross connection of the transducers, and strong isolation between channels,  $\geq 30dB$ . The layered multiplexer described here provides the required flexibility and performance with an acceptably small effect on the existing T/R circuit.

The retention of the existing system, given the constraints it imposes, deserves comment. As stated in Chapter 2, the BASS DTT “method was chosen because of its

high accuracy and linearity and because of its extreme robustness to environmental conditions.” The familiarity and long experience of this laboratory with the technique and the fact that the BASS Rake developments described below will contribute significantly to the next generation of BASS were also factors. Beyond this, however, BASS is a physical implementation of good sensor design philosophy. The high accuracy and linearity are partly the result of direct reductions in the strengths of sources of error. This is true of most sensors. The design of BASS takes a further step, recognizing that those sources cannot be completely eliminated. The measurement is purposefully structured so that the sources that do remain cancel each others’ effects. It will be shown in subsequent sections of this chapter that the constraints imposed by requiring a MUX and retaining the BASS T/R circuit, while severe, can be satisfied. The high accuracy and linearity of the BASS DTT measurement can be applied in the WBBL.

### 3.3 Interface Design

The functional blocks and structure of the interface are developed in this section. This process is independent of the circuit modifications necessary for successful operation of the 2.5 mm P3 transducers. Those changes, including additions to the multiplexer, will be described in Section 3.4. Where pertinent, the impedance, loading, and drive characteristics of the P3 transducers are referred to in this section. These properties are expected to be similar in higher frequency transducers of the same diameter. However, precise values for these quantities are not required for the optimization of the MUX.

#### 3.3.1 Switching Element Selection

Meeting the interface specifications outlined in Section 3.2 depends, critically, on the switching elements chosen to multiplex the signals. Mechanical switches, such as reed relays, have the advantages of effectively zero on resistance and negligibly small series and shunt capacitances, typically less than 1 pF. However, the duration

of contact bounce in a reed switch is on the order of  $10\text{ ms}$ . That is relatively fast for a mechanical switch. It is also three orders of magnitude above the switching speed specification and amply sufficient to disqualify mechanical relays from further consideration. Some form of electronic switch with much faster state changes and extremely low through resistance is required.

Packaged arrays of electronic switches are commercially available in many forms from most manufacturers of integrated circuits (ICs). Eight and sixteen channel multiplexers packaged in a single IC are particularly common. They are also functionally applicable to the task of multiplexing the T/R circuit to the transducer array. To avoid confusion, these commercially available multiplexers will be referred to here as CMUXs or “commercial MUXs” and the MUX label will continue to denote the overall BASS Rake multiplexer. The through resistance of an electronic switch that has been selected will be denoted  $R(\text{on})$ . Most CMUX ICs designated as “low resistance”, or even “very low resistance”, have  $R(\text{on})$  values in the range  $80\ \Omega \leq R(\text{on}) \leq 100\ \Omega$ . Only one commercial MUX is available with a through resistance below this range. In that case  $R(\text{on}) = 20\ \Omega$ . All of these values are far too large to meet the specification of the BASS Rake MUX.

A very limited number of specialty MOSFETs<sup>4</sup> are currently available with drain-source on resistances below  $1\ \Omega$ . FETs can approximate the behavior of ideal switches and are in common use for this purpose. The switching elements in commercial multiplexers are, in fact, FETs. However, it will be seen in the discussion that follows that the approximation is not exact.

The VN3205 N-Channel Enhancement Mode Vertical DMOS FET (Supertex, Inc.©), with  $R_{DS}(\text{on}) = 0.3\ \Omega$ , has been chosen for this project. This is the smallest value of  $R_{DS}(\text{on})$  currently available and  $0.3\ \Omega$  is acceptably small compared to the source and load resistances of the T/R circuit. The VN3205 turns on in less than  $25\text{ ns}$  and off in less than  $50\text{ ns}$ , nearly three orders of magnitude faster than the specification. These are promising qualities for the MUX, but there are other char-

---

<sup>4</sup>MOSFET is the acronym for Metal Oxide Silicon Field Effect Transistors. MOSFETs are one of several varieties of Field Effect Transistors, FETs. The behavior, terminology, and pathology of FETs are readably and concisely described by Horowitz and Hill [34].



Figure 3.3: VN3205 N-CHANNEL ENHANCEMENT MODE VERTICAL DMOS FET - A schematic representation of the VN3205 is shown on the left with the gate, drain, source, and body/substrate appropriately labeled. On the right an equivalent model of the electrical characteristics of the VN3205 is shown. The schematic symbol and the form of the model would be the same for any N-Channel MOSFET. The stray capacitances in the model result from the geometry and proximity of the gate, drain, and source regions on the silicon substrate. The diode is formed by the  $n$ -type channel region, which is in contact with the drain, and the  $p$ -type body, which is internally connected to the source terminal.

acteristics of MOSFETS, including the VN3205, that make its use in this situation more complicated than treatment as an ideal switch. An equivalent model of the VN3205 is shown schematically in Figure 3.3.

The capacitive coupling between each pair of terminals shown in the model results from the size, shape, and proximity of the gate, drain, and source regions on the silicon substrate of the transistor. For the VN3205, the nominal (maximum) values of these stray capacitances are:  $C_{DS} = 50(100) pF$ ,  $C_{GD} = 20(30) pF$ , and  $C_{GS} = 200(270) pF$ . These values are quite high compared to MOSFETs with larger values of  $R_{DS(on)}$ . Relatively high capacitance is one of the performance costs associated with reduction of the on resistance. This is a consequence of the modifications to the geometry of the  $p$ - and  $n$ -type regions on the substrate used to reduce  $R_{DS(on)}$ . In a simplistic sense, greater surface areas decrease the resistance by providing a wider region for current flow between the contacts. The capacitance increases because it is proportional to the surface area of those same contacts.<sup>5</sup>

The drain-source diode is formed by the  $n$ -type channel region, which is in contact with the drain, and the  $p$ -type body, which is internally connected to the source

<sup>5</sup>Higher capacitance is also associated with increased loading and reduced switching speed. A through resistance on the order of  $100 \Omega$  is almost always acceptable because in most designs the other circuit impedances are at least on the order of  $1 K$ . It is loading and switching speed that most commonly constrain performance and the characteristics of available CMUXs reflect those more widespread needs. The requirements of the BASS Rake are well outside the norm.



terminal. IC packages containing a single FET are invariably fabricated with this internal connection [34]. This is unfortunate because the effect of the virtual diode can be eliminated simply by connecting the substrate to the most negative gate potential if that connection is externally available. Curiously, commercial MUXs are invariably fabricated with the substrate internally connected to the lowest gate potential so that there is no diode effect. The stray capacitances and the diode complicate the interface design in several ways.

### 3.3.2 Development of the L-Section

Consider the insertion of an N-channel MOSFET in the transmission line. The drain is connected to the T/R circuit and the source to the transducer. The state of this “switch” is determined by the voltage applied to the gate. The first difficulty is feedthrough coupling of the signal by the drain-source capacitance. The transmitter signal driving the transducer is a short burst of a  $\pm 5\text{ V}$  square wave with a frequency on the order of  $1\text{ MHz}$ . The received signal sent from the transducer to the receiver is also bipolar but only a few tenths of a volt or less in amplitude. The gate voltage controlling the state of the FET is  $\pm 12\text{ V}$ . When the FET is on, the low value of  $R_{DS(on)}$  effectively shorts  $C_{DS}$  and it can be ignored. In the off state, however, the drain-source capacitance makes the “open” switch look like a mere  $1\text{ K}$  to  $2\text{ K}$ , rather than the  $10^4\text{ M}\Omega$ , or more, one would expect for  $R_{DS(off)}$ .  $C_{DS}$  couples the transmitter signal intended for the selected channel through to the deselected transducers. These transducers broadcast signals, which are received by the other end of the selected channel. The acoustic signals are also received by other deselected channels and coupled through each  $C_{DS}$  to the receiver. In all cases the chosen velocity signal is contaminated by velocities from other levels of the boundary layer.

A shunt FET, as shown in Figure 3.4, is a common and attractive way to eliminate the feedthrough coupling [34]. When the series FET is on, selecting that transducer for use, the shunt is turned off. The series  $R_{DS(on)}$  and the shunt  $C_{DS}$  then form a voltage divider with entirely negligible,  $< 0.1\%$ , signal attenuation. The relatively high impedance of the shunt makes it effectively invisible. When the transducer is

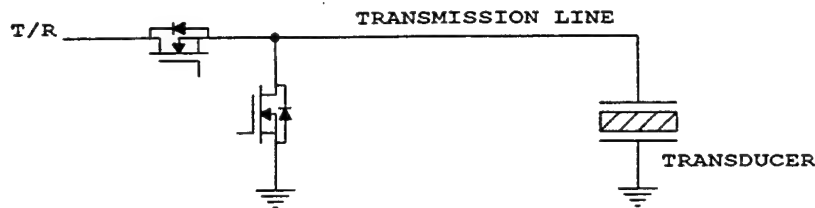


**Figure 3.4: REMOVING CAPACITIVE FEEDTHROUGH COUPLING WITH AN FET SHUNT SWITCH**  
 - In the selected state the series FET is on, allowing bi-directional signal passage, and the shunt FET is off, effectively removing it from the circuit. In the deselected state the series FET is off and the shunt FET is on. This shorts the transmission line to ground and effectively eliminates the signal due to capacitive feedthrough coupling. This has the added and highly beneficial side effect of strongly increasing cross-channel isolation. Unfortunately, the shunt also causes half-wave rectification of the transmitted signal, requiring further modification of the switching circuit.

deselected the situation is reversed. The series FET is off and the shunt FET is on, essentially shorting the capacitive feedthrough signal to ground. This action of the shunt has the added and highly desirable side effect of strongly increasing cross-channel isolation. Unfortunately, the shunt FET also causes half-wave rectification of the transmitted signal.

The rectification is a result of the drain-source diode created by the internal source-substrate connection of the FET. In the deselected state the shunt diode conducts whenever the bipolar transmitted signal is more than a diode drop negative, clipping that portion of the signal to a single diode drop below ground. The series diode behaves similarly in the deselected state. The result is half wave rectification of every burst transmitted on all channels. The rectification is eliminated at negligible cost by the circuit configuration shown in Figure 3.5. A second VN3205 FET is added to each branch of the L-section and connected source to source. This places the diodes of each branch in series with opposite polarity and eliminates the rectification. The change doubles  $R(on)$  to  $0.6\ \Omega$ , but this is still within acceptable limits.

Now consider the effects of the mechanical design and geometry of the BASS Rake sensor head. Acoustic coupling occurs when deselected channels are permitted to transmit and receive acoustic signals. The design of the BASS Rake actively invites acoustic coupling. Capacitive coupling occurs in the tines between long, parallel, wires in close proximity. Shielding each signal wire would largely eliminate this type of

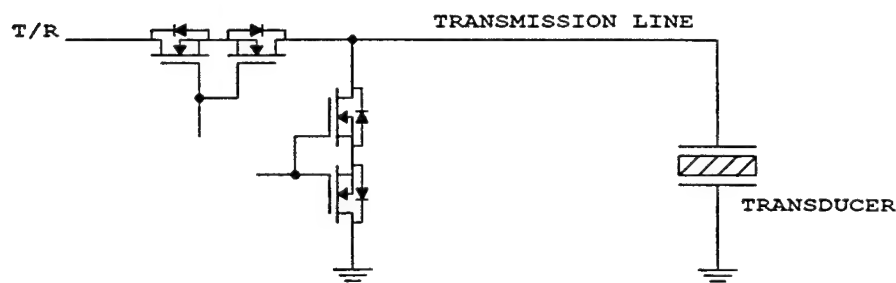


Figure 3.5: QUAD FET L-SECTION - The shunt and series portions of the L-section are each composed of two FETs connected source to source. This arrangement prevents halfwave rectification of the signal on all channels by the drain-source diode in the "open" branch of the L-section.

interference, but it would introduce other problems as previously discussed. However, in the absence of sufficient isolation provided by some other facet of the design, the option of shielding would have to be exercised. Thus the emphasis on cross-channel isolation provided by the MUX. Observe that the path leading to contamination of the received signal depends on both forms of coupling. First, the transmitted signal is capacitively coupled to other transducers in the tine. Then these transducers emit weighted acoustic signals along with the selected transducer. The receiving transducer of the selected channel collects all of the acoustic signals with some additional weighting. Each of the other transducers on the receiving tine also collects some weighted average of the acoustic signals. Finally those collections are capacitively coupled onto the already contaminated signal from the receiving transducer of the selected channel.

If the capacitive coupling could be eliminated, or at least limited, there would be little or no acoustic coupling. Limiting transducer action would further increase isolation. This is precisely the effect of the shunt FET in a deselected channel. It strongly grounds the transmission line, and through it the signal connection of the transducer, during both transmission and reception, sharply limiting capacitive and acoustic coupling. A single stage, series-shunt L-section, composed of four VN3205 has proven surprisingly effective at reducing all forms of signal coupling. Controlled tests with a single direction of acoustic propagation were conducted with the P2 tines using one meter of unshielded wire in each transmission line. The isolation of

deselected channels from capacitive coupling was approximately 35 dB in each tine. The acoustic isolation was approximately 25 dB for physically adjacent axes. The figure for acoustic loss is in addition to the in water signal attenuation. The overall cross-channel isolation provided by a MUX using just one layer of L-sections is clearly well in excess of the specification. Subsequent experience with the P2 and P3 tines and the layered MUX supports that conclusion that cross-channel coupling in the BASS Rake is entirely negligible.

For completeness, it should be noted that electronic switches are often arranged in T or  $\Pi$  geometries, rather than an L, to improve isolation through the switch section. In these circuits the impedance of the load forms a voltage divider with the additional series component to provide a greater level of signal attenuation. These geometries would be a poor choice here.  $C_{DS}$  is approximately equal to the capacitance of the transducer, so the T or  $\Pi$  would provide only a small increase in attenuation through the section. The price for this small gain would be the loss of the hard ground across the transmission line and transducer provided by the shunt branch. The overall cross-channel isolation would be entirely lost and all measurements would be contaminated with velocities from other levels of the boundary layer. The L geometry is a far better choice in this situation.

The final complication associated with the stray capacitances of the FET is signal loading. Each T/R circuit drives a pair of signal lines that are multiplexed through the L-sections to the two ends of the selected acoustic axis. Using the model of the FET shown in Figure 3.3, the equivalent capacitance of an L-section for the selected and deselected states can be readily calculated. That equivalent capacitance appears as a shunt from the signal line to ground. The physical path of the equivalent shunt is primarily through the four gate terminals of the FETs. The equivalent shunts of all the L-sections attached to a particular signal line are in parallel and combine additively. That combined capacitance is the shunt equivalent denoted by  $C_{M_2}$  in the reception model of Figure 3.2 and it is an additional load for each receiving transducer. The transmitter must drive both signal lines and is therefore loaded by both equivalent shunts in parallel. The additional load on each signal line is denoted

by  $C_{M_1}$  in the transmission model of Figure 3.2.

Any increase in measurement flexibility requires an increase in the number of L-sections connected to each signal line. This increases the shunt capacitances represented by  $C_{M_1}$  and  $C_{M_2}$ . Current preferentially flows through these branches as the impedance they present to the signal line drops. During transmission the current actually delivered to the dissipative element in the transducer is reduced. During reception the current delivered to the receiver load is reduced. Both reductions can seriously degrade performance.

If a single T/R board is used, each T/R circuit is multiplexed to 48 transducers with 24 L-sections on each signal line. The impedance of the equivalent shunt seen by the receiving transducer is comparable to the receiver load resistance,  $R_L$ , it is trying to drive. The receiver load current,  $i_L$ , is reduced by half. The equivalent shunt impedance seen by the transmitter is considerably smaller than the transducer impedance and very little acoustic energy would be delivered to the water. Accurate velocity measurements could not be made under these loading conditions. However, using additional T/R boards to decrease the load to a reasonable level is undesirable because it entails a significant loss of measurement flexibility. The solution is a multiplexer configuration that can hide most of the stray capacitance from the signal line without sacrificing measurement flexibility.

### 3.3.3 The Layered Multiplexer

A major portion of the stray load can be hidden by adding layers to the multiplexer in a branching double tree structure as shown schematically in Figure 3.6. It will be shown below that there is a configuration that maximizes the equivalent shunt impedance of the multiplexer subject to constraints on the level of measurement flexibility, the number of FETs used, and the switching speed of the MUX. The trees work by hiding some of the equivalent capacitance on each signal line of a T/R circuit behind deselected L-sections in each layer. The shunt switch of a deselected L-section grounds the input to the remainder of that branch, eliminating further contributions to the equivalent shunt load. In the two layer trees shown, only the two selected

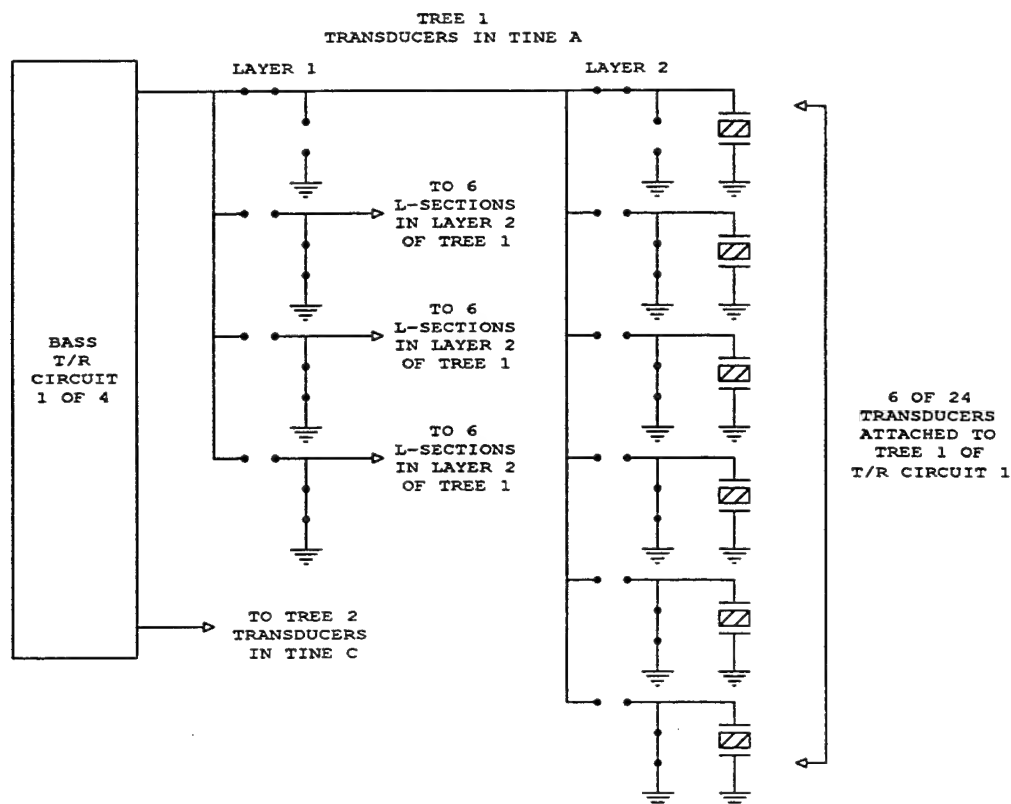


Figure 3.6: TWO LAYER MULTIPLEXER - The tree structure hides a portion of the equivalent shunt load behind deselected L-sections. The arrangement shown is demonstrably optimal for a 192 element array driven by a single T/R board. For simplicity, the branches of the FET L-sections are drawn as ideal switches and only a portion of the first tree is shown. The upper L-sections in each level of the first tree are selected. One L-section in each level of the second tree, not shown, is also selected. All other L-sections in both trees are deselected.

L-sections leading to the selected transducer, and the deselected L-sections within the selected branch and the first layer, are visible to the signal line.

Note that each additional layer in the MUX increases the cross-channel isolation. While this is not essential, given the level of isolation already produced by a single layer, it is beneficial, so it should not constrain the load optimization. Of more concern is the  $0.6\Omega$  increment in the through resistance of the MUX associated with each layer. Each increase is approximately 5% of the T/R impedances. This suggests an upper limit of three or four layers to maintain compliance with the design specification on  $R(on)$ . Obviously, two layers would be preferable. Potentially, this limit could constrain the reduction in loading through layering, requiring some sacrifice in

measurement flexibility.

The equivalent capacitance of a tree loads the signal line, decreasing the currents delivered to the dissipative element of the transducer during transmission and the receiver load during reception. As noted above, the imbalance can seriously degrade performance if it is not controlled. Performance is improved by decreasing the equivalent capacitance. The increased impedance of the stray shunt load then biases the current towards the dissipative element and the receiver load. To determine the shunt impedance presented by each tree, consider a general structure with  $\ell$  layers and  $n_i$  L-sections in each group of the  $i^{th}$  layer. For this tree the following relationships hold:

- The number of transducers multiplexed by the tree is

$$N_T = \prod_{i=1}^{i=\ell} n_i = n_1 \cdot n_2 \cdot n_3 \cdots n_\ell \quad (3.3)$$

- The number of selected L-sections seen by each signal line is equal to  $\ell$ , the number of layers.
- The number of deselected L-sections contributing to the load on each side of the T/R circuit is

$$N_{DSL} = \left[ \sum_{i=1}^{i=\ell} n_i \right] - \ell = [n_1 + n_2 + n_3 + \cdots + n_\ell] - \ell \quad (3.4)$$

For example, the trees in Figure 3.6 each multiplex 24 transducers through two layers with  $n_1 = 4$  and  $n_2 = 6$ . Each signal line is shunted by two selected and eight deselected L-sections.

For a fixed number of transducers connected to the tree, structuring the layers to arrange the elements of a given set,  $\{n_i\}$ , in ascending order will minimize the number of FETs required with no change to the net impedance. Changing the structure to reduce the range spanned by the elements in  $\{n_i\}$  increases the number of FETs, but has the more important consequence of maximizing the shunt impedance for a given number of layers. These properties are trivially evident from the arithmetic

relationships describing the tree. They can also be demonstrated by direct calculation for the limited number of possible combinations. It is desirable to maximize the shunt impedance and then minimize the number of FETs necessary to achieve that impedance. Applying the two structural properties in this order determines the optimum set,  $\{n_i\}_{op}$ , for a given number of layers and transducers. If a single T/R board is used with each half of a T/R circuit multiplexed to 24 transducers, the optimum structures for trees of 1, 2, 3, and 4 layers are  $\{24\}$ ,  $\{4, 6\}$ ,  $\{2, 3, 4\}$ , and  $\{2, 2, 2, 3\}$ . The second of these is shown in Figure 3.6.

Now observe that each added layer increases the load by one selected L-section and decreases it by some number of deselected sections. Assuming that the optimal set,  $\{n_i\}_{op}$ , is used at each level, the optimal configuration for a given number of T/R circuits, that is, for a given level of measurement flexibility, follows as a simple consequence of the different shunt values for the two L-section states. For a selected L-section the nominal equivalent shunt capacitance is  $505\text{ pF}$  with a maximum of  $716\text{ pF}$ . The values for a deselected L-section are  $65\text{ pF}$  and  $116\text{ pF}$ . The selected to deselected capacitance ratios are 8:1 and 6:1. Therefore, when adding a layer removes more than six to eight deselected L-sections from view, the net shunt impedance is increased. When fewer are eliminated, the net shunt impedance decreases. With the number of T/R boards set by a desired level of measurement flexibility, the structure of the tree can be optimized for maximum shunt impedance.

For a single T/R board each half of a T/R circuit would be multiplexed to 24 transducers placed at odd or even vertical levels. This is a very reasonable level of measurement flexibility. The change from one to two layers hides 15 deselected L-sections from each signal line. The change from two to three layers removes only two more from view. Therefore the two layer configuration shown in Figure 3.6 is demonstrably the optimum layered multiplexer when a single T/R board is used. The effective  $R(on)$  of a two layer multiplexer is certainly acceptable and therefore does not constrain the minimization of signal loading. Two layers is also optimal when either two or three boards are used. Additional boards increase the shunt impedance on the signal line at the cost of measurement flexibility. The degree of



cross connectivity lost with additional boards limits the vertical sampling scale for angled measurements. Turbulent length scales in the wave boundary layer suggest that two to three T/R boards (eight to twelve T/R circuits) is the practical limit if the transducer connection pattern along the time is periodic.

The question now arises, does the optimal, single T/R board, layered multiplexer, which meets all of the other stated requirements for the interface, provide a sufficiently high shunt impedance to prevent excessive signal loading? There are a number of other loads on the signal line that should be considered. The transducers are primarily capacitive loads. The 2.5 mm P3 transducers average 80 pF. At the operating frequency this is an impedance of approximately 1 K. The impedance of higher frequency transducers of this diameter will be smaller. Higher operating frequencies require thinner transducers and, to first order, the capacitance is inversely proportional to transducer thickness. The impedance is inversely proportional to the product of frequency and capacitance. This will be important to the determination of signal loading during future development. The transmission line is a shunt load of  $\approx 50$  pF or  $\approx 2$  K. The transmitter source impedance is 5  $\Omega$  to 10  $\Omega$  and the receiver load impedance is 12  $\Omega$  to 16  $\Omega$ . The shunt load presented by the two layer, single board tree shown in Figure 3.6 is 1500 pF to 2400 pF, 40  $\Omega$  to 60  $\Omega$ . The range for a two layer, two board tree, 1300 pF to 2000 pF, 45  $\Omega$  to 70  $\Omega$ , is similar.

The structure of the circuits during transmission and reception was shown in Figure 3.2. Because of transmitter diodes and receiver blanking in the T/R circuit, the transmitter is loaded, through the source resistance, by the shunt loads along both signal lines, but not by the receiver load [90]. These elements form a voltage divider with a response dominated by the impedance of the multiplexers. The divider attenuates the transmitter voltage by 15 % to 35 %. Clearly, signal loading during transmission is heavy, but perhaps not absolutely prohibitive. The transmitter voltage can be adjusted from  $\pm 2.5$  V to 3.5 V. A modification to the backplane could raise this to  $\pm 5$  V. The largest available voltage is  $\pm 12$  V<sup>6</sup>, however, the maximum transmitter amplitude is limited to  $\pm 8$  V. This is set by the  $\pm 12$  V gate control voltage and

---

<sup>6</sup>+5 VDC and  $\pm 12$  VDC are the existing power supply voltages on a BASS backplane.

the  $\pm 20\text{ V}$  gate-source breakdown voltage common to FETs. The  $\pm 5\text{ V}$  level is to be strongly preferred for two reasons. First, it prevents or reduces small variations in  $R_{DS(on)}$  that depend on the signal level. More importantly, it avoids the real possibility at higher voltages of wholesale destruction of the MOSFETS in the MUX due to burn through of the  $\text{SiO}_2$  insulating layer between the gate terminal and the substrate.

When receiving an acoustic signal each transducer is loaded by its own capacitance and transmission line, a single multiplexer tree, and the receiver load. As noted earlier, the transducer is best modeled as a current source driving these loads. The receiver is a cascode circuit which converts the current through the receiver resistance, the small equivalent impedance seen looking into the cascode emitter input, into a voltage signal at the cascode output [34, 90]. The response of the current divider formed by the various loads, like the voltage divider of the transmitting circuit, is dominated by the impedance of the multiplexers. 70 % to 80 % of the transducer current is delivered to the receiver. This range in the efficiency of current delivery to the receiver load applies to both the 2.5 mm and the 6 mm transducers.

The equivalent circuit fragment in BASS, because of the long coaxial transmission line and the normally 1 cm diameter transducer used, presents essentially the same capacitive shunt load to the transducer current source. 75 % of that current is delivered to the receiver. This suggests that signal loading during reception will also be acceptable. Unfortunately, the smaller transducers used in the BASS Rake, particularly the 2.5 mm transducers, have a much reduced current drive capability. Recall as well, from the discussion in Chapter 2, that the voltage output of the receiver is proportional to the fourth power of transducer radius for given transmitter voltage and operating frequency. At a minimum,  $\pm 0.5\text{ mA}$  should be delivered to the cascode receiver load for good signal quality [90]. At this level of measurement flexibility, the 6 mm P2 transducers are marginally functional. The 2.5 mm P3 transducers do not have sufficient drive capability and will require the additional modifications described in Section 3.4 to operate. However, a loss of measurement flexibility to reduce signal loading is not yet necessary. One additional modification to the basic L-section can

be made to increase the overall shunt impedance of the multiplexer.

It was noted earlier that the primary path of the MUX shunt is through the gate terminals of the FETs to the  $\pm 12V$  power supplies. Gate resistors will therefore increase the shunt impedance. They will also increase the switching time of the tree. The capacitance looking into the gate depends on the state of the FET switch. To maintain an RC time constant below  $2\mu s$  independent of the state, gate resistors up to  $3K$  in size may be used. A time constant up to  $10\mu s$  using a  $15K$  input resistor is the largest value still acceptable to the switching time specification. The effect of the added impedance on the tree is to flatten the optimum impedance peak and shift it slightly towards deeper layering. The effect increases with resistance, but the rate of change is steepest for low resistance. Given the constraint on  $R(on)$  and the smoothness of the optimizing peak, a two layer tree remains the best choice. The nominal shunt impedances of the tree shown in Figure 3.6 for  $1K$ ,  $3K$ , and  $15K$  gate resistors are  $154\Omega$ ,  $230\Omega$ , and  $258\Omega$ . The minimum values are  $108\Omega$ ,  $134\Omega$ , and  $140\Omega$ . With  $3K$  resistors and a  $2\mu s$  time constant, 90 % to 95 % of the transducer current is delivered to the receiver load.

This level of efficiency in current delivery is 20 % greater than in a standard BASS instrument. It is sufficient for the  $6mm$  P2 transducers used in the laboratory prototype to operate in fully round tines with the attenuation provided by several millimeters of polyurethane. However, the signal-to-noise (S/N) ratio was weaker than is normally considered desirable in BASS. As described in Chapters 2 and 5, the polyurethane of the P2 tines was carved down to a halfround cross-section to evaluate some characteristics of the flow disturbance. Without the attenuation of the polyurethane, the operation of the P2 tines, using the optimized, two layer,  $\{4,6\}$  multiplexer with  $3K$  gate resistors described above, could not be faulted. The noise floor reached during calibration was below  $0.5mm \cdot s^{-1}$ . The established minimum is  $0.3mm \cdot s^{-1}$ .

A schematic diagram of the complete L-section, as described above with the gate resistors, is shown in Figure 3.7 for reference. This functional block is the basic switching unit used successfully in the laboratory prototype with the P2 tines. A full

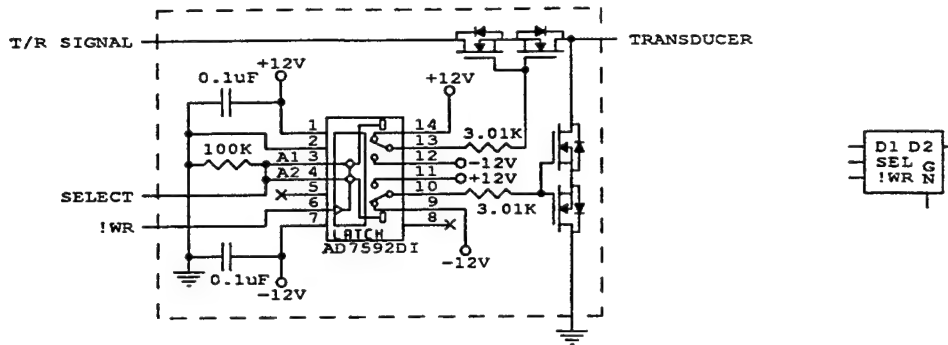


Figure 3.7: SCHEMATIC DIAGRAM OF THE COMPLETED L-SECTION - The schematic is shown on the left with a functional block symbol on the right. The quad FET L-section with 3 K gate resistors is visible on the right side of the schematic. The 7592 is a dual SPDT electronic switch. !WR is a state latching input for both switches. The "!" denotes the Boolean or logical "NOT" operator. It is held low in this design, enabling the switch control pins. The independent switch control pins of the 7592 are externally tied together and the  $\pm 12V$  connections are made such that the single SELECT input fully controls the state of the L-section. This particular block is drawn in the selected state. The 100 K resistor defines a deselected default state and the two capacitors suppress switching transients.

schematic wiring diagram for a {4, 6} branch of the MUX can be found in Appendix B.

### 3.3.4 Addressing the Array

This section describes the design of the hardware and firmware necessary to control the operation of the multiplexer trees. The large address space of the transducer array was first mentioned in Section 3.2. To support the measurement flexibility provided by the MUX and the mechanical design, the address must be wide enough to freely choose and control two of 192 transducers. To accomplish this the address must select two of 192 L-sections in Layer 2, two of 32 L-sections in Layer 1, and one of four T/R circuits on the single T/R board used by this design. The N/R measurement state must also be determined and greater address width would be needed if additional T/R boards were required to reduce signal loading.

It is the desire for flexibility in making and changing measurement patterns that makes it necessary to address the individual transducers. This is in contrast to the normal BASS addressing scheme, which is based on the selection of acoustic

axes. Consider that the number of axes in a measurement pattern is necessarily half the number of transducers. However, axis based addresses would require hardware alterations to change the pattern of measurements. Addressing the transducers is the better approach.

To begin with, the circuit design can reduce address width by logically combining essentially redundant information in hardware. This has already been done in the L-section shown in Figure 3.7. A single SELECT line controls both the series and the shunt branches, and thus the state of the switch. Separate lines are not required because the desired state of one FET absolutely determines the desired state of all the FETs in an L-section. A similar savings is possible using the layered structure of the tree. A logical OR of the SELECT lines in a single Layer 2 branch, performed in hardware, unambiguously provides the correct SELECT line state for the Layer 1 L-section at the base of the branch. Clearly this is applicable to a MUX with any number of layers, with logical ORs feeding back from each Layer  $m$  to each Layer  $m - 1$ . The physical OR gates performing this function can be seen on the P2 and P3 multiplexer board schematics in Appendix B.

Further reductions can be made because only a subset of the complete set of pairings is sensible or functional. For example, transducers in the same tine have no utility as an acoustic pair. Such a pairing has already been rendered unusable by the allocation of T/R circuits. Transducers in the same tine are either multiplexed to different T/R circuits or to the same side of the same T/R circuit. Similarly, pairings other than A-C and B-D with even or odd commonality can be excluded.<sup>7</sup> The address space does not need to encompass these extraneous combinations, but it does need to be structured properly to benefit from their exclusion. The structure used here reduces the number of address bits to a near minimum of twelve to select the transducer pair. Three additional bits are used to control the T/R board and one final bit is introduced as a programming convenience. This scheme allows for

---

<sup>7</sup>Tine and transducer designations were defined in Section 3.2. A-C and B-D are the diagonal acoustic paths between the tines. Even numbered transducers are multiplexed to the same T/R circuit. Similarly for the odd numbered transducers. This pattern is described in Section 3.3.3. No other paths are both acoustically and electrically functional.

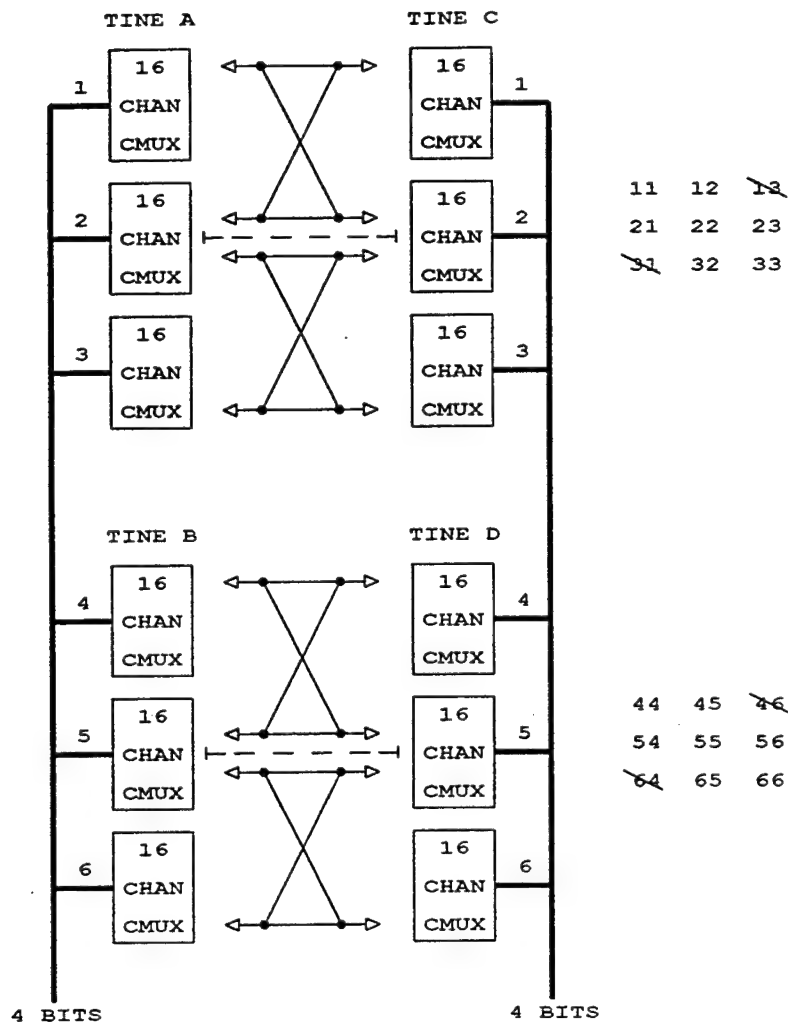


Figure 3.8: ADDRESS STRUCTURE FOR THE MUX - The channels of the CMUXs of each time drive the Layer 2 L-section SELECT lines. Three 16 channel CMUXs are exactly sufficient for the 48 transducers in each time. Tines A and B are never used at the same time, so they share a 4 bit bus which selects 1 of 16 channels and connects to all 6 CMUXs. Only 1 of the 6 is actually ENABLED at any given time. The same structure is used for tines C and D. In Tine A, even numbered transducers are selected by CMUX 1 and half of CMUX 2. Odd numbered transducers are selected by the other half of CMUX 2 and by CMUX 3. Similar distributions are made in the other tines. Because of this allocation, CMUX A1 is never enabled at the same time as CMUX C3. Similarly for A3 and C1. The other 7 CMUX pairings, as shown in the table, are allowed. Similarly, there are 7 allowed B-D CMUX pairings. 4 bits are sufficient to select 1 of 14 possible pairs. The total address width is 12 bits.

future expansion of the array to 256 transducers without widening the 16 bit address. The structure is shown in Figure 3.8. Should it ever prove necessary, the hardware implementation allows a straightforward expansion of address width.

The twelve CMUXs shown in Figure 3.8 are commercially available ICs. They are referred to here and in Appendix B as Lower Level CMUXs (LLMUXs) because they are partly controlled by a single Upper Level CMUX (ULMUX). The channels of the LLMUXs of each tine drive the Layer 2 L-section SELECT lines. Three 16 channel LLMUXs are exactly sufficient for the 48 transducers in each tine. Observe first that tines A and B are never used at the same time. Therefore they may share a 4 bit bus which selects one of 16 channels and connects to all six LLMUXs. Only one of the six is actually ENABLED at any given time. The same structure is used for tines C and D.

The LLMUX ENABLE signals also depend on careful structuring. In Tine A, even numbered transducers are selected by LLMUX 1 and half of LLMUX 2. Odd numbered transducers are selected by the other half of LLMUX 2 and by LLMUX 3. Similar distributions are made in the other tines. Because of this allocation, LLMUX A1 and LLMUX C3 are never enabled at the same time. Similarly for LLMUXs A3 and C1. The other seven LLMUX pairings, as shown in Figure 3.8 and Table 3.1, are allowed. Similarly, there are seven allowed B-D LLMUX pairings, also shown in Figure 3.8 and Table 3.1. Four bits are sufficient to select one of 14 possible pairs. The total address width is twelve bits. Note that the array can be expanded to 256 transducers without additional address bits. Four LLMUXs would be exactly sufficient for each tine. If the even numbered transducers are selected by LLMUXs 1 and 2, and the odd numbered transducers are selected by LLMUXs 3 and 4, there will be only eight allowed A-C LLMUX pairings and a further eight allowed B-D LLMUX pairings. Four bits are exactly sufficient to select one of 16 possible pairs.

The four bits selecting the ENABLE lines of the LLMUXs are connected to the four address lines of the single ULMUX, a 16 channel CMUX IC identical to the LLMUX ICs. The ULMUX is always enabled. The 14 LLMUX pairings are ENABLED by 14 of the ULMUX channels through a network of twelve 3-input OR gates. The analogous 16 gate network would be necessary for a 256 transducer array. The ENABLE line of each LLMUX is driven by the output of a single OR gate. The inputs of each OR gate are connected to the two or three channels of the ULMUX that code for pairings including that associated LLMUX. This structure is shown in detail in

Tables 3.1 to 3.3 below. The small fragment of the OR gate network necessary to operate the BASS Rake laboratory prototype can be seen on the MUX sequencer board schematic in Appendix B.

In addition to the twelve bits used to select transducers from the array, three bits are used to control the T/R board. Two of these bits are used to select one of the four T/R circuits on the board. The third bit determines the N/R state of the measurement. These are standard inputs to a BASS T/R board and must be supported for the board to operate with the BASS Rake. These three bits are normally provided by the TattleTale V (TTV, Onset Computer Corporation©) microprocessor along with three bits to select one of eight possible T/R boards. These six bits are the standard BASS axis address described in Section 3.2. They are the only I/O lines available to control the MUX and even the most efficient structuring will not allow a reduction of the BASS Rake address width to six bits. There is simply too much information to encode.

The solution used here is the generalized counter described by Bartee [4]. A counter, in the general sense, is a simple state machine with each state entirely determined by the immediately preceding state. The state of the counter is defined to be the ordered set of binary bits in the output of the counter. There is no requirement that the sequence of bit patterns occur in sequential numerical order, only that the sequence is cyclic and without repetition within a cycle. The sequence of BASS Rake addresses, 15 bits selecting two transducers and controlling the T/R board, is non-repeating (each address is unique), cyclic (the addresses are repeated for each profile measurement), and nonsequential (there is no bit ordering that produces a monotonic sequence of the counting numbers with a uniform increment of one). The sequence of BASS Rake addresses can be provided by a generalized counter.

With this approach the limit of six I/O lines is removed. The BASS Rake address may now contain any number of bits, including all of the six available I/O lines, while a single I/O line is used to CLOCK the counter sequence. Of course, reducing the address to a minimal and well structured set, as done above, is still a desirable objective. Bartee describes the construction of a generalized counter in hardware. This



### A-C LLMUX Pairings

A1C1	A1C2	-
A2C1	A2C2	A2C3
-	A3C2	A3C3

### B-D LLMUX Pairings

B4D4	B4D5	-
B5D4	B5D5	B4D6
-	B6D5	B6D6

Table 3.1: ALLOWED LLMUX PAIRS - Letter designations denote times, numerical designations denote LLMUXs. The two matrices show the 14 allowed LLMUX pairings for the address structure shown in Figure 3.8.

ULMUX Channel	ENABLED LLMUXs	ULMUX Channel	ENABLED LLMUXs
1	A1 C1	8	B4 D4
2	A1 C2	9	B4 D5
3	A2 C1	10	B5 D4
4	A2 C2	11	B5 D5
5	A2 C3	12	B5 D6
6	A3 C2	13	B6 D5
7	A3 C3	14	B6 D6

Table 3.2: ULMUX CODES FOR LLMUX PAIRS - ULMUX Channel 1 SELECTS the A1C1 pairing. Similarly for the other lines in the table. The ULMUX channels are the inputs to the OR gate network defined in Table 3.3. The outputs of the OR gates ENABLE the LLMUX ICs.

OR Gate Inputs ULMUX Channels			OR Gate Output LLMUX ENABLE	OR Gate Inputs ULMUX Channels			OR Gate Output LLMUX ENABLE
1	2	GND	A1	1	3	GND	C1
3	4	5	A2	2	4	6	C2
6	7	GND	A3	5	7	GND	C3
8	9	GND	B4	8	10	GND	D4
10	11	12	B5	9	11	13	D5
13	14	GND	B6	12	14	GND	D6

Table 3.3: OR GATE I/O ASSIGNMENTS - GND indicates an input held low. The OR gate inputs are ULMUX channels coding for particular LLMUX pairs. The OR gate outputs ENABLE the LLMUX ICs coded for by the ULMUX channels. For example, LLMUX A2 is ENABLED if ULMUX Channels 3 OR 4 OR 5 are selected. Refer to Table 3.2.

choice is inappropriate here because hardware changes would be needed to change the measurement pattern described by the sequence of addresses. However, the function is flexibly implemented with a sequential counter and an EPROM.<sup>8</sup> Both are widely available ICs.

The BASS Rake addresses are programmed, in order, into the EPROM, beginning with the first EPROM address. The address sequence can be changed at any time simply by reprogramming the EPROM. A single I/O line CLOCKS the sequential counter. The counter output sequences through the EPROM addresses in order. The EPROM output is therefore the BASS Rake address sequence in order. The BASS Rake address sequence is not long enough to fill the EPROM, so a second I/O line is used to RESET the sequential counter when a profile measurement is complete. As a programming convenience, an end-of-file (EOF) bit is added to the BASS Rake address and read on a third I/O line. In the absence of the EOF, the program running on the TTV would have to be changed to include the length of each new sequence. This involves a change in assembly level code and subsequent reprogramming of the TTV EPROM. It is operationally safer to avoid those steps. When the EOF bit is used only the EPROM containing the address sequence needs to be changed. The sequential counter and EPROM ICs of this implementation can be seen on the MUX sequencer board schematic in Appendix B.

The address and control structure can now be summarized. The BASS Rake address is 16 bits wide. Two 8 bit EPROMs are used to store the address sequence. More EPROMs can be added if a wider address is ever needed. Twelve of the 16 bits are used to select two transducers from the array. Three bits are used to select the T/R circuit and determine the N/R measurement state. This frees three of the six I/O lines. The final address bit is the EOF mark. The three available I/O lines are used to CLOCK the sequence, read the EOF bit, and RESET the sequential counter when a profile is complete.

The three remaining I/O lines of the standard BASS address can be made avail-

---

<sup>8</sup>EPROM is the acronym for Erasable Programmable Read Only Memory. Information can be programmed into these memory ICs only with a hardware interface designed for the purpose. Once programmed and installed for use the information is read only and nonvolatile.

able, if necessary, in the future. When only one T/R board is used, hardwiring the backplane or the BASS channel select board would be sufficient. Alternatively, the function could be incorporated in a wider BASS Rake address. In the laboratory prototype, to avoid changes to existing, standard cards and backplanes, the three TTV I/O lines remained connected to the BASS channel select card. They were set to select the single T/R connector in use on the BASS backplane by the BASS Rake program running on the TTV. The dual backplane structure of the laboratory prototype is described in Appendix B.

The address structure of the laboratory prototype differs from the scheme above in one particular. Early in the development it was thought that firmware control of !WR would be necessary and one bit of the address was allocated to this use. !WR, the state latching input to the multiplexer L-sections, is described in Figure 3.7. There was originally no EOF bit and the end of the address sequence was determined by a software down counter in the TTV program. When it became clear that active control of !WR was unnecessary it was also noted that the Boolean sense of that bit in EPROM was appropriate for use as an EOF marker. Modifications were made to the TTV program, then running in RAM rather than EPROM as the development progressed, and the BASS Rake backplane. The address sequence EPROM was unchanged. The bit continued to disable the state latch and was also read by the TTV as the EOF. In the future, the state latch function will be hardwired or simply eliminated by using an unlatched version of the dual SPDT switch IC in the L-sections.

### 3.4 Circuit Modifications for the P3 Transducers

As previously noted, the electrical characteristics and drive capabilities of the 2.5 mm P3 transducers preclude their use with an unmodified BASS T/R circuit. These problems are independent of the presence of the MUX. The poor electrical characteristics, largely caused by the small diameter, were corrected with the modifications to the Layer 2 L-sections described in Section 3.4.1. The weak current drive during reception is strongly a function of transducer diameter. Section 3.4.2 describes the design

and integration of a gain block into the existing signal path. Neither of these modifications was used in the prototypes described in Chapters 5 and 6. They are included here because they are applicable to 2.5 mm transducers operating at 5 MHz and will therefore be important in future development.

### 3.4.1 Modification of the L-Section for Small Transducer Operation

A transducer efficiently radiates sound to the water to the extent that it appears electrically resistive. Resistors are dissipative elements and the characteristic of the piezoelectric transducer resistance is simply that dissipation occurs through radiated sound rather than radiated heat as in a more typical resistor. This concept was introduced in Section 3.2. The impedance of the P3 transducers and transmission line, measured at their 850 KHz resonant operating frequency, is mostly capacitive reactance. The resistive component of the impedance is comparatively small and the transducer voltage and current are out of phase. Thus, the poor transfer of acoustic energy to the water. During testing, transmit voltages as high as  $\pm 37 V$  were applied to the P3 transducers through a special test fixture in the BASS Rake backplane (see Appendix B). The received signal strength was still completely inadequate for velocity measurement. At  $\pm 5 V$ , the maximum safe value for the MUX, the received signal could only be detected with difficulty. A solution that improves the efficiency of the energy transfer is essential.

To understand the solution presented here, the reader should recall that impedance is a complex quantity. The real part of the impedance is the resistance. The resistance dissipates energy and is nonnegative for all passive components. The imaginary part of the impedance is the reactance. Reactance stores and returns energy, but does not dissipate it. In general, reactance is a function of frequency. When not explicitly stated, it is the reactance (impedance) at the operating frequency that is meant here. Capacitive reactance is a negative imaginary quantity. Inductive reactance is a positive imaginary quantity. As with any complex quantity, impedance can be

described by real and imaginary components or by a magnitude and an angle. Both descriptions are used here.<sup>9</sup>

The magnitude of the P3 impedance is approximately  $700\ \Omega$  with an angle of  $-60^\circ$ . The impedance angle of a larger transducer is considerably closer to  $0^\circ$ . For example, the measured value for a 1 cm BASS transducer is  $-35^\circ$ . The weak energy transfer associated with the high P3 phase angle is made worse by the relatively large magnitude of the impedance. The voltage driving the transducer is fixed by the T/R circuit and for a fixed voltage, the power delivered to the load is inversely proportional to the magnitude of the load impedance. For comparison, the impedance magnitude of a 1 cm BASS transducer is only  $160\ \Omega$ .<sup>10</sup>

To improve operation, the transducer load must be made less reactive. Reducing the angle of the impedance will improve the efficiency of the energy transfer by bringing the transducer voltage and current closer in phase. Reducing the magnitude of the impedance will increase the power delivered to the load. Both reductions are accomplished by connecting an inductor in series between the MUX and the transmission line leading to the transducer. A value of  $120\ \mu H$  closely balances the existing capacitive reactance at the P3 operating frequency and effectively brings the overall reactive component of the load close to zero. What remains is the resistive component of the original impedance. Both the angle and the magnitude have now been greatly reduced and the radiation of acoustic energy is significantly enhanced. The received signal is easily detectable, though not strong enough to make velocity measurements, when the transmit voltage is restricted to  $\pm 5\ V$ , a level safe for use through the MUX.

It is also accurate to view this procedure as tuning the circuit for a series resonance. Cancelling the capacitive reactance with an inductive reactance that is of

---

<sup>9</sup>The reader unfamiliar with these concepts is referred to the discussions in Horowitz and Hill [34] and in Skilling [69] for additional information. The discussion in Skilling is far more complete, but considerably longer.

<sup>10</sup>The impedance measurements reported in this chapter were made using a Hewlett-Packard HP4195A Network/Spectrum Analyzer with an HP41951A Impedance Test Kit. The frequency range of the analyzer is  $10\ Hz$  to  $500\ MHz$ . The calibration procedure for the analyzer and test kit was carefully followed before each set of measurements. The magnitude and phase of the impedance of each component or circuit was measured as a function of frequency from  $500\ KHz$  to  $5\ MHz$ . The measurements were used to determine the location and quality of transducer resonance and to study the effects of circuit changes.

equal magnitude at the operating frequency makes the circuit resonant at that frequency. When driven at  $850\text{ KHz}$ , energy oscillates between the inductance and the capacitance. Damping is provided by the relatively small resistive component already in place. The result is a significant voltage gain across the inductor. The  $\pm 5\text{ V}$  signal sent through the MUX becomes a measured  $\pm 17\text{ V}$  signal driving the transmission line and transducer.

Normally, it would be desirable to reduce the component count by placing the inductor between the MUX and the T/R circuits. In that position only eight inductors would be needed, rather than 192. Recall, however, the  $\pm 20\text{ V}$  gate-source breakdown voltage of the FETs (see Section 3.3.3). The voltage gain across the inductor and the  $\pm 12\text{ V}$  gate control voltage would be amply sufficient to destroy every series branch FET in the interface during the first profile measurement. The shunt branch FETs are not in danger because the high voltage appears between drain and source and between drain and gate in the shunts. The drain-source or gate-drain potential difference must exceed  $\pm 50\text{ V}$  to cause breakdown. The position of the inductor is also restricted by FET switching characteristics. Each time the source terminals of the series branch FETs become more positive than the gate terminals, because of the enhanced signal voltage, the FETs will turn off. Again, this does not affect the shunt FETs because the voltage is applied at the drain, not the source. For both reasons, one inductor is required for each transducer in the array.

Unfortunately, given the performance improvement of this approach, the inductor creates two new problems. First, because a significant voltage can develop across the inductor at the operating frequency, the cross-channel isolation provided by the shunt branch of the Layer 2 L-section is lost. All velocity measurements will be wholly contaminated. Measurement contamination was described in Section 3.3.2. It is the discussion of the effects of T and  $\Pi$  geometries, compared to the L geometry used in the MUX, that is particularly pertinent here. Fortunately, there is a ready and effective solution to this problem. Cross-channel isolation can be fully restored by adding a second FET shunt branch on the transducer side of the inductor. The same control voltage is applied to both shunts in the extended, Layer 2, switch section.

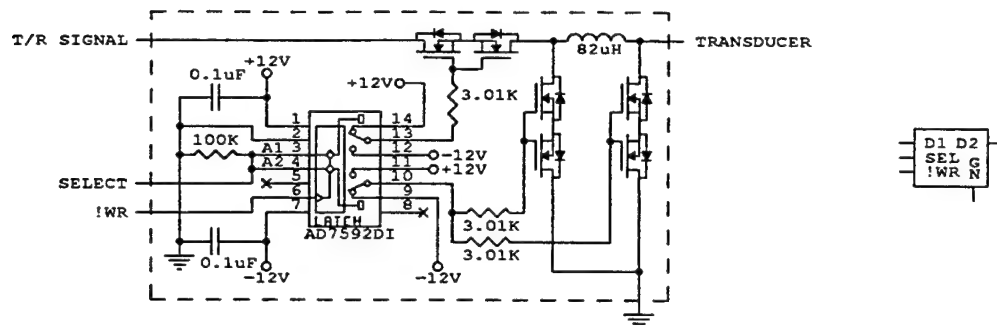


Figure 3.9: EXTENDED L-SECTION FOR P3 OPERATION - A schematic drawing of the switching element is shown on the left with a functional block symbol on the right. The hex FET L-section with two shunt branches and tuning inductor is visible on the right side of the schematic. Other components and all signal and control connections are defined in Figure 3.7. The inductor improves the efficiency of acoustic radiation by tuning the load for resonant behavior. The second shunt branch is required to restore cross-channel isolation.

A schematic diagram of this circuit is shown in Figure 3.9. Comparison should be made to Figure 3.7. A complete wiring diagram for a {4,6} branch of the P3 MUX can be found in Appendix B. Note that the impedance of the second shunt changes the load impedance seen from the position of the inductor. To properly balance the new reactive component, the size of the inductor is reduced to  $82\mu H$ . The measured voltage gain across the inductor is still slightly in excess of three. The signal driving the transmission line and transducer is  $\pm 17V$ .<sup>11</sup>

Now consider the second problem introduced by the presence of the inductor. At the operating frequency, the impedance of the inductor is more than  $400\Omega$ . With the extended L-section in the selected state, that impedance violates the stricture against significant increase of the T/R circuit source and load resistances. Recall the importance of small source and load resistances to measurement accuracy and stability described in Section 3.2. However, because of the shunt capacitance of the MUX, the inductor is not strictly in series with  $R_S$  and  $R_L$ . It is necessary to revisit the equivalent model of the transmit/receive process to understand the effects of the inductor on the velocity measurement. The equivalent circuits are shown in Figure 3.10.

<sup>11</sup>In hindsight, the inductor might be placed between the series and shunt branches of the L-section. A second shunt would not be necessary. That variation may be pursued in future.

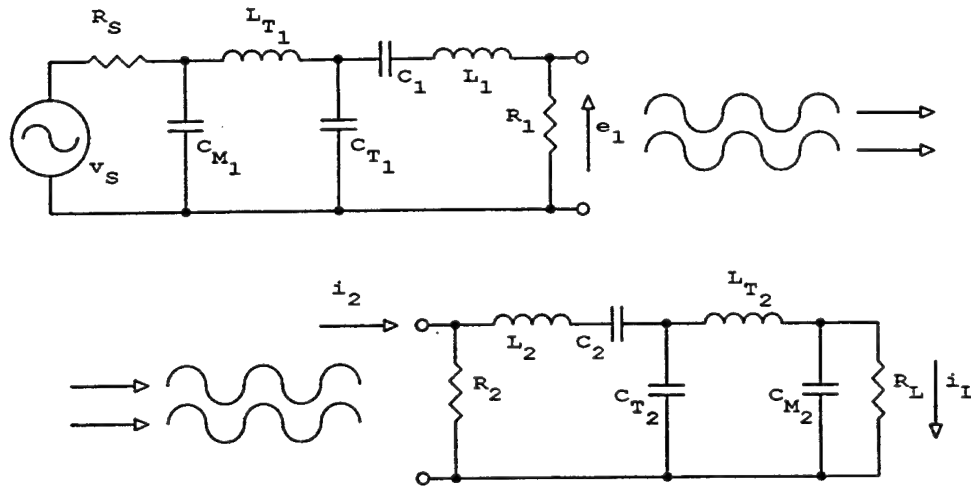


Figure 3.10: EQUIVALENT MODEL OF THE TRANSMIT/RECEIVE PROCESS WITH AN EXTENDED P3 L-SECTION - The equivalent model of the transmitter is shown in the upper portion of the figure with a similar model for the receiver in the lower portion.  $R_S$  and  $R_L$ , the source and load resistances, both include the through resistance of the MUX. Similarly,  $C_{T1}$  and  $C_{T2}$ , the shunt capacitances of the transducers and transmission lines, also include the capacitances of the second shunt branches of the extended P3 L-sections.  $L_{T1}$  and  $L_{T2}$  are the tuning inductors. The other equivalents model the shunt capacitance of the rest of the MUX and the behavior of the piezoelectric material. Comparison should be made to Figures 3.1 and 3.2 where these quantities were first defined. The inductors increase the zero offset of the velocity measurement, but the mechanical design of the tines prevents the production of a large, limiting noise floor.

The radiation transfer function from  $e_1$  to  $i_2$  was given in Equation 3.1 and is used again here. As before, the balance of the transfer function relating the receiver load current to the transmitter source voltage is determined by applying voltage and current divider equations to the equivalent circuits. The resulting expression, Equation 3.5, should be compared to Equation 3.2.

$$\begin{aligned}
 i_L(t) &= v_s(t - \Delta)G \\
 &\times \frac{R_1}{R_S \left( \underbrace{\frac{Z_1}{X_{C_{M1}}} + \frac{Z_1 X_{L_{T1}}}{X_{C_{T1}} X_{C_{M1}}} + \frac{X_{L_{T1}}}{X_{C_{M1}}} + \frac{Z_1}{X_{C_{T1}}} + 1}_{A} \right) + \underbrace{\left( Z_1 + \frac{Z_1 X_{L_{T1}}}{X_{C_{T1}}} + X_{L_{T1}} \right)}_B} \\
 &\times \frac{R_2}{R_L \left( \underbrace{\frac{Z_2}{X_{C_{M2}}} + \frac{Z_2 X_{L_{T2}}}{X_{C_{T2}} X_{C_{M2}}} + \frac{X_{L_{T2}}}{X_{C_{M2}}} + \frac{Z_2}{X_{C_{T2}}} + 1}_{A} \right) + \underbrace{\left( Z_2 + \frac{Z_2 X_{L_{T2}}}{X_{C_{T2}}} + X_{L_{T2}} \right)}_B}
 \end{aligned} \tag{3.5}$$



As in the earlier expression,  $t$  is time,  $G$  is the transconductance gain, and  $\Delta$  is the time needed for the acoustic signal to propagate from the transmitter to the receiver. The other quantities are defined in Figure 3.10.

The reactive elements are again confined to the denominator. Recall that it is only the reactive components that affect the phase of the signal, introducing the fixed and varying velocity offsets that it is desirable to suppress. The expressions within the transfer function labeled  $\mathcal{A}$  are each multiplied by the source or the load resistance. As described in Section 3.2, the original design of the BASS T/R circuit limited sensitivity to reactive variations by keeping  $R_S$  and  $R_L$  small. Both are approximately  $10\ \Omega$ . As described in Section 3.3, the design of the BASS Rake MUX preserves that quality.  $R_S$  and  $R_L$  are still approximately  $10\ \Omega$ . As a result, the phase effects of the  $\mathcal{A}$  expressions are negligible. They will cause small offsets, on the order of  $1\ \text{cm} \cdot \text{s}^{-1}$ , and no measurable noise. The design requirement of small source and load resistance remains important when the tuning inductors are used.

Now consider the expressions within the transfer function labeled  $\mathcal{B}$ .  $Z_1$  and  $Z_2$  model the behavior of the piezoelectric material and are fixed quantities. The reactances of the inductors,  $X_{L_{T_1}}$  and  $X_{L_{T_2}}$ , are also fixed.  $X_{C_{T_1}}$  and  $X_{C_{T_2}}$  each model the capacitance of the second shunt branch in the extended P3 L-section in parallel with the capacitance of the transmission line and transducer electrodes. The capacitance of the shunt branch is nominally  $65\ \text{pF}$ , but it may be as high as  $116\ \text{pF}$  depending on manufacturing variations in the VN3205 FETs. The actual value within that range is fixed. The P3 transducers average  $80\ \text{pF}$  and the transmission lines average  $50\ \text{pF}$ . Only the transmission line capacitance has the potential to vary with time.

The mechanical design of the BASS Rake prevents large dynamic changes in transmission line capacitance by using short, unshielded wires, firmly embedded in polyurethane. This was discussed in Section 3.2. Further, the effects of any changes that do occur are reduced by the relative sizes of the capacitances contributing to  $C_{T_1}$  or  $C_{T_2}$ . The shunt branch, transmission line, electrode capacitances are additive with a minimum total of approximately  $200\ \text{pF}$ . The transmission line capacitance is

at most one quarter of the total. A 1 % change in the capacitance of the transmission line causes at most a 0.25 % change in  $C_{T_1}$  or  $C_{T_2}$ . The practical result is that the phase effects of the  $B$  expressions may be large, but they are nearly constant. In terms of the BASS Rake P3 velocity measurement this means potentially large, fixed, zero offsets and a marginally elevated noise floor.

Laboratory measurements were performed with the laboratory prototype and the P3 tines. Carrageenan gel was used to establish a precise zero flow condition [53]. Observed offsets were as large as  $\pm 50 \text{ cm} \cdot \text{s}^{-1}$  and stable over time. The noise floor was measured to be  $0.5 \text{ mm} \cdot \text{s}^{-1}$  to  $0.7 \text{ mm} \cdot \text{s}^{-1}$ . The established BASS noise floor is  $0.3 \text{ mm} \cdot \text{s}^{-1}$ . Some of the excess is associated with the dual backplane construction of the laboratory prototype (see Appendix B). Noise between the backplanes was not reduced to negligible levels until after the P3 tines were replaced with the P2 tines. Another factor is acoustic reverberation due to the wide beam of the P3 transducers and the small size of the laboratory tank. The amplifier described in Section 3.4.2 introduces a small amount of noise, but the amplification is needed for operation and cannot be discounted here. The actual noise floor is no more than  $0.5 \text{ mm} \cdot \text{s}^{-1}$ , based on subsequent test with the P2 tines. This is far below the sensor head wake noise of most flows and certainly an acceptable level of accuracy. The zero offsets decrease the dynamic range of the instrument. The linear range of the DTT measurement is in excess of  $\pm 240 \text{ cm} \cdot \text{s}^{-1}$  [92]. The offsets reduce this to approximately  $\pm 200 \text{ cm} \cdot \text{s}^{-1}$ . For the expected velocity range within 30 cm of the bottom on the continental shelf, it is unlikely that the offset limit will play a role, even under relatively severe conditions. This is an acceptable restriction.

The tuning inductors are empirically necessary for P3 operation with the MUX. It seems likely inductors will be necessary with any transducer of this diameter. The performance of these transducers benefits enormously from the increase in the efficiency of energy transfer to the water. The design of the BASS Rake demonstrably preserves a low noise level when the inductors are in place. Given that, the large offset is an acceptable trade-off for the finer vertical resolution provided by the 2.5 mm transducers.

### 3.4.2 The COSAC Receiver Amplifier

The description of the small transducer amplifier is prefaced with a brief description of the BASS receiver and detector. The background information is necessary because these circuits had a significant influence on the design. A few comments about amplifiers and component selection are included for similar reasons. In addition to the texts by Horowitz and Hill [34] and by Skilling [69] that have already been mentioned, the application notes by Sherwin [70] and by Williams [95], particularly the latter, are recommended background reading on high gain amplifiers.

The BASS receiver is a cascode circuit physically located on the T/R board. The circuit is composed of two bipolar transistors operating at a steady collector current of  $3.6\text{ mA}$ . That set point is stabilized by a third transistor. The current input of the receiver is the emitter terminal of one of the cascode transistors and the voltage output is at the collector terminal of the other cascode transistor. The output drives a  $1\text{ K}$  small signal impedance and is capacitively coupled to the input of a Schmitt trigger detector. The DC collector resistor is chosen so that the set point current places the collector near the middle of its voltage range. This permits the fullest symmetrical and linear swing of the bipolar received signal. The Schmitt trigger is physically located on the differential time to voltage board where the DTT measurement is made. The cascode output is passed to the detector on the backplane. The minimum signal voltage for operation of the detector is  $1 V_{p-p}$ . The subscript indicates a peak-to-peak voltage for a bipolar signal. The minimum requirement is for the strongest portion of the signal pulse. The amplitude of the first cycle, which must be detected cleanly by both receivers, will be approximately  $50\text{ mV}$  at this level. A detector input level of  $2.5 V_{p-p}$  to  $3 V_{p-p}$  is strongly preferred to the minimum requirement [90].

The cascode circuit was originally chosen for BASS because the design strongly reduces capacitive coupling between the two receivers of an acoustic axis and because of the extremely low input resistance it provides [90]. The cascode is unusual in this respect as most designs feature high input impedance to avoid heavy loading. The importance of low receiver input resistance in BASS has already been discussed. The small signal or incremental impedance looking into the emitter of a bipolar

transistor is readily calculated from the Ebers-Moll model [34, 90]. Over the range of expected operating temperatures the incremental emitter impedance,  $z_e$ , is accurately approximated by  $z_e = \frac{24}{i_C}$ , where  $i_C$  is the set point collector current in  $mA$ . The actual value is  $12\Omega \leq z_e \leq 16\Omega$ .  $z_e$  is the receiver load resistance,  $R_L$ , of the T/R circuit.

The voltage output of the cascode is  $10mV_{p-p}$  to  $20mV_{p-p}$  when tuned P3 transducers are used.  $40dB$  to  $50dB$  of gain in the signal path is required to make velocity measurements. The transmitter voltage cannot be increased because of the gate-source breakdown voltage limitation of the FETs in the MUX. The gain of the cascode is fixed.<sup>12</sup> The logical place to insert a gain stage is between the cascode and the detector. This position does not interfere with the careful balances of the T/R circuit and the interface to the transducers. The location also avoids significant wiring changes. The cascode signal can be taken off the backplane, amplified on a separate board, and passed on to the detector along the backplane again. A single minor change is required on the detector board. The amplifier board is referred to as the COSAC, Cascode Output Signal Amplifier Circuit.

Signal amplification, particularly at frequencies above  $100KHz$ , introduces the possibility of a number of detrimental effects and should not be undertaken lightly or haphazardly [34, 95]. As a general rule, both the S/N ratio and the stability of the signal path will be reduced as amplification increases [34, 62, 69, 95]. The required overall gain is  $40dB$  to  $50dB$ . However, amplifiers introduce noise, so bandpass filtering about the signal frequency will be required to recover the original signal-to-noise ratio. For operating frequencies of a few hundred kilohertz and above, filters should generally be implemented with passive components [34, 94]. The active part of the circuit has to provide  $\approx 60dB$  of gain to cover losses in the passive filters.

Several distinct versions of the COSAC board were fabricated or partially fabricated for evaluation. Most went through several revisions. The high gain and oper-

---

<sup>12</sup>Examination of the Ebers-Moll equations will, at first, suggest that the gain of the cascode could be increased by reducing  $i_C$ , the operating point collector current. This would also increase  $z_e$  ( $R_L$ ), the receiver load resistance, but a small increase might acceptably be traded for increased gain. However, the change in  $i_C$  requires a balancing change of the DC collector resistor to keep the cascode output voltage near the middle of the range. As a result, there is no net change in the transresistance (current to voltage) gain of the cascode.

ating frequency are beyond the capabilities of all but a handful of currently available operational amplifier (op-amp) ICs. The gain in these COSAC designs was provided in two or three stages. This has several benefits. It tends to reduce the degradation of the signal to noise ratio [34, 70, 95]. Multiple buffering also permits more control over the input and output impedances of the COSAC and the filter section. For example, the input to the COSAC is driven by the cascode and should preserve the  $1\text{ K}$  small signal load characteristics and DC biasing of the Schmitt trigger input. Similarly, the output of the COSAC should present the source impedance and voltage levels expected by the Schmitt trigger. Stabilizing the op-amps also placed some constraints on the input and output impedances of the bandpass filter. Multiple stages, high overall gain, and high frequency all contribute to reduced stability. For a two stage COSAC, the minimum necessary gain-bandwidth product (GBW) of the op-amps is still  $80\text{ MHz}$  to  $100\text{ MHz}$ . As noted, this is a nontrivial requirement. The minimum GBW drops somewhat for a three stage amplifier but stability problems increase. COSAC designs have to balance the gain, filtering, bandwidth, and loading needs against available GBW, added amplifier noise, greatly amplified background noise, and circuit stability.

The most successful of these designs is described below. P3 performance characteristics given in this chapter are based on this amplifier. The op-amps, HFA1114s (Harris Semiconductor, Inc.©), have an enormous GBW of  $850\text{ MHz}$ . Operation is very stable and linear, but the HFA1114 is not a low noise op-amp. Calculation of the added noise based on gain, source impedance, and specified voltage and current noise equivalents indicate the COSAC could raise the measurement noise floor by  $0.1\text{ mm} \cdot \text{s}^{-1}$  to  $0.2\text{ mm} \cdot \text{s}^{-1}$  [70]. During P3 testing the effect appeared to be considerably smaller than this and could not be measured directly. Elevation of the noise floor above  $0.3\text{ mm} \cdot \text{s}^{-1}$  was largely due to the dual backplane construction of the laboratory prototype. The added noise calculated for a three stage amplifier based on the extremely low noise AD745 op-amp (Analog Devices, Inc.©) was several orders of magnitude smaller. However, the GBW of the AD745 is only  $20\text{ MHz}$ . Stable operation was possible with carefully balanced parallel capacitance in the feedback

path<sup>13</sup>, but the operating point was overly close to the edge of the performance envelope for reliable operation. The AD745 could not support that level of gain at 5 MHz. A moderately low noise alternative, the HA-5147 (Harris Semiconductor, Inc.©), has a 120 MHz GBW, but was not available at the time the COSAC was being developed. Calculated added noise for the HA-5147 is negligibly small and the specified GBW suggests good linearity and stability at 5 MHz. This is a reasonable direction to take during future development. However, the more than adequate performance of the HFA1114 based COSAC is empirically proven and has demonstrated that accurate velocity measurements can be made with small transducers. Based on developmental testing and experience, operation of the HFA1114 at 5 MHz should present no serious difficulties.

A schematic wiring diagram of the COSAC board is shown in Figure 3.11. The drawing is repeated in Appendix B. The board supports two identical, high gain, narrow band COSAC amplifiers. Each COSAC supports the received signal path at one end of the selected acoustic axis.

The components on the board are physically located above a heavy groundplane. The groundplane helps to reduce noise, particularly transient spiking due to power supply switching and system clocks by providing a return path with extremely low impedance. It also contributes to high frequency stability. The circuit is powered from a +12 VDC supply. The power distribution rail is filtered at multiple points with paired capacitors to suppress noise and prevent dips due to demand by the active components of the circuit. The capacitor types and sizes are chosen to compensate for component deviation from ideal behavior at high frequency. Similar pairings are used at a number of other points in the circuit. The power supply capacitor pairs are placed physically close to power distribution points on the rail. Each power connection to a biasing network or an op-amp is made through an LC attenuator to further decouple the signal line from system and power supply noise. Because of the large overall gain

---

<sup>13</sup>This technique is described by Williams [95] and is analogous to the use of balanced capacitors in oscilloscope probes with gain. The feedback capacitor maintains the gain at high frequencies where the gain resistors begin to deviate from ideal behavior. The capacitance also changes the phase of the feedback, increasing high frequency stability.



it is particularly important to suppress noise coupling to the signal line before the first gain stage.

The output of the cascode is biased to approximately  $7.7\text{ V}$  through the  $1.21\text{ K}$  resistor. This is the DC collector resistor through which  $i_C$ , the cascode set point collector current, flows. The collector resistor, series capacitor, and the parallel resistance of the two  $8.45\text{ K}$  biasing resistors and the  $50\text{ K}$  noninverting input resistance of the HFA1114 precisely duplicate the load characteristics normally presented to the output of the cascode. The biasing resistors set the operating point of the signal line at  $6\text{ V}$ . The first HFA1114 gain stage is physically and electrically supported above the groundplane on several capacitors. Because of the capacitors, it has unity gain at DC, so the operating point of the output is also biased to  $6\text{ V}$ . The same biasing control and capacitive support is used in the second gain stage.  $6\text{ V}$  is the midpoint between the rails of the single sided power supply and therefore provides the maximum symmetric range and linearity for the bipolar signal.  $12\text{ V}$  is the maximum rail differential of the HFA1114.

The two gain stages in each channel are identical. The HFA1114 is manufactured in an 8 pin DIP (dual in-line package) with the internal functional blocks shown schematically in Figure 3.11. If allowance is made for the presence of the fixed, internal resistor network, the standard op-amp pin assignments are used [34]. The internal resistors are each  $300\ \Omega$ . The input resistor is also the input impedance of the external inverting input.  $300\ \Omega$  is too small for the network loading the cascode, so the first gain stage is connected for noninverting operation. It is desirable, for reasons described below, that the bandpass filter between the two stages is loaded by a  $2\text{ K}$  resistance. Therefore, the second gain stage is also connected for noninverting operation. Noninverting operation also preserves the expected positive polarity of the first cycle of the received signal at the detector.

The summing node (SN) of the HFA1114 is directly accessible on pin 5 and this terminal is used in the COSAC to program the gain. The  $10\ \Omega$  resistor is in parallel with the  $300\ \Omega$  input resistor setting the gain to  $30\text{ dB}$ , a factor of 32. The external connection from pin 2 to the  $10\ \Omega$  resistor makes the parallel relationship explicit, but



is not necessary for operation. The unity DC gain of the amplifier holds those points to a common potential of  $6\text{ V}$  and the gain is unchanged if the wire is removed. The wire is included in the circuit because it suppresses noise at the summing node. The combined gain of the two HFA1114 stages is the required  $60\text{ dB}$ . Observation and testing show the gain is linear and stable.

Unlike many op-amps, the AD745 for example, the HFA1114 does not generally require capacitance in the feedback path for stability and linearity at high gain. During testing the addition actually appeared to be detrimental and it is not used in this amplifier.<sup>14</sup> The HFA1114 is, however, quite sensitive to the characteristics of the circuit loading the output. If the load is capacitive, the HFA1114 invariably becomes unstable, producing uncontrolled, rail-to-rail, high frequency oscillations and a fair amount of heat. During the development of the COSAC two of these op-amps were destroyed by this method. Empirically, the load must be largely resistive and the critical value for stable operation increases with gain. A  $2\text{ K}$  resistor between the output of the gain stage and the rest of the load provides a wide margin of stability with  $30\text{ dB}$  of gain. At the output of the COSAC, the  $2\text{ K}$  resistor is part of a relatively wide RC bandpass filter. This network drops the operating point of the bipolar received signal to  $0\text{ V}$  so that the Schmitt trigger will operate. It also duplicates the characteristics of the source impedance normally driving the detector.

The passive LC network between the gain stages is a narrow, six pole, Bessel bandpass filter. The high gain of the COSAC amplifies ambient noise as well as the signal. As noted above, the op-amps also add new noise to the signal. The added noise is largely due to semiconductor shot noise and is normally specified in terms of equivalent voltage and current noise sources. A bandpass filter is needed to remove added noise and improve the S/N ratio. Filtering is also needed to suppress stray signals occurring well above the operating frequency. This is of concern only because the high GBW product of the HFA1114 makes it possible to amplify such signals. A

---

<sup>14</sup>This is probably due to the very low,  $2\text{ pF}$ , input capacitance. Capacitors small enough to balance a gain of  $30\text{ dB}$  would need to be smaller than  $0.1\text{ pF}$ . The leads alone would exhibit substantially more capacitance. There may be internal compensation through existing parasitic capacitances.

Bessel filter was chosen because it provides maximally flat delay in the pass band [94]. Without flat delay the received signal would be distorted and measurement accuracy would be lost. A filter with a flat delay is also commonly referred to as a linear phase filter because of the behavior of the transform in the frequency domain. As previously discussed, changes in the phase of the received signal are of some concern. Bessel filters are also minimally sensitive to departures from ideal behavior by the reactive components. This is particularly important as the number of poles increases [94].

The form and component values of the filter were determined by scaling and transforming a normalized, three pole, Bessel low pass filter. These operations are described by Williams and Taylor [94]. The scaling matches the filter to both the geometric center frequency and the source and load impedances. The source impedance was set at  $2K$  to insure stability of the first gain stage. Filter characteristics are improved by symmetrical loading, so the output at the second gain stage, the parallel resistance of the biasing resistors and the noninverting input, is also  $2K$ . For reference, the calculated magnitude and phase of the frequency response are shown in Figures 3.12 and 3.13. Note that the filter is also supported on capacitors to maintain the  $6V$  DC bias. The loss through the filter is  $6dB$ . There is also some loss in the RC networks at the input and output of the COSAC. The overall gain through each channel is approximately  $50dB$  and the signal presented to the Schmitt trigger detector is typically  $3V_{p-p}$  to  $4V_{p-p}$ . The noise floor is  $0.5mm \cdot s^{-1}$ . Using the tuning inductors and the COSAC, velocity measurements can be made accurately with  $2.5mm$  transducers mounted in a BASS Rake tine.

### 3.5 Conclusions

This concludes the description of the integrated mechanical and electronic design of the BASS Rake. A complete and detailed set of schematic wiring diagrams is provided for reference in Appendix B. These drawings present the circuit design used in the BASS Rake laboratory prototype during the tow tank and flume tests described in Chapter 5. Chapter 5 also includes several photographs of the laboratory prototype.

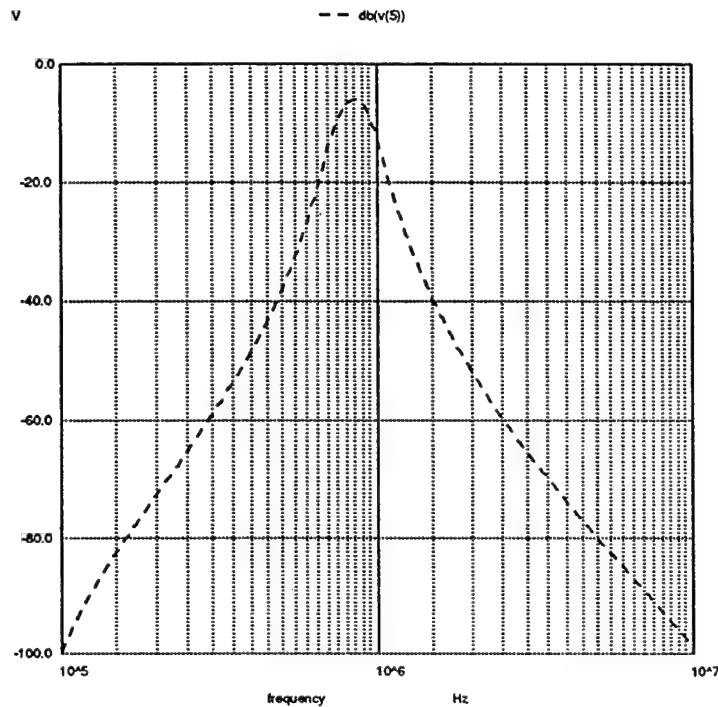


Figure 3.12: BESSEL BANDPASS FILTER FREQUENCY RESPONSE - MAGNITUDE - Two decades of the frequency response are shown. The vertical scale is in  $dB$ . The biasing capacitors distort the response below  $100\text{ KHz}$ , but the skirt stays below  $-80\text{ dB}$  and effect is negligible. The plotted response is calculated based on the actual component values, rather than the virtual values determined by transforming and scaling the normalized LP filter characteristics.

The physical scales of the wave bottom boundary layer impose a number of constraints on the design of an instrument intended to image the dynamic structure of the flow. Meeting these sensor constraints and those of the BASS T/R circuit requires a multiplexer interface providing low through resistance, rapid switching, flexible cross connection, and good isolation. Laboratory use has demonstrated that all of the design and performance criteria established for the interface are met by the layered multiplexer.

The multiplexer and addressing scheme described in this chapter were used successfully with the P2 tines in the BASS Rake laboratory prototype. Those tests are described in Chapter 5. Tests of received signal strength both with and without the

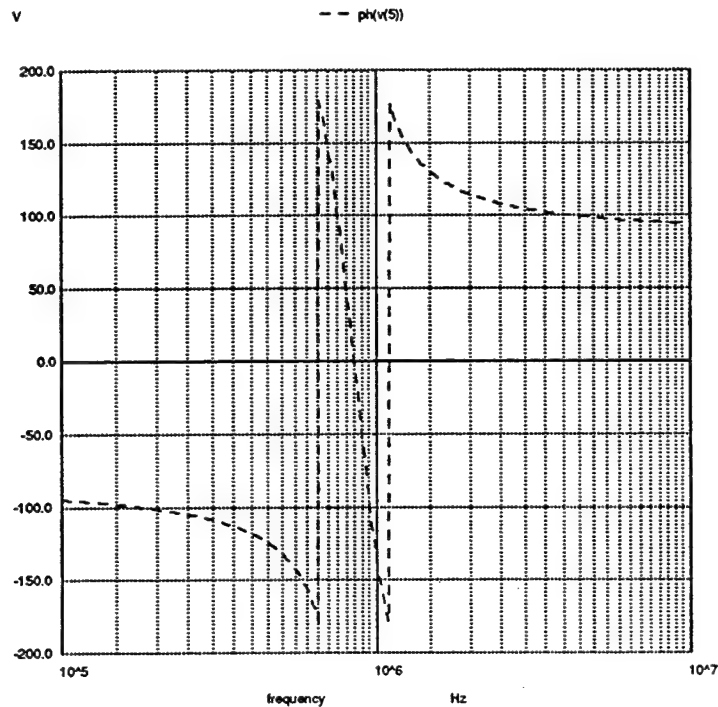


Figure 3.13: BESSEL BANDPASS FILTER FREQUENCY RESPONSE - PHASE - Two decades of the frequency response are shown. The vertical scale is in degrees. The apparent discontinuities occur as the phase is wrapped at  $180^\circ$ . The plotted response is calculated based on the actual component values, rather than the virtual values determined by transforming and scaling the normalized LP filter characteristics.

MUX showed that the calculated shunt load of the MUX is accurate. 90 % to 95 % of the transducer current is delivered to the receiver load. The layered MUX was, in fact, shown to be an inconsequential rather than a limiting load on the signal line. Overall measurement performance was excellent. In particular, the noise level is below  $0.5 \text{ mm} \cdot \text{s}^{-1}$ , essentially the established BASS noise floor. Single measurement accuracy of the BASS Rake electronics is thus a fraction of a millimeter per second. The true limit of measurement accuracy will be set by the distortion of the flow by the tines. Instrument calibration for the flow disturbance will be discussed in Chapters 5 and 6.

Modifications to the basic design, including tuning inductors and amplification of

the receiver signal, will be needed to to build future versions of the BASS Rake with smaller, higher frequency, transducers. The performance of these modifications and the ability to make accurate velocity measurements with small transducers has also been empirically established.

## Chapter 4

# The Single Axis Sample Volume

### 4.1 Introduction

Historically, it has not been necessary to determine the actual volume of water sampled by a single BASS acoustic axis. The arrangement of the four crossing acoustic axes necessarily averages the velocity field over a volume that is large compared to any reasonable estimate of the volume sampled by each path. Additionally, BASS sensors are always placed 30 *cm* or more above the bottom. This is done so that the most energetic turbulent scales present in the volume are not hidden by the implicit spatial average [19, 54, 90]. In consequence, the sample volume of an individual path never interacts with the boundary. Recently, Terray has studied the single path sample volume [75]. However, this ongoing work is restricted to understanding the response of an acoustic path to turbulence, particularly at scales that are small compared to the path length. The development of the BASS Rake has made it necessary to clearly define the single axis sample volume and to understand the effect it has on a measurement of the non-turbulent wave and steady components of the flow.

The necessity arises both because of the fine vertical resolution of horizontal velocity the BASS Rake is designed to provide and because of the intended proximity of the bed during operation. In BASS, differential arrival time is measured from a particular zero crossing of the received wave form. The wave form is the sum of signals arriving along multiple rays with disparate lengths and along-ray fluid velocities,

both of which affect arrival phase. It can be shown, by summing these sine wave bursts, that the measured velocity is an average, weighted by signal strength, of the integrated fluid velocities along all of the constructively contributing rays. A pair of transducers placed at a particular height above bottom will report a fluid velocity averaged over the cross-axis extent of the ray bundle. The averaging smooths the velocity profile, limiting resolution. More seriously, the averaging produces systematic errors when the profile is non-linear. For example, the average over some range of a logarithmic profile will always be low because the mean slope of the profile is greater above the transducer centerline than below it. The error increases as the boundary is approached. An additional error occurs if the sample volume and the boundary overlap. That error will depend on the geometry of the sample volume, its proximity to the bottom, and the nature of the signal's interaction with the bed. Quantifying these effects is essential to a full characterization of the sensor response. This is the first time this phenomenon has been evaluated for a BASS acoustic axis both for a non-turbulent component of the flow and for any flow in the immediate vicinity of a boundary.

A formal description of the sample volume for a single acoustic axis is developed in Section 4.2. The formula, a Fresnel integral, is solved for three instructive cases at the end of the section. Descriptions of wave diffraction, which gives rise to the sample volume, can be found in many texts on optics or acoustics. Crawford [12], Fowles [18], Monk [50], Morgan [51], and Rayleigh [64] are useful in this respect. Of these, Rayleigh [64] is particularly lucid and interesting. An explanation of the scattering of the diffracted wave by inhomogeneities within the sample volume can be found in Monin and Yaglom [49]. The initial portion of the mathematical development in Section 4.2.3 depends heavily on this text. In Section 4.3, a simplified, parametric model is presented and shown to yield substantially the same results as the Fresnel integral. The differences are well below the measurement accuracy of the sensor and the computational overhead is reduced by at least two to three orders of magnitude. The parametric model is used to estimate the measurement error for canonical continental shelf wave bottom boundary layers in Section 4.4. Calculations

using the parametric model are compared to measurements obtained in steady flume flow over a sand bed in Chapter 5.

## 4.2 Formal Description and Solution

The concentric rings of the diffraction pattern produced by a flat wave front incident on a round aperture in a large, flat sheet will be familiar to most readers. The process can be understood in terms of Huygens' Principle, which holds that each point on a wave front acts as a spherical radiator. The field at any subsequent point is the sum of the waves arriving from each radiator. Because the radiators are at different distances the waves will arrive with different phases and add either constructively or destructively to produce the diffraction rings. The Huygens construction can be found in several of the texts listed above. A homogeneous, non-scattering medium is an implicit assumption of the classical formulation. Obviously this is not the case for acoustic propagation in the ocean. However, the initial discussion focuses on the simpler case of a medium that does not alter the wave. This will provide the necessary background for the following discussion of the sample volume that results when the propagating sound wave, the moving, inhomogeneous sea, and the bottom interact.

### 4.2.1 Diffraction and Wave Propagation Between Two Transducers

One problem with Huygens' Principle is the prediction of a backwardly propagating wave produced by the spherical radiators. Additionally, the original construction did not explain the observed bending of light (or sound) into the geometrical shadow of an object that was opaque to the waves. These difficulties were later resolved by Fresnel, based on an understanding of wave interference [18, 51]. Fresnel derived a mathematical description of the modified Huygens' Principle now known as the Fresnel-Kirchoff Formula. This formula is given in Equation 4.1 for the case of a



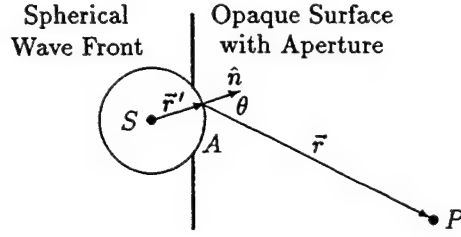


Figure 4.1: DEFINITION SKETCH FOR THE FRESNEL-KIRCHOFF FORMULA - A point source,  $S$ , lying on the centerline of a round aperture in an otherwise opaque wall, generates a spherical wave front. A portion of the expanding wave front is incident on the opening and a spherical cap,  $A$ , on the front and bounded by the edge of the aperture, can be defined. The Huygens radiator at  $\vec{r}'$  on  $A$  makes a contribution to the field at the point  $P$ .  $\vec{r}$  locates  $P$  relative to  $\vec{r}'$ .  $\hat{n}$  is the surface normal of  $A$  at  $\vec{r}'$  and  $\theta$  is the angle between  $\hat{n}$  and  $\vec{r}$ . The Fresnel-Kirchoff Formula sums the contributions of the elements of  $A$  to the field at  $P$ .

point source located on the centerline of a round aperture.

$$W_P = -\frac{ik}{4\pi} \iint_A \frac{W_o e^{i(kr')}}{r'} \frac{e^{i(kr-\omega t)}}{r} [\cos(\theta) + 1] dA \quad (4.1)$$

The variables and geometry of this formulation are defined in Figure 4.1.  $W_P$  is the optical (acoustic) disturbance at  $P$ . In this form,  $|W|^2$  describes the scalar intensity field.  $\frac{W_o e^{i(kr')}}{r'} = W_A$  is the complex amplitude of the incident wave on the spherical cap bounded by the aperture.  $k$  and  $\omega$  are the wave number and radian frequency of the wave. Each element,  $dA$ , on the cap, makes a contribution  $W_A \frac{e^{i(kr-\omega t)}}{r}$  to the field at  $P$ .  $\cos(\theta) + 1$ , the obliquity factor, accounts for the direction of propagation and prevents the formation of the backwardly propagating wave that was inherent in Huygens' original formulation [18]. Only the leading order terms are retained in the derivation of the Fresnel-Kirchoff Formula and it is not strictly applicable for  $P$  in the immediate vicinity of the aperture. However, it is not necessary to assume the larger values of  $r$  required by the far field approximation discussed below.

A transducer with a radiating surface matched to  $W_A$  would produce the same field at any point  $P$  as that produced by the point source,  $S$ , and the aperture [12]. If  $S$  stays on the centerline but is moved away from the aperture so that  $r' \rightarrow \infty$ , the incident wave front becomes a plane wave. The surface,  $A$ , becomes flat and the

equivalent transducer is a flat disk like those used in the BASS Rake. Each point on the surface of the transducer acts as a Huygens radiator and the pattern of sound produced is the classic Fresnel diffraction field of concentric shells [12, 18, 50, 51].

Some simplification is permitted if the Rayleigh length,  $L_{Rayleigh} = \frac{D^2}{\lambda}$ , where  $D$  is the diameter of the transducer and  $\lambda$  is the wavelength of the sound, is small compared to the distance,  $r$ , to the point of interest,  $P$ , in the radiated field (see Figure 4.1). In particular, the physical extent of the transducer is no longer relevant and a locally planar wave front can be assumed. This is commonly called Fraunhofer diffraction or the far field solution. It is a limiting case of the more general Fresnel formulation [12, 18, 50, 51].

Now consider the case of the BASS Rake with a receiving transducer located on the centerline of the transmitting transducer. The point of interest in the radiated field now ranges over the face of the receiver. This geometry is axially symmetric in the absence of a boundary. There is also a mirror symmetry across the plane perpendicular to the transmission axis and including the midpoint between the transducers because of reciprocity; a transducer receives with the same pattern that it transmits. If the Fraunhofer approximation is assumed the source and receiver can be treated as points. Referring now to Figure 4.2 and taking advantage of the symmetry, when the wave front from the transmitter reaches  $x_1$ , the Huygens radiator at  $x_1$  transmits to the receiver. The locus of points,  $x_i$ , with a common travel distance is an ellipsoid with the transducers at the foci. The signals defined by the ellipsoid all arrive at the receiver with the same phase and add constructively. In a practical sense, the propagation of sound from transmitter to receiver is not restricted to the straight path between them.

The travel distance along the centerline is nearly equal to that through the adjacent ellipses. These arrivals have a similar phase and add constructively. Farther out from the centerline there is a region where the travel distance is greater by approximately  $\frac{\lambda}{2}$  and the arrival phases relative to the centerline signal are near  $\pi$ . Sound in this shell subtracts from the received signal. Continuing outward from the centerline, shells which alternately add to and subtract from the received signal can be easily

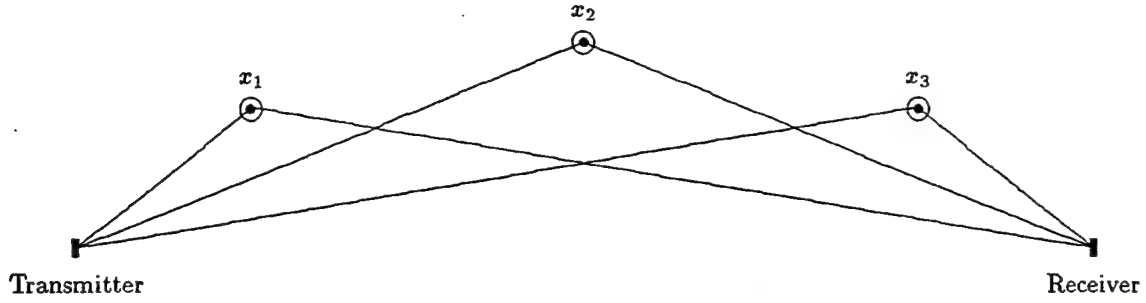


Figure 4.2: CONSTRUCTION OF THE ELLIPSOIDAL SAMPLE VOLUME - As the wave front from the transmitter reaches each point,  $x_i$ , it transmits, in the Huygens sense, to the receiver. Contributions from the radiators lying on an ellipsoid with the transducers at the foci arrive with the same phase and add constructively, a consequence of a common path length.

visualized. A cross section of the shells taken perpendicular to the centerline would reveal a pattern of concentric positive and negative rings. It can be shown that the area of each of the annuli is the same [50]. Necessarily the rings get rapidly thinner with increasing distance from the centerline. In this idealized construction the positive and negative contributions exactly cancel, leaving only the central ray. However, if the physical extent of the transducers is retained, the cancellation is incomplete because of the obliquity factor. A set of the ellipsoidal Huygens-Fresnel zones exists for each path from an element on the transmitter to an element on the receiver. The collective contribution of the rapidly alternating outer shells tends to zero for each set, leaving the central region, its exact extent somewhat fuzzy, as the effective sample volume.

What assumptions are appropriate for the BASS Rake? Recall the P2 and P3 transducers described in Chapter 2. The Rayleigh length of the  $2.5\text{ mm}$ ,  $0.85\text{ MHz}$  P3 transducers is  $3.5\text{ mm}$ . For the P2 transducers, with  $D = 6\text{ mm}$  and  $f = 1.75\text{ MHz}$ ,  $L_{\text{Rayleigh}} = 42\text{ mm}$ . For the  $15\text{ cm}$  path length used in the laboratory prototype, the far field would appear to be a reasonable assumption for the P3 transducers. However, the wide mainlobe (Fraunhofer) of the P3 transducers has prevented their use in the immediate vicinity of the boundary where the assumption could be tested. Over the length of the acoustic axis, the P2 transducers exhibit a Fresnel rather than a Fraunhofer pattern. Empirically, an ellipsoid of additional travel distance  $\frac{1}{4}\lambda$  to  $\frac{1}{2}\lambda$

is a reasonable approximation of the actual sample volume between a pair of the P2 transducers.

#### 4.2.2 Defining the Scattering Mechanism

The systematic study of wave scattering has more recent antecedents than the classical description of diffraction. However, the origins of both are largely found in the classical investigations of optics. Monk credits Rayleigh with the first detailed treatment of scattering and the first accurate description of the underlying principles, citing a series of published papers spanning nearly half a century [50]. In this century, Monin and Yaglom cite a large body of literature concerned primarily with atmospheric scattering of electromagnetic (EM) waves [49]. This work has had importance for optical and radio astronomy, satellite communications, and over-the-horizon radio transmission.<sup>1</sup> Monk's summary of Rayleigh's work on the propagation of light through a gas is concise and instructive:

The molecules of gas traversed by the incident light may be considered as sources of secondary waves. Each molecule acts on the light individually, *i.e.*, as if unaffected by the presence of other molecules. Between the primary wave incident upon a molecule and the secondary wave given off from it there exists a definite phase relation. Because the molecules are distributed at random, the phases of the individual scattered waves have no fixed relation to each other, except in the direction of propagation, where they will have the same phase. Hence, in order to express the intensity of the scattered light, the sum of the intensities of the individual scattered waves is taken instead of the sum of the amplitudes. *The effect of all the molecules in a layer is arrived at by summing up the effects of Fresnel zones into which the layer is divided* [emphasis added]. The resultant vibration thus obtained is combined with the vibration of the incident wave, the result being a change of phase which may be considered as due to a change in velocity like that which occurs when light enters a refracting medium. This accounts for the entry of the index of refraction into the final formula. [50]

---

<sup>1</sup>Monin and Yaglom also cite a mid century body of work concerned with the scattering of acoustic signals by atmospheric turbulence [49]. However, their discussion is restricted to a purely turbulent, zero mean, velocity field. The EM development is more general and has been preferred here as being more suitable for adaptation to the case of the BASS Rake.

The classically derived Fresnel zones are necessarily part of the formulation and it can be anticipated that the solution will now involve an integral of the incident and secondary waves over a scattering volume described by fluctuations in the index of refraction field. This mathematical development will be undertaken in Sections 4.2.3 and 4.2.4. Conceptually, scattering modulates the signal along each ray in an otherwise phase coherent, ellipsoidal bundle. This prevents, in the general case, mutual cancellation of concentric Fresnel zones of opposite sign. The outer zones alternate sign increasingly rapidly with increasing radial distance from the central axis and therefore tend toward a vanishingly small contribution. However, even in the idealized far field case, with point source and receiver, the inner Fresnel zones no longer collapse to the central ray except in very specific cases.

The scattering of acoustic waves in the ocean, particularly over kilometer scale path lengths, is an area of active research. Scattering is a problem for acoustic communications. However, scattering of a known signal is also used to probe the structure of the ocean. It is accurate, in the case of EM propagation in the atmosphere, to regard local variations in the index of refraction, caused by turbulent inhomogeneities, as the underlying physical mechanism of scattering. In the ocean, spatial and temporal inhomogeneities in the speed of propagation relative to the source and receiver, caused both by variation in sound speed and by relative movement of the water, provide the equivalent physical mechanism. Scattering should be thought of in the general sense of modulations to the individual rays in a bundle. The modulations include changes to both the amplitude and the phase of each arrival.

Note that the relative movement of the medium in the frame of the transducers matters for acoustic signals. This is, in fact, the only significant mechanism of scattering when making a measurement with the BASS Rake. Consider that the continental shelf bottom boundary layer is typically well mixed. Sound speed varies by significantly less than 1 % across the bottom few meters of the boundary layer [19, 54]. In contrast, fluid velocities can vary by an order of magnitude over the same distance. The horizontal length scale for similar variations in both sound speed and velocity is typically an order of magnitude or more larger than the vertical scale. Both length

scales are significantly larger than the corresponding dimensions of the BASS Rake. The BASS differential travel time measurement is, to first order for small changes, linearly dependent on local sound speed. The sensitivity along each ray in a bundle is linear in fluid velocity over the range  $\pm 240 \text{ cm} \cdot \text{s}^{-1}$ . Measurement accuracy of the undisturbed flow is not below 1 %, primarily because of the intrusion of the sensor into the flow (see Chapter 5).

Temporal variations in sound speed of a few percent generally occur only over tidal and longer time scales. Large changes in fluid velocity occur over the full range of tidal, wave, and turbulent time scales [19, 54]. However, variation of propagation speed can reasonably be assumed not to occur during the  $300 \mu\text{s}$  duration of a measurement. The sound speed variations could be removed, if necessary, by measuring *in situ* temperature, salinity, and depth reasonably near the sample volume and applying an equation of state for sound speed (e.g., [43]). For practical purposes, sound speed is a constant over the sample volume for any given measurement, while fluid velocity can vary significantly.

From this line of reasoning, I conclude that, for the BASS Rake, the field of propagation speed in the frame of the transducers can be reduced to the fluid velocity field in the same frame. The field of EM index of refraction fluctuations is replaced by the fluid velocity field normalized by the speed of propagation. This is equivalent, within the accuracy of the derivation below, to normalizing the fluid velocity field by the constant local speed of sound.

Time averaging leads to a further simplification of the velocity field, which consists of steady, wave, and turbulent components. The logarithmic and Bessel profiles of the boundary layer models are time averages from which the turbulent fluctuations have been removed (see Appendix A). Those profiles are assumed to depend, over the horizontal scale of the sensor, only on distance from the bed. The effects of Fresnel zone averaging in a scattering medium for time averaged measurements can therefore be evaluated using a velocity field that depends only on distance from the bed. This will greatly simplify the calculation developed in Section 4.2.3. The effective sample volume for the turbulent component of the flow is considered separately. Terray

reports an analytic solution in this case in which the integral collapses, to very high order, down to the central ray [75]. This may be caused by the stochastic nature of the turbulent scattering. If the turbulent modulation of the rays in each Fresnel zone bundle is unbiased, the concentric zones may still tend to cancel and only a relatively small central region would remain. This is merely speculation as the issue has not yet been satisfactorily resolved.

### 4.2.3 The Fresnel Integral in a Scattering Medium

A mathematical description of atmospheric scattering of EM signals, based in part on earlier work by other investigators, is given in Monin and Yaglom [49]. The central points of their argument are recounted here. The validity of approximations and simplifications required by their derivation for the BASS Rake and the continental shelf bottom boundary layer are examined as the development proceeds. Modifications suitable to the BASS Rake are applied where necessary, and the resulting Fresnel integral describing the sample volume of an acoustic axis is evaluated. The critical assumptions of the Monin and Yaglom argument are that (1) the fluctuations in the index of refraction are small compared to one, (2) the fluctuations are time independent, (3) the signal propagation time is small compared to the time scale of the fluctuations, (4) the wavelength of the incident signal is small compared to the length scale of the fluctuations, and (5) the far field approximations of Fraunhofer diffraction are satisfied. The discussion of Section 4.2.2 suggests that the first four conditions are reasonable for the continental shelf boundary layer and the BASS Rake. Condition (5) may be inappropriate for the P2 transducers with  $L_{Rayleigh} = 42\text{ mm}$  (Section 4.2.1), however, Monin and Yaglom state that the last condition is more stringent than is strictly necessary [49].

The major implication of condition (5) for the BASS Rake is only that the transducers will be treated as point source and receiver. Terray and the author argue that the physical extent of the transducers could be recovered, to first order, by evaluating the Fresnel integral for the scattering case from each element on the transmitter face to each element on the receiver face and summing the results. The sum would need

to account for phase as well as amplitude and the physical extent of each element would necessarily be small compared to the wavelength of the signal. The Fraunhofer assumption would be strictly valid for each element pair. Unfortunately, the integrand would increase in complexity to account for the geometry of the generally angled paths through the velocity field [75]. It will be seen in what follows that this construct would require enormous computational resources to solve in a reasonable period of time. The summing approach has not been pursued because the results presented here appear to validate both the single integral approach and a simpler parametric model (Section 4.3).

Consider now the propagation of a plane wave,  $E_o = A_o e^{iS_o} = e^{\psi_o}$  through a volume,  $V$ , containing index of refraction fluctuations,  $n'(\mathbf{x})$ .  $E_o$  is any of the Cartesian components of the incident electric field with amplitude  $A_o$ .  $S_o = \mathbf{k}\mathbf{x}$  is the phase of the incident field.  $\mathbf{k} = (k, l, m)$  and  $\mathbf{x} = (x, y, z)$  are the wave number and location vectors.  $\psi_o = \ln A_o + iS_o$  is called the eikonal. This is the (relatively) general case of EM wave scattering in the atmosphere. The incident field is modulated by the fluctuations in the index of refraction and the resulting field is described by  $E = A e^{iS} = e^{\psi}$ . Fluctuations in the value of the eikonal at a particular point, the receiver, are of interest. The eikonal fluctuations are given by  $\psi' = \psi - \psi_o = \ln\left(\frac{A}{A_o}\right) + i(S - S_o)$ .

The real part of  $\psi'$  describes the change in amplitude of the signal. In an idealized case, with the Fresnel integral collapsing to the central ray, the amplitude would not change and  $\psi'$  would be purely imaginary. For small  $n'$ ,  $\Re(\psi')$  is expected to be small. The imaginary part of  $\psi'$  describes changes in the arrival phase relative to the incident wave. In the case of the BASS Rake, with the sound speed assumed constant over the sample volume, changes in the arrival phase of a ray are strictly proportional to changes in the fluid velocity along the ray. To the extent that the integral collapses to the central ray,  $\Im(\psi')$  is expected to follow the velocity profile. This is, of course, exactly the idealized form of the BASS velocity measurement, Equation 2.1, discussed in Chapter 2. To the extent that the integral does not collapse, the measured velocity is a weighted average of the velocity pattern over the sample volume. The Fresnel integral is the mathematical description of that averaging process.



Returning to the argument of Monin and Yaglom for the case of atmospheric scattering, if the assumptions outlined above are met, the electric field must satisfy

$$(\nabla^2 + |k|^2)E = -2|k|^2 n' E \quad (4.2)$$

Substituting the expression for  $E$  as a function of the eikonal and assuming sufficiently smooth  $\psi'(\mathbf{x})$ ,  $\psi'$  must satisfy the linearized eikonal equation,

$$\nabla^2 \psi' + 2i|k|\nabla\psi' = -2|k|^2 n' \quad (4.3)$$

For small  $\overline{(\Re(\psi'))^2}$ , Equation 4.3 is rewritten in the form

$$(\nabla^2 + |k|^2)\psi' e^{ikx} = -2|k|^2 n' e^{ikx} \quad (4.4)$$

which has the solution

$$\psi'(\mathbf{x}) = \frac{|k|^2}{2\pi} \int_V n'(\mathbf{x}_1) \frac{e^{-i\mathbf{k}(\mathbf{x}-\mathbf{x}_1) + i|k||\mathbf{x}-\mathbf{x}_1|}}{|\mathbf{x}-\mathbf{x}_1|} \quad (4.5)$$

Equation 4.5 expresses the fluctuations in the eikonal at the point  $\mathbf{x}$  caused by the scattered waves arriving from all points in the scattering volume,  $V$ . However, the expression is difficult to work with in this general form. If  $\mathbf{x}$  is an internal point of  $V$ , large angle scattering can be ignored because of condition (4). Specifically, if  $\alpha = \frac{\lambda}{l_{fluc}} \ll 1$ , where  $l_{fluc}$  is the length scale of the fluctuations, then it is sufficient to confine the integration to a cone,  $K(\mathbf{x})$ , with angle of revolution  $\alpha$  and apex at  $\mathbf{x}$ .  $\alpha \ll 1$  is a questionable assumption for the BASS Rake only for turbulence measurements within a few millimeters of the boundary. At that height the most energetic turbulent length scales are approaching the acoustic wavelength,  $\lambda$ , from above. For time averaged measurements in the continental shelf bottom boundary layer the assumption is valid down to the lowest BASS Rake acoustic paths.

Without loss of generality, the incident wave is assumed to propagate along the  $x$ -axis so that  $\mathbf{kx} = kx$ . Recall that the incident wave is considered to be planar.

Therefore,  $V$  can be assumed to lie within the region  $x > 0$  and  $K(\mathbf{x})$  is the set of points,  $\mathbf{x}_1$ , that satisfy

$$x - x_1 \geq 0 \quad \text{and} \quad \frac{\sqrt{(y - y_1)^2 + (z - z_1)^2}}{(x - x_1)} = \frac{\rho}{(x - x_1)} \leq \alpha \ll 1 \quad (4.6)$$

Now let  $\mathbf{x}$ , the position where the fluctuations of the eikonal are to be determined, be given by  $\mathbf{x} = (L, y, z)$ . In anticipation of the development below,  $L$  can be identified as the physical separation of the transducers. If  $L \ll \frac{l_{fluc}^2}{\lambda}$ , it will be sufficient to retain only linear terms in an expansion of  $|\mathbf{x} - \mathbf{x}_1|$  in powers of  $\frac{\rho^2}{(x - x_1)^2}$ . As with the exclusion of large angle scattering, this is only a questionable approximation within a few millimeters of the bottom and only for measurements of turbulence; the assumption is fully justified for the steady and wave components of the flow. This linear approximation simplifies the integrand of Equation 4.5. That solution can now be written

$$\psi'(\mathbf{x}) = \frac{k^2}{2\pi} \int_{V \cdot K(\mathbf{x})} n'(\mathbf{x}_1) \frac{\exp\left(\frac{ik\rho^2}{2(x - x_1)}\right)}{x - x_1} d\mathbf{x}_1 \quad (4.7)$$

Recall the physical picture of the propagating signal presented in Sections 4.2.1 and 4.2.2. The sign of the concentric, ellipsoidal ray bundles oscillates very rapidly as the distance from the centerline increases so that the contribution of the outer shells tends to zero. This behavior is incorporated into the integrand of Equation 4.7 through the function  $(x - x_1)^{-1} \exp\left(\frac{ik\rho^2}{2(x - x_1)}\right)$ . For the assumed smooth variations of the normalized velocity field described by  $n'(\mathbf{x})$ , contributions to the integral from the region outside of  $K(\mathbf{x})$  must tend to zero and integration over the volume  $V \cdot K(\mathbf{x})$  can be replaced by integration over the volume  $0 \leq x_1 \leq L$ . For the new bounds of integration, Equation 4.7 is an exact solution for Equation 4.3 if the Laplacian in  $\mathbf{x}$ ,  $\frac{\partial^2 \psi'}{\partial x^2}$ , is neglected. Variations in the eikonal are caused by the characteristics of  $n'(\mathbf{x})$ , which is asserted to represent the normalized velocity field. Therefore, Equation 4.7 is completely consistent with the basic assumption that there is no horizontal variation in the time averaged velocity field over the horizontal scale of the instrument. Realistically,  $\frac{\partial^2 \psi'}{\partial y^2}$  can also be neglected.

Equation 4.7 can now be written

$$\psi'(L, y, z) = ik \int_0^L dx_1 \int_{-\infty}^{\infty} \int_{-\infty}^{\infty} n'(x_1, y_1, z_1) \left[ \frac{\exp(-\rho^2/2\sigma^2)}{2\pi\sigma^2} \right] dy_1 dz_1 \quad (4.8)$$

where  $\sigma^2 = \frac{i(L-x_1)}{k}$ . Equation 4.8 is the concluding expression for the fluctuations in the eikonal from the development of Monin and Yaglom [49]. Their interpretation of this expression, a portion of which appears below, provides some physical insight.

...it is clear that the value of  $\psi'$  at the point  $x_1 = L, y_1 = y, z_1 = z$  depends on the refractive-index inhomogeneities not only on the segment  $0 \leq x_1 \leq L$  of the straight line  $y_1 = y, z_1 = z$ , but also on a certain region around this segment. This is so because in the plane  $x_1 = L$  we observe not simply the geometric shadows of the inhomogeneities lying in the layer  $0 \leq x_1 \leq L$ , but the shadows "spread" by diffraction. The factor in brackets in the integrand describes this diffraction spread. Its length scale is of the order of  $|\sigma| \sim \sqrt{\lambda L}$ . The length  $\sqrt{\lambda L}$  is, in this case, the radius of the so-called Fresnel zone, i.e., a circular region on the surface of the incident wave front (in our case, a plane wave), the center of which lies on the straight line joining the observation point and the light source (at a distance  $L$  from the observation point), the path difference between the edges and the center of the zone being  $\frac{\lambda}{2}$ . [49]

#### 4.2.4 Calculating the BASS Rake Sample Volume

The results of the previous sections can now be applied to the particular case of a single BASS Rake acoustic axis. The geometry and coordinate system are defined in Figure 4.3. The Cartesian frame of Section 4.2.3 has been preserved, however, the  $y$  coordinate of the acoustic axis is now fixed at  $y = 0$ . The transmitter is located at  $(x = 0, y = 0, z)$  and the receiver is located at  $(x = L, y = 0, z)$ . The Cartesian frame is fixed to the bottom at  $z = 0$  and the effect of Fresnel zone averaging as a function of  $z$  for a given velocity profile is to be determined. As previously discussed, the time averaged velocity profile is assumed. It has already been established that  $n'(\mathbf{x})$  describes the normalized velocity field. Explicitly,  $n'(\mathbf{x}) = \frac{u(\mathbf{x})}{c}$ , where  $u(\mathbf{x})$  is the actual velocity field and  $c$  is the local sound speed, assumed to be constant over the sample volume. The time averaged and turbulent components of the flow are

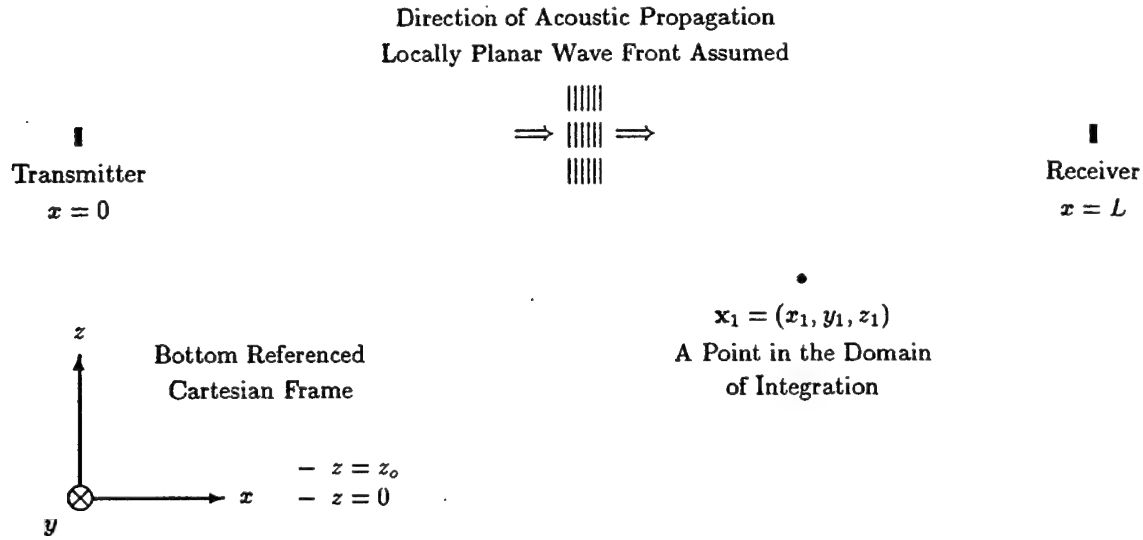


Figure 4.3: BASS RAKE ACOUSTIC AXIS GEOMETRY FOR THE FRESNEL INTEGRAL IN A SCATTERING MEDIUM - The bottom referenced Cartesian coordinate system,  $\mathbf{x} = (x, y, z)$ , is fixed to the bottom at  $z = 0$  with the  $x$ -axis parallel to the bottom and to the beam axis. A locally planar wave front is assumed. The transmitter is located at  $(x = 0, y = 0, z)$  and the receiver is located at  $(x = L, y = 0, z)$ .  $\mathbf{x}_1 = (x_1, y_1, z_1)$  is an arbitrary point within the domain of integration.  $z = z_0$  is the "level of zero flow" of the boundary layer velocity profile (see Appendix A).

separated such that the normalized velocity field is given by

$$n'(\mathbf{x}) = \bar{n}'(z) + n''(\mathbf{x}) \quad (4.9)$$

$\bar{n}'(z)$  describes the time averaged wave-current profile and depends only on distance from the bottom.  $n''(\mathbf{x})$  describes the turbulent flow and is assumed to have zero mean. Fluctuations in the eikonal are separately attributed to the two flow components such that

$$\psi'(\mathbf{x}) = \bar{\psi}'(z) + \psi''(\mathbf{x}) \quad (4.10)$$

$\bar{\psi}'(z)$  describes fluctuations in the eikonal caused by the waves and steady currents. That solution is pursued below.  $\psi''(\mathbf{x})$  describes fluctuations caused by the turbulent flow. As mentioned, that solution has been separately pursued by Terray [75]. Terray has determined an analytic solution which, to high order, collapses to an average taken along the centerline. This suggests that, for the BASS Rake, the effect of

turbulent flow on vertical Fresnel zone averaging can be ignored. However, that solution did not consider the effects of a boundary nor the physical extent of the transducer. This remains an open question for the BASS Rake. It is worth noting here that the differential travel time technique appears, from measured turbulent spectra, to accurately sense scales of turbulence that are significantly smaller than the acoustic path length [29, 75, 84]. This suggests that the intuitive path integral may not be the appropriate physical model. The actual processes involved are not currently understood [75, 84].

In this context, Equation 4.8 can be written

$$\overline{\psi'}(z) = \frac{k^2}{2\pi} \int_{x_1=0}^L \int_{y_1=-\infty}^{\infty} \int_{z_1=-\infty}^{\infty} \overline{n'}(z_1) \frac{\exp\left(\frac{ik[y_1^2 + (z-z_1)^2]}{2(L-x_1)}\right)}{L-x_1} dz_1 dy_1 dx_1 \quad (4.11)$$

Numerical evaluation of Equation 4.11 as given would be extremely difficult because of the behavior of the integrand as  $x_1 \rightarrow L$ . The denominator is singular at  $x_1 = L$  and the exponential oscillates increasingly wildly during the approach. Other difficulties are associated with  $\overline{n'}(z)$ , which would, for example, take the form  $\frac{u_*}{\kappa c} \ln\left(\frac{z_1}{z_o}\right)$  in a steady boundary layer.  $u_*$  is the shear velocity and  $\kappa$  is von Karman's constant (see Appendix A, Equation A.31). This expression is not physically meaningful for  $0 < z_1 < z_o$ , is singular at  $z_1 = 0$ , and acquires an imaginary part for  $z_1 < 0$ . Some manipulation is, therefore, required.

First, Equation 4.11 is rewritten to isolate the integration over  $y_1$ .

$$\overline{\psi'}(z) = \frac{k^2}{2\pi} \int_{x_1=0}^L \int_{z_1=-\infty}^{\infty} \overline{n'}(z_1) \frac{\exp\left(\frac{ik(z-z_1)^2}{2(L-x_1)}\right)}{L-x_1} dz_1 dx_1 \int_{y_1=-\infty}^{\infty} \exp\left(\frac{iky_1^2}{2(L-x_1)}\right) dy_1 \quad (4.12)$$

That integral can then be evaluated independently.

$$\begin{aligned}
\int_{y_1=-\infty}^{\infty} \exp\left(\frac{iky_1^2}{2(L-x_1)}\right) dy_1 &= \sqrt{\frac{2(L-x_1)}{k}} \int_{-\infty}^{\infty} e^{i\xi^2} d\xi \\
&= \frac{(1+i)}{\sqrt{2}} \sqrt{\frac{2(L-x_1)}{k}} \int_{-\infty}^{\infty} e^{-r^2} dr \\
&= \sqrt{\pi}(1+i) \sqrt{\frac{L-x_1}{k}} \quad (4.13)
\end{aligned}$$

The second step above uses a closed contour in the complex  $\xi$  plane. The contour extends along the real axis, follows first and third quadrant arcs of infinite radius, and is closed along the line through  $e^{i\frac{\pi}{4}}$  and  $e^{i\frac{3\pi}{4}}$ . The contribution to the integral along the arcs is zero in the limit of infinite radius. There are no contained singularities and the Cauchy integral theorem establishes the equivalence of the integrals along the two infinite line segments. Fluctuations in the eikonal are now given by

$$\bar{\psi}'(z) = \frac{k^2}{2\sqrt{\pi}} \frac{(1+i)}{\sqrt{k}} \int_{x_1=0}^L \int_{z_1=-\infty}^{\infty} \bar{n}'(z_1) \frac{\exp\left(\frac{ik(z-z_1)^2}{2(L-x_1)}\right)}{\sqrt{L-x_1}} dz_1 dx_1 \quad (4.14)$$

The limits of the integration over  $z_1$  must now be established. The boundary and the behavior of  $\bar{n}'(z_1)$  restrict the range of integration to  $z_o \leq z_1 \leq \infty$ . The interaction of the acoustic signal with the bottom is also important. The finite diameter of an actual transducer restricts  $z$  to positive values of at least a few millimeters. Contributions to the integral for large values of  $|z - z_1|$  are negligible because of the oscillation of the integrand. Finite limits are also desirable in anticipation of a numerical evaluation.

To accommodate these constraints, the bounds of the vertical integration during numerical evaluation are restricted in two stages. The physical limits shown by the thick outline in Figure 4.4 are applied first. The straight lines are the Fraunhofer beam width at the first null. This can be viewed as excluding either high scattering angles or regions where there is little acoustic energy available to scatter into the receiver. The ellipse is based on the timing of a BASS measurement. Differential arrival times are determined from the 14<sup>th</sup> negative going zero crossing of the received signal [90]. To

affect the received waveform, diffracted and scattered signals must follow a path from transmitter to receiver that has a propagation duration of no more than the centerline time ( $\approx 100 \mu s$ ) plus 14 signal periods. The large ellipse with the transducers at the foci defines that timing window mapped to a Cartesian frame using a sound speed of  $1500 m \cdot s^{-1}$ . The curves are drawn to scale in Figure 4.4 based on the characteristics of the P3 transducers ( $2.5 mm$ ,  $0.85 MHz$ ). The anticipated  $\frac{\lambda}{2}$  effective Fresnel zone ellipse is shown for comparison. The relative regions of coverage suggest that the restrictions on  $z_1$  are reasonable. A numerical evaluation of  $\bar{\psi}'(z)$  for a logarithmic velocity profile and the P3 characteristics is presented in Section 4.2.4.2. The same calculation is also carried out for the P2 transducers ( $6 mm$ ,  $1.75 MHz$ ). However, the higher frequency and larger diameter of these transducers produce a much narrower first null beam width that falls entirely inside the timing window. Therefore, the beam width alone is used as the first stage restriction on the bounds of integration for the P2 case. It will be seen in what follows that these restrictions on the bounds of integration are justified.

The combination of beam width and timing restrictions is sufficient when the value of  $z$ , the height above bottom of the transducer centerline, is such that the resulting bounds of the integration lie entirely above  $z_o$ , the effective bottom. The second stage in establishing the bounds of integration is applied when the beam width and timing window extends below the effective bottom. It can be shown [14, 63] that, for grazing angles below  $\approx 20^\circ$ , natural bottoms behave like acoustic mirrors. The reflected signal is phase shifted, but suffers no loss of amplitude. The loss increases to more than  $10 dB$  for higher grazing angles. Unfortunately, this simple description is not rigorously applicable in the near field of the reflecting surface. It will be shown below that the interaction model only has an effect within  $1 cm$  of the bottom, well within the near field for either transducer frequency. A second eikonal describing scattering from the boundary may be the appropriate form for a detailed model, but the structure and behavior of reflection on the scale of the BASS Rake, the information necessary to construct  $\bar{n}'_{bottom}(x, y, 0)$ , remains unclear. The additional computational overhead of such a model, particularly when applied over an irregular

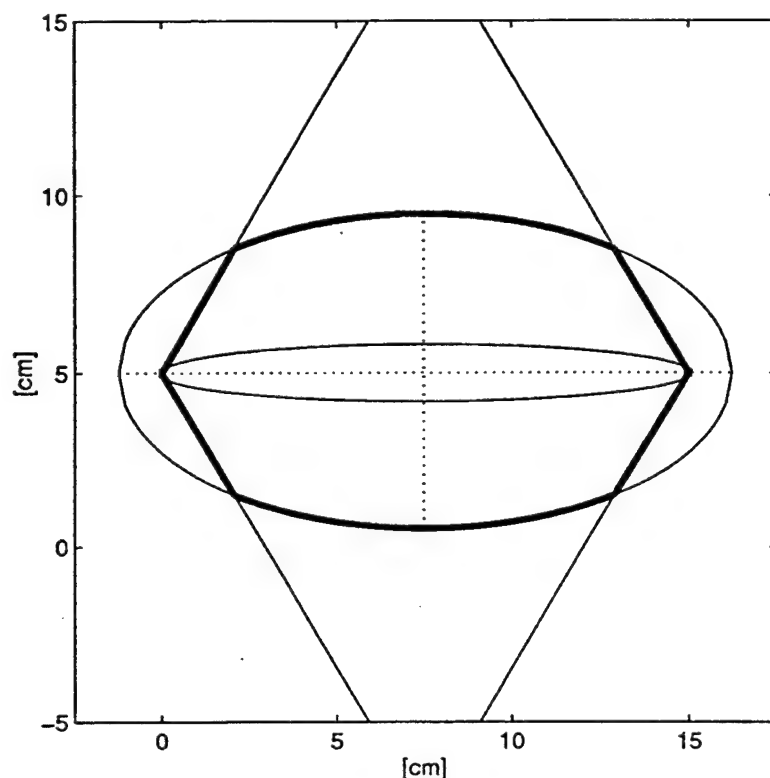


Figure 4.4: ACOUSTIC AXIS BEAM WIDTH AND TIMING WINDOW - The thick outline is used to set integration limits for the numerical evaluation of the Fresnel integral. The straight lines are the Fraunhofer beam width at the first null and the large ellipse is a function of BASS measurement timing. The small, inner ellipse, marks the  $\frac{1}{2}$  effective Fresnel zone. The drawing is to scale for the P3 transducers (2.5 mm, 0.85 MHz).

zone of overlap, would be difficult to accommodate or justify.

The first null of the P3 transducers is  $\approx 60^\circ$  from the centerline. Much of the energy in the beam has a grazing angle well above  $20^\circ$  and only very close to the bottom do low grazing angle paths connect the transducers. Therefore, as an approximation, the integration window was simply truncated at  $z_o$  for P3 calculations. This may sound reasonable, but it is, empirically, a very poor approximation. Significant levels of acoustic energy were found to reflect incoherently off of a sand bottom, arrive successfully at the receiver from many angles, and produce badly distorted, time varying waveforms that had no utility for the measurement of fluid velocity. The P3 calculation using truncation, however, retains some utility and is presented below. The first



null angle of the P2 transducers is  $\approx 9^\circ$ . The phase shift for a  $9^\circ$  grazing angle is  $\approx 100^\circ$ . In the detailed calculation of Section 4.2.4.2, the P2 domain of integration is also truncated at  $z = z_o$ . This was done in the expectation that only a small portion of the reflected energy would actually be incident on the receiver. Empirically, this proved to be an excellent approximation of the actual behavior of the P2 transducers. The small grazing angle and narrow beam apparently result in a much cleaner, if still poorly described, interaction.

A few comments on the truncation approximation are warranted. First, to the accuracy of the bottom boundary layer models, the calculated result is not sensitive to the structure of the interaction. From a practical standpoint, more complicated models of the bottom interaction are simply not needed. The detailed structure of the acoustic interaction with the bottom for the geometry of a BASS Rake acoustic axis is beyond the scope of this research. The truncation model appears to describe the actual measurements made with the P2 transducers quite accurately. Finally, it should be emphasized that these calculations serve primarily to promote a greater understanding of the response of the sensor. It is the empirically calibrated response itself that must be used when interpreting and processing the data.

Notationally, the upper and lower bounds on the vertical integration are denoted by  $f(x_1, z)$  and  $g(x_1, z)$ , and Equation 4.14 is rewritten

$$\overline{\psi}'(z) = \frac{k^2}{2\sqrt{\pi}} \frac{(1+i)}{\sqrt{k}} \int_{x_1=0}^L \int_{z_1=g(x_1,z)}^{f(x_1,z)} \overline{n}'(z_1) \frac{\exp\left(\frac{ik(z-z_1)^2}{2(L-x_1)}\right)}{\sqrt{L-x_1}} dz_1 dx_1 \quad (4.15)$$

The remaining difficulties with the behavior of the integrand can now be addressed. To this end,  $x_1$  is shifted and scaled.

$$\begin{aligned} \gamma &= \frac{(L-x_1)}{L} & d\gamma &= \frac{-dx_1}{L} \\ x_1 &= L(1-\gamma) & dx_1 &= -Ld\gamma \end{aligned}$$

Substitution into Equation 4.15 yields

$$\begin{aligned}\bar{\psi}'(z) &= \frac{k^2}{2\sqrt{\pi}} \frac{(1+i)}{\sqrt{k}} \int_{\gamma=1}^0 \int_{z_1=g(L(1-\gamma),z)}^{f(L(1-\gamma),z)} \bar{n}'(z_1) \frac{\exp\left(\frac{ik(z-z_1)^2}{2\gamma L}\right)}{\sqrt{\gamma L}} dz_1 (-L\gamma) \\ &= \frac{k^2\sqrt{L}}{2\sqrt{\pi}} \frac{(1+i)}{\sqrt{k}} \int_{\gamma=0}^1 \int_{z_1=g(L(1-\gamma),z)}^{f(L(1-\gamma),z)} \bar{n}'(z_1) \frac{\exp\left(\frac{ik(z-z_1)^2}{2\gamma L}\right)}{\sqrt{\gamma}} dz_1 d\gamma\end{aligned}\quad (4.16)$$

Similarly,  $z_1$  is shifted and scaled.

$$\begin{aligned}\eta &= \frac{z_1}{z} - 1 & d\eta &= \frac{dz_1}{z} \\ z_1 &= z(\eta + 1) & dz_1 &= z d\eta\end{aligned}$$

Substitution into Equation 4.16 yields

$$\bar{\psi}'(z) = \frac{k^2\sqrt{L}}{2\sqrt{\pi}} \frac{(1+i)}{\sqrt{k}} \int_{\gamma=0}^1 \int_{\eta=\frac{g(L(1-\gamma),z)-z}{z}}^{\frac{f(L(1-\gamma),z)-z}{z}} \bar{n}'(z(\eta+1)) \frac{\exp\left(\frac{ikz^2\eta^2}{2\gamma L}\right)}{\sqrt{\gamma}} z d\eta d\gamma \quad (4.17)$$

$\gamma$ , the along-axis variable, is now scaled.

$$\begin{aligned}x_1 &= \sqrt{\gamma} & dx_1 &= \frac{d\gamma}{2\sqrt{\gamma}} = \frac{d\gamma}{2x_1} \\ \gamma &= x_1^2 & d\gamma &= 2x_1 dx_1\end{aligned}$$

Substitution into Equation 4.17 yields

$$\begin{aligned}\bar{\psi}'(z) &= \frac{k^2\sqrt{L}}{2\sqrt{\pi}} \frac{(1+i)}{\sqrt{k}} \int_{x_1=0}^1 \int_{\eta=\frac{g(L(1-x_1^2),z)-z}{z}}^{\frac{f(L(1-x_1^2),z)-z}{z}} \bar{n}'(z(\eta+1)) \frac{\exp\left(i\frac{kz^2}{2L} \left(\frac{\eta}{x_1}\right)^2\right)}{x_1} z 2x_1 d\eta dx_1 \\ &= \frac{k^2\sqrt{L}}{\sqrt{\pi}} \frac{(1+i)}{\sqrt{k}} \int_{x_1=0}^1 \int_{\eta=\frac{g(L(1-x_1^2),z)-z}{z}}^{\frac{f(L(1-x_1^2),z)-z}{z}} \bar{n}'(z(\eta+1)) \exp\left(i\frac{kz^2}{2L} \left(\frac{\eta}{x_1}\right)^2\right) z d\eta dx_1\end{aligned}\quad (4.18)$$

Finally,  $\eta$  is scaled.

$$\begin{aligned}z_1 &= \sqrt{\frac{k}{2L}} \frac{z\eta}{x_1} & dz_1 &= \sqrt{\frac{k}{2L}} \frac{z}{x_1} d\eta \\ \eta &= \sqrt{\frac{2L}{k}} \frac{x_1 z_1}{z} & d\eta &= \sqrt{\frac{2L}{k}} \frac{x_1}{z} dz_1\end{aligned}$$

After substitution into Equation 4.18 and some reorganization of terms, the final expression for fluctuations of the eikonal is

$$\overline{\psi'}(z) = \frac{kL\sqrt{2}(1+i)}{\sqrt{\pi}} \int_{x_1=0}^1 \int_{z_1=\sqrt{\frac{k}{2L} \frac{f(L(1-x_1^2),z)-z}{x_1}}}^{\sqrt{\frac{k}{2L} \frac{f(L(1-x_1^2),z)-z}{x_1}}} \overline{n'} \left( \sqrt{\frac{2L}{k}} x_1 z_1 + z \right) x_1 e^{iz_1^2} dz_1 dx_1 \quad (4.19)$$

The original physical domain of integration has been stretched and flipped by these manipulations.  $x_1$  is still recognizably the along-beam variable, however, it runs from receiver to transmitter now and has been mapped from a linear to a square-root distribution.  $z_1$  is still the cross-beam variable. The cross-beam manipulations were symmetrical about the centerline; the exponential still oscillates strongly as distance from the centerline increases. For convenience the domain of Equation 4.19 will be referred to as the numerical integration space (NIS). As desired, the integrand is now well behaved throughout the NIS. In achieving this, it may appear that the mapping has introduced a singularity into the bounds on the vertical integration. However, because of the linear beam width constraint, the numerator of each bound approaches 0 more quickly than the denominator and both bounds go smoothly to 0 as  $x_1 \rightarrow 0$  (Figure 4.5).

#### 4.2.4.1 Analytic Solution for Two Canonical Profiles

It is instructive to solve Equation 4.19 analytically for two canonical velocity profiles. The first case is a uniform flow,  $\overline{n'}(z_{1_{physical}}) = \frac{u(z_{1_{physical}})}{c} = \frac{U}{c}$ , extending over all physical  $z_{1_{physical}} \in (-\infty, \infty)$ . There is no boundary in this case. In the NIS the cross-beam variable satisfies  $z_{1_{NIS}} \in (-\infty, \infty)$  and  $\overline{n'} \left( z \left[ \sqrt{\frac{2L}{k}} \frac{x_1 z_1}{z} + 1 \right] \right) = \frac{U}{c}$ . Under these conditions the integral should collapse to the centerline ray. Recall that fluctuations of the eikonal are given by  $\overline{\psi'} = \psi - \psi_o = \ln \left( \frac{A}{A_o} \right) + i(S - S_o)$ . The collapsed transmission is lossless compared to the undisturbed signal, so the result is expected to be purely imaginary.  $S - S_o$  is the phase difference at the receiver between the signal as perturbed by the fluid velocity and the signal as it would have arrived if the fluid was motionless. For  $U \ll c$ , as assumed throughout the derivation, the difference

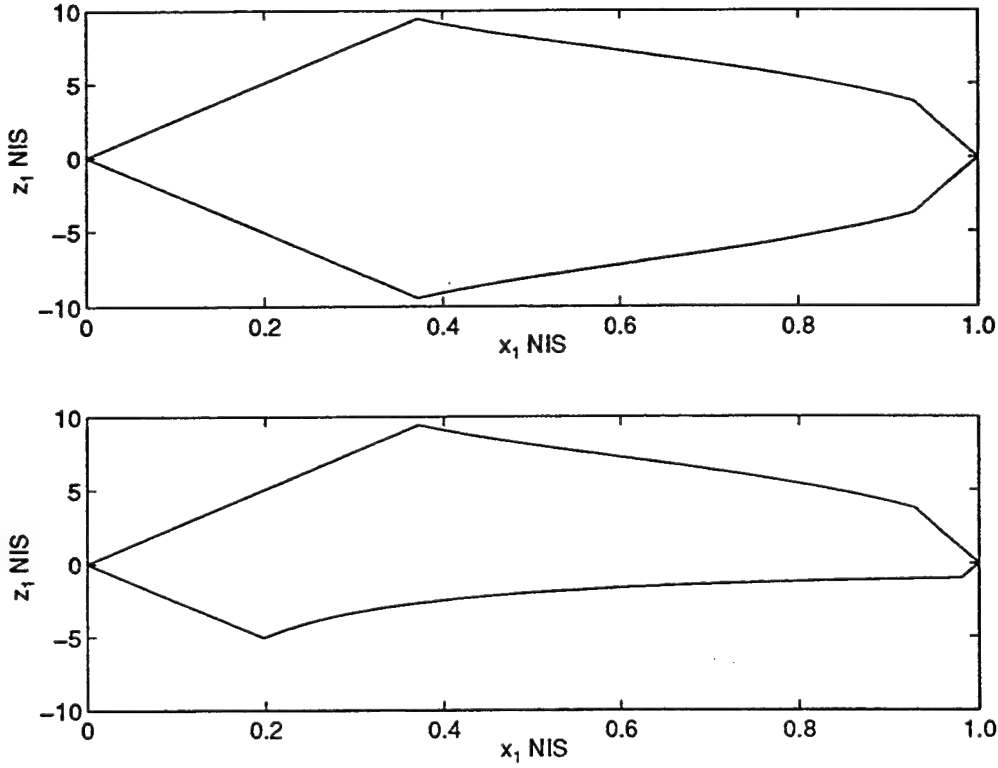


Figure 4.5: ACOUSTIC AXIS BEAM WIDTH AND TIMING WINDOW MAPPED TO THE NIS - The domain of integration in physical space is bounded by the contour shown in Figure 4.4. The variable manipulations described in Section 4.2.4 map the physical contour to the contours shown here. For a centerline height of 5 cm, the physical contour does not intersect the bottom and the mapping yields the symmetrical contour in the upper panel. For a centerline height of 1 cm, the physical domain is truncated and the mapping produces the asymmetrical contour in the lower panel. The mapping also flips the along-beam variable. The transmitter is located at  $x_{1\text{NIS}} = 1$ ,  $z_{1\text{NIS}} = 0$ , and the receiver is located at  $x_{1\text{NIS}} = 0$ ,  $z_{1\text{NIS}} = 0$ . Propagation is from right to left.

in arrival times is  $\delta t = \frac{LU}{c^2}$ . The expected phase difference is, therefore,  $kL\frac{U}{c}$ .

$$\begin{aligned}
 \overline{\psi'} &= \frac{kL\sqrt{2}(1+i)}{\sqrt{\pi}} \int_{x_1=0}^1 \int_{z_1=-\infty}^{\infty} \frac{U}{c} x_1 e^{iz_1^2} dz_1 dx_1 \\
 &= \frac{kL\sqrt{2}(1+i)}{\sqrt{\pi}} \frac{U}{c} \frac{(1+i)}{\sqrt{2}} \sqrt{\pi} \int_{x_1=0}^1 x_1 dx_1 \\
 &= 2ikL \frac{U}{c} \frac{1}{2} \\
 &= ikL \frac{U}{c}
 \end{aligned} \tag{4.20}$$

This is the predicted result. The symmetry of the expression about the centerline dictates the same result for symmetrical, finite limits. This is consistent with physical intuition about the process; the average of a constant velocity is the velocity.

The second canonical case is a linear velocity profile,  $\bar{n}'(z_{1\text{physical}}) = \frac{u(z_{1\text{physical}})}{c} = \frac{az_{1\text{physical}}}{c}$ , with the conditions otherwise unchanged from the uniform flow.  $a$  is a positive, real constant with dimensions of inverse time. Because of the symmetry of the profile, the high bias from the faster velocities above the centerline is exactly balanced by the low bias of the slower velocities below the centerline. The integral should collapse to  $ikL\frac{az}{c}$ , which corresponds to the velocity at the centerline height.

$$\begin{aligned}
\bar{\psi}'(z) &= \frac{kL\sqrt{2}(1+i)}{\sqrt{\pi}} \int_{x_1=0}^1 \int_{z_1=-\infty}^{\infty} \left( \sqrt{\frac{2L}{k}} \frac{ax_1z_1}{c} + \frac{az}{c} \right) x_1 e^{iz_1^2} dz_1 dx_1 \\
&= \frac{kL\sqrt{2}(1+i)}{\sqrt{\pi}} \frac{az}{c} \int_{x_1=0}^1 \int_{z_1=-\infty}^{\infty} x_1 e^{iz_1^2} dz_1 dx_1 \\
&\quad + \frac{kL\sqrt{2}(1+i)}{\sqrt{\pi}} \sqrt{\frac{2L}{k}} \frac{a}{c} \int_{x_1=0}^1 \int_{z_1=-\infty}^{\infty} x_1^2 z_1 e^{iz_1^2} dz_1 dx_1 \\
&= ikL\frac{az}{c} + \frac{2kL(1+i)}{\sqrt{\pi}} \sqrt{\frac{L}{k}} \frac{a}{3c} \int_{z_1=-\infty}^{\infty} z_1 e^{iz_1^2} dz_1 \\
&= ikL\frac{az}{c} + \frac{2kL(1+i)}{\sqrt{\pi}} \sqrt{\frac{L}{k}} \frac{a}{3c} \int_{r=-\infty}^{\infty} r \frac{(1+i)}{\sqrt{2}} e^{-r^2} \frac{(1+i)}{\sqrt{2}} dr \\
&= ikL\frac{az}{c} + \frac{2kL(1+i)}{\sqrt{\pi}} \sqrt{\frac{L}{k}} \frac{a}{3c} \frac{-i}{2} \int_{r=-\infty}^{\infty} e^{-r^2} (-2r) dr \\
&= ikL\frac{az}{c} + \frac{2kL(1+i)}{\sqrt{\pi}} \sqrt{\frac{L}{k}} \frac{a}{3c} \frac{-i}{2} e^{-r^2} \Big|_{r=-\infty}^{\infty} \\
&= ikL\frac{az}{c} + 0 \\
&= ikL\frac{az}{c}
\end{aligned} \tag{4.21}$$

The complex contour described in Section 4.2.4 is used in the evaluation above in the transition from  $z_1$  to  $r$ . This case also yields the intuitive result. Clearly the two canonical cases can be combined to produce the most general form of a linear profile. That construct readily supports the physical picture of acoustic axis averaging over a symmetrical Fresnel zone. To the extent that the flow is linear across a symmetrical sample volume, the measurement will return the centerline velocity, defined to be

the “correct” answer. Realistically, the profile across the sample volume can be considered linear whenever the averaging error is small compared to the accuracy of the measurement. That accuracy is  $O(5\%)$ , depending on time averaging, flow stationarity, and flow disturbance (see Chapters 5 and 6).

It has already been established that the central region of the Fresnel zone is much more strongly weighted in the averaging process than are the outer fringes. The central region has been referred to here as the effective Fresnel zone. Assuming the  $\frac{\lambda}{2}$  approximation, the diameter of the effective zone is  $O(1\text{ cm})$  for BASS frequencies. This suggests that the effect of Fresnel averaging in the bottom boundary layer will only be apparent very close to the bottom, the working environment of the BASS Rake. Two effects occur as the bottom is approached. Below some height, the effective Fresnel zone intersects the bottom, symmetry is lost, and the measurement acquires a growing bias. Additionally, it is near the bottom that the curvature of the velocity profile becomes most extreme. The measurement acquires the second bias as the profile loses linearity across the sample volume. Both of these effects are clearly apparent in the calculation below.

#### 4.2.4.2 Numerical Solution for a Logarithmic Profile

Consider the logarithmic velocity profile of a steady current boundary layer described in Appendix A.

$$u(z) = \frac{u_*}{\kappa} \ln \left( \frac{z}{z_o} \right) \quad (\text{A.31})$$

For this profile,  $\overline{n'}(z_{1\text{physical}})$  takes the form

$$\overline{n'}(z_{1\text{physical}}) = \frac{u(z_{1\text{physical}})}{c} = \frac{u_*}{\kappa c} \ln \left( \frac{z_{1\text{physical}}}{z_o} \right) \quad (4.22)$$

In the NIS the integral has the form

$$\begin{aligned} \overline{\psi}'(z) = & \frac{kL\sqrt{2}(1+i)u_*}{\sqrt{\pi}\kappa c} \\ & \times \int_{x_1=0}^1 \int_{z_1=\sqrt{\frac{k}{2L}\frac{g(L(1-x_1^2),z)-z}{x_1}}}^{\sqrt{\frac{k}{2L}\frac{f(L(1-x_1^2),z)-z}{x_1}}} \ln \left( \sqrt{\frac{2L}{k}} \frac{x_1 z_1}{z_o} + \frac{z}{z_o} \right) x_1 e^{iz_1^2} dz_1 dx_1 \end{aligned} \quad (4.23)$$

$\overline{\psi}'(z)$  was evaluated for 30 values of  $z$ , logarithmically spaced from 1 *mmab* to 10 *cmab*. The variables describing the flow were assigned the values  $u_* = 1 \text{ cm} \cdot \text{s}^{-1}$  and  $z_o = 0.002 \text{ cm}$ . Von Karman's constant,  $\kappa$ , has a value of 0.4. This corresponds to a steady flow over a flat bed of 250  $\mu\text{m}$  sand grains with a reference velocity of roughly  $20 \text{ cm} \cdot \text{s}^{-1}$  at a height of 1 *m*. The assigned values, while not atypical, were essentially arbitrary. The flow variables control the shape of the profile. They enter the equation as multiplicative and additive constants; however, the error curve that will be calculated cannot be normalized and applied universally because the process averaging the profile across the sample volume is non-linear. The flow variables do not affect the physical extent of the Fresnel zone. One goal of this calculation was to see how close  $z$ , the centerline height, could get to the bottom before the calculated response deviated strongly from the velocity profile. This calculation establishes the radius of the effective Fresnel zone, independent of the velocity profile.

The wave number,  $k$ , was first assigned the value of the nominally 0.85 *MHz* P3 transducers,  $k \approx 35.7 \text{ cm}^{-1}$ . This does affect the physical extent of the Fresnel zone. The beam width and timing window discussed in Section 4.2.4 was used to set the bounds of integration. Any portion of the window extending below  $z_o$  was truncated. The rationale for this is also discussed in Section 4.2.4. The  $x_1$  and  $z_1$  integrations were both performed by adaptive recursive Newton-Cotes eight panel quadratures converging to a relative error tolerance of  $10^{-3}$ . The real and imaginary parts of the integrand were evaluated separately and then combined. Note that the real and imaginary parts of the integrand do not directly correspond to the real and imaginary parts of the eikonal because the multiplier outside the integral is complex. When the

integration was complete, the imaginary part of the eikonal was multiplied by  $\frac{c}{kL}$  to map the phase difference to the velocity profile. The real part of the eikonal was also multiplied by  $\frac{c}{kL}$ . This is not physically meaningful, but it allows a direct comparison with the size of the imaginary part. The real part is expected to be small for the assumption of small  $n'(x)$  used in the derivation of Section 4.2.3.

The real and imaginary surfaces defined by the integrand of Equation 4.23 are shown in Figures 4.6 and 4.7. The surfaces are drawn in the NIS and correspond to a physical centerline height of 5 cm. The domain of integration is untruncated at that height, so the boundary of the surfaces, as seen in Figure 4.7, is symmetric in  $z_1$ , the cross-beam variable. However, the asymmetry produced by the logarithmic velocity profile is visible in Figure 4.7. This asymmetry increases as the centerline approaches the bottom. This is independent of the surface boundary asymmetry produced by truncation. Both effects modulate the degree of cancellation in the fringe pattern and produce bias in the measurement. The end view of the surfaces in Figure 4.7 clearly shows the importance of the central region of the Fresnel pattern, the effective Fresnel zone, in the sample volume averaging process.

The calculated Fresnel zone averages, essentially simulated measurements, are compared to the actual velocity profile in Figures 4.8 (linear axes) and 4.9 (semilog axes). Observe first that the uppermost six points of the calculated profile are systematically low. The error in each case is 1.55% of the velocity at that height. Note that all six points lie more than 4.5 cm above the bottom, so the domain of the integration is untruncated. The velocity profile is also relatively flat at these heights (see Figure 4.8). While the profile must introduce some bias, it is demonstrably well below 1%; numerical evaluation of a uniform profile over the same domain of integration is low by the same factor, 1.55% of the actual velocity. The residual error is also not a function of the relative error tolerance. The result for the uniform profile was constant to at least one part in  $10^5$  when the tolerance was reduced from  $10^{-3}$  to  $10^{-4}$ .

The residual is actually inherent in the underlying structure of the integrand. The real and imaginary parts of an unbiased Fresnel integral, evaluated between symmet-



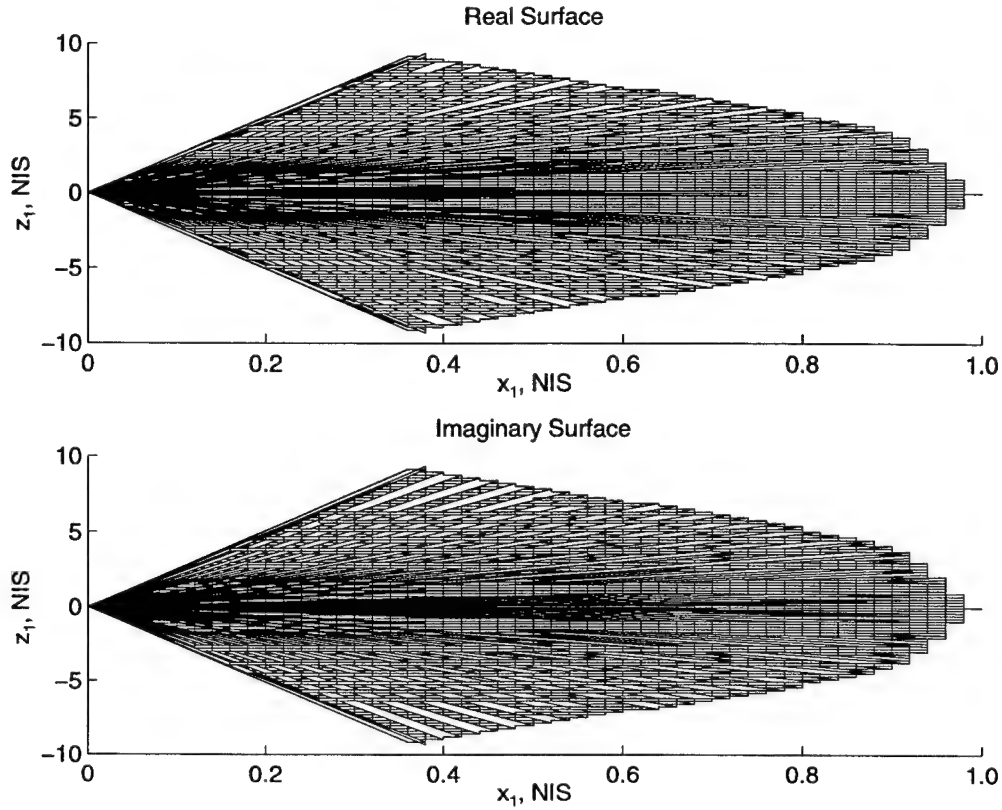


Figure 4.6: REAL AND IMAGINARY NIS INTEGRAND SURFACES FOR A LOGARITHMIC VELOCITY PROFILE - TOP VIEW - Top view of the real and imaginary NIS surfaces defined by the integrand of Equation 4.23. The surfaces are drawn for a physical centerline height of 5 cm. At this height the domain of integration is untruncated and the boundary is symmetric in  $z_1$ , the cross-beam variable. The transmitter is located at  $x_1 = 1$  and the receiver is located at  $x_1 = 0$ .

ric limits, for example  $\psi = \int_{-\ell}^{\ell} \exp\left(i\frac{\pi}{2}t^2\right) dt$ , exhibit oscillations of monotonically decreasing amplitude as  $\ell$  increases, converging to fixed values as  $\ell \rightarrow \infty$ . For limits of order 10, a representative width for the domain of integration in the NIS, the magnitude of the oscillations is still several percent of the converged value. Additionally, there is a phase difference of  $\frac{\pi}{2}$  between the real and imaginary parts. In general the signs and magnitudes of the residuals will be different [1]. The real part of the logarithmic eikonal, normalized to velocity space, is shown in Figure 4.10. The uppermost six real points also have a systematic bias proportional to the centerline velocity. Clearly the known behavior of these expressions as a function of the limits readily explains the systematic error of the uppermost points.

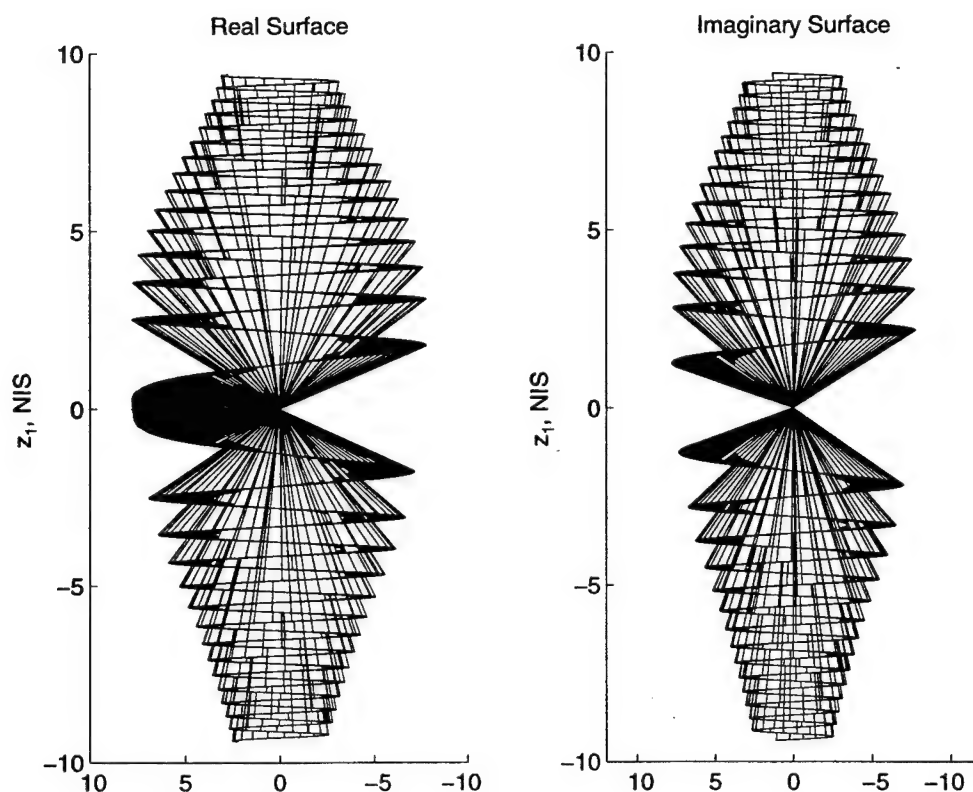


Figure 4.7: REAL AND IMAGINARY NIS INTEGRAND SURFACES FOR A LOGARITHMIC VELOCITY PROFILE - END VIEW - End view of the real and imaginary NIS surfaces defined by the integrand of Equation 4.23. The surfaces are drawn for a physical centerline height of 5 cm and the view is from the transmitter at  $x_1 = 1$  towards the receiver at  $x_1 = 0$ . The velocity profile produces a small asymmetry in  $z_1$ , the cross-beam variable, at this height. The asymmetry increases as the centerline approaches the bottom and the curvature of the profile increases. This end view clearly shows the importance of the central region of the Fresnel pattern, the effective Fresnel zone, in the sample volume averaging process.

The systematic error caused by the finite limits of integration can be removed from both the real and the imaginary parts of the eikonal as a fixed percentage of the actual velocity at each height. The real and imaginary systematic errors were determined from the uppermost six points of each part of the complex profile. Those percentages are constant to less than one part in  $10^2$  for each set of six points. The corrected profiles are plotted in Figure 4.11. With the bias of the finite boundary removed, remaining deviations from the centerline profile can be attributed to the interaction of the Fresnel pattern and the bottom. The correction is clearly justified

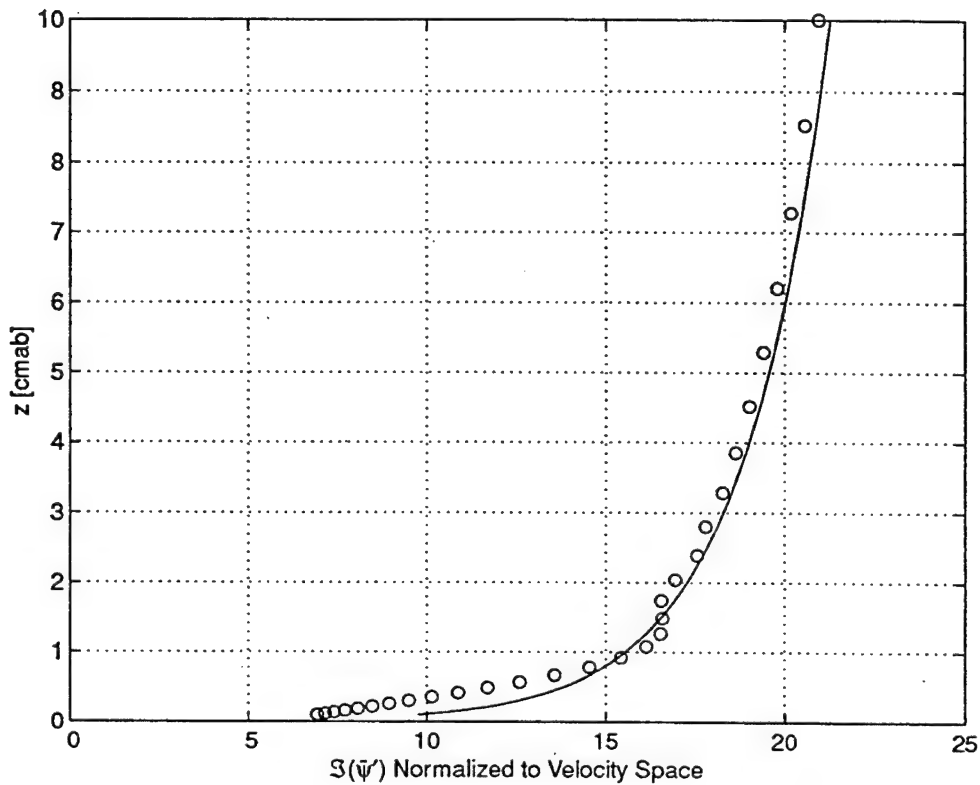


Figure 4.8: CALCULATED FRESNEL ZONE AVERAGES ALONG A LOGARITHMIC VELOCITY PROFILE - LINEAR AXES - The solid line is the logarithmic velocity profile of Equation A.31. The open circles,  $\circ$ , are the imaginary part of the eikonal of Equation 4.23, normalized to velocity space. They are accurately described as simulated measurements of the given velocity profile. The pattern of deviations as the bottom is approached is caused by increasing curvature of the velocity profile, the oscillating sign of the Fresnel pattern, and asymmetric truncation of that pattern by the bottom. The residual error well above the bottom is related to the finite bounds of the integration.

for the untruncated points. Closer to the bottom the domain of integration, and therefore the systematic bias, should be viewed as unchanged. Rather, a portion of the Fresnel field within that domain has a value of zero. That view is consistent with the results of the simple parametric model presented in Section 4.3. The correction eliminates the bias while preserving the effect of the bottom on the pattern of Fresnel averaging, the target of this calculation.

Points between  $2.5 \text{ cmab}$  and  $4.5 \text{ cmab}$  exhibit nearly the same systematic error as the uppermost values and the correction places these points essentially on the actual velocity profile. At  $\approx 2.5 \text{ cmab}$  the first fringe outside the central lobe of the

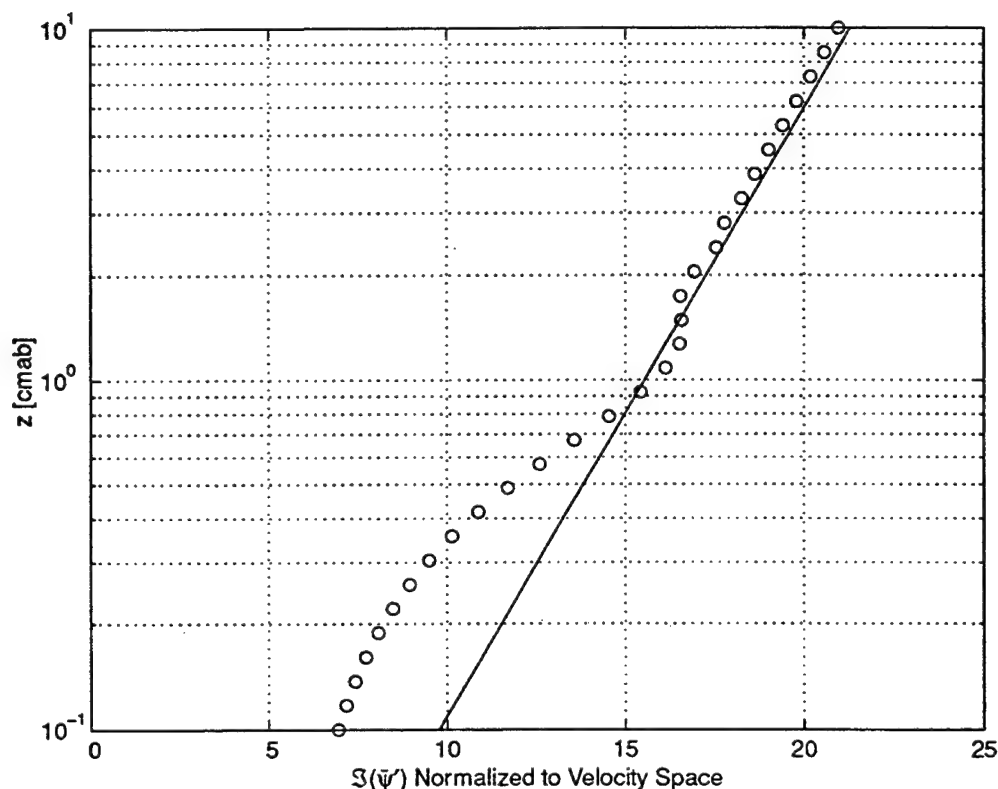


Figure 4.9: CALCULATED FRESNEL ZONE AVERAGES ALONG A LOGARITHMIC VELOCITY PROFILE - SEMILOG AXES - This figure presents the same information as Figure 4.8 on semilog axes. The solid line is the logarithmic velocity profile of Equation A.31. The open circles,  $\circ$ , are the imaginary part of the eikonal of Equation 4.23, normalized to velocity space. They are accurately described as simulated measurements of the given velocity profile. The pattern of deviations as the bottom is approached is caused by increasing curvature of the velocity profile, the oscillating sign of the Fresnel pattern, and asymmetric truncation of that pattern by the bottom. The pattern shows that the effective radius of the sample volume is  $O(1 \text{ cm})$ . The residual error, most notable well above the bottom, is related to the finite bounds of the integration. The residual is a constant percentage of the centerline velocity.

eikonal pattern begins to interact with the bottom. The extensive region of flat bias above  $2.5 \text{ cmab}$  and the weak response to truncation of the first fringe suggest that, as expected, the central lobe of the pattern very strongly dominates the averaging process. Asymmetric truncation of diffraction zones beyond the first ring has no noticeable effect. These observations support the idea of an effective Fresnel zone and identify it with the central lobe of the eikonal. The region of flat bias above the near-bottom features in the profile also shows that the selected domain of integration,

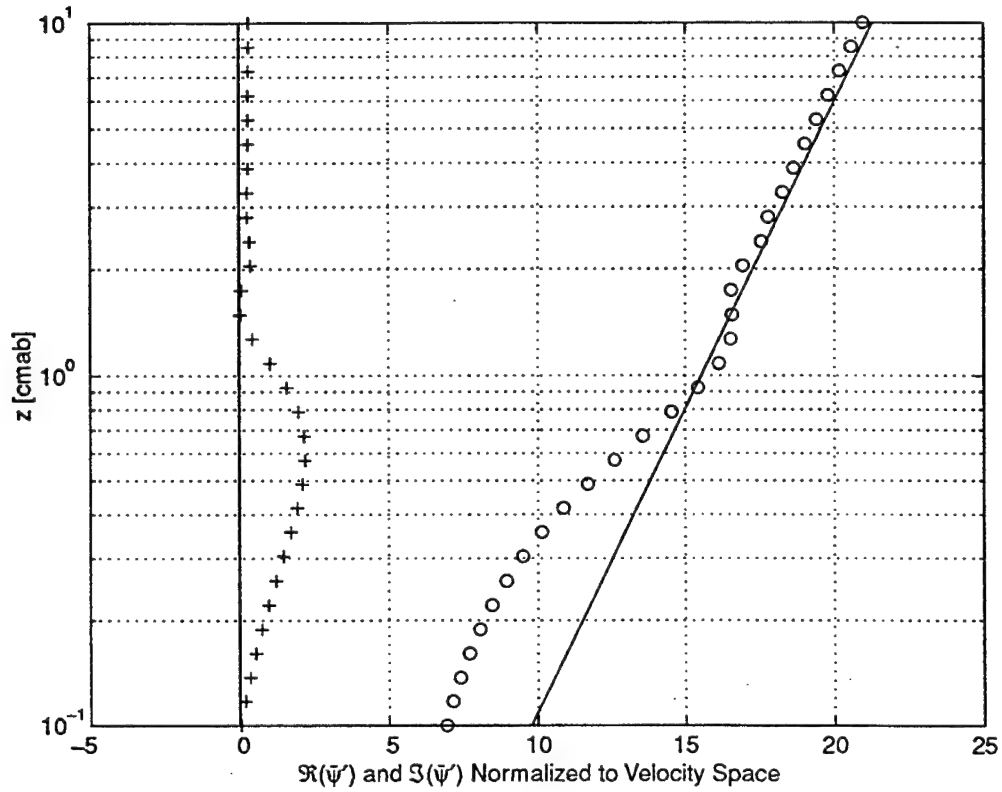


Figure 4.10: REAL AND IMAGINARY PARTS OF THE EIKONAL NORMALIZED TO VELOCITY SPACE - The open circles,  $\circ$ , are the imaginary part of the eikonal of Equation 4.23, normalized to velocity space. The plus symbols,  $+$ , are the real part of the eikonal normalized by the same factor. The solid lines mark the logarithmic velocity profile and zero. The systematic bias of the uppermost points in both profiles is a function of the finite bounds of integration. As expected, the interesting behavior occurs near the bottom where truncation makes the effective Fresnel zone asymmetric.

for the P3 transducers, is sufficiently large to preserve the averaging and truncation effects being investigated.

The most interesting feature of the calculated profile is found within  $1\text{ cm}$  of the bottom. The radius of the central lobe, the mid-axis radius of a  $\frac{\lambda}{2}$  ellipse, is  $8\text{ mm}$  for the P3 transducers. As the acoustic axis approaches the bottom and passes through  $8\text{ mmab}$ , the non-linearity of the profile across the sample volume becomes large enough to produce a significant and increasing bias. The simulated measurements are well below the centerline velocity. Near  $3\text{ mmab}$  the negative bias begins to reverse. This is due to truncation of the sample volume. The region of relatively fast velocities above the centerline is beginning to dominate the shrinking region of

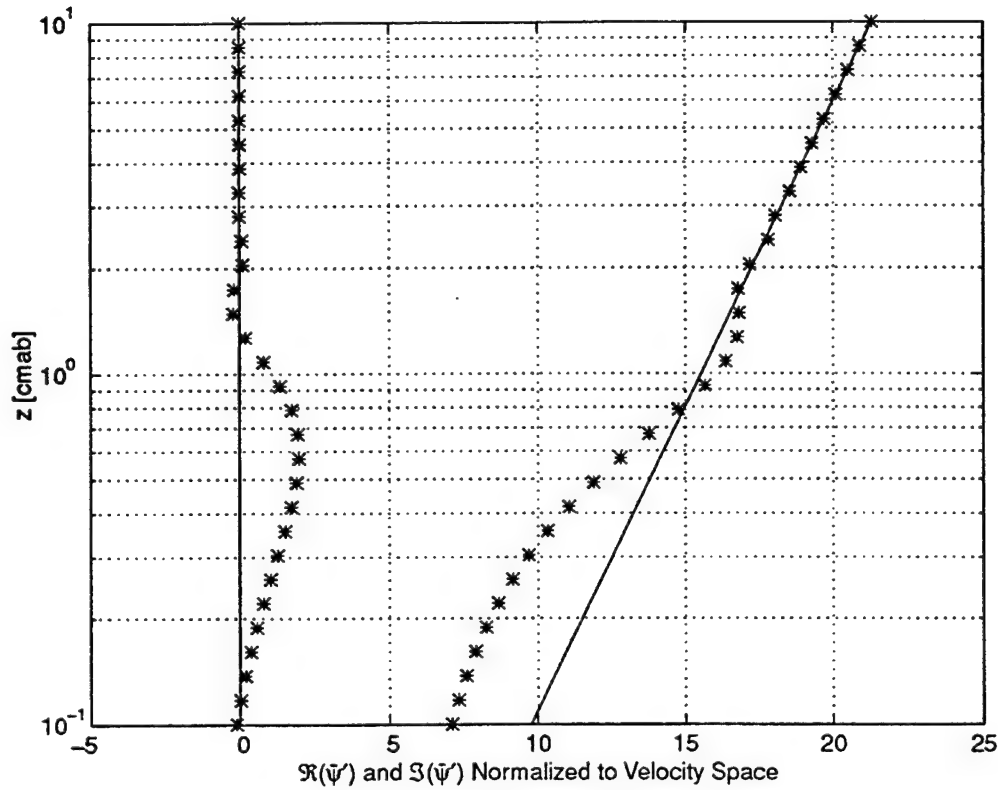


Figure 4.11: REAL AND IMAGINARY PARTS OF THE EIKONAL NORMALIZED TO VELOCITY SPACE AND CORRECTED FOR SYSTEMATIC BIAS - The asterisks, \*, mark the real and imaginary parts of the eikonal of Equation 4.23, normalized to velocity space and corrected for the systematic bias introduced by the finite limits of the integration. The solid lines mark the logarithmic velocity profile and zero. The systematic bias was removed as a fixed percentage of the actual velocity at each height. The percentages were determined from the uppermost six points in the real and imaginary profiles. Those percentages are constant to less than one part in  $10^2$  for the uppermost six points in each part of the profile. The correction eliminates the systematic error while preserving the effect of the bottom on the pattern of Fresnel averaging. The small size of the real part is consistent with the assumption of small  $n'(x)$  used in the derivation of Section 4.2.3. The amplitude of the scattered signal at the receiver is comparable to the undisturbed amplitude for all  $z$ .

relatively slow velocities between the descending centerline and the bottom. Closer to  $z_0$  the calculation returns values with a positive bias.

A simulated measurement profile was also calculated for the P2 transducers using the eikonal model. As described in Section 4.2.4, the beam width alone defines the preliminary restriction on the domain of integration. This limits the complex surfaces of the integrand in the NIS essentially to the central lobe of the eikonal. The restric-

tion is valid to the extent that the central lobe represents the sample volume. As shown above, this is a very reasonable approximation. To avoid adding considerable complexity to the code, the domain of integration was simply truncated at  $z_0$  when necessary. The result and the result corrected for the finite bounds of integration are shown in Figure 4.12.

The mid-axis radius of the  $\frac{\lambda}{2}$  ellipse of the P2 transducers is 0.6 cm. The behavior is comparable in magnitude to the P3 calculation, but occurs somewhat closer to the bed. This is consistent with the change in wave number. There is no trace of the outer fringes interacting with the bottom because they were excluded by the bounds of the integration. It is also noted that a number of simplifications were applied which are not as rigorously justified for the larger transducers. In particular, the underlying far field approximation is somewhat questionable. However, the increase and subsequent decrease in received amplitude, indicated by the real part of the eikonal as the centerline nears the bottom, are consistently observed experimentally as a P2 acoustic axis approaches a sand bottom. The low bias in the velocity measurement within a few millimeters of the bed is completely consistent with the flume measurements reported in Chapter 5. The model based calculation and the empirical measurement are in agreement.

The results of this calculation are, at least qualitatively, predictable from a physical picture of the Fresnel pattern. However, the formal description of the phenomena and solution of the eikonal model have been carried out with a reasonable level of mathematical rigor to provide support for the conclusions and to validate the simplifications of the parametric model described in Section 4.3.

In summary, the outer fringes of the Fresnel zone do not make a significant contribution to the averaging process and the effective sample volume of a BASS Rake acoustic axis can be identified with the central lobe of the Fresnel pattern. For practical purposes, the cross-beam extent of that volume is the mid-axis diameter of a  $\frac{\lambda}{2}$  ellipsoid with the transducers at the foci. Most importantly, it does not appear that measurements with the BASS Rake are compromised by Fresnel averaging except within 1 cm of the bottom. The error in that range may be 20 % to 30 %, but

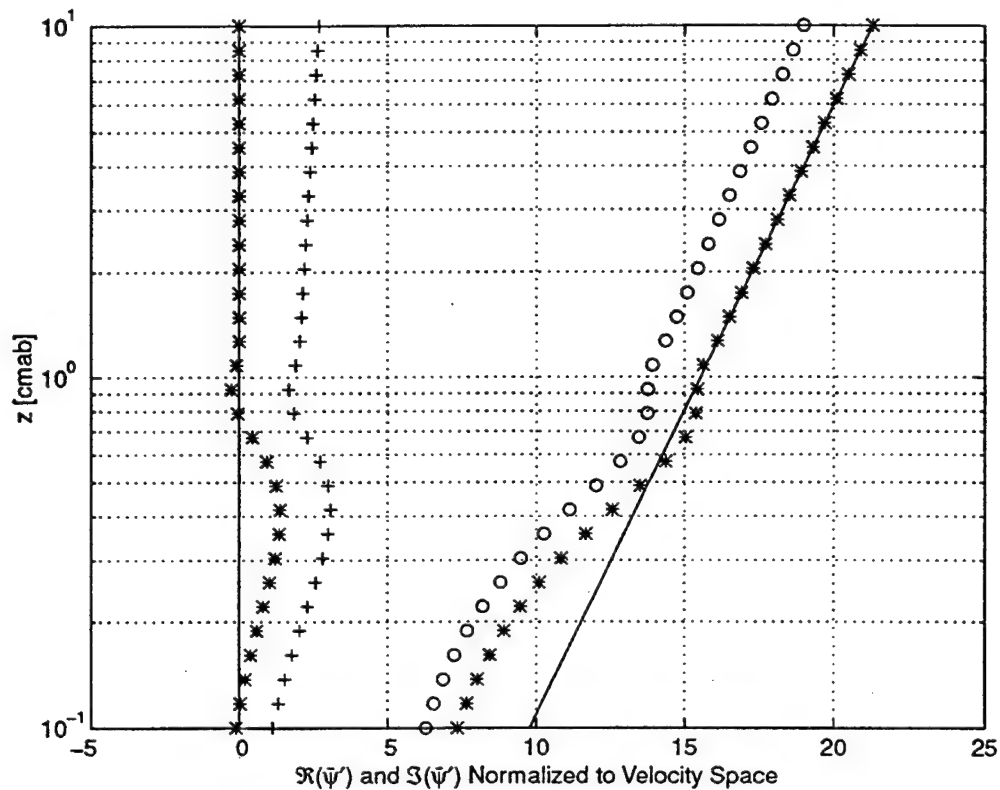


Figure 4.12: REAL AND IMAGINARY PARTS OF THE P2 EIKONAL NORMALIZED TO VELOCITY SPACE AND CORRECTED FOR SYSTEMATIC BIAS - The open circles,  $\circ$ , are the imaginary part of the eikonal of Equation 4.23 for the P2 transducers, normalized to velocity space. The plus symbols,  $+$ , are the real part of the P2 eikonal normalized by the same factor. The solid lines mark the logarithmic velocity profile and zero. The asterisks,  $*$ , mark the real and imaginary parts of the P2 eikonal normalized to velocity space and corrected for the systematic bias introduced by the finite limits of the integration. The systematic bias was removed as a fixed percentage of the actual velocity at each height. The percentages were determined from the points located more than 2 *cmab* in the real and imaginary profiles. Those percentages are constant to less than one part in  $10^2$  in each part of the profile. The correction eliminates the systematic error while preserving the effect of the bottom on the pattern of Fresnel averaging. The  $\frac{\lambda}{2}$  mid-axis radius of the P2 transducers is 0.6 *cm*. The increase in received amplitude 0.4 *cmab* to 0.5 *cmab*, indicated by the real part of the eikonal, is consistently observed experimentally. The low bias in the velocity measurement within a few millimeters of the bed is consistent with the flume measurements reported in Chapter 5.

it is systematic and may be estimated with some accuracy from the flow model and the precise measurements higher in the profile. This procedure also provides an independent consistency check on the nominal height of the sensor above the bottom. It is worth noting that the accuracy of wave-current boundary layer models may be



no greater than 20% [46, 47, 48]. A measurement of this accuracy, within 1 *cm* of the bottom, is actually quite useful without extensive postprocessing. The value of an accurate profile from 1 *cmab* to 10 *cmab* to the study of oceanic processes on the continental shelf is enormous.

### 4.3 A Simplified Parametric Model of the Sample Volume

Several references have been made to the computational complexity of the eikonal calculations. This is largely a function of the need to accurately integrate the rapidly oscillating surfaces of the eikonal integrand. The evaluation of one early profile required nine days of computer time distributed on three different platforms. The performance has been improved by compiling formerly interpreted loops. However, the limiting operation remains the already optimized quadrature and the many iterative evaluations of the bounds of integration and of the integrand. The duration of a calculation is still sufficiently long to justify simplification of the bottom interaction model and effectively to prohibit large scale investigation of the sensor response to different velocity profiles. Summing the eikonals over small elements of the faces of both transducers to approximate the effect of their physical extent is also ruled out.

The eikonal calculations of the previous section were carried out on a Sun-4/110© work station. The code was written, compiled, and executed using MATLAB© numerical and graphics software.<sup>2</sup> The running time for the P3 calculation was approximately 30 hours. The execution time averaged 1 hour for each point, but there was also a weak dependence on the value of  $z$ . The P2 profile required 3 hours. The relatively quick execution of the P2 evaluation is due to the exclusion of the fringes of the eikonal from the domain of integration. The need to limit the number of floating point operations involved at each step of the eikonal quadrature is obvious.

The need for a computationally simpler approximation that accurately duplicates

---

<sup>2</sup>Sun-4© is a registered trademark of Sun Microsystems, Inc. MATLAB© is a registered trademark of The MathWorks, Inc.

the significant physical behavior of the sample volume is also clear. The eikonal calculations have demonstrated that the fringes of the Fresnel pattern may be ignored, but retaining the eikonal form and evaluating the central lobe alone still requires several hours for a given logarithmic profile. The Bessel functions describing profiles in a turbulent wave boundary layer require even more floating point operations. Plotting several rudimentary approximations of the P2 beam pattern suggests a very elementary approach. Figure 4.13 shows the 3 dB and first null beam widths, extended from the edges of a pair of P2 transducers defining an acoustic axis. Both widths are far field approximations. The Rayleigh length of the P2 transducers is  $L_{Rayleigh} = 4.2 \text{ cm}$ , so the far field characterization is rather questionable. Justification will be found in the result. The upper and lower halves of a  $\frac{\lambda}{2}$  ellipse, extending from the edges of the transducers, are also plotted in the figure. Anchoring the curves at the edges of the transducers partially accounts for the physical extent of the disks.

Observe that the modified ellipse in Figure 4.13 is closely approximated by a rectangle. Averaging the velocity profile over that simple domain of integration, even with truncation included to account for the bottom, is computationally trivial. The radius,  $r$ , the distance from the centerline, is treated as a parameter with a value chosen to match the results of a one time eikonal calculation for particular transducer characteristics. Portions of the domain falling below  $z_0$  are truncated, but all values are averaged over  $2r$  for consistency with the eikonal calculation. This approach was applied to the logarithmic profile used in the eikonal evaluations of the previous section. The radius was varied from  $2 \text{ mm}$  to  $1 \text{ cm}$ . The result is shown in Figure 4.14 with the P2 and P3 eikonal profiles.

The parametric model reproduces the eikonal calculations to a very high degree of accuracy. Differences between the two calculations are smaller than the measurement accuracy of the BASS Rake and well below the accuracy of boundary layer flow models. Appropriate values of the model parameter for the transducers appear to be  $r_{P2} = 4 \text{ mm}$  and  $r_{P3} = 6 \text{ mm}$ . These values are comparable to the radii of the  $\frac{\lambda}{2}$  ellipses and consistent with both the relative wave numbers and the relative diameters of the two transducers. The total computation time for all five parametric

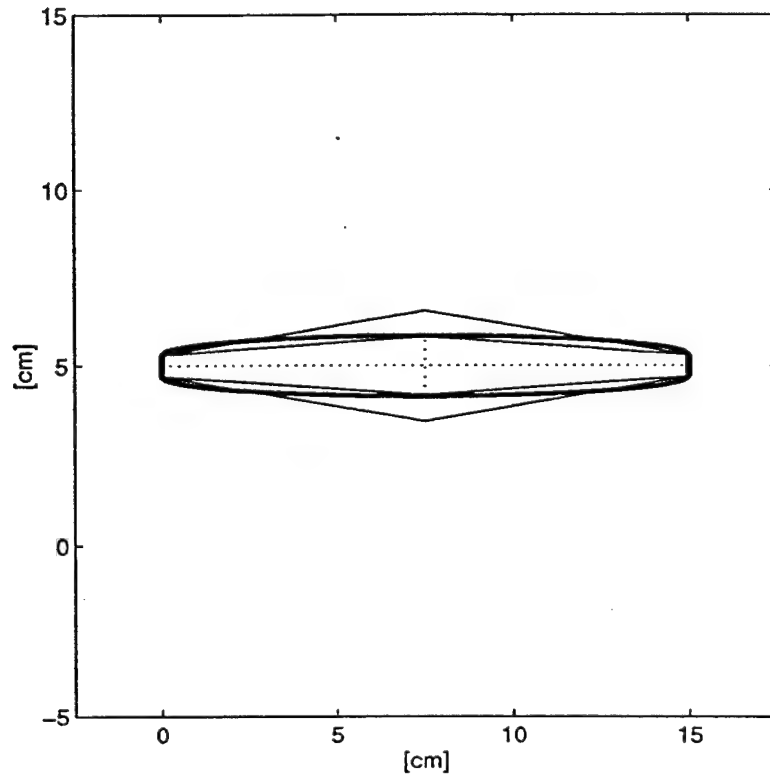


Figure 4.13: BEAM PATTERN APPROXIMATIONS FOR A P2 TRANSDUCER AXIS - The straight, solid lines mark the 3 dB and first null beam widths. The heavy curves mark a  $\frac{\lambda}{2}$  ellipse. All curves are extended from the edges of the transducers to account for the physical extent of the disks. Transducers and curves are drawn to a common horizontal and vertical scale.

model parameters was a small fraction of a second.

Patently, the parametric model has the accuracy and the speed to replace the eikonal calculation, particularly when rapid assessment and processing of data is required. The simple apparent relationship of the parametric model to the physical averaging process is also appealing. However, unlike the eikonal model, the parametric model is not based on the underlying physics of wave propagation and scattering. It is based on the effects of those processes on the BASS velocity measurement. The parametric formulation does not provide the signal amplitude information contained in the eikonal. All information about the arrival phase of the signal is also lost. For example, summing the response over the elements of the transducer faces to determine the effect of the physical extent of the disks on the response will still require repeated

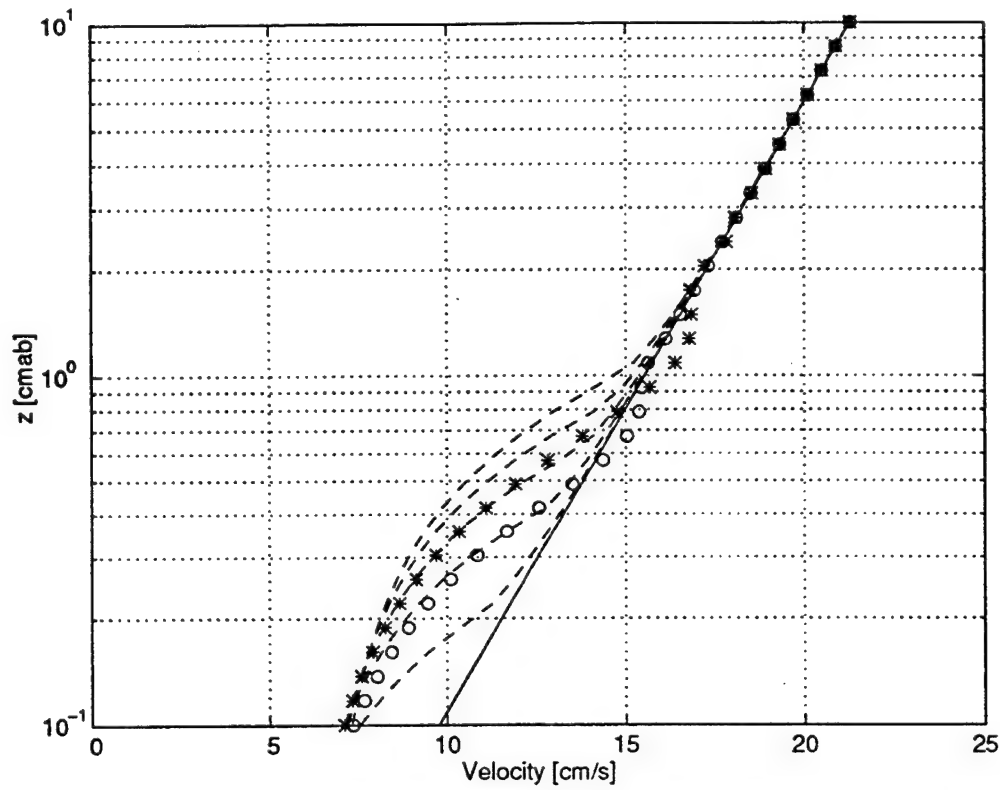


Figure 4.14: COMPARISON OF THE EIKONAL AND PARAMETRIC MODELS OF FRESNEL ZONE AVERAGING - The solid line marks the logarithmic velocity profile. The dashed lines mark measurement profiles calculated with the parametric model for  $r = 2\text{ mm}$  to  $r = 1\text{ cm}$  in  $2\text{ mm}$  increments. The divergence of the parametric profiles from the actual velocity increases with  $r$ . The open circles,  $\circ$ , and the asterisks,  $*$ , mark, respectively, the P2 and P3 profiles derived from the eikonal calculations.  $r_{P2} = 4\text{ mm}$  and  $r_{P3} = 6\text{ mm}$  reproduce the eikonal calculations to a high degree of accuracy.

evaluation of the eikonal with a geometrically complicated  $\bar{n}'(\mathbf{x})$ . The parametric model is a computational convenience and it should be recognized as such in any analysis.

## 4.4 The Effect of Fresnel Averaging On Continental Shelf Wave Bottom Boundary Layer Measurements

The obvious advantage of the parametric model is rapid application to data. An accurate assessment of the error in measurements made very close to the bottom or in strong, non-linear, shear can be made easily. In many cases the analysis could be carried out with a hand calculator. A less obvious, but far more important advantage, is performance assessment of the transducer array against expected boundary layer velocity profiles. Vertical resolution of the BASS Rake depends on both the vertical spacing of the transducers and on the averaging effect of the sample volume on that profile. The design process is iterative. It depends strongly on the ability to get a rapid and accurate answer to the question, "What can be gained by changing this parameter?" This use is considered here for the laminar and turbulent wave bottom boundary layers described in Appendix A.

The velocity in a laminar wave boundary layer is given by

$$u_{w_{lam}}(z, t) = \Re \left\{ u_{bm} \left[ 1 - e^{-(1+i)\frac{z}{\delta_w}} \right] e^{i\omega t} \right\} \quad (\text{A.40})$$

$u_{bm}$  is the amplitude of the wave motion at the bottom. The value is determined from linear surface gravity wave theory.  $\delta_w$  is a vertical length scale for the thickness of the wave boundary layer and  $\omega$  is the radian frequency of the waves. The velocity in a turbulent wave boundary layer is given by

$$u_{w_{turb}}(z, t) = \Re \left\{ u_{bm} \left[ 1 - \frac{K_0 \left( i^{\frac{1}{2}} 2 \sqrt{\frac{z}{\delta_w}} \right)}{K_0 \left( i^{\frac{1}{2}} 2 \sqrt{\frac{z_0}{\delta_w}} \right)} \right] e^{i\omega t} \right\} \quad (\text{A.46})$$

The notation is the same as that used in Equation A.40. These formulas are derived in Appendix A, based on the wave-current bottom boundary layer model of Grant and Madsen [24, 27, 46]. Further bibliographic references can be found in the appendix.

Two scenarios typical of the near shore continental shelf are considered in Appendix A. Flow calculations follow the Grant-Madsen model [46]. In both scenarios the water depth is 10 m and the bottom is a fixed, flat bed of 250  $\mu\text{m}$  sand grains. The laminar wave boundary layer is produced by locally generated wind waves with a period of 6 s and an amplitude of 0.5 m. The turbulent boundary layer is produced by remotely generated swell propagating across the shelf. The period of the swell is 8 s and its local amplitude is 1 m. Velocity and stress profiles for these two boundary layers are shown in Figures A.2 and A.4. The profiles are drawn for nine evenly spaced values of the phase of the oscillation spanning a half period. Observe particularly that the vertical extent of these boundary layers is quite small. The range  $0.5\text{ cm} \leq \delta_w \leq 2.5\text{ cm}$  is typical for the shelf over a broad range of conditions [24, 27, 46].

One of the most important distinctions between the laminar and turbulent wave boundary layers is the phase lead of the near-bottom velocity,  $u_w$ , compared to the irrotational forcing velocity,  $u_\infty = \Re(u_{bm}e^{i\omega t})$ , above the boundary layer. The laminar phase lead is  $45^\circ$ , but the turbulent lead is only  $10^\circ$ . The change in phase occurs quite dramatically over a very narrow range of the wave Reynolds number,  $RE = \frac{u_{bm}A_{bm}}{\nu}$ , where  $A_{bm} = \frac{u_{bm}}{\omega}$  is the bottom excursion amplitude and  $\nu$  is the kinematic viscosity. The phase lead provides a target for BASS Rake measurements, particularly if the wave boundary layer is thin compared to vertical transducer spacing. However, the phase leads both decrease rapidly to zero with distance from the bottom. Additionally, the phase lead difference between the two scenarios considered here actually changes sign a few millimeters above the bed. Making the detection depends critically on the height of the lowermost sample volume above the bed. The degree to which the wave signal is spectral rather than monochromatic may be the limiting consideration for the phase leads of less than  $10^\circ$  expected several millimeters above the bed for both laminar and turbulent wave bottom boundary layers. Profiles of the phase lead for these two cases are shown in Figures A.3 and A.6.

For a tine diameter,  $D \leq 1\text{ cm}$ , the vertical spacing of the 6 mm diameter P2 transducers is no less than 6 mm between centers. Measurements can be made down

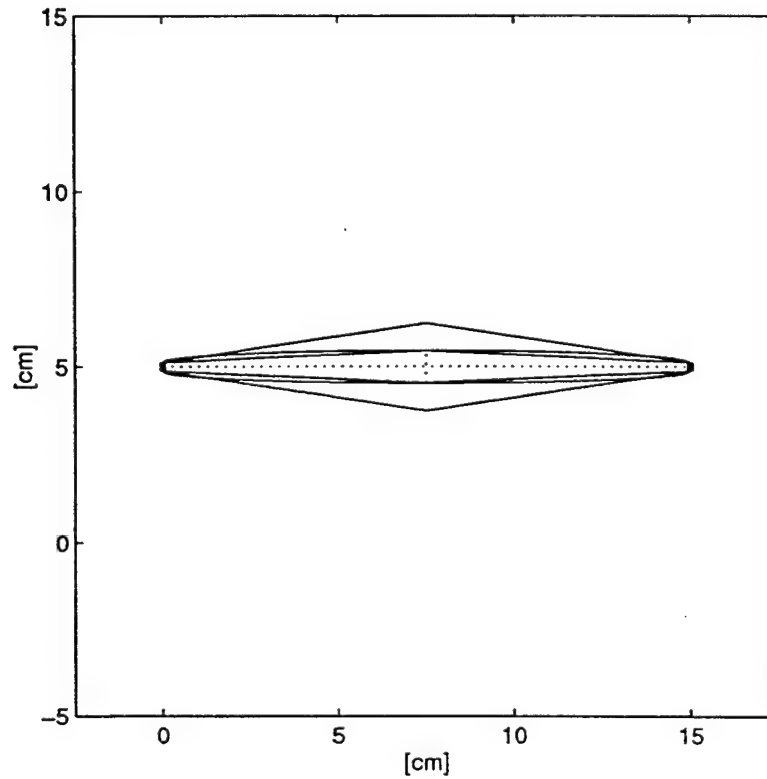


Figure 4.15: BEAM PATTERN APPROXIMATIONS FOR AN ACOUSTIC AXIS USING  $5\text{ MHz}$ ,  $2.5\text{ mm}$  TRANSDUCERS - The straight, solid lines mark the  $3\text{ dB}$  and first null beam widths. The heavy curves mark a  $\frac{\lambda}{2}$  ellipse. All curves are extended from the edges of the transducers to account for the physical extent of the disks. Transducers and curves are drawn to a common horizontal and vertical scale.

to  $3\text{ mmab}$ . The  $2.5\text{ mm}$  diameter P3 transducers, arranged in three offset columns, can achieve  $1\text{ mm}$  vertical spacing (Chapter 2). Transducers of smaller diameter are difficult to manufacture [76] and have extremely poor power transfer and electrical characteristics (Chapter 3). It is recognized that the P3 transducers do not actually work in the immediate vicinity of a boundary because of their wide beam pattern. However, transducers of this diameter, operating at higher frequency, are of some interest. An operating frequency of  $5\text{ MHz}$  would produce an  $8.5^\circ$  first null beam width, similar to the beam width of the P2 transducers. The beam width and effective Fresnel zone characteristics of these  $5\text{ MHz}$  transducers are shown in Figure 4.15. The  $5\text{ MHz}$  eikonal profiles are shown in Figure 4.16. Comparison with the P2 and P3

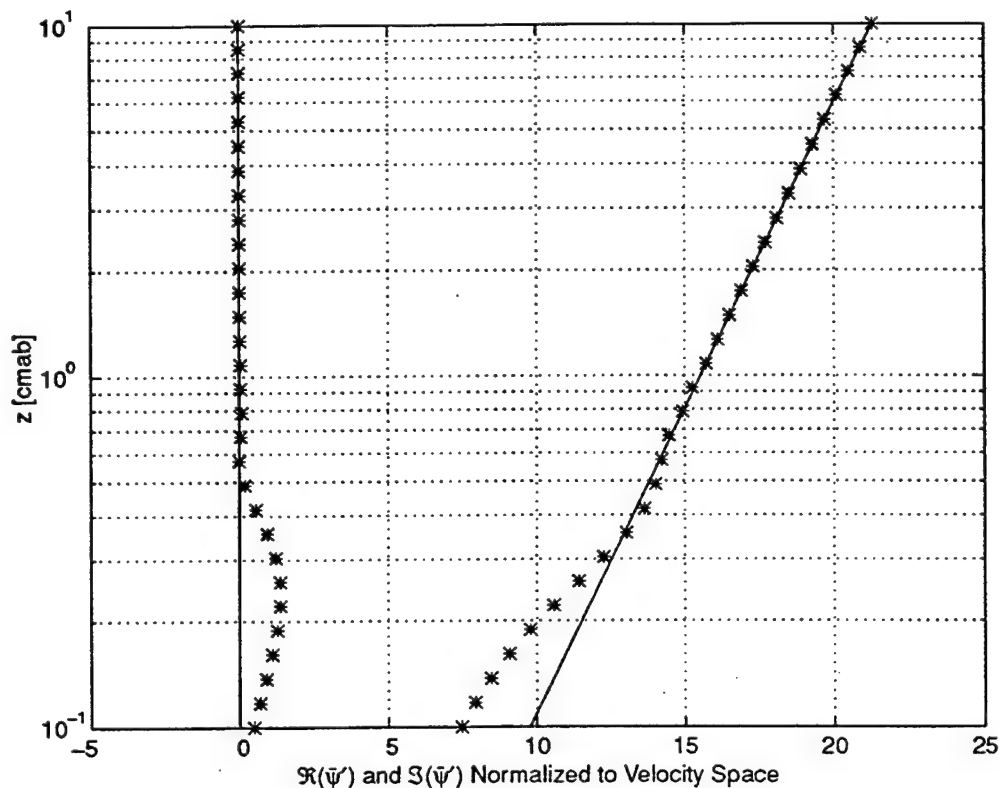


Figure 4.16: REAL AND IMAGINARY PARTS OF THE 5 *MHz* EIKONAL NORMALIZED TO VELOCITY SPACE AND CORRECTED FOR SYSTEMATIC BIAS - The solid lines mark the logarithmic velocity profile and zero. The asterisks, \*, mark the real and imaginary parts of the 5 *MHz* eikonal normalized to velocity space and corrected for the systematic bias introduced by the finite limits of the integration. The systematic bias was removed as a fixed percentage of the actual velocity at each height. The percentages were determined from the points located more than 1 *cmab* in the real and imaginary profiles. Those percentages are constant to less than one part in  $10^2$  in each part of the profile. The correction eliminates the systematic error while preserving the effect of the bottom on the pattern of Fresnel averaging. Note the performance improvement compared to the P2 and P3 transducers. Measurement bias for this logarithmic profile is significant only within 2 *mm* to 3 *mm* of the bottom.

eikonals in Figures 4.11 and 4.12 shows a clear improvement in performance.

The eikonal and parametric model comparison of Figure 4.14 is replotted in Figure 4.17 with the addition of the 5 *MHz* eikonal calculation. A parametric model radius  $r_{5\text{ MHz}} = 2\text{ mm}$  reproduces the eikonal profile to a high degree of accuracy. There are technical problems associated with the smaller transducers and with higher frequency, but, as described in Chapter 3, these have largely been solved. This is a



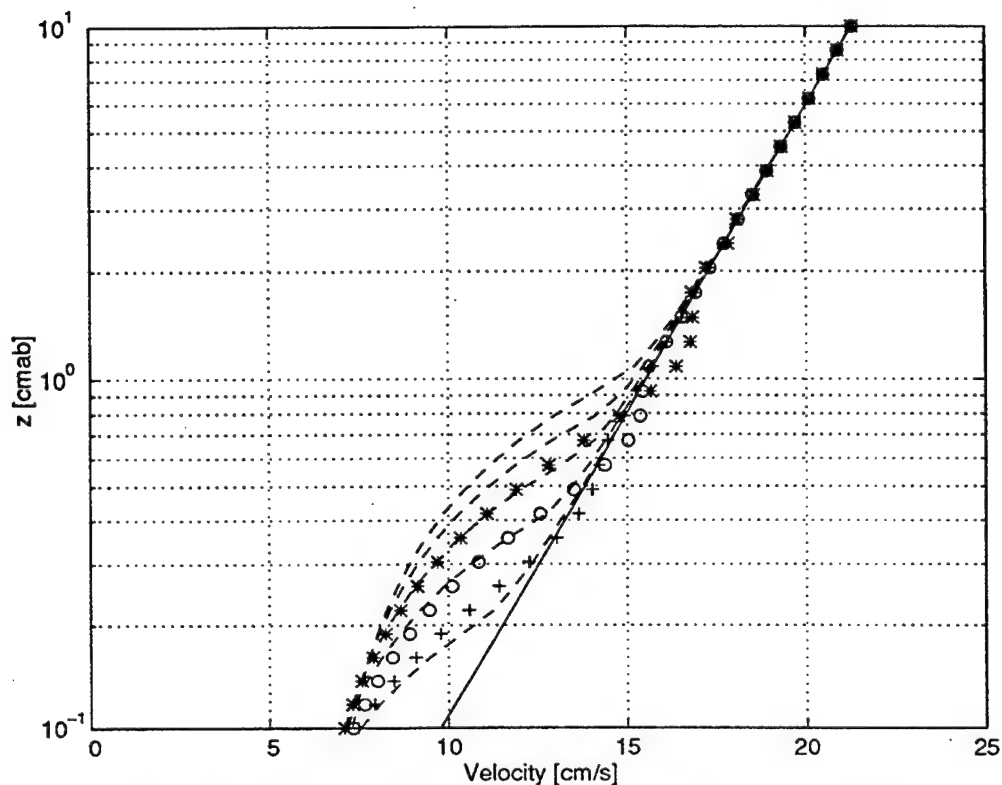


Figure 4.17: FURTHER COMPARISON OF THE EIKONAL AND PARAMETRIC MODELS OF FRESNEL ZONE AVERAGING - The solid line marks the logarithmic velocity profile. The dashed lines mark measurement profiles calculated with the parametric model for  $r = 2\text{ mm}$  to  $r = 1\text{ cm}$  in  $2\text{ mm}$  increments. The divergence of the parametric profiles from the actual velocity increases with  $r$ . The open circles,  $\circ$ , and the asterisks,  $*$ , mark, respectively, the P2 and P3 profiles derived from the eikonal calculations.  $r_{P2} = 4\text{ mm}$  and  $r_{P3} = 6\text{ mm}$  reproduce the eikonal calculations to a high degree of accuracy. The  $5\text{ MHz}$  eikonal profile is marked by the plus symbols,  $+$ , and is well described by  $r_{5\text{ MHz}} = 2\text{ mm}$ .

promising direction for future research. The opportunity is taken here to demonstrate the ability of the parametric model to estimate the gain in vertical resolution from such changes in frequency and spacing compared to the functional P2 transducers. The potential improvement in WBBL imaging capability is surprising.

The laminar wave boundary layer velocity profiles are shown in Figure 4.18. The response of a P2 acoustic axis, as predicted by the parametric model, is shown by the open circles. Errors associated with both non-linearity of the velocity profile and truncation of the sample volume are clearly visible. The errors get particularly

large below  $5\text{ mmab}$ . Note that measurements would be biased high, because of truncation, if they could be taken within  $1\text{ mmab}$ . This behavior was noted during the discussion of the steady current profile in Section 4.2.4.2. Also shown are the levels where measurements could actually be taken with tines built using P2 transducers. Obviously the vertical structure of this laminar boundary layer would not be well resolved by P2 tines. The phase of the boundary layer velocity  $3\text{ mmab}$  compared to the phase of the forcing velocity would be  $\approx 6^\circ$ . Conceivably this could be measured if the sampling period was sufficiently small compared to a wave period and the wave field was relatively monochromatic. Under most conditions the detection would be very difficult.

Figure 4.19 shows the improvement that might be realized with  $5\text{ MHz}$  transducers and  $1\text{ mm}$  vertical spacing. The open circles show greatly improved measurement accuracy at all heights. The reduction of the effective Fresnel radius from  $4\text{ mm}$  to  $2\text{ mm}$  is responsible for the greater accuracy. An accurate six to eight point profile measurement through the boundary layer would apparently be possible with these transducers. The structure of the laminar boundary layer could actually be resolved if these design changes were implemented. As a consequence of the advancements made during the development of the P3 laboratory prototype, these changes are probably within the current envelope of BASS and BASS Rake technology.

The dependence of wave boundary layer profile measurements on both sample volume and spacing is evident in the hypothetical response of the P3 transducers shown in Figure 4.20. Although fine vertical spacing is possible with these transducers, the  $6\text{ mm}$  effective Fresnel radius would result in very poor measurement accuracy. Details of the velocity structure, the height dependence of both magnitude and phase, would be smoothed out and lost by the large effective sample volume.

The response of the P2 and  $5\text{ MHz}$  transducers in the turbulent wave boundary layer is shown in Figures 4.21 and 4.22. As before, the solid lines mark the velocity, the open circles show the response at that phase and height, and the plus symbols show the location of the actual measurements. The top frame in each figure shows the structure of the turbulent wave boundary layer up to  $15\text{ cmab}$ . The lower frame

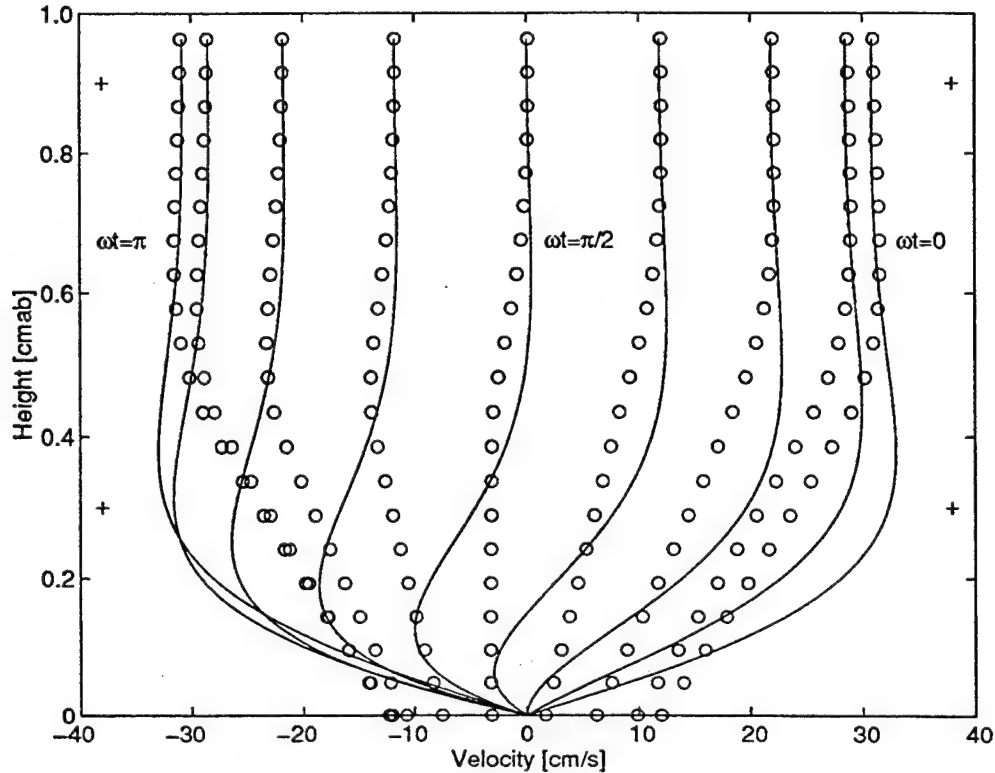


Figure 4.18: IMAGING A LAMINAR WAVE BOUNDARY LAYER WITH P2 TRANSDUCERS - The solid lines are the laminar velocity profiles at nine values of the phase,  $\omega t$ , of the forcing velocity,  $u_\infty$ . The evenly spaced values span  $\omega t = 0$  to  $\omega t = \pi$ . The open circles,  $\circ$ , show the measured velocity profiles for each value of  $\omega t$  predicted by the parametric model. Errors associated with both non-linearity of the velocity profile and truncation of the sample volume are clearly visible. The errors get particularly large below 5 *mmab*. Note that measurements would be biased high if they could be taken within 1 *mmab*. The plus symbols, +, along the edge of the plot mark the actual measurement heights of P2 transducers. The laminar boundary layer would not be well resolved spatially. The phase of the boundary layer velocity 3 *mmab* relative to  $u_\infty$  would be  $\approx 6^\circ$  and might be measurable under some conditions.

provides a detailed view of the region within 2 *cm* of the bottom. The P2 transducer performs quite well in this thicker boundary layer. Six to eight measurements are made across the region of sheared flow. Of these, only the measurement at 3 *mmab* has an accuracy problem. The vertical structure of the turbulent boundary layer could be resolved with these transducers. It should be noted here that the tests described in Chapter 5 have already demonstrated that the P2 transducers function well right up to a natural sand bottom and that this model accurately describes their

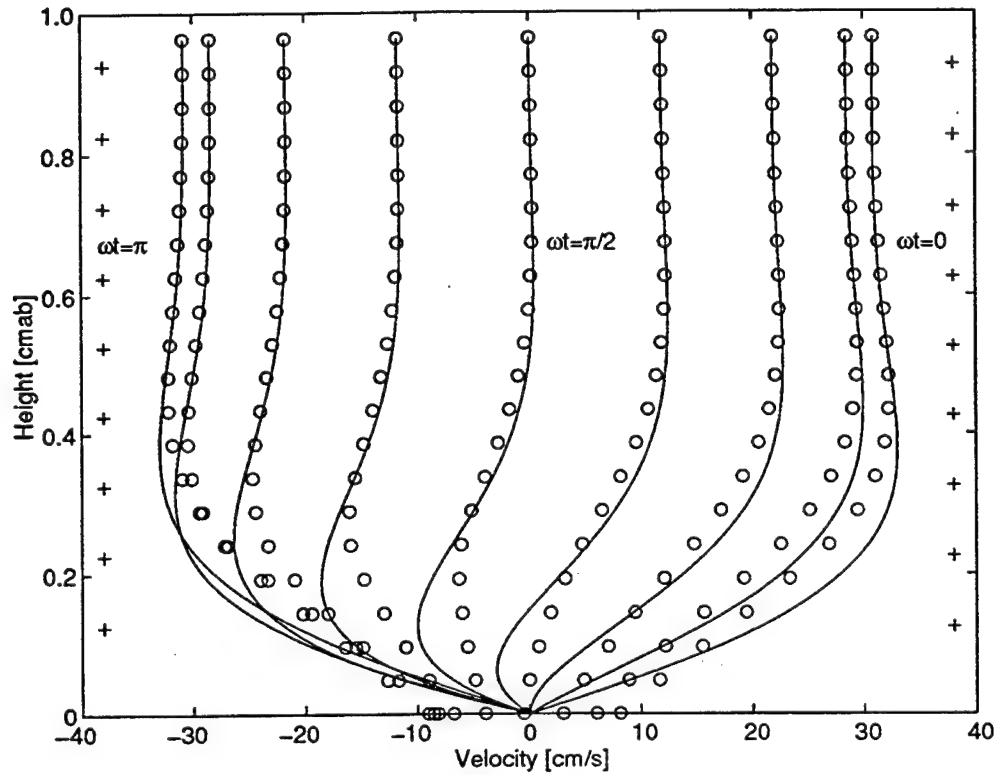


Figure 4.19: IMAGING A LAMINAR WAVE BOUNDARY LAYER WITH 5 MHz, 2.5 mm TRANSDUCERS - The solid lines are the laminar velocity profiles at nine values of the phase,  $\omega t$ , of the forcing velocity,  $u_\infty$ . The evenly spaced values span  $\omega t = 0$  to  $\omega t = \pi$ . The open circles, o, show the measured velocity profiles for each value of  $\omega t$  predicted by the parametric model. The effective Fresnel radius of these transducers is approximately 2 mm. Note the significant improvement in predicted measurement accuracy at each height compared to the P2 transducers with a 4 mm effective Fresnel radius. The plus symbols, +, along the edge of the plot mark the actual measurement heights for 2.5 mm transducers arranged in three offset columns with 1 mm vertical spacing. The structure of the laminar boundary layer could actually be resolved if these design changes were implemented.

response.

The proposed 5 MHz transducers provide both more detail and greater accuracy in resolving the vertical structure of the wave boundary layer. That there would be some improvement was easily predictable at a qualitative level. The importance of the result lies in the degree of improvement and the rapidity with which it was determined. The implication of this calculation is not simply that a shift to 5 MHz would provide significantly greater resolution. It also shows that a shift to 10 MHz or 20 MHz, frequencies that would present enormous technical challenges to implement,

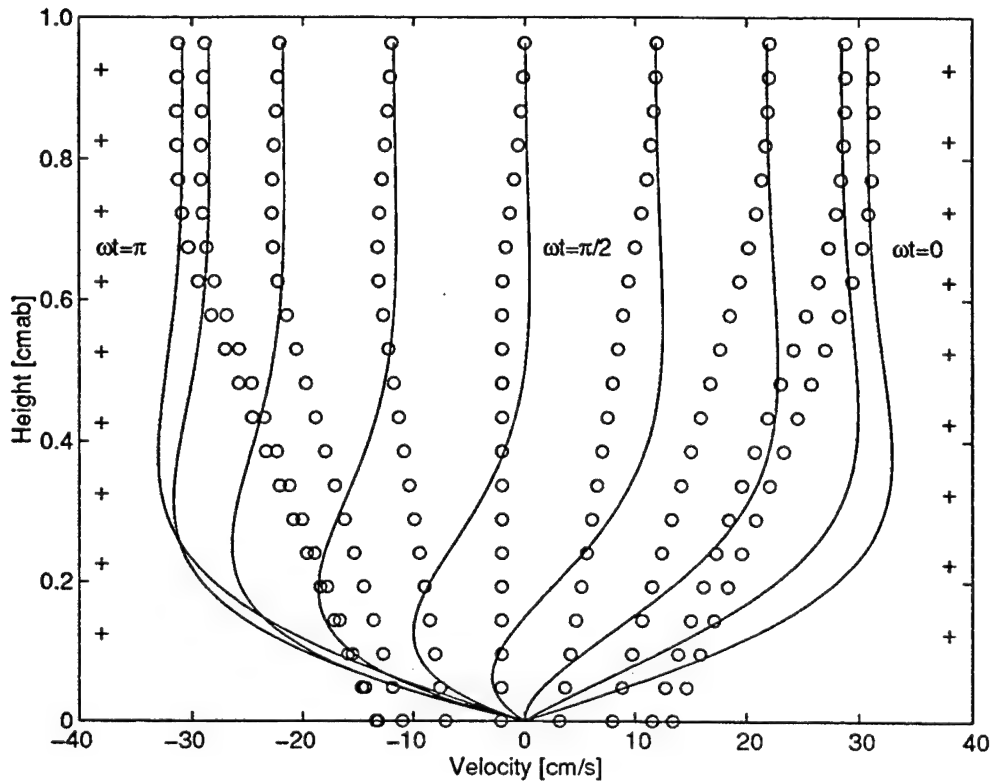


Figure 4.20: HYPOTHETICALLY IMAGING A LAMINAR WAVE BOUNDARY LAYER WITH P3 TRANSDUCERS - The solid lines are the laminar velocity profiles at nine values of the phase,  $\omega t$ , of the forcing velocity,  $u_\infty$ . The evenly spaced values span  $\omega t = 0$  to  $\omega t = \pi$ . The open circles,  $o$ , show the measured velocity profiles for each value of  $\omega t$  predicted by the parametric model. The effective Fresnel radius of these transducers is  $6\text{ mm}$ . The plus symbols,  $+$ , along the edge of the plot mark the actual measurement heights for  $2.5\text{ mm}$  transducers arranged in three offset columns with  $1\text{ mm}$  vertical spacing. The relatively fine vertical spacing of measurement heights would not compensate for the effects of averaging over a relatively large sample volume. The details of the velocity structure, the height dependence of both magnitude and phase, would be smoothed out and lost.

is not necessary. The continental shelf wave bottom boundary layer could be imaged in detail with transducers that are already inside the BASS Rake technology envelope. That result demonstrates the importance of the parametric model as a design tool.

## 4.5 Summary

The investigation into the BASS Rake sample volume has been unexpectedly productive. The volume was originally, and naively, assumed to be delineated by the

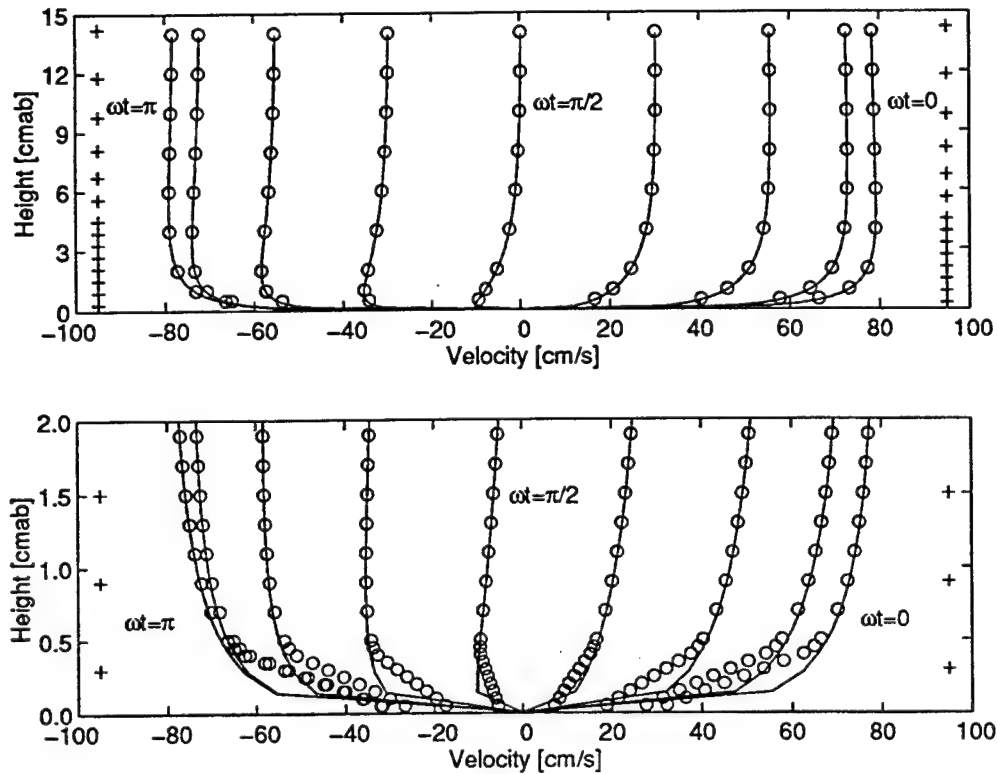


Figure 4.21: IMAGING A TURBULENT WAVE BOUNDARY LAYER WITH P2 TRANSDUCERS - The solid lines are the turbulent velocity profiles at nine values of the phase,  $\omega t$ , of the forcing velocity,  $u_\infty$ . The evenly spaced values span  $\omega t = 0$  to  $\omega t = \pi$ . The open circles,  $\circ$ , show the measured velocity profiles for each value of  $\omega t$  predicted by the parametric model. The effective Fresnel radius of these transducers is 4 mm. The plus symbols, +, along the edge of the plot mark the actual measurement heights. Transducers are spaced linearly close to the bottom to achieve maximum measurement density. The spacing is logarithmic further from the bottom, reflecting the lengthening of the characteristic vertical length scale. The upper frame shows the turbulent wave boundary layer structure up to 15 cmab and the lower frame provides a detailed view of the region within 2 cm of the bottom. The vertical structure of the turbulent wave boundary layer could be resolved using these transducers.

right circular cylinder between the transducer faces. It was ignored in the face of other development priorities. When revisited, after a precipitous leap to the top of the priority list, the sample volume had grown to a much larger, more ill defined region, with what were then very poorly understood effects. Those effects were potentially an insurmountable obstacle, preventing accurate and precise boundary layer measurements using this technique.

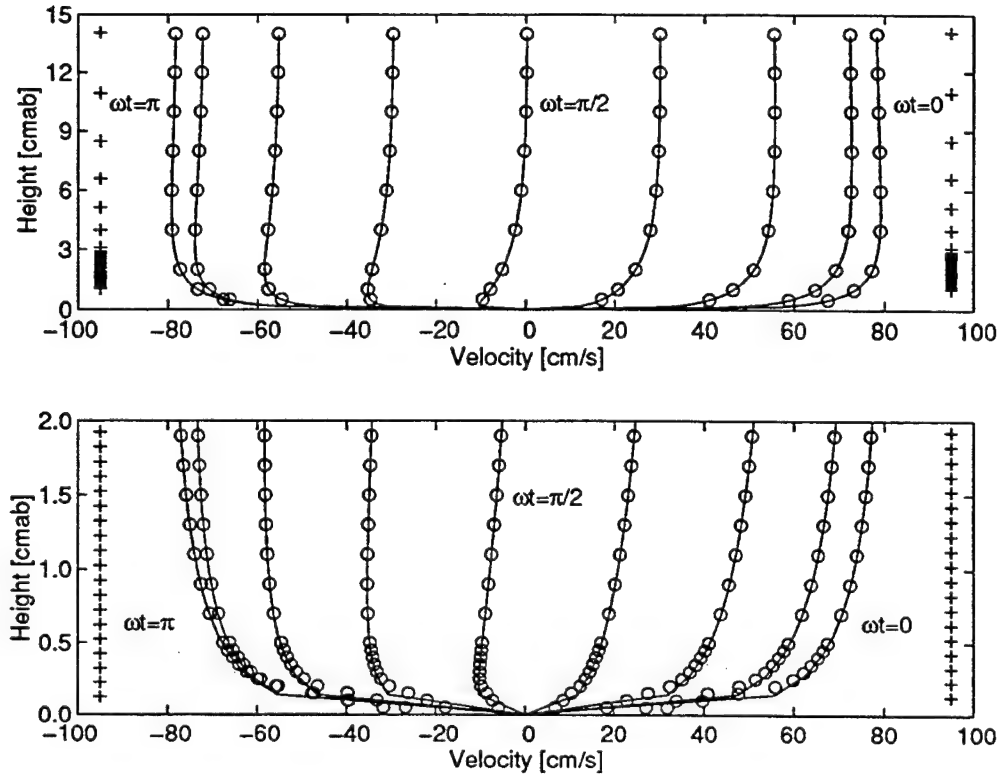


Figure 4.22: IMAGING A TURBULENT WAVE BOUNDARY LAYER WITH 5 MHz, 2.5 mm TRANSDUCERS - The solid lines are the turbulent velocity profiles at nine values of the phase,  $\omega t$ , of the forcing velocity,  $u_\infty$ . The evenly spaced values span  $\omega t = 0$  to  $\omega t = \pi$ . The open circles,  $\circ$ , show the measured velocity profiles for each value of  $\omega t$  predicted by the parametric model. The effective Fresnel radius of these transducers is 2 mm. The plus symbols, +, along the edge of the plot mark the actual measurement heights for 2.5 mm transducers arranged in three offset columns with 1 mm vertical spacing. Transducers are spaced linearly close to the bottom to achieve maximum measurement density. The spacing is logarithmic further from the bottom, reflecting the lengthening of the characteristic vertical length scale. The upper frame shows the turbulent wave boundary layer structure up to 15 cmab and the lower frame provides a detailed view of the region within 2 cm of the bottom. Detailed and accurate measurements of the vertical structure of a turbulent continental shelf wave bottom boundary layer could be made with these transducers.

Subsequent investigation showed that the problems are not severe. The induced errors are, in general, negligible. Where the errors are significant, they are also systematic and predictable. Most importantly, the P2 transducers, which had been shown to function next to a boundary, were also shown to be capable of returning useful information from the wave bottom boundary layer on the continental shelf. The investigation also revealed the Fresnel zone as a phenomenon with a physical

and mathematical symmetry that was both pleasing and challenging to work with. However, the eikonal calculation required far too much time to be used in the analysis of the expected large data sets.

The computational overhead demanded a simpler approach. The eikonal calculation had shown that the averaging process was very strongly center weighted. That suggested limiting the bounds of integration to the central lobe of the eikonal pattern. However, this still required several hours to evaluate. The idea of integrating the velocity over fixed, parametric, limits was a direct result of plotting the beam width and modified  $\frac{\lambda}{2}$  ellipse in Figure 4.13. The original intention had been to use the ellipse as a bound and to retain the two dimensional integral. It was the appearance of the curves that suggested that a simpler, one dimensional evaluation would be feasible.

The accuracy of the simple parametric model, as measured by the eikonal calculation, is very high. Computation time drops by at least two to three orders of magnitude. The accuracy and speed of the parametric model have made it useful not just for data analysis, but for instrument design. That metamorphosis, from an apparently insurmountable obstacle into a design tool has been quite valuable. In particular, it has shown that a relatively modest increase in operating frequency could provide a significant increase in resolution. It has also shown that the proven P2 tines could accurately probe the continental shelf wave bottom boundary layer.





## Chapter 5

# Tow Tank and Flume Evaluation of the Laboratory Prototype<sup>†</sup>

### 5.1 Introduction

This chapter documents the laboratory testing and evaluation of the BASS Rake technique. The construction of the laboratory prototype is briefly described in Section 5.2. An analysis of the flow distortion caused by the tines is presented in Section 5.3. The analysis suggests that measurements with the BASS Rake will depend on the Reynolds number and possibly on the Keulegan-Carpenter number. This is a new finding for BASS based instrumentation. In Section 5.4 the Reynolds number dependence is demonstrated and quantified in a tow tank under controlled conditions. The empirically derived correction for steady flow is then shown to apply to oscillatory flow over a broad range of the Keulegan-Carpenter number.

Section 5.5 describes a suite of measurements made above a bed of natural sand in a flume. The along-flume velocity is measured at  $0.45\text{ cmab}$ ,  $2.4\text{ cmab}$ , and  $4.9\text{ cmab}$  for six nominal flow speeds between  $5\text{ cm} \cdot \text{s}^{-1}$  and  $50\text{ cm} \cdot \text{s}^{-1}$ . All measurements are compared to LDV measurements taken concurrently. After the correction derived in the tow tank is applied to the flume measurements, there is no significant difference

---

<sup>†</sup>Some of the material presented in this chapter was originally published in *Proceedings OCEANS '96* [58].

between the BASS Rake and LDV values for the steady flow. Bed load transport was significant at the faster flow speeds and did not adversely affect the performance of the BASS Rake. The results are summarized in Section 5.6.

## 5.2 The Laboratory Prototype

The prototype is assembled on two chassis. The first is a standard BASS backplane with the transmit/receive (T/R) card removed. A jumper carrying power, logic, and analog signals on twisted pairs connects the T/R slot to the BASS Rake backplane. The T/R board is mounted on the BASS Rake backplane. Of the four T/R circuits on the board, only one is used. The MUX and address sequencer described in Chapter 3 are also mounted on the backplane and multiplex the T/R circuit to the tines through the tine board assemblies. The MUX boards support only half of each of the two {4,6} multiplexer trees. This is the optimized structure developed in Chapter 3 for connection to a single T/R circuit. The balance of the VN3205 L-sections, with capacitors in place of the absent transmission lines and transducers, are mounted on a dummy load board. The dummy load was used in all tests and demonstrated that the calculated signal loading by the MUX is accurate. 90 % to 95 % of the transducer current is delivered to the receiver load.

A heavy ground strap joins the two chassis, independently of the jumper. Both chassis are locally connected to signal and power grounds. However, the #22 ground wires of the jumper have insufficiently low impedance at  $1\text{ MHz}$  to keep the two chassis at the same high frequency electric potential. In the absence of the strap these in-band, differential EMF fluctuations add  $20\text{ mV}$  of RMS noise to the signal at the Schmitt trigger detector. This is equivalent to  $2\text{ cm} \cdot \text{s}^{-1}$  of RMS noise in the velocity measurement. The equivalence was observed experimentally using the P3 tines. It can also be established by a simple calculation. Consider that the slope,  $S$ , of the received signal, at the detector as it goes through zero, is measurable, with units of  $\text{mV} \cdot \mu\text{s}^{-1}$ . Added noise modulates the time of the zero crossing in inverse proportion to  $S$  and Equation 2.1 relates the change in time,  $\Delta t$ , to a change in

velocity,  $\Delta u$ . For an RMS signal noise voltage,  $\bar{e}_n \text{ mV}$ , the RMS noise in the velocity measurement is

$$\Delta U_{rms} = \frac{\bar{e}_n c^2}{2LS} \quad (5.1)$$

where  $c$  is the acoustic sound speed and  $L$  is the path length.  $S$  is typically in the range  $5000 \text{ mV} \cdot \mu\text{s}^{-1}$  to  $10000 \text{ mV} \cdot \mu\text{s}^{-1}$ . The strap reduces the dual chassis contribution to the established  $0.3 \text{ mm} \cdot \text{s}^{-1}$  Johnson noise floor of BASS. In the future, it will be possible to assemble the BASS Rake on a single backplane and chassis and this problem will be eliminated. Schematic wiring diagrams of the circuit boards and the backplane, along with further information about the dual chassis construction, can be found in Appendix B.

A single pair of P2 tines spaced a nominal  $15 \text{ cm}$  apart and oriented with the acoustic axes at  $45^\circ$  to the direction of flow was used to make all of the measurements described below. Each tine supports four  $6 \text{ mm}$  transducers located  $0.45 \text{ cm}$ ,  $1.2 \text{ cm}$ ,  $2.4 \text{ cm}$ , and  $4.9 \text{ cm}$  from the end of the tine. Consistent with the tine and transducer designations defined in Chapter 3, the tines are denoted A and C and the transducers are numbered 0 to 3 from the bottom. The along-axis velocity is defined to be positive from A to C. All tow tank runs were performed in both directions to check for asymmetry. A negligibly small bias was observed (Section 5.4). Tine A was placed upstream during the unidirectional flume testing. The acoustic path at  $1.2 \text{ cm}$ , A1-C1, operated only intermittently and those measurements are not reported here. The failure mechanism is related to the fragile nature of the miniature shielded wire used for the P2 transmission lines.<sup>1</sup> The tines have a halfround cross-section with a diameter, the width of the flat face, of  $1 \text{ cm}$ . The mechanical construction of the tines is described in Chapter 2 and the acoustic characteristics of the transducers are described in Chapter 4. A photograph of a single P2 tine is shown in Figure 5.1.

During the tow tank and flume tests described here the tines were rigidly mounted to a horizontal bar attached to a light rectangular frame. The bar was oriented at an angle of  $45^\circ$  to the sides of the frame and the sides of the frame were oriented parallel

---

<sup>1</sup>Shielded wire is not required for operation because of the cross-channel isolation provided by the layered multiplexer and will probably not be used in the final design.

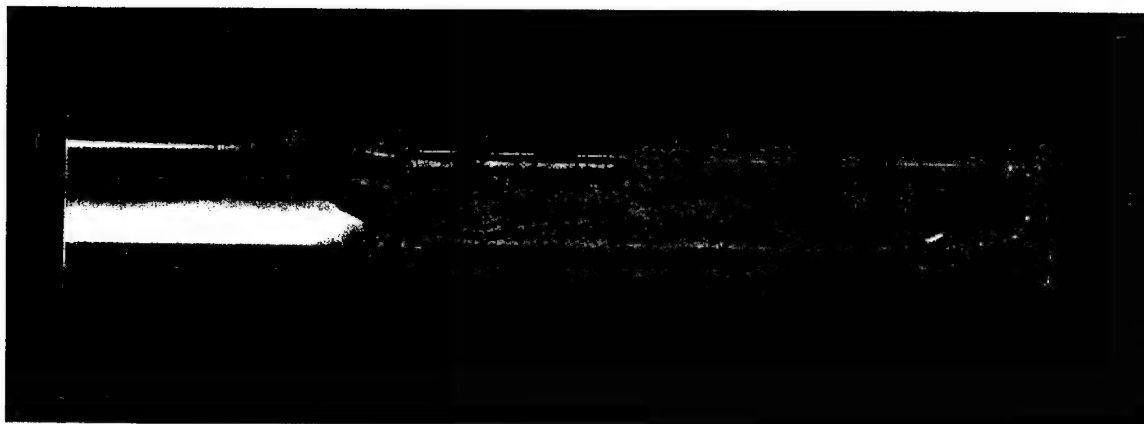


Figure 5.1: P2 TINE SHOWING TRANSDUCERS - The four 6 mm transducers are located 0.45 cm, 1.2 cm, 2.4 cm, and 4.9 cm from the end of the tine. The cross-section from the end of the tine to approximately 6 cm is halfround with a diameter, the width of the flat face, of 1 cm. Further from the end the tine is filled out with polyurethane and fully round. Photograph by Tom Kleindinst, WHOI.

to the flow during tests. The width of the frame is, by intent, a fairly precise fit to the width of the flume. Components of the frame that enter the water are sufficiently small and far away that they do not distort flow in the neighborhood of the tines. The vertical position of the bar relative to the frame can be adjusted continuously along sliders. The BASS Rake backplane and chassis were rigidly fixed to the tine bar and moved with it relative to the frame. This was done so that the transmission lines of the tine board assemblies could be immobilized relative to the tines, MUX, and T/R boards. The immobilization is essential to accurate calibration as described in Chapters 2 and 3. The separate BASS chassis was attached to the test frame.

During tow tank tests the height of the bar was adjusted to keep the tine mounting blocks, a 3 cm square cross-section, above the water surface. A line level taped to the bar was used to align the acoustic axes with the water surface. In the flume the bottoms of the tines were in contact with the sand bottom and the acoustic axes were therefore aligned with the bed. The water depth in the flume tests kept the mounting blocks above the water surface. In all flume tests there was some vibration of the tines, leading to elevated noise levels in the measurement. The vibrations appeared to be caused by the nearby operation of heavy machinery. The test frame was too light

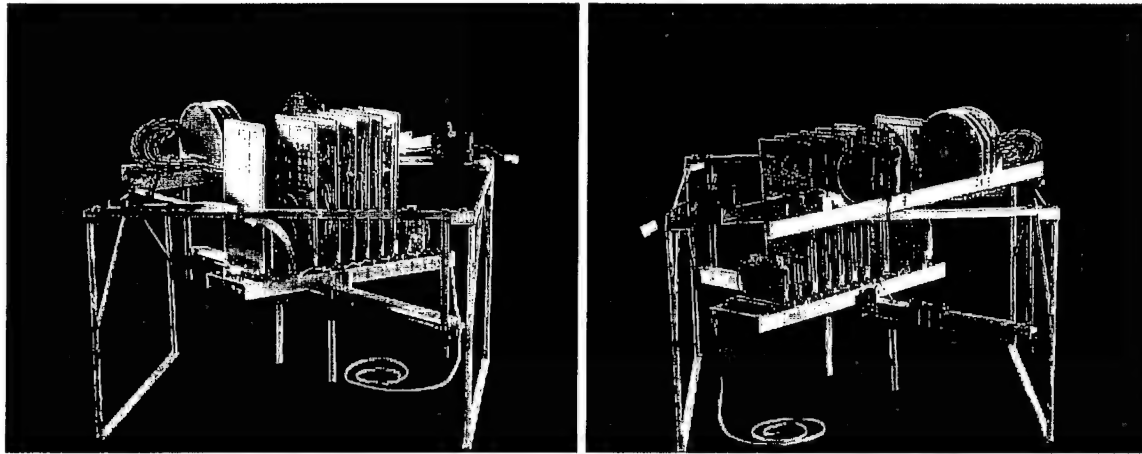


Figure 5.2: BASS RAKE LABORATORY PROTOTYPE - The BASS Rake backplane holds the large, rectangular circuit boards and is mounted on the vertically adjustable, horizontal tine bar. The P2 tines are visible, extending down from the bar. The D shaped circuit boards are mounted on the BASS backplane, which is attached directly to the test frame. The frame is 60 cm wide and 35 cm tall. The looping jumper of twisted pairs is visible in both views. The heavy ground strap connecting the chassis can be seen in the view on the left, running along the upper cross bar of the frame. The braided strap coiled beneath the frame is an electrode connecting power and signal grounds to the water. Photograph by Tom Kleindinst, WHOI.

to prevent the excitation. Isolated front and rear views of the laboratory prototype, mounted on the test frame, are shown in Figure 5.2.

The velocity measurement at each level, inclusive of both normal and reverse cycles, requires  $320\ \mu s$  [90]. During P3 testing, acoustic echos from the sidewalls of a small laboratory tank were observed to interfere with and distort the received signal. A delay of 1 ms between N/R pairs was added in software to allow time for acoustic reverberations to expire. Although not strictly necessary with the narrow beam of the P2 transducers, the delay remained in the software as a precaution. A profile therefore requires 4 ms to complete. Profiles were obtained at 1 Hz during all tow tank and flume tests. In the tow tank the duration of data acquisition varied with the speed of the run. The duration of data acquisition for all flume runs was six minutes. Historically, an average over six minutes has been necessary to suppress most flow variations in the flume [82]. The data presented in Section 5.5 will demonstrate both the variable nature of the flume and the benefits of multiple sampling volumes

on short and long time scales.

A nanosecond delay circuit [92] was used to precisely calibrate the conversion within the BASS receiver/detector from differential arrival time to velocity. This is a fixed constant for the electronics once assembled. The conversion from along-axis fluid velocity to differential arrival time was determined by measuring the transducer separation and the speed of sound. This relationship is described by Equation 2.1. The sound speed was determined by measuring temperature and applying the formula of MacKenzie at zero salinity [43]. The normal conversion for path length and sound speed, based on a 15 *cm* path length and a sound speed of  $1485 \text{ m} \cdot \text{s}^{-1}$ , differs from the measured conversion by approximately 1 %. The more precise value is used here to reduce uncertainty in the evaluation of the prototype. A geometric conversion for the  $45^\circ$  orientation of the acoustic axis to the flow is straightforward. This three part calibration constant, hereinafter the “standard calibration”, was applied to all velocities reported from the tow tank and flume tests. It is strictly accurate to regard these reported velocities simply as the along-stream velocity measured by the BASS Rake. A Reynolds number dependent correction to the measured velocities will be discussed in subsequent sections.

### 5.3 Modeling the Flow Distortion

The tines of the BASS Rake are physically intrusive and necessarily distort the flow. The velocity returned by the sensor is an accurate measurement of the disturbed, rather than the undisturbed, flow field. It is the degree of flow distortion, not the precision of the DTT measurement, that limits sensor accuracy. The extent of the flow disturbance and the magnitude of its effect on the measurement can be estimated with a simple model. Consider the case shown in Figure 5.3. The tines are modeled as circular cylinders in a uniform, two dimensional, potential (irrotational, inviscid) flow,  $U$ .  $U$  is oriented at  $45^\circ$  to the line connecting the cylinders.

The uniform velocity field is distorted by the tines, but does not separate as it flows around them. The effect of the distortion at each point on the acoustic axis

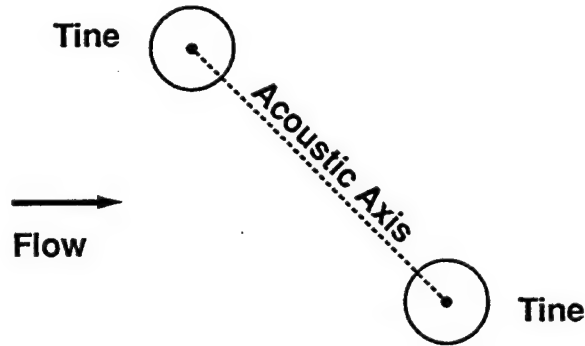


Figure 5.3: DISTORTION OF A UNIFORM POTENTIAL FLOW BY TWO ROUND TINES - The center line of the acoustic axis between the tines is oriented at  $45^\circ$  to a uniform flow from the right. Flow is distorted around the tines, but does not separate. The effect of the distortion at each point on the acoustic axis is to twist the velocity vector counterclockwise towards an alignment perpendicular to the axis. This reduces the along-axis component of the velocity and biases the measurement low. The figure is not drawn to scale.

is to twist the velocity vector counterclockwise towards an alignment perpendicular to the axis. This reduces the along-axis component of the velocity and biases the measurement low. The magnitude of the bias can be calculated. Let  $r_t = 0.5 \text{ cm}$  be the radius of the tines and  $L = 15 \text{ cm}$  be the separation of their centers. For these values  $\left(\frac{r_t}{L}\right)^2 \approx 10^{-3} \ll 1$ . Therefore, the two flow distortions interact only weakly and the dipole potential functions describing the tines can be treated independently. The along-axis velocity,  $u_{axis}(r)$ , where  $r$  runs from 0 at the center of one tine to  $L$  at the center of the other, can be written down by inspection [5, 39].

$$u_{axis}(r) = \frac{U}{\sqrt{2}} \left[ 1 - \frac{r_t^2}{r^2} - \frac{r_t^2}{(L-r)^2} \right] \quad (5.2)$$

The integral of  $u_{axis}(r)$  averaged over the path length is  $u_{meas}$ , the velocity reported by BASS. Note that the length  $L$  acoustic axis includes regions of known zero flow at



each end of the path.

$$\begin{aligned}
 u_{meas} &= \frac{1}{L} \int_{r_t}^{L-r_t} u_{axis}(r) dr \\
 &= \frac{U}{\sqrt{2}L} \int_{r_t}^{L-r_t} \left( 1 - \frac{r_t^2}{r^2} - \frac{r_t^2}{(L-r)^2} \right) dr \\
 &= \frac{U}{\sqrt{2}} \left[ 1 - \frac{4r_t}{L} + \frac{2r_t^2}{L(L-r_t)} \right] \quad (5.3)
 \end{aligned}$$

The third term in Equation 5.3 is small,  $O(10^{-3})$ , compared to the leading order term and can be ignored. The leading order term,  $\frac{1}{\sqrt{2}}U$ , is the accurate, undisturbed flow along the axis.  $\frac{4r_t U}{\sqrt{2}L}$  is the expected error, approximately 13 %, in the reported along-axis velocity. Half of this,  $\frac{2r_t U}{\sqrt{2}L}$ , is caused by the twisting of the flow towards the cross-axis direction and is localized to the axis between the cylinders. The effect of the other pair of tines in a complete BASS Rake is to rotate the velocity back into alignment with the undisturbed flow. This portion of the error would be smaller in a four tine BASS Rake. The balance of the expected error,  $\frac{2r_t U}{\sqrt{2}L}$ , is due to the regions of zero flow at each end of the path. There is no flow within the tines so the ends of the acoustic path make no contribution to the integrated velocity,  $u_{meas}$ .

A more realistic representation of the flow is shown in Figure 5.4. The tines are halfround and the full length of the acoustic axis is in the water. The flow separates from the tines and wake regions form downstream of each tine. The point and angle of flow separation and the characteristics of the flow in the wake depend on the Reynolds number for the tine and the velocity,  $Re_t = \frac{Ud}{\nu}$ .  $U$  is the undisturbed velocity,  $d$  is the diameter of the tine, and  $\nu$  is the kinematic viscosity.

The simple flow model identified two distinct components of the expected measurement error. The first is caused by reorientation of the flow around the tines. The second is caused by short regions of zero contribution at both ends of the path. This result can be applied to the more realistic situation in Figure 5.4. First, it is potential flow, outside the region of fully round tines, that describes the reorientation component of the error and potential flow is generally a good approximation outside of boundary layers and wakes. The portion of the acoustic axis that would not over-

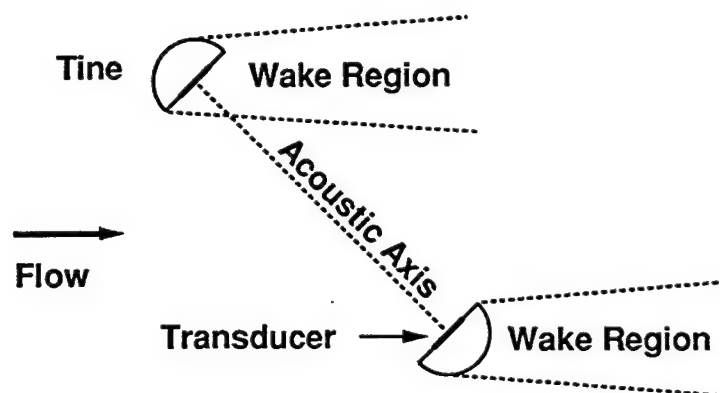


Figure 5.4: STEADY FLOW DISTURBED BY TWO HALFROUND TINES - The halfround tines of the prototype are shown here in plan view from above. The centerline of the acoustic axis is oriented at  $45^\circ$  to a uniform flow from the right. The tines are  $1\text{ cm}$  across the flat face and their separation is nominally  $15\text{ cm}$ . Flow past the tines separates and wake regions form on the downstream sides. Rough approximations to the downstream wake regions are indicated. The point and angle of flow separation and the characteristics of the flow in the wake depend on the Reynolds number for the tine and the velocity,  $Re_t = \frac{Ud}{\nu}$ .  $U$  is the undisturbed velocity,  $d$  is the diameter of the tine, and  $\nu$  is the kinematic viscosity. The figure is not draw to scale.

lap a fully round tine does not substantially intersect either a boundary layer or a wake. While the tine is no longer fully round, it is a bluff, two dimensional body with the same characteristic length scale. It is reasonable to conclude that a measurement using only the standard calibration will be approximately 7 % low due to twisting of the flow between the tines.

Referring now to Figure 5.4, the flow near the face of the downstream tine must be parallel to the face and thus makes no contribution to the average along-axis velocity. The thickness of the face parallel region depends on  $Re_t$  in general, but there is a reasonable expectation that it is scaled by  $r_t$ . The sharp lower edge of the upstream tine localizes the point of flow separation and causes a vortex or a series of vortices to form immediately in front of the face. Again, the characteristics of the vortices depend, in general, on  $Re_t$ , but there is a reasonable expectation that its size scales with  $r_t$ . A small vortex also makes no contribution to the average along-axis velocity. It is reasonable to expect an additional low bias of approximately 7 % in the measurement caused by these effects.

This line of reasoning should not be taken as a quantitative description of the flow. It is a qualitative model that provides a simple, but reasonable, structure for the testing and calibration of the laboratory prototype described in Section 5.4. Based on the argument, an additive, flow dependent, correction of 10 % to 20 % is anticipated. Expressed as a multiplicative gain correction of the measured velocity, after the standard calibration is applied, this range is approximately 1.10 to 1.25.

The empirically determined behavior of the gain correction as a function of the Reynolds number is described in Section 5.4. However, that behavior can be anticipated based on the qualitative model.  $Re_t$  is less than  $10^5$  for oceanic velocities and a 1 cm characteristic length. In that range, flow in the boundary layer around a cylinder is stable and laminar up to the point of flow separation. The angular location of that point and the characteristics of the resulting wake are known to depend on  $Re_t$  [5, 39, 66]. Consider the effect as the angular position of flow separation moves forward (upstream). The wake angle widens around the cylinder, wake vortices grow larger, and a greater fraction of the acoustic axis makes a reduced contribution to the along-axis velocity. The gain correction increases. Conversely, as the point of separation moves backwards and the wake angle narrows, less of the axis is obscured and the gain correction decreases. Recall that this is precisely the mechanism producing  $Re_t$  dependent changes in  $C_D$ , the coefficient of drag for a two dimensional bluff body. The changes have the same sense, increasing or decreasing together, and behavior qualitatively similar to published curves for  $C_D$  can be anticipated.

This mechanism also suggests the possibility of a Keulegan-Carpenter number dependence as exhibited by the drag coefficients of two dimensional bluff bodies in oscillatory flow. The Keulegan-Carpenter number is  $KC = \frac{U_m T}{d}$  where  $U_m$  is the amplitude of the flow and  $T$  is the period. As before,  $d$  is the diameter of the tine.  $KC$  is the ratio of the excursion length of the flow to the characteristic length of the body. As such, it is a measure of the degree to which the body interacts with its own wake. The increase at small  $KC$  values of the oscillatory drag compared to the steady drag ( $KC \rightarrow \infty$ ) for the same characteristic velocity and two dimensional cross-section is well documented [6, 15, 23, 52, 66, 67]. Given the intended use of

the BASS Rake in the oscillatory wave boundary layer, the characterization of a Keulegan-Carpenter dependence, if any, is particularly important.

Several comments should be made before closing this section. The second pair of tines in a four tine BASS Rake rotate the velocity vector in the central region back into alignment with the undisturbed flow. Nearer the tines, flow is still twisted towards the cross axis direction and affected by the wakes, causing a low bias. However, the obstruction of the sensor head also tends to accelerate the flow between the tines, causing a high bias. A smaller error, less than 10 %, is a reasonable expectation for the final instrument when it is oriented with the two crossing sets of axes both at a 45° angle to the streamlines. The response of the instrument as that base orientation changes will be of great interest for field deployments. The experimental determination of the cosine response of the four tine field prototype is described in Chapter 6. For azimuthal rotations within  $\pm 20^\circ$  of the base orientation the low bias of the field prototype is below 10 %, as predicted. In contrast, it has not been necessary to model or measure the cosine response of the laboratory prototype. It is intended that this instrument will always be oriented with the acoustic axes crossing the flow at a 45° angle.

Finally, the measurement error associated with the flow disturbance caused by the support structure of BASS is up to an order of magnitude below 10 %. The large difference can be attributed to the dimensionality of the flow obstructions. The largest obstructions on the BASS structure are the polyurethane encapsulated transducer assemblies [78, 90]. These are three dimensional bluff bodies with a characteristic length of 1 *cm* to 2 *cm*. The tines of the BASS Rake are a two dimensional flow obstruction with a characteristic length of 1 *cm*. The significantly larger flow disturbance of two dimensional bodies compared to three dimensional bodies of comparable size is well established.

## 5.4 Tow Tank Calibration

### 5.4.1 Steady Flow

To determine the flow dependent gain correction the laboratory prototype was towed at speeds between  $1\text{ cm} \cdot \text{s}^{-1}$  and  $50\text{ cm} \cdot \text{s}^{-1}$  in the Woods Hole Oceanographic Institution (WHOI) tow tank. The multiplicative gain correction, as defined in Section 5.3, is the ratio of the known tow cart speed to the along-tank velocity measured by the BASS Rake. The WHOI tow tank is approximately  $1.5\text{ m}$  wide,  $1\text{ m}$  deep, and  $20\text{ m}$  long. During the calibration the water was mixed as necessary to reduce stratification. Temperature stratification would have permitted the propagation of internal waves that can bias the velocity measurements at slow tow speeds. Before starting the tow cart, the internal motions of the water in the tank were always determined to be small compared to the speed of the tow. This was accomplished by introducing a dye profile at several points in the tank and making visual observations. Some patience was required before initiating the slowest tows.

The prototype was rigidly fixed to the tow cart using heavy brackets and no relative motion was observed during calibration. The tow tank and cart with the laboratory prototype attached are shown in Figure 5.5. All tows were made in both directions to correct for asymmetry in the response. A consistent but negligibly small bias was observed. Commanded tow speeds were checked during each run using a stopwatch to measure the elapsed time over a measured interval. The error in the stated speed was always below 1% and consistent with the accuracy limits of the author's operation of the stopwatch. The speed range of the tow cart is  $1.2\text{ cm} \cdot \text{s}^{-1}$  to  $90\text{ cm} \cdot \text{s}^{-1}$ . Actual tow speeds were limited to  $50\text{ cm} \cdot \text{s}^{-1}$ . This was done to avoid contamination of the results by a Froude number effect. Above  $50\text{ cm} \cdot \text{s}^{-1}$  surface deformations in the wake of the tines became significant compared to the depth of the acoustic axes below the still surface. As described in Chapter 2, using the P2 tines in the tests of the laboratory prototype was not originally intended. The P2 tines are relatively short and extend only  $11\text{ cm}$  below the mounting blocks. Surface deformations at two tow speeds are shown in Figure 5.6.

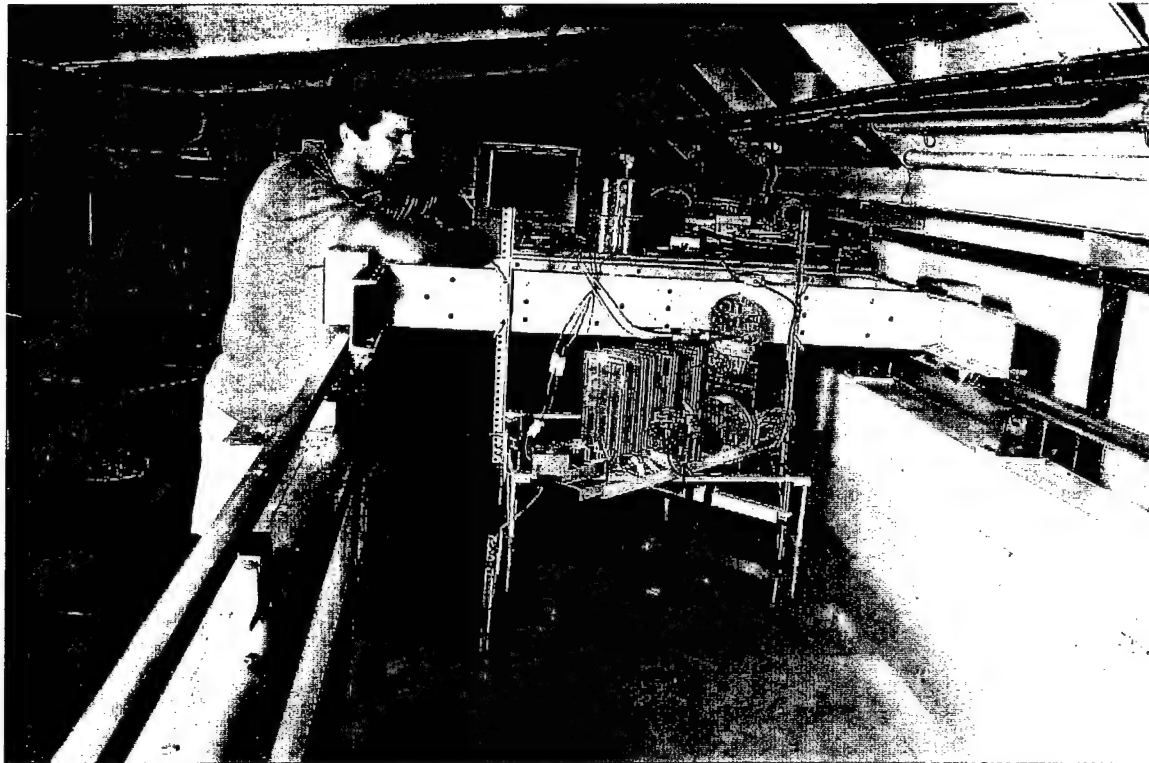


Figure 5.5: WHOI TOW TANK AND CARRIAGE WITH THE BASS RAKE LABORATORY PROTOTYPE - The view is along the tow tank. The laboratory prototype with the P2 tines immersed in the water is visible in the foreground. The frame is attached to the front of the cart by two vertical brackets. The laptop PC communicating with the TattleTale V microprocessor that controls the prototype and the batteries providing power are visible on top of the cart. The author has been included for scale. The PC controlling the cart is located on a stationary bench beyond the author. Photograph by Tom Kleindinst, WHOI.

It should be noted that the tow carriage is driven by a PC and motor controller using 8 bit integer math. As a result, the cart has a limited repertoire of trajectories and exhibits several blatantly pathological behaviors. These behaviors were identified and corrected in the course of the calibration and a clean, sequential suite of tows covering the full range of velocities under these controlled conditions was obtained at the conclusion of the procedure. While the results of all runs are reported here, the gain correction is calculated solely from those runs in the controlled suite.

The velocity records for the forward and reverse tows at  $30 \text{ cm} \cdot \text{s}^{-1}$  are shown in

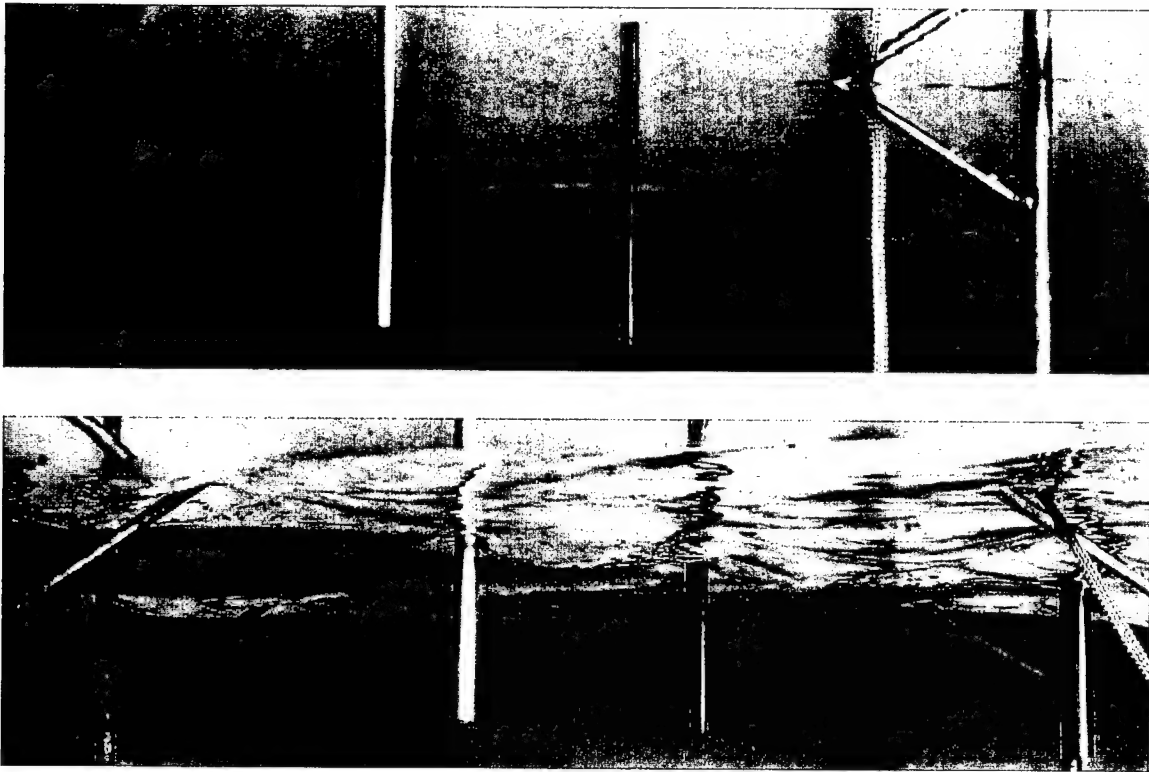


Figure 5.6: SURFACE DEFORMATION DURING TOW TANK CALIBRATION OF THE LABORATORY PROTOTYPE - The view in each panel is across the tow tank with the camera positioned slightly below the still water level. Some reflection from the underside of the surface is visible. The photographs were taken through the clear side wall of the tank as the prototype passed a fixed point during each tow. The tines extending below the surface are clearly visible. The top photograph shows the deformation of the surface at  $15 \text{ cm} \cdot \text{s}^{-1}$ . The direction of tow was to the right. A von Karman vortex street can be discerned extending to the left from each tine. The street is quite clear when viewed from above. The bottom photograph surface deformations during a  $50 \text{ cm} \cdot \text{s}^{-1}$  tow towards the left. The possibility of Froude number contamination is evident. Photograph by Tom Kleindinst, WHOI.

Figure 5.7. The standard calibration has been applied to the data. Zero offsets for each of the three axes are determined from the first 40 s to 50 s of each run, before cart motion begins. For purposes of illustration, the offsets have not been applied to the data in the figure. The zero offsets exhibited are representative. No changes were observed during testing. The gain correction is determined from the data in the latter portion of each run after the offset has been subtracted. Note that the measured along-tank velocity is on the order of 10 % low, as predicted.

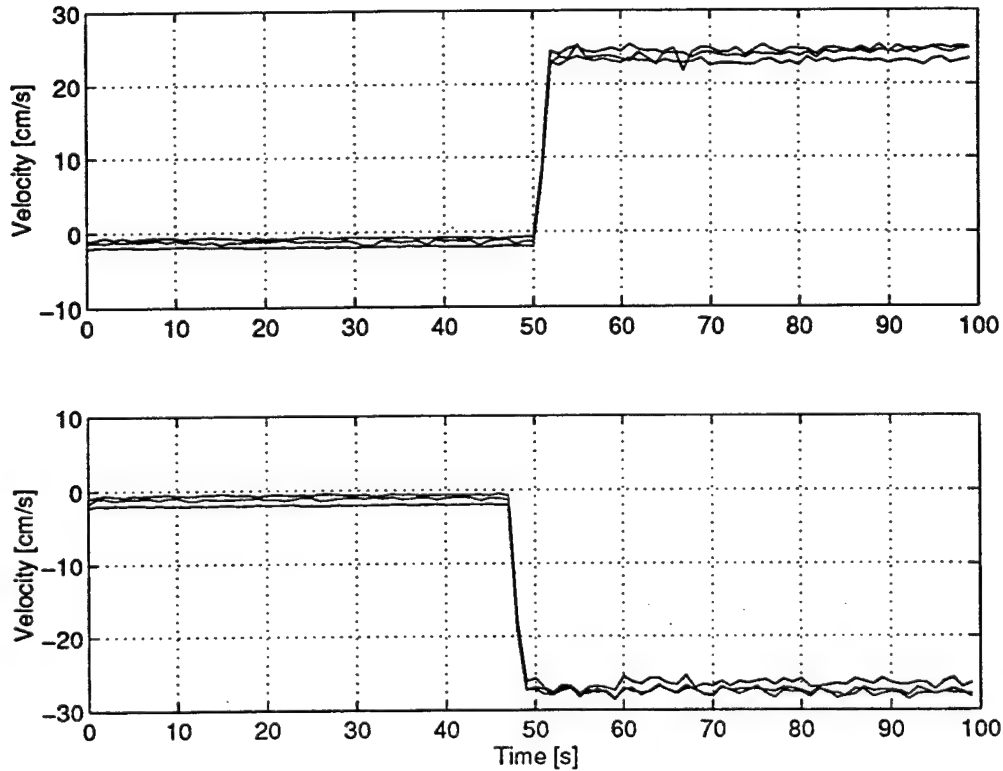


Figure 5.7: MEASURED VELOCITY DURING  $30 \text{ cm} \cdot \text{s}^{-1}$  FORWARD AND REVERSE TOWS - The velocity records of the  $0.45 \text{ cm}$ ,  $2.4 \text{ cm}$ , and  $4.9 \text{ cm}$  axes are shown after multiplication by the standard calibration. The top panel shows the forward tow and the bottom panel shows the reverse tow. The zero offsets are determined from the first  $40 \text{ s}$  to  $50 \text{ s}$  of each run, before cart motion begins. For purposes of illustration, the offsets have not been applied to the data shown here. The gain correction is determined from the data in the latter portion of each run after the offset has been subtracted. Note that the measured along-tank velocity is on the order of  $10\%$  low, as predicted.

The gain correction is defined by

$$G_{\text{corr}} = \frac{u_{\text{cart}}}{u_{\text{meas}}} \quad (5.4)$$

where  $G_{\text{corr}}$  is the multiplicative correction to be applied to the measured velocity,  $\bar{u}_{\text{meas}}$ , to recover the actual velocity,  $u_{\text{cart}}$ .  $\bar{u}_{\text{meas}}$  is an average over the three acoustic axes. It should be emphasized that it is not the DTT measurement that is inaccurate.  $u_{\text{meas}}$  is the integrated velocity between the tines to very high accuracy, approximately  $0.3 \text{ mm} \cdot \text{s}^{-1}$ . The gain correction,  $G_{\text{corr}}$ , recovers the undisturbed velocity, the veloc-



ity that would be measured by non-intrusive tines, from the accurate measurement of the disturbed flow. The gain corrected velocity is not as accurate as the DTT measurement. As stated in Chapter 3, the limiting noise floor of the BASS Rake is set by the flow disturbance, not by the electronic design. The noise floor is determined below.

Figure 5.8 shows the gain corrections calculated from Equation 5.4 for all tows plotted against  $Re_t$ . A value of  $0.01 \text{ cm}^2 \cdot \text{s}^{-1}$  was assumed for  $\nu$ , and  $d$ , the tine diameter, is  $1 \text{ cm}$ . The tow velocity,  $u_{cart}$ , is, therefore,  $\frac{Re_t}{100}$  with units of  $\text{cm} \cdot \text{s}^{-1}$ . The  $G_{corr}$  values denoted by  $\circ$  in Figure 5.8 are derived from the clean suite of tows. At each value of  $Re_t$  the upper circle is from the forward run and the lower circle is from the reverse run, indicating a small, but consistent bias. The bias may be associated with a slight asymmetry in the tine cross-sections. The originally fully round tines were carved and filed down to the halfround cross-section by hand. The bias is too small to be significant. The  $G_{corr}$  values denoted by  $+$  are derived from other tow tank runs. In the range  $Re_t \geq 3500$  the Froude number may have some effect on the data. That interpretation is consistent with the results for the field prototype presented in Chapter 6. Note that the gain corrections fall almost entirely in the anticipated range, based on the model of Section 5.3. Additionally, a smooth curve drawn through the data, the dashed line in the figure, is strikingly reminiscent of published  $C_D$  curves for two dimensional bodies with simple cross-sections in the given range of  $Re_t$  [15, 66]. The qualitative model appears to be a reasonable guide towards understanding the flow distortion caused by the BASS Rake sensor head.

A Reynolds number dependent gain correction is implicit in the calibrated response of most intrusive instruments and should not be disconcerting here. Consider, for example, the instrument developed by Sleath [71, 72] (see Chapter 2), which used the drag induced tension in a wire to sense velocity. The non-linear response of heated element sensors is another example. The dependence is a new result for BASS instruments, however, one may reasonably speculate that an effect does exist and is simply uniform and negligibly small for a standard BASS sensor. It may be that the two dimensional nature of the BASS Rake flow obstructions raises the dependence to a level

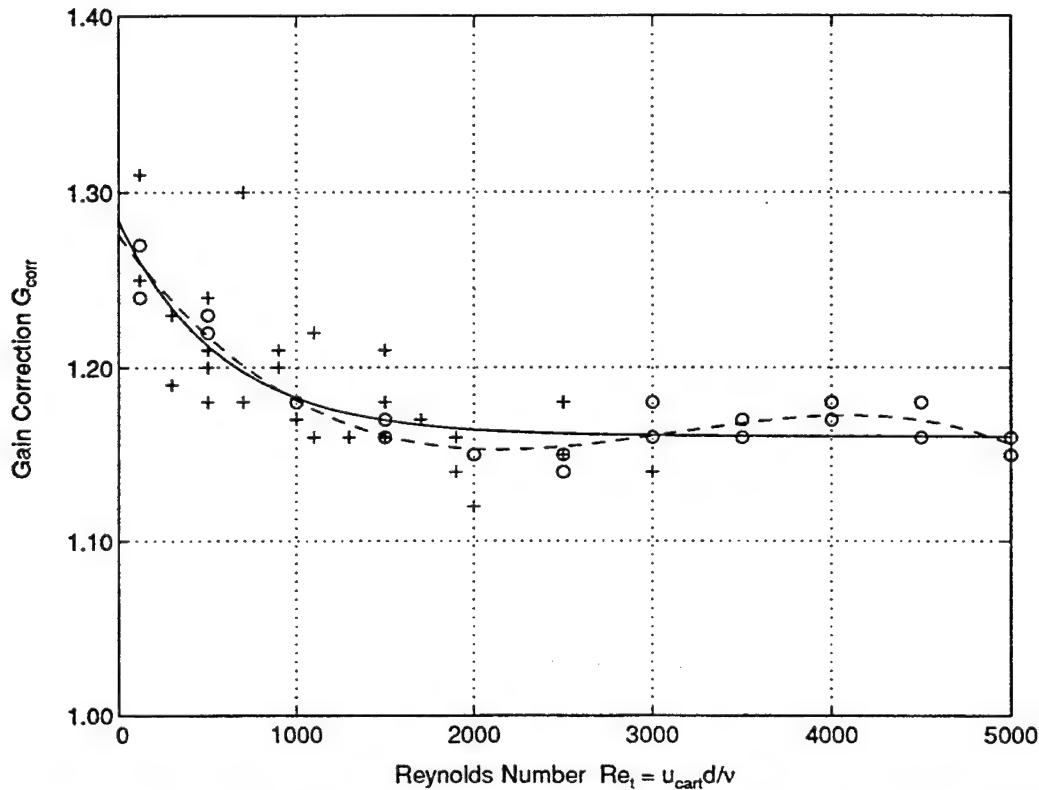


Figure 5.8: GAIN CORRECTION AS A FUNCTION OF REYNOLDS NUMBER - The gain corrections are calculated from Equation 5.4 for all tows and plotted against  $Re_t$ . The gain correction values denoted by  $\circ$  are derived from the clean suite of tows. The gain correction values denoted by  $+$  are derived from other tow tank runs. Note that the gain corrections fall in the anticipated range, based on the model of Section 5.3. The dashed line is the best fit of a cubic polynomial to the data from the clean suite of tows. The curve is reminiscent of published data for the drag coefficients of two dimensional bodies with simple cross-sections. The solid line is the best fit of an exponential form to the data from the clean suite of tows. The solid line is used to define a single-valued mapping from the measured velocity to the undisturbed velocity.

that can no longer be ignored. As with other intrusive sensors, the dependence will be incorporated into the sensor response curves during calibration. The dependence is discussed explicitly here because it is important to characterize the behavior of the sensor and to understand the sources of error in the measurement while development continues.

The solid line in Figure 5.8 is the best fit of an exponential form to the data from

the clean suite of tows. The curve is described by

$$G_{corr}(Re_t) = 0.123 \exp(-0.00172 Re_t) + 1.161 \quad (5.5)$$

The three parameters minimize the error in the least squares sense between the cart velocity,  $u_{cart}$ , and the gain corrected velocity,  $u_{gc} = G_{corr} u_{meas}$ . The curve can also be expressed in terms of the tow speed.

$$G_{corr}(u_{cart}) = 0.123 \exp(-0.172 u_{cart}) + 1.161 \quad (5.6)$$

The exponential model is preferred to the cubic polynomial shown by the dashed line in Figure 5.8 for several reasons. Intuitively, the exponential may still be applicable at higher values of  $Re_t$ . Fitted polynomials extrapolate poorly, particularly as the order of the model increases. This cubic drops quickly beyond  $Re_t = 5000$ . Froude number effects associated with the distortion of the surface may influence the measurements for  $Re_t \geq 3500$ . The exponential is flat in this region, averaging over the data rather than following the variations. The flat region of the exponential is also consistent with the calibration measurements made with the field prototype and described in Chapter 6. The long tines of the field prototype prevented Froude number contamination. Finally, the error associated with the cubic model as  $u_{cart} \rightarrow 0$  became larger than the velocity because of the uncanceled constant term. The exponential model is well behaved with a decreasing error as  $u_{cart} \rightarrow 0$ . While the actual behavior may be more complex than the exponential model, the accuracy and spread of the measurements are not sufficient to support a solution with more parameters.

The gain correction must be formulated as a mapping from  $u_{meas}$  to  $u_{gc}$  to be incorporated into the calibrated response of the instrument. The best fit exponential form based on the measured corrections from the clean suite of tows is

$$u_{gc} = 4160 \exp(2.78 \cdot 10^{-4} u_{meas}) - 4160 \quad (5.7)$$

This relationship is shown graphically in Figure 5.9.

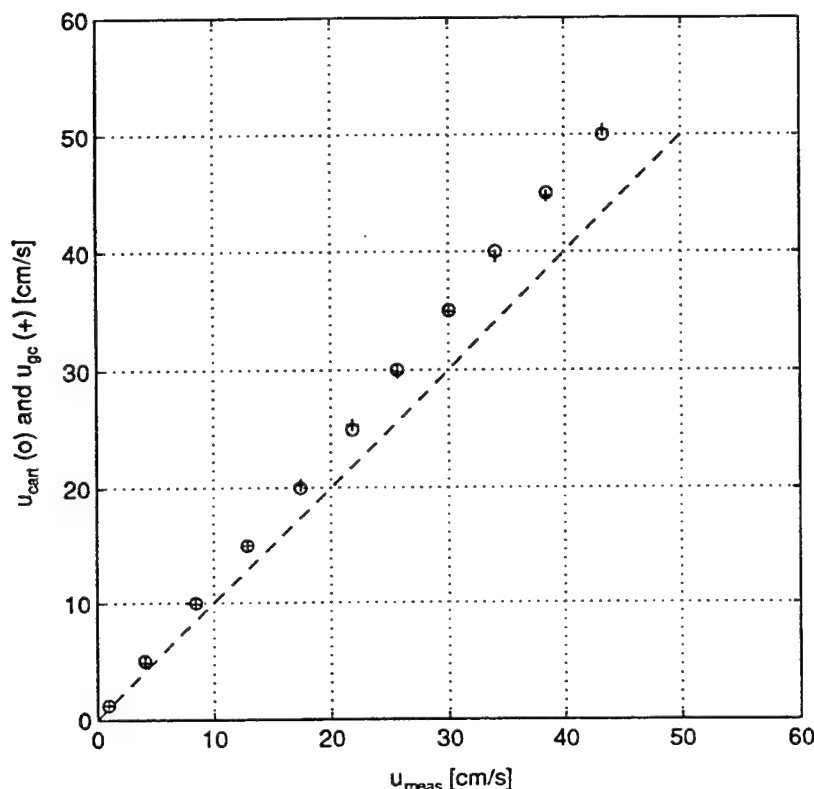


Figure 5.9: SINGLE-VALUED MAPPING FROM  $u_{meas}$  TO  $u_{gc}$  - Tow velocities,  $u_{cart}$ , are denoted by (o). The calibrated measurements,  $u_{gc}$ , calculated using Equation 5.7, are denoted by +. Both  $u_{cart}$  and  $u_{gc}$  are plotted against the raw measured velocity,  $u_{meas}$  to show the mapping graphically. The mapping is single-valued and almost linear over the range. The dashed line marks a 1:1 mapping from  $u_{meas}$  to  $u_{gc}$  for comparison.

In the figure the actual velocities,  $u_{cart}$ , and the calibrated measurements,  $u_{gc}$ , are plotted against the measured velocity,  $u_{meas}$  (standard calibration), to show the behavior of the mapping. The mapping is single-valued so there is no ambiguity in the calibrated response. It is also nearly linear in this range of  $u_{meas}$ .<sup>2</sup> A 1:1 mapping

<sup>2</sup>The best fit linear mappings,  $u_{gc} = 1.161u_{meas} + 0.0868$  and  $u_{gc} = 1.164u_{meas}$ , have the same standard deviation of the error as Equation 5.7 for this range of  $u_{meas}$ . Both are well behaved and could have been used in the laboratory prototype mapping without significant change to the results and conclusions. The exponential form was originally chosen because the shape of the  $G_{corr}$  curve suggested there would be greater non-linearity in the velocity mapping. The simplicity of the linear mappings is attractive, but the exponential form is not complicated and that form is necessary in the analogous velocity magnitude and angular orientation mapping for the field prototype. That mapping is also nearly linear for each fixed value of the azimuthal rotation angle between the flow and the tines. However, a mapping with exponential form in both the velocity magnitude and the rotation angle variables lowers the standard deviation of the error compared to a mapping that is

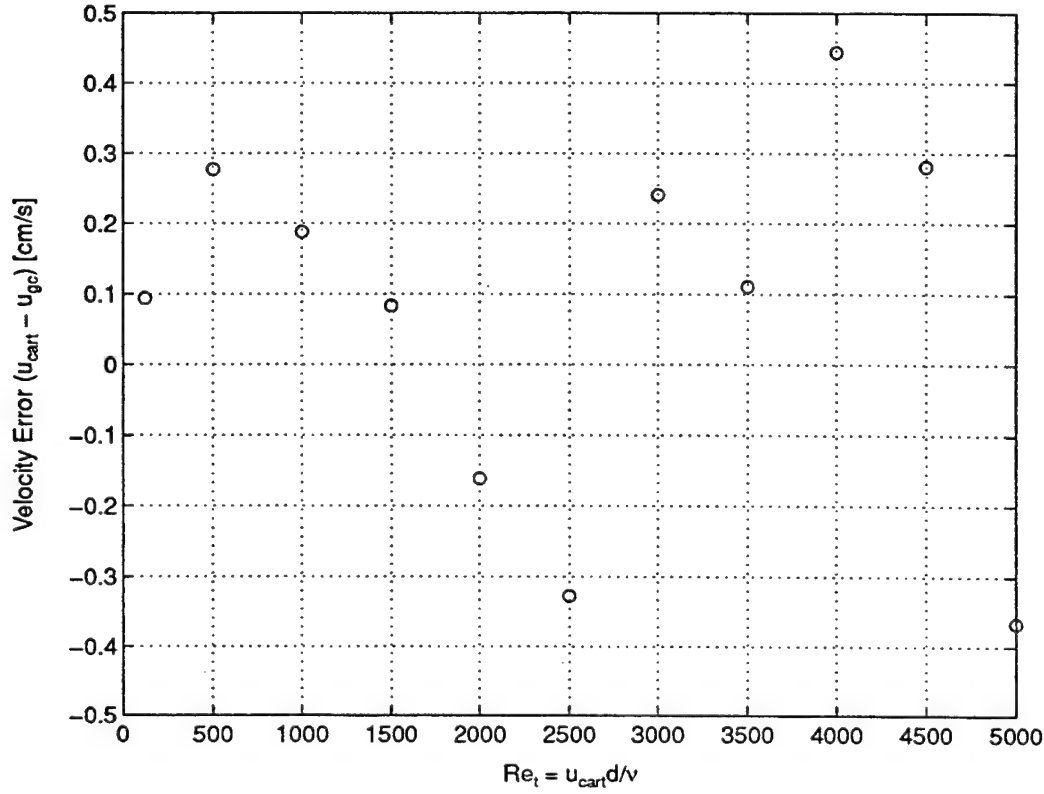


Figure 5.10: CALIBRATED MEASUREMENT ACCURACY OF THE LABORATORY PROTOTYPE - The error of the calibrated measurement is defined as  $u_{cart} - u_{gc}$ . The standard deviation of the error is  $0.26 \text{ cm} \cdot \text{s}^{-1}$ . This is a reasonable measure of the accuracy of the calibrated measurement mapping. It is comparable to, but smaller than, the standard deviations of measurements during a tow. Therefore the accuracy of the mapping does not limit the accuracy of the instrument.

from  $u_{meas}$  to  $u_{gc}$  is shown for comparison. The flume measurements reported in Section 5.5 are based on Equation 5.7 and Figure 5.9.

The error of the calibrated measurement is  $u_{cart} - u_{gc}$ . This quantity defines the accuracy of the calibrated measurement mapping for the BASS Rake laboratory prototype and is plotted as a function of  $Re_t$  in Figure 5.10.

The standard deviation of the velocity error is  $0.26 \text{ cm} \cdot \text{s}^{-1}$ . This is a reasonable measure of the accuracy of the mapping. The standard deviation of the data in Figure 5.7, which shows the measured velocity records during forward and reverse  $30 \text{ cm} \cdot \text{s}^{-1}$  tows, is  $0.07 \text{ cm} \cdot \text{s}^{-1}$  while the cart is stationary. However, during the

---

linear in the velocity magnitude variable by a factor of two to three.

tow the standard deviation is at least  $0.29 \text{ cm} \cdot \text{s}^{-1}$ . The standard deviation has some dependence on  $u_{cart}$ , but this is a representative value for all of the tows. Therefore, the accuracy of the BASS Rake is limited by the flow disturbance caused by the intrusive sensor head and not by the electronics nor by the accuracy of the instrument calibration model. The accuracy limit of the laboratory prototype is a few millimeters per second. Any future effort to improve accuracy and reduce measurement noise must first focus on reducing the flow disturbance.

### 5.4.2 Oscillatory Flow

The possibility that the gain correction for oscillatory flow might depend on the Keulegan-Carpenter number,  $KC = \frac{U_m T}{d}$ , has already been discussed. The coefficient of drag for two dimensional cross-sections differs from the steady flow,  $KC \rightarrow \infty$ , value by up to an order of magnitude as the value of  $KC$  gets small [6, 15, 23, 52, 66, 67]. Variations begin for smooth cylinders when  $KC < \approx 40$ . For some sharp-edged cross-sections differences only develop for  $KC < \approx 5 \sim 10$ . These limiting values have some dependence on  $\beta = \frac{Re_t}{KC}$  [6, 15, 23, 66, 67]. The hypothesized  $KC$  dependence was investigated using the WHOI tow tank. The PC and motor controller driving the tow carriage are not capable of generating a simple harmonic oscillation. Oscillatory motions are restricted to steeply ramping near square waves with the period and amplitude entered by the operator. The harmonics this trajectory introduces have smaller periods and amplitudes and, therefore, smaller Keulegan-Carpenter numbers than the primary. In this sense, the square wave oscillation extends the  $KC$  range of the investigation to lower values. Table 5.1 shows the excursion lengths and the Keulegan-Carpenter numbers for the period-amplitude pairs that were tested. The  $KC$  range of the tests,  $8 \leq KC \leq 600$ , includes the full range of expected continental shelf values for 1 cm tines.

The velocity records from three of the period-amplitude pairs are shown in Figures 5.11, 5.12, and 5.13. The standard calibration and Equation 5.7 mapping  $u_{meas}$  to  $u_{gc}$  have both been applied to the raw data. A  $KC$  range from 8 to 100 is represented.

Amplitude [cm · s <sup>-1</sup> ]	Period [s]				
	2	4	6	10	20
2	– –	4 8	6 12	– –	– –
5	5 10	10 20	– –	– –	– –
10	– –	– –	30 60	50 100	100 200
20	– –	– –	60 120	100 200	200 400
30	– –	– –	90 180	150 300	300 600

Table 5.1: KEULEGAN-CARPENTER NUMBERS FOR OSCILLATORY TOW CART MOTIONS - The PC and motor controller driving the tow carriage are not capable of generating a simple harmonic oscillation. Oscillatory motions are restricted to steeply ramping near square waves with the period and amplitude entered by the operator. The table shows the excursion lengths in centimeters (upper-left entries) and the Keulegan-Carpenter numbers (lower-right entries) for the period-amplitude pairs that were tested. The  $KC$  range of the tests,  $8 \leq KC \leq 600$ , includes the full range of expected continental shelf values for 1 cm tines. Deviations from the steady ( $KC \rightarrow \infty$ ) coefficient of drag occur, for some two dimensional cross-sections, when  $KC < \approx 40$  [6, 15, 23, 66, 67]. Equation 5.7, derived under steady flow conditions, provided an accurate calibration for the oscillatory tows over the full range of the Keulegan-Carpenter number.

The records show no systematic bias in  $u_{gc}$ , the calibrated velocity measurement. Systematic bias is also absent from the  $KC$  trials that are not shown here. These measurements demonstrate that the Keulegan-Carpenter number dependence of the laboratory prototype is negligible over the expected range of surface gravity wave periods and near-bottom wave orbital velocity amplitudes on the continental shelf. The mapping described by Equation 5.7 is suitable for both steady and oscillatory measurements made with the laboratory prototype. The standard calibration and the mapping are both applied to the flume boundary layer measurements described in Section 5.5.

It is possible that the  $KC$  independence of the response is owed to the sharp edges of the halfround tine cross-sections. This would be consistent with the published literature for the drag coefficients of some two dimensional bodies with sharp edged cross-sections [23, 66]. As described by Graham [23], the sharp edges fix the point of

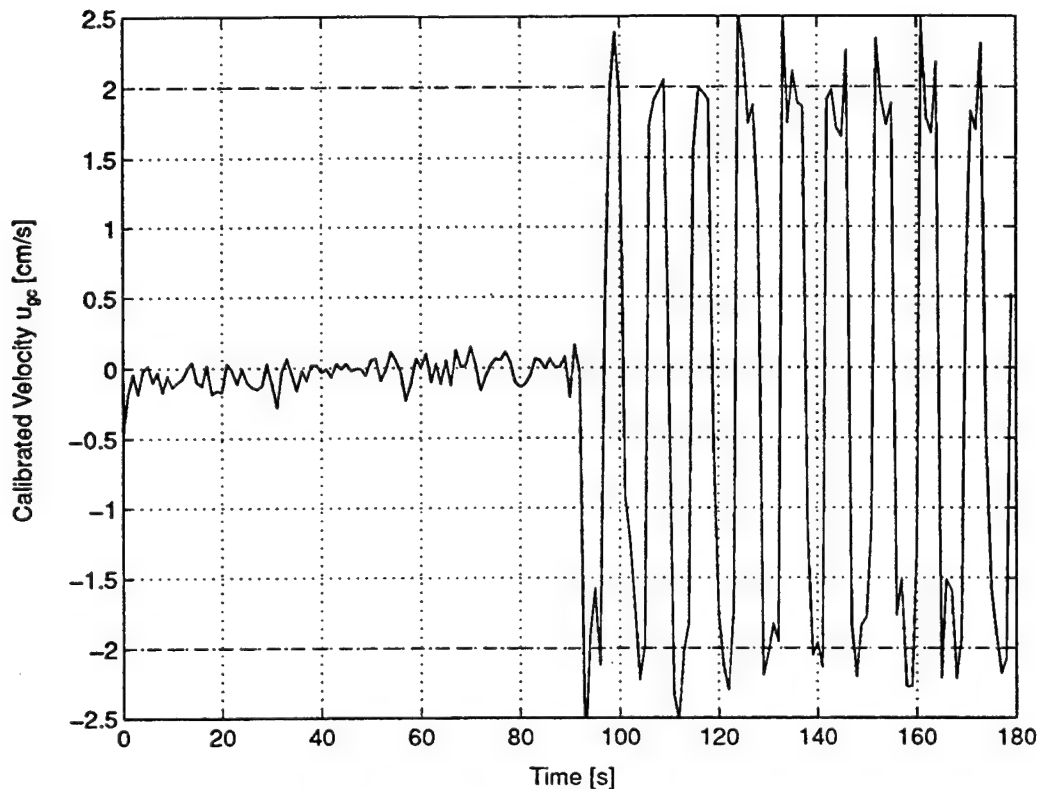


Figure 5.11: CALIBRATED RESPONSE IN OSCILLATORY FLOW AT  $KC = 8$  - The commanded period and amplitude for this run were  $4\text{ s}$  and  $2\text{ cm} \cdot \text{s}^{-1}$ . The dashed lines near the top and bottom of the plot mark the nominal amplitude of the carriage velocity. The calibrated velocity measurement does not exhibit a systematic error.

flow separation and exercise some control over the angle of the wake, shifting the  $KC$  dependence towards lower values. The round cross-section was originally chosen so that the characteristics of the wake would not change drastically with the orientation of the sensor head to the flow. The round shape might also flatten or stabilize the  $Re_t$  dependence by removing the path length ambiguity. However, the analysis of Section 5.3 and the observations in this section have shown that it is the shape of the tine that now limits reduction of the noise floor. Smoother or tapered cross-sections might reduce noise, but only for a restricted range of the flow orientation. This would make the instrument more difficult to use in the field. The added polyurethane used to shape the tine would attenuate the signal and might refract the beam. For smooth shapes the  $KC$  dependence might become significant as well. The shape of the tine



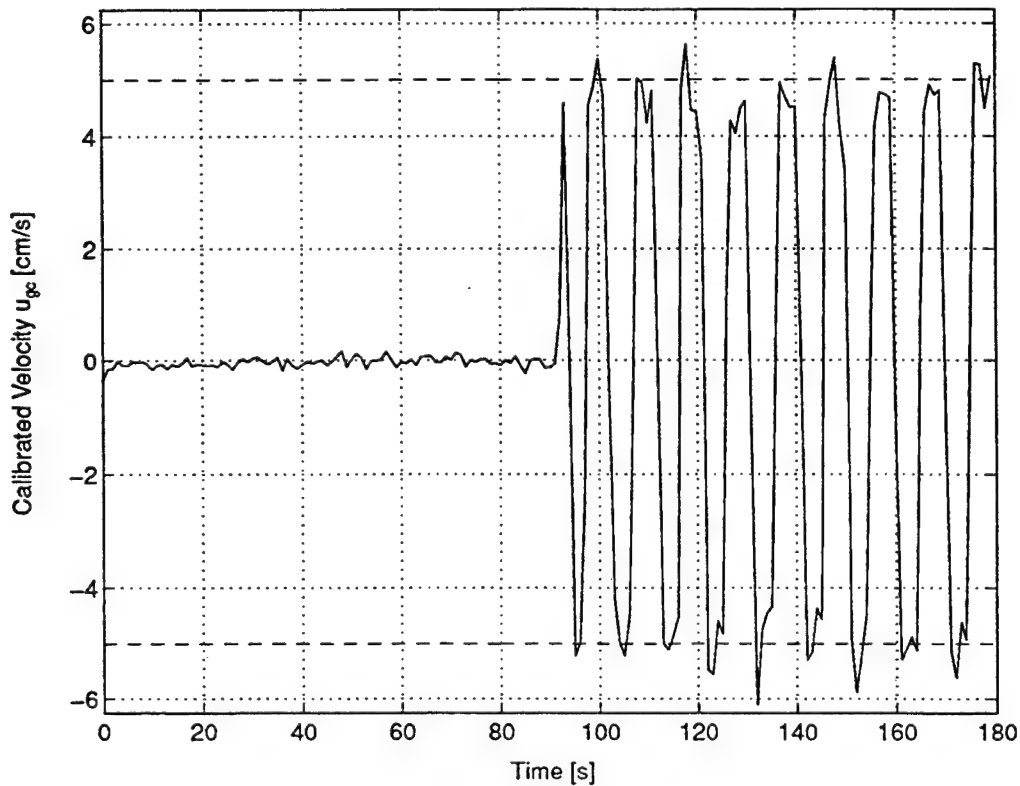


Figure 5.12: CALIBRATED RESPONSE IN OSCILLATORY FLOW AT  $KC = 20$  - The commanded period and amplitude for this run were  $4\text{ s}$  and  $5\text{ cm} \cdot \text{s}^{-1}$ . The dashed lines near the top and bottom of the plot mark the nominal amplitude of the carriage velocity. The calibrated velocity measurement does not exhibit a systematic error.

cross-section is an area for future investigation.

## 5.5 Flume Measurements Over a Sand Bed

### 5.5.1 Test Conditions and Equipment

The flume tests were conducted in the WHOI  $17\text{ m}$  flume, located in the Coastal Research Laboratory (CRL). The hydrodynamic behavior of the flume has been well characterized by Trowbridge, *et al.* [82]. The flume is  $60\text{ cm}$  wide with smooth walls. The light support frame of the laboratory prototype was designed to fit this dimension. The bottom of the flume was covered to a depth of approximately  $6\text{ cm}$  with natural sand obtained from a local harbor. The median grain size of the sand was

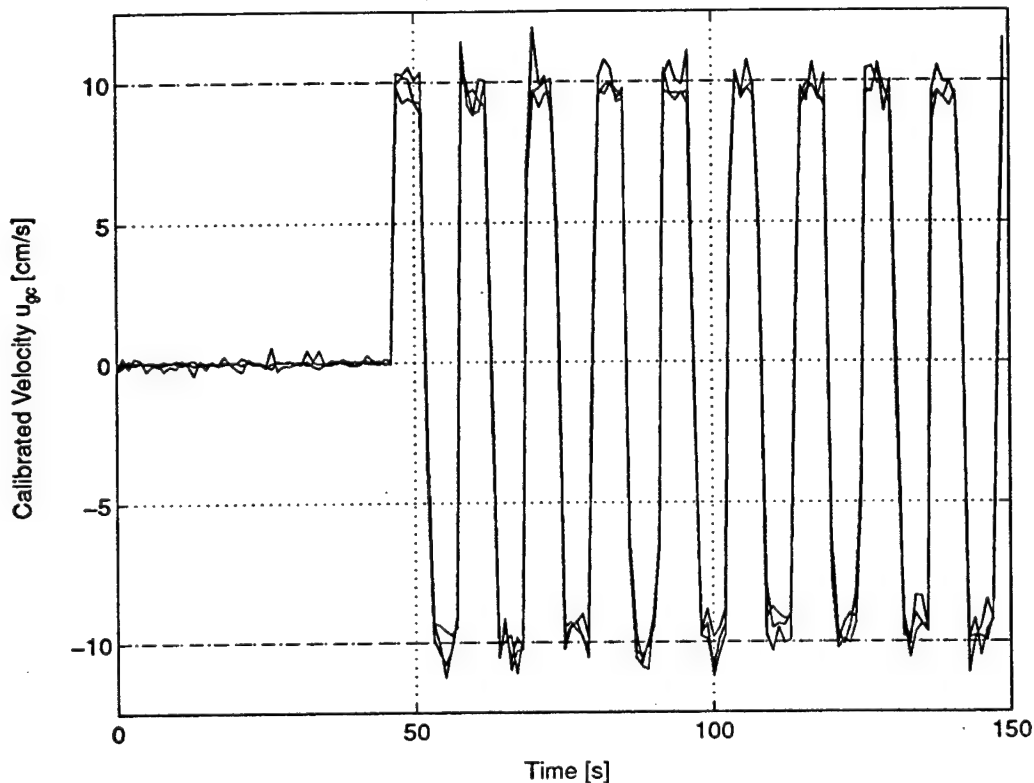


Figure 5.13: CALIBRATED RESPONSE IN OSCILLATORY FLOW AT  $KC = 100$  - The commanded period and amplitude for this run were 10 s and  $10 \text{ cm} \cdot \text{s}^{-1}$ . The dashed lines near the top and bottom of the plot mark the nominal amplitude of the carriage velocity. The calibrated velocity measurement does not exhibit a systematic error.

$\approx 250 \mu\text{m}$  [20]. The base of the support frame rested on the flume bottom beneath the sand and remained fixed for the duration of the experiment. The bed was smoothed and leveled at the beginning of the experiment and the tines were adjusted vertically such that both ends were in contact with the bed and the acoustic axes were parallel to the sand. After this initial adjustment, the position of the tines relative to the frame remained fixed for the duration of the experiment. The sand was free to move under the influence of the flow and bedload transport, with attendant bedform formation, migration, and growth, were significant at the faster flume speeds. Water depth relative to the initially flat sand bottom was kept within  $\pm 4 \text{ mm}$  of  $10 \text{ cm}$  at all speeds. This depth kept the acoustic axes well below the surface to reduce Froude effects without immersing the  $3 \text{ cm}$  square tine mounting blocks and creating a se-

vere distortion of the flow. Several photographs of the flume and the equipment are presented below.

Tests were conducted at six velocities, nominally  $8 \text{ cm} \cdot \text{s}^{-1}$ ,  $14 \text{ cm} \cdot \text{s}^{-1}$ ,  $18 \text{ cm} \cdot \text{s}^{-1}$ ,  $23 \text{ cm} \cdot \text{s}^{-1}$ ,  $31 \text{ cm} \cdot \text{s}^{-1}$ , and  $47 \text{ cm} \cdot \text{s}^{-1}$ . The trials were conducted over two days and in the monotonically increasing order listed. The measurements at  $8 \text{ cm} \cdot \text{s}^{-1}$  and  $14 \text{ cm} \cdot \text{s}^{-1}$  were made on the first day and the remaining four sets were collected on the second day. Approximate speeds were chosen to span the calibrated range from  $0 \text{ cm} \cdot \text{s}^{-1}$  to  $50 \text{ cm} \cdot \text{s}^{-1}$ . The actual speeds reflect the practical difficulties involved in adjusting the bypass valve and weir for steady flow at a fixed depth. For example,  $8 \text{ cm} \cdot \text{s}^{-1}$  is the slowest stable speed with a nominal depth of  $10 \text{ cm}$ . Attempts to further reduce the flow produced depth oscillations of  $\pm 5 \text{ cm}$  with periods on the order of a minute.

The bed remained flat and there was no observable motion of the sand during the  $8 \text{ cm} \cdot \text{s}^{-1}$  and  $14 \text{ cm} \cdot \text{s}^{-1}$  runs. At  $18 \text{ cm} \cdot \text{s}^{-1}$  and  $23 \text{ cm} \cdot \text{s}^{-1}$  there was no observable transport, however, shallow pits formed under both tines. The depth of the pits was approximately  $1 \text{ mm}$ . Tines constructed to extend into the sediment, as described in Chapter 2 would not induce pitting. Surface ripples at the air-water interface were noticeable in the wakes of the tines beginning at  $23 \text{ cm} \cdot \text{s}^{-1}$ .

When the nominal flume speed was increased to  $31 \text{ cm} \cdot \text{s}^{-1}$  bedload transport was observed to be steady but light. Pitting under the tines deepened and bedforms appeared in the wakes of the tines and the vertical members of the support structure. Over time, lines of bedforms extended further downstream from these initiation points. The bedforms generated immediately behind the flow obstructions were stable over time. Lateral spreading occurred with increasing distance downstream and an irregular field of ripples and mounds gradually formed. The change in elevation from the pits under the tines to the stable ripples immediately downstream was approximately  $1 \text{ cm}$ . The change occurred over approximately  $3 \text{ cm}$  horizontally. Bedforms did not form upstream on the flat, unobstructed portion of the bed, however, bedload transport was continuous in that region. At  $47 \text{ cm} \cdot \text{s}^{-1}$  the bedload was very heavy and continuous. Organized, cross-flume ripples formed upstream and propagated

through the test section. Trough to crest elevation changes ranged from 1 *cm* to 5 *cm* over horizontal distances of 3 *cm* to 20 *cm*.

The BASS Rake was positioned 12 *m* from the flume entrance. Comparison measurements were made with a nonintrusive, two axis, laser Doppler velocimeter (LDV) positioned 1.25 *m* upstream of the BASS Rake. The CRL LDV operates in a forward scatter mode with the three beams passing through the clear side walls of the flume test section. Both instruments were in the region of fully developed flow. The LDV measurements were noticeably degraded near the bottom during bedload transport, exhibiting an enhanced rate of measurement dropout. The BASS Rake measurements were not strongly affected. During the 47 *cm · s<sup>-1</sup>* trial, the LDV measurements were made over the more organized, cross-flume ripples. It will be clear in the photographs below that these bedforms were qualitatively different from the irregular shapes closer to the BASS Rake. The contrast in bedform shapes is caused by the dissimilar mechanisms triggering formation.

The flume speed is known to fluctuate over short periods (< 1 minute), particularly at slow nominal velocities [82]. Examples of these fluctuations can be seen in the data records presented below. As mentioned in Section 5.2, historically, each measurement of flume velocity with the LDV has been an average over six minutes to suppress the fluctuations. Longer period fluctuations have also been observed and there remains some potential error in the LDV "profiles". The advantage of simultaneous measurements at multiple heights is obvious.

During each concurrent 6 minute run the LDV sampled a single height at 25 *Hz* while the BASS Rake obtained three level profiles at 1 *Hz*. The LDV height was then adjusted for the next run, leaving the flume speed constant until the LDV had built up a complete, three level, profile. The height of the LDV measurement above the local bed was carefully matched to the centerline heights of the three acoustic axes. The accuracy of the placement is estimated to be  $\pm 0.5$  *mm*, comparable to the median grain diameter. Each of the six profiles was constructed from 4.9 *cmab* down to 0.45 *cmab*, however, there is no LDV measurement at 0.45 *cmab* for the final flume speed, 47 *cm · s<sup>-1</sup>*. In the short interval between the 2.4 *cmab* and the 0.45 *cmab*

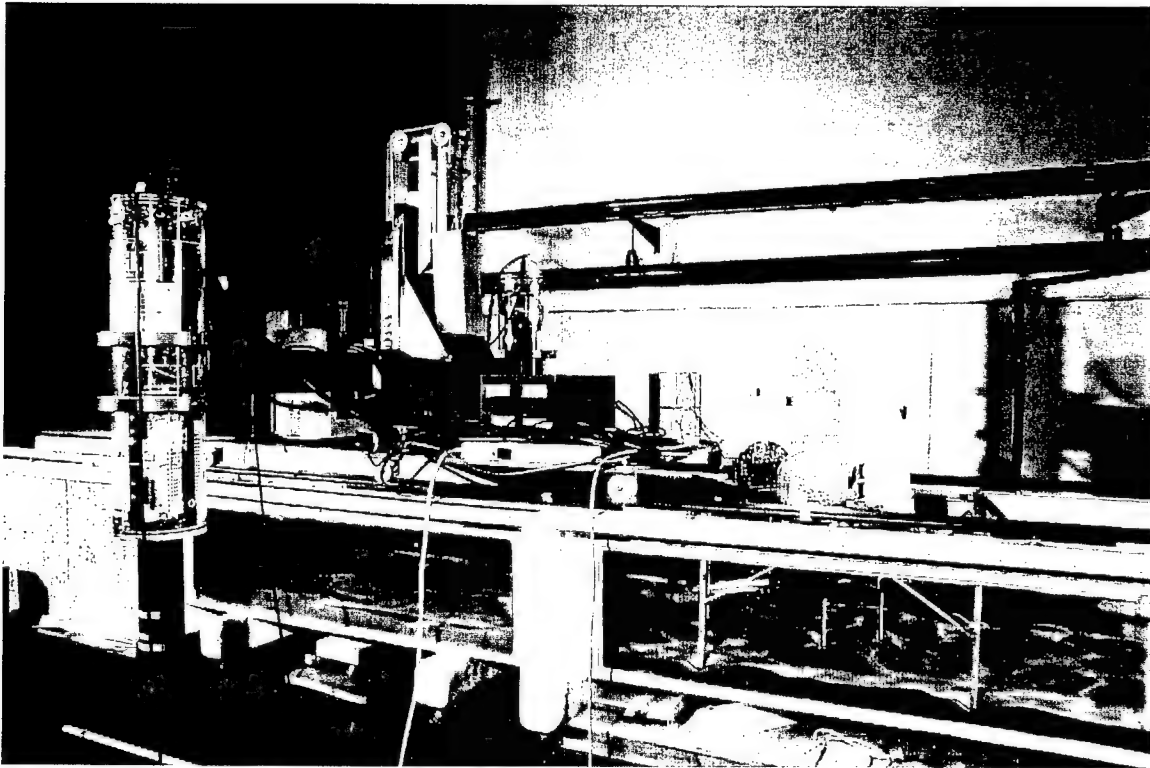


Figure 5.14: THE 17 *m* FLUME WITH THE BASS RAKE PROTOTYPE AND LDV IN POSITION - The clear side walls of the flume test section are visible in the foreground. Flow was from left to right. The transmitting and receiving towers of the LDV are visible on either side of the flume towards the left of the photograph. BASS Rake circuit boards mounted on the backplane are visible above the top of the flume side wall and towards the right of the photograph. The tines, elements of the support frame, and the bedform field are visible through the window of the test section. The along-flume separation of the two instruments is 1.25 *m*. Photograph by Tom Kleindinst, WHOI.

measurements, a gasket internal to the pump system failed and the flume was shut down for repair. Further evaluation of the laboratory prototype was foregone. Note that the BASS Rake had already recorded two measurements at the missing LDV point.

After the gasket failure, the BASS Rake, LDV, and bedforms were photographed in place and undisturbed. The bed was then smoothed and leveled, duplicating the conditions at the beginning of the experiment for additional photographs. A selection of these photographs is presented in Figures 5.14 through 5.18.

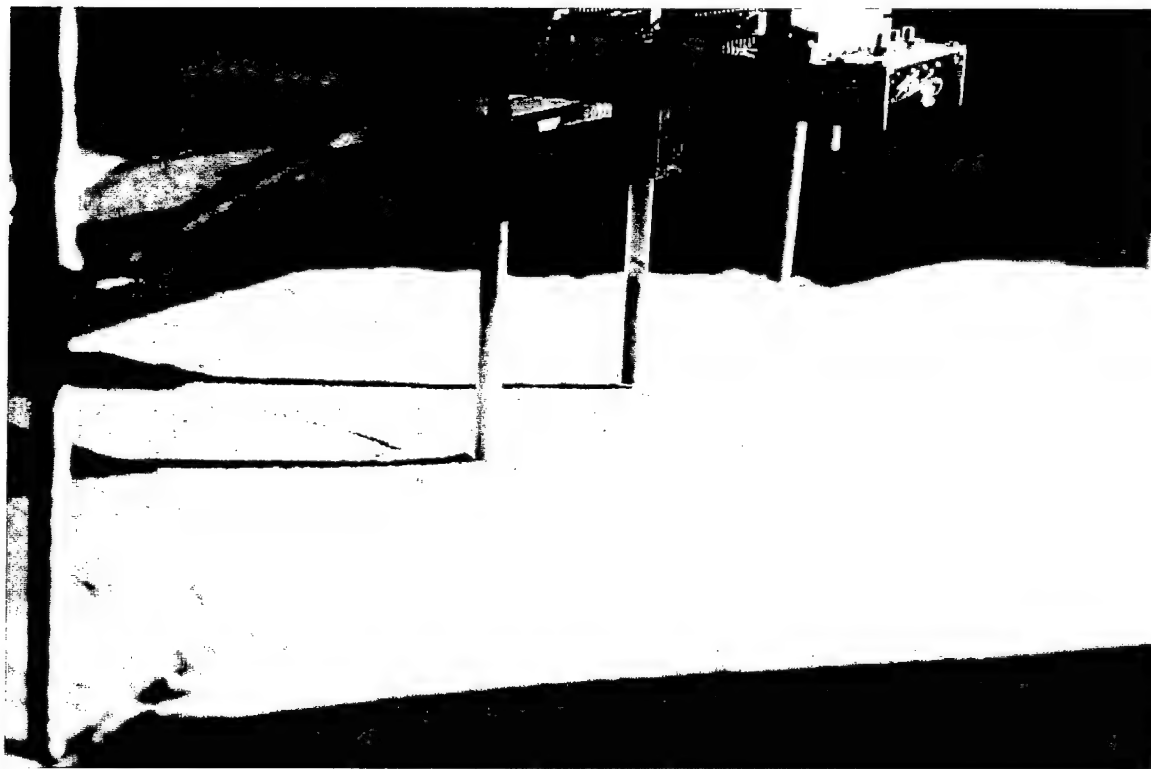


Figure 5.15: BASS RAKE TINES POSITIONED OVER A FLAT SAND BED - This is an oblique view across the flume, taken through the clear side wall. The tines are shown positioned in contact with a smoothed and leveled sand bed, duplicating the conditions of the low speed trials. The bed was manually re-smoothed after the measurement trials for this photograph. Photograph by Tom Kleindinst, WHOI.

### 5.5.2 Zero Calibration

After the photographic record was completed the BASS Rake was removed from the flume and the tines were immersed in a standing bucket of water to calibrate the zero offsets [53]. The transition from flume to bucket was accomplished with no movement of the transmission lines or the tines relative to the BASS Rake backplane. A 50 minute velocity record from the offset calibration is shown in Figure 5.19. The data shown are the raw along-axis velocities in  $cm \cdot s^{-1}$ . The geometry and gain corrections have not been applied. Note that the  $Re_t$  dependent gain correction only applies to data from which the zero offsets have been removed.

The mean values of the records are the fixed zero offsets applied to the flume

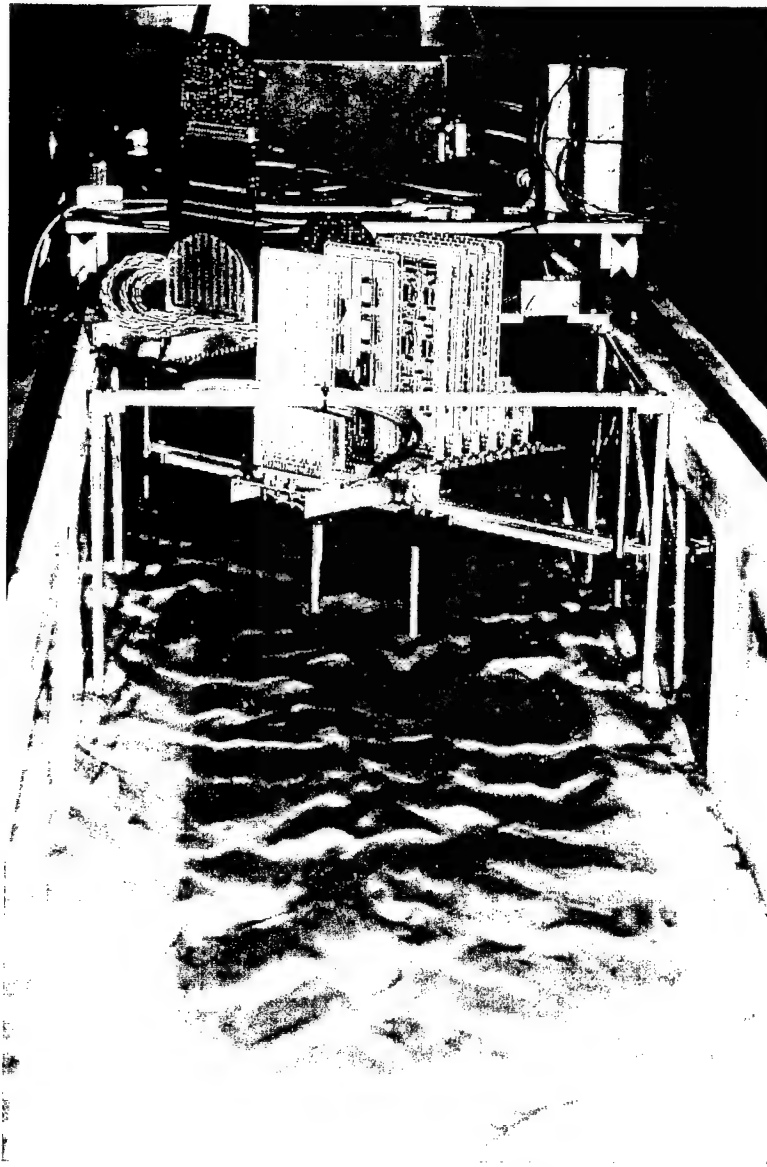


Figure 5.16: ALONG-FLUME VIEW OF LABORATORY PROTOTYPE AND THE DOWNSTREAM FIELD OF BEDFORMS - This is a view looking upstream, showing the field of irregular bedforms that developed downstream of the BASS Rake. Flow was towards the camera. The support frame, tines, and circuit boards are visible in the center of the photograph. The base of the frame is firmly mounted on the bottom of the flume and buried beneath the sand bed. Portions of the LDV are visible in the background. Photograph by Tom Kleindinst, WHOI.

measurements presented below. These offsets are fairly typical for BASS. In addition to the along-axis velocities, Figure 5.19 shows running averages taken over 100 mea-

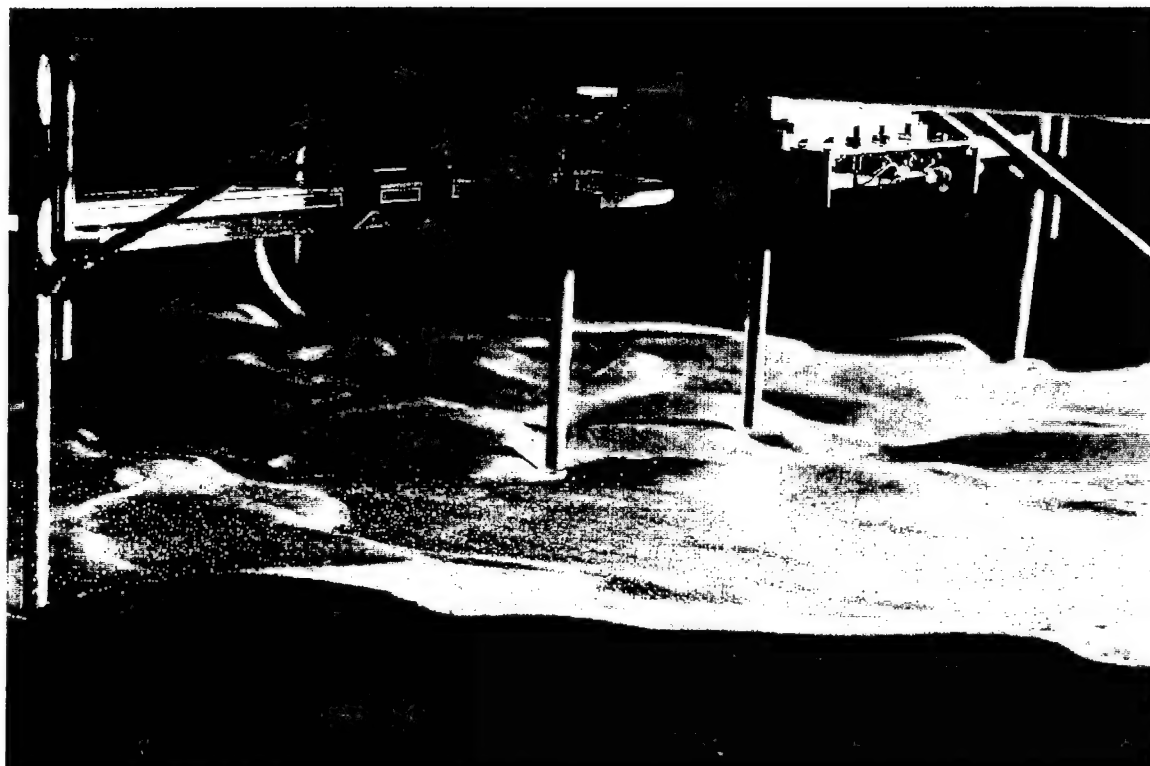


Figure 5.17: BEDFORM FIELD UNDER BASS RAKE SAMPLE VOLUMES - This is a cross-flume view showing the characteristics of the bedform field beneath the BASS Rake acoustic axes. The tines are visible in the center of the photograph. Flow was from left to right. The bedforms are disorganized and irregular compared to the cross-flume ripples beneath the LDV sample volume. Those ripples are shown in Figure 5.18. Small differences in the  $0.45\text{ cmab}$  measurements of the two instruments taken in the presence of the bedforms are consistent with the differing characteristics and the changing relative proximity of ripples and sample volumes at the two locations. Photograph by Tom Kleindinst, WHOI.

surements for each axis.<sup>3</sup> The small variations occurring on ten minute and longer time scales and most clearly visible in the running averages are velocities caused by thermal convection in the bucket. The standard deviations of the velocities around the running average are  $0.4\text{ mm} \cdot \text{s}^{-1}$  to  $0.5\text{ mm} \cdot \text{s}^{-1}$ , the electronic noise floor of the laboratory prototype. The zero velocity record from a single acoustic axis is shown in Figure 5.20 to demonstrate the velocity resolution of the laboratory prototype.

<sup>3</sup>The running averages are taken over 50 measurements in each direction of a bi-directional pass through the filter. The effective average is over 100 measurements. The bi-directional passes bring the phase shift of the averaging filter to zero. All running averages referred to in this chapter were calculated in this manner.





Figure 5.18: BEDFORM FIELD UNDER LDV SAMPLE VOLUME - This is a cross-flume view showing the characteristics of the bedform field beneath the LDV sample volume. Flow was from right to left. The receiver of the LDV is visible in the center of the photograph beyond the field. The cross-flume ripples are organized and regular compared to the bedforms that formed downstream of the BASS Rake. Those bedforms are shown in Figure 5.17. Small differences in the 0.45 *cmab* measurements of the two instruments taken in the presence of the bedforms are consistent with the differing characteristics and the changing relative proximity of ripples and sample volumes at the two locations. Photograph by Tom Kleindinst, WHOI.

### 5.5.3 Test Results and Analysis

The BASS Rake and LDV 6 minute averages at three heights for the six nominal velocities are shown in Figure 5.21. There are multiple BASS Rake measurements at each height, however, the direct comparisons are made between averages taken concurrently. The standard calibration and Equation 5.7 have both been applied to the BASS Rake measurements.

In the figure the LDV measurements are denoted by  $\circ$  and the concurrent BASS Rake measurements are denoted by  $*$ . The solid lines are logarithmic profiles based on

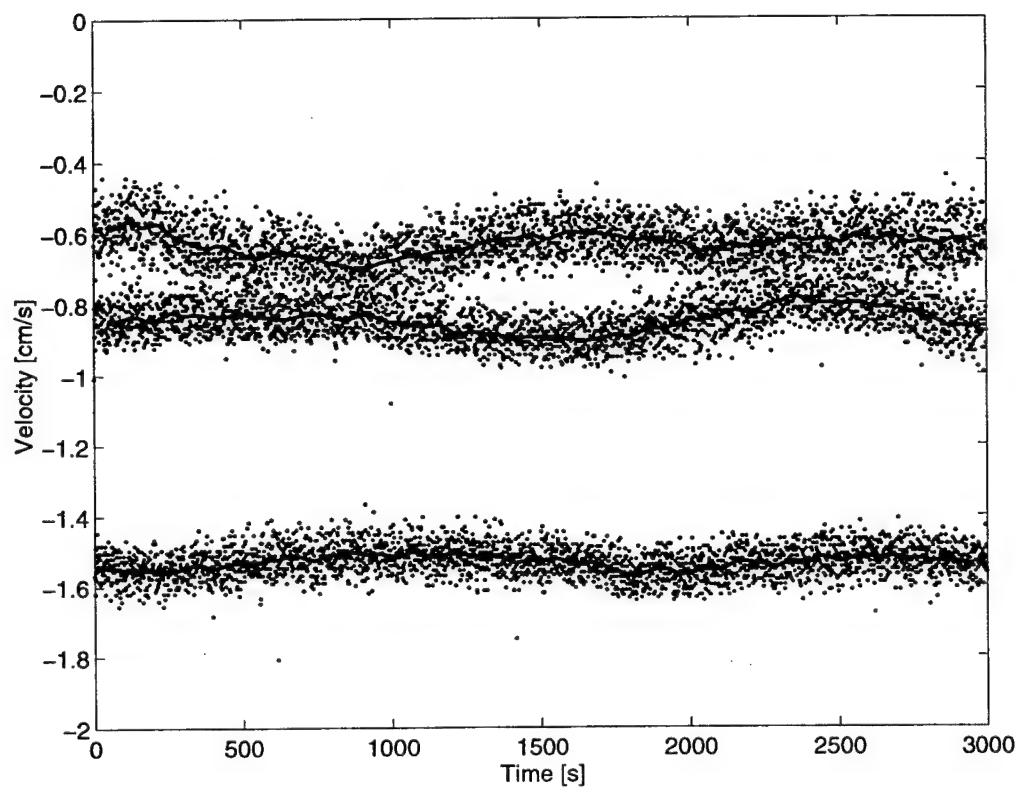


Figure 5.19: VELOCITY RECORDS FROM THE ZERO OFFSETS CALIBRATION - The dots mark along-axis velocities for the three acoustic axes. The heavy solid lines are running averages taken over 100 velocity measurements for each axis. The initial and final portions of the running averages exhibit end effects caused by the filtering process and have been removed. The mean values of the records are the fixed zero offsets applied to the flume measurements. These offsets are fairly typical for BASS. The small variations occurring on ten minute time scales and most clearly visible in the running averages are velocities caused by thermal convection in the bucket.

the LDV measurements. The calculation assumes the nominal height above bottom is accurate, rather than using an unknown offset as a fitting parameter. This is due to the focus on comparative measurements rather than further characterization of flume flow. The values of  $u_*$ , the shear velocity, and  $z_o$ , the hypothetical level of zero flow, characterize the solid lines. The value of  $z_o$  before sediment transport begins is approximately constant, particularly if the result of the slowest run is discounted. The stability of the flume velocity is known to be poorest at nominal speeds below  $10 \text{ cm} \cdot \text{s}^{-1}$ . Discounting the value of  $z_o$  for the first run is justified. Note that a calculation of the flow parameters based on the BASS Rake profiles has greater

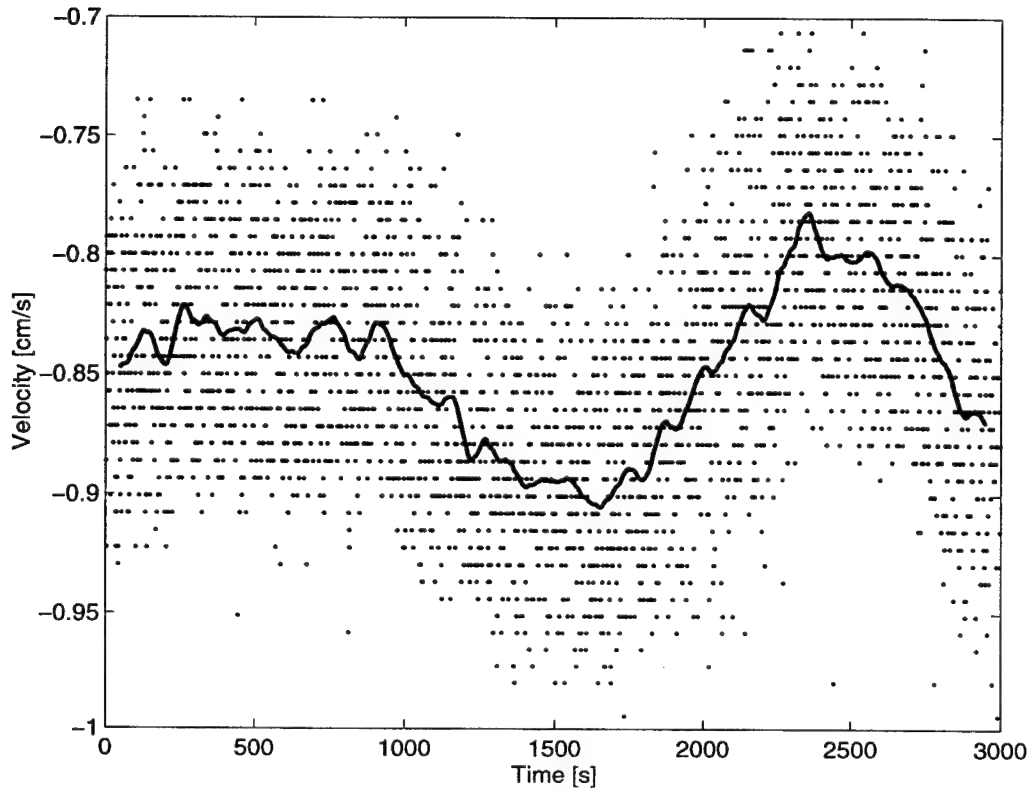


Figure 5.20: MEASUREMENT OF A  $1 \text{ mm} \cdot \text{s}^{-1}$  CURRENT DRIVEN BY THERMAL CONVECTION - The dots mark the along-axis velocity measurements and the heavy solid line is a running average over 100 measurements. The initial and final portions of the running average exhibit end effects caused by the filtering process and have been removed. The signal is a  $1 \text{ mm} \cdot \text{s}^{-1}$  current caused by thermal convection in the bucket. The plot graphically demonstrates the velocity resolution of the laboratory prototype.

immunity to errors induced by fluctuations in the nominal velocity. The increasing values of  $z_o$  at  $31 \text{ cm} \cdot \text{s}^{-1}$  and  $47 \text{ cm} \cdot \text{s}^{-1}$  reflect the movable bed roughness and the generation of bedforms. The bottom stress due to the current,  $\tau_c$ , can be determined from the shear velocity (see Appendix A).

$$\tau_c = \rho u_*^2 \quad (5.8)$$

The vertical velocity fluctuations,  $w'$ , were not measured, so an independent measure of  $\tau_c$  based on the Reynolds stress,  $-\rho \overline{u'w'}$  is not available.

The balance of the BASS Rake measurements are denoted by +. These measure-

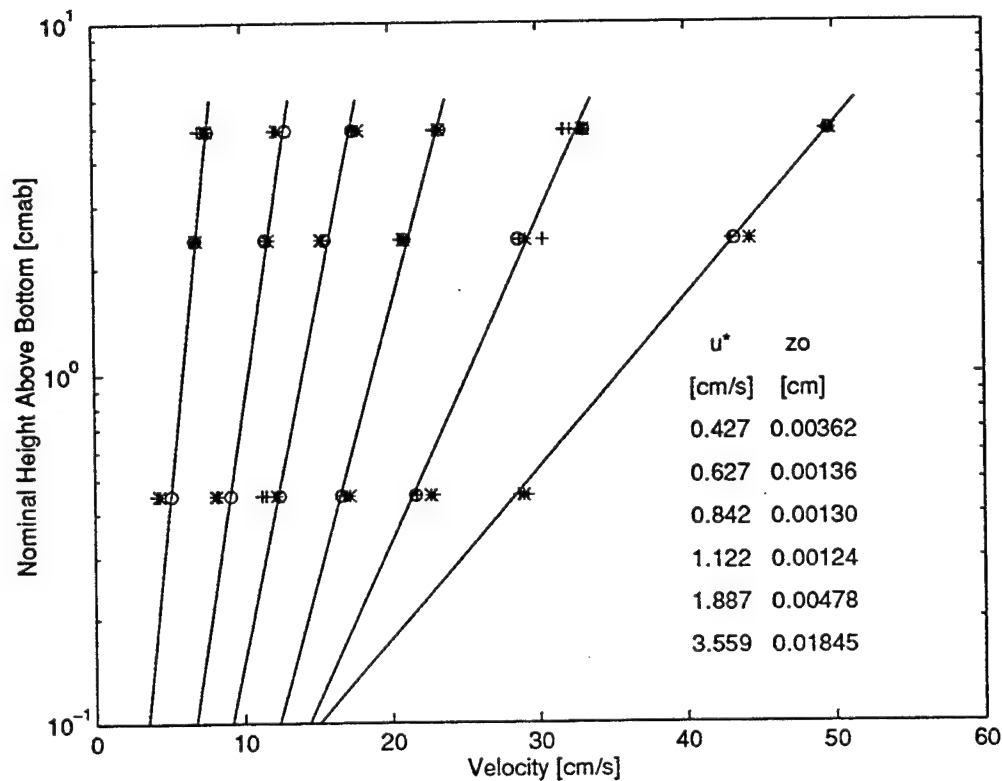


Figure 5.21: 6 MINUTE BASS RAKE AND LDV AVERAGES AT SIX NOMINAL VELOCITIES - The LDV measurements are denoted by  $\circ$ . The concurrent BASS Rake measurements are denoted by  $*$  and the balance of the BASS Rake measurements are denoted by  $+$ . The solid lines are logarithmic profiles based on the LDV measurements. The calculation assumes the nominal height above bottom is accurate, rather than using an unknown offset as a fitting parameter. The values of  $u_*$ , the shear velocity, and  $z_0$ , the hypothetical level of zero flow, characterize the solid lines.

ments demonstrate the variability of the flume over time for periods longer than six minutes. The temporal variability is small, but not insignificant. It is larger than the  $0.3 \text{ cm} \cdot \text{s}^{-1}$  noise floor set by the flow distortion of the tines. As noted above, the variation over time invalidates the constructed LDV profiles. A given BASS Rake profile, independent of the averaging time, is more accurate than a constructed profile because the velocities at all heights are measured concurrently.

The agreement between the concurrent BASS Rake and LDV measurements is high. The differences at each height and nominal velocity are shown in Figure 5.22. All of the differences are less than 5% of the local velocity except for the  $0.45 \text{ cmab}$  measurements at  $8 \text{ cm} \cdot \text{s}^{-1}$  and  $14 \text{ cm} \cdot \text{s}^{-1}$ , which are higher.

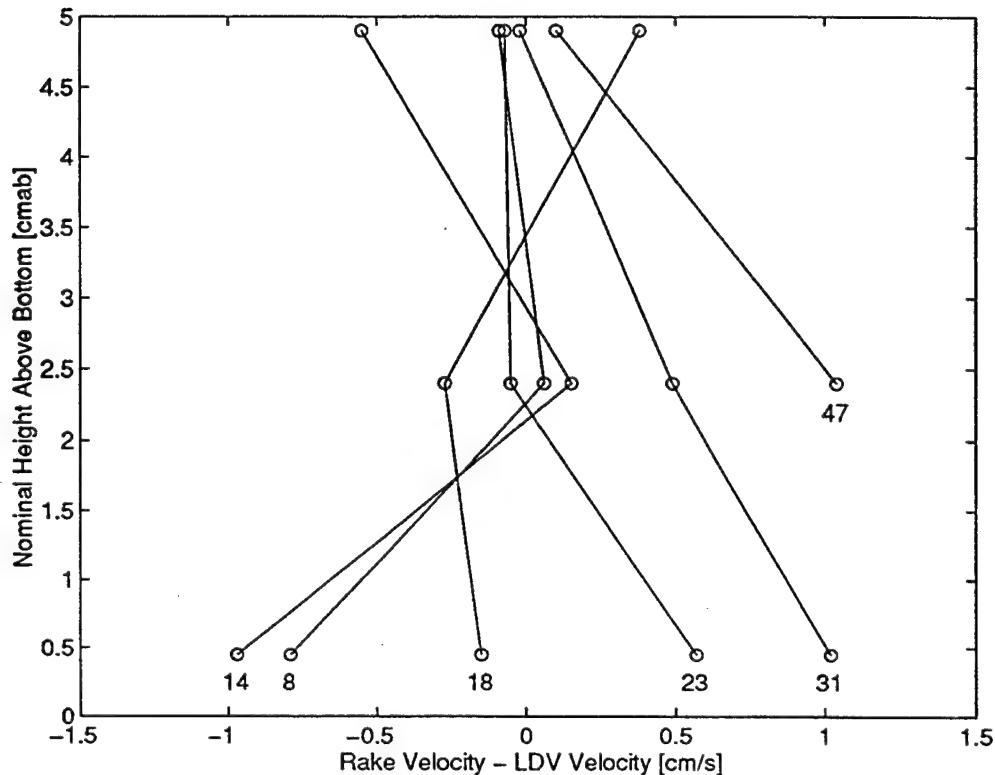


Figure 5.22: BASS RAKE AND LDV DISAGREEMENT AS A FUNCTION OF HEIGHT FOR EACH TRIAL - The difference between the concurrent velocity measurements for each height and nominal velocity is denoted by a  $\circ$ . The solid lines join data from a common trial. The nominal velocity in  $\text{cm} \cdot \text{s}^{-1}$  for each trial is indicated. All but two of the differences are less than 5% of the local velocity. The percentage for the 0.45 *cmab* measurements at  $8 \text{ cm} \cdot \text{s}^{-1}$  and  $14 \text{ cm} \cdot \text{s}^{-1}$  is approximately 10%.

The differences in the concurrent velocities can be largely attributed to local variations in the flow. At 2.4 *cmab* and 4.9 *cmab* the differences are confined to the two trials with significant bedform generation. The large variations in local topography along the flume are visible in Figures 5.14 through 5.18. It should be emphasized that the local variations are also temporal on scales both shorter and longer than six minutes. An example of bedforms propagating past the BASS Rake tines during a measurement averaging period and altering the steady value of the flow will be presented below.

The differences in the 0.45 *cmab* measurements have several causes. No bedforms were generated and no pitting occurred beneath the tines during the  $8 \text{ cm} \cdot \text{s}^{-1}$  and

$14 \text{ cm} \cdot \text{s}^{-1}$  trials. However, the differences can be brought close to zero by assuming the BASS Rake measured velocities  $0.5 \text{ mm}$  closer to the sand than the LDV and by invoking Fresnel averaging as discussed in Chapter 4. Both corrections are, at most, a few millimeters per second. During the four higher velocity trials the differences are completely attributable to deformations of the bed. Fresnel averaging and inaccuracy in the measurement height may be invoked, but these corrections are comparatively small and in the wrong direction. Local flow variations five times larger than the differences exhibited here are present in the time series record of the propagating bedforms mentioned above.

This collection of comparison measurements demonstrates the ability of the BASS Rake to make accurate velocity measurements within millimeters of a natural sand bed. The velocity records also show that performance is not degraded by the passage of heavy bedload transport through the sample volume. The BASS Rake is also capable of measuring near-bottom turbulence as shown in Figure 5.23. The figure shows the standard deviations of the concurrent velocity records of both instruments. Agreement between the two sensors is fairly close, with the BASS Rake consistently reporting lower values. This may be a function of the different sample volumes over which the turbulence is averaged. Terray has shown that the characteristic averaging length of the BASS DTT measurement for turbulence is quite small, on the order of a millimeter or less [75]. This is comparable to the sample volume of the LDV and is consistent with the close but imperfect agreement. The generally larger disagreement at the lowest measurement level may be related to either the higher dropout rate of the LDV measurements near the bed or the truncation of the lowest BASS Rake sample volume by the bottom (see Chapter 4). The shear velocities calculated from the constructed LDV profiles are shown for comparison. The standard deviations and the shear velocities show reasonable agreement at all heights for the  $8 \text{ cm} \cdot \text{s}^{-1}$  to  $31 \text{ cm} \cdot \text{s}^{-1}$  trials.

The  $47 \text{ cm} \cdot \text{s}^{-1}$  trial exhibits similar agreement between the standard deviation and shear velocity only well above the bed. The measurements at  $2.4 \text{ cmab}$  and  $0.45 \text{ cmab}$  appear to indicate enhanced levels of turbulence near the bottom. Careful

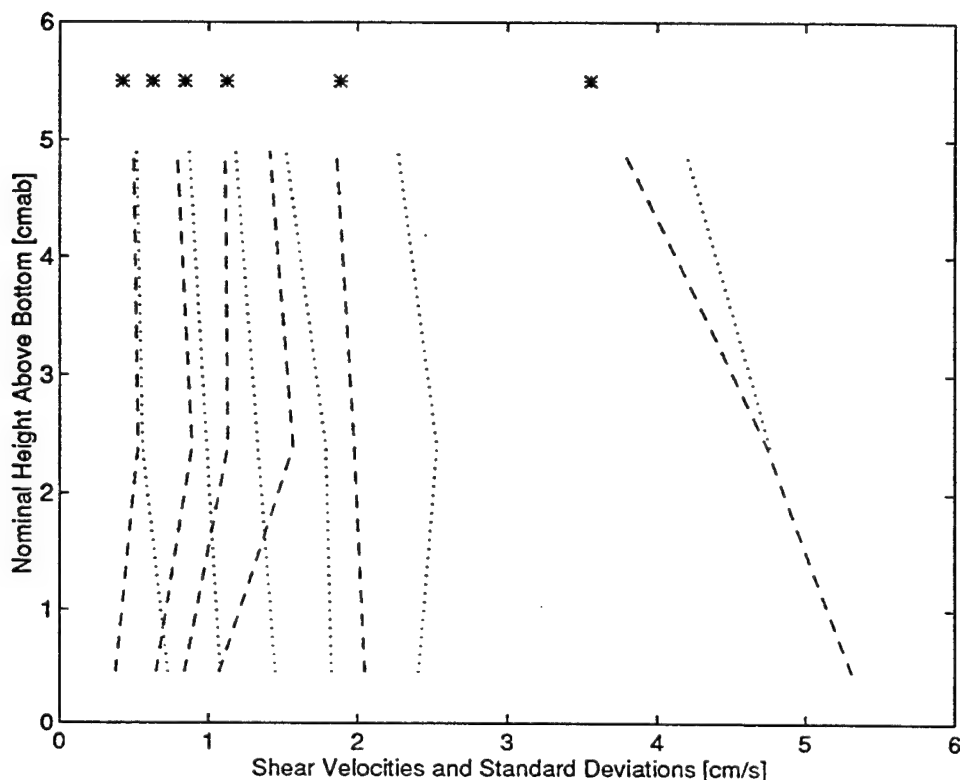


Figure 5.23: BASS RAKE AND LDV MEASUREMENTS OF TURBULENT FLUCTUATIONS - The standard deviations of the concurrent velocity records are shown for the BASS Rake (---) and the LDV (···). The data are a measure of the velocity of turbulent fluctuations as a function of height. The two sensors largely agree, with the BASS Rake consistently reporting lower values. The difference is variable and may be caused by the different sample volumes. The shear velocities calculated from the constructed LDV profiles, denoted by \*, are shown for comparison. There is a near match of the standard deviations and the shear velocities for  $8 \text{ cm} \cdot \text{s}^{-1}$  to  $31 \text{ cm} \cdot \text{s}^{-1}$  trials. The apparent enhancement of near-bottom turbulence during the  $47 \text{ cm} \cdot \text{s}^{-1}$  trial is an artifact introduced by propagation of bedforms past the sample volumes.

examination of the time series records indicates some elevation of near-bottom turbulence, but most of the apparent enhancement is a low frequency bias introduced by the propagation of bedforms past the sample volumes. The time series shows the migration of the bed over a period of approximately fifteen minutes. Bed elevations during the  $47 \text{ cm} \cdot \text{s}^{-1}$  are sufficiently large that localized flow distortions caused by individual bedforms are important within a few centimeters of the nominal bottom. The movement of the bedforms is shown in Figures 5.24 and 5.25.

The velocity records in the figures were acquired sequentially during the  $47 \text{ cm} \cdot \text{s}^{-1}$

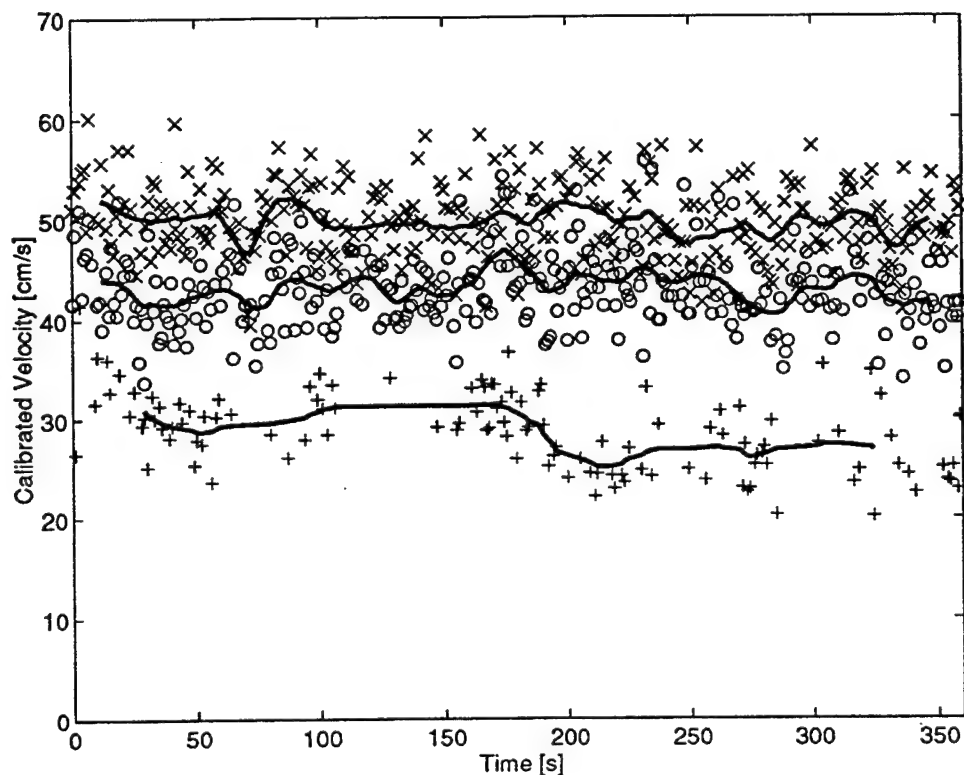


Figure 5.24: BEDFORM PROPAGATION PAST THE BASS RAKE SAMPLE VOLUMES, PART 1 - The velocity measurements at 0.45 *cmab*, 2.4 *cmab*, and 4.9 *cmab* are denoted by +, o, and x. The heavy solid lines are running averages over 20 measurements for each acoustic axis. The initial and final portions of the running averages exhibit end effects caused by the filtering process and have been removed. The velocity records were acquired during the first 6 minute averaging period of the 47  $\text{cm} \cdot \text{s}^{-1}$  trial. The movement of the bedforms causes a 5  $\text{cm} \cdot \text{s}^{-1}$  change in the average value of the 0.45 *cmab* velocity over a 50 s period in the middle of the trial. The 2.4 *cmab* and 4.9 *cmab* are affected to a lesser extent.

trial when bedload transport was heaviest. The second record begins approximately 2 minutes after the conclusion of the first record. The gasket failure occurred no more than 3 minutes after the second record was acquired. The bedforms beneath the tines at the time of failure are shown in Figure 5.17. Qualitatively, that topography is representative of the condition of the bed as these measurements were made. The motion of the bedforms is responsible for local changes in the average 0.45 *cmab* velocity of 5  $\text{cm} \cdot \text{s}^{-1}$  to 10  $\text{cm} \cdot \text{s}^{-1}$  over periods shorter than a minute. There are noticeable, but less extreme, changes, correlated with the bedform propagation, in



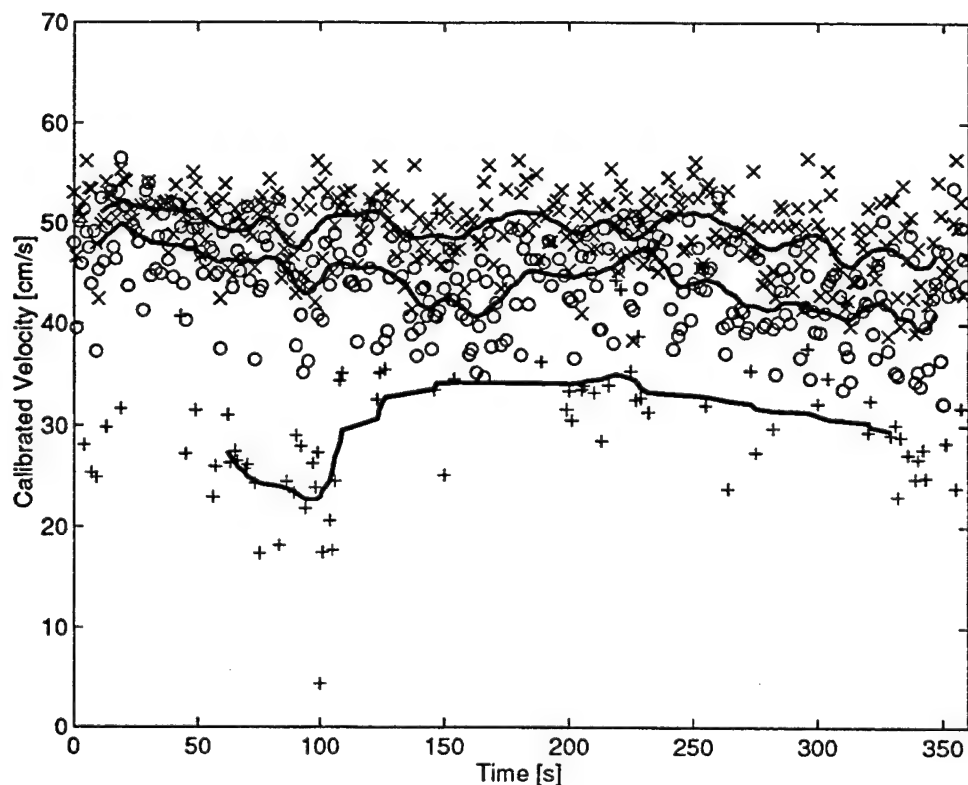


Figure 5.25: BEDFORM PROPAGATION PAST THE BASS RAKE SAMPLE VOLUMES, PART 2 - The velocity measurements at  $0.45\text{ cmab}$ ,  $2.4\text{ cmab}$ , and  $4.9\text{ cmab}$  are denoted by +, o, and x. The heavy solid lines are running averages over 20 measurements for each acoustic axis. The initial and final portions of the running averages exhibit end effects caused by the filtering process and have been removed. The velocity records were acquired during the second 6 minute averaging period of the  $47\text{ cm} \cdot \text{s}^{-1}$  trial. This averaging period began approximately 2 minutes after the conclusion of the first averaging period. The continued movement of the bedforms causes a  $10\text{ cm} \cdot \text{s}^{-1}$  change in the average value of the  $0.45\text{ cmab}$  velocity over a 50 s period. The  $2.4\text{ cmab}$  and  $4.9\text{ cmab}$  are affected to a lesser extent.

the average velocities at  $2.4\text{ cmab}$  and  $4.9\text{ cmab}$  as well. It is the large changes in the average velocity that are responsible for the enhanced near-bottom values of the standard deviation shown in Figure 5.23.

Fluctuations in flume speed on 10 s and longer scales are also visible in the figures. One example is the coherent decrease and following rise in the average  $2.4\text{ cmab}$  and  $4.9\text{ cmab}$  velocities between 50 s and 100 s in Figure 5.24. Similar fluctuations are apparent in the velocity records at all nominal speeds, including those with no motion of the sand in the bed. Measurements taken during the  $8\text{ cm} \cdot \text{s}^{-1}$  trial

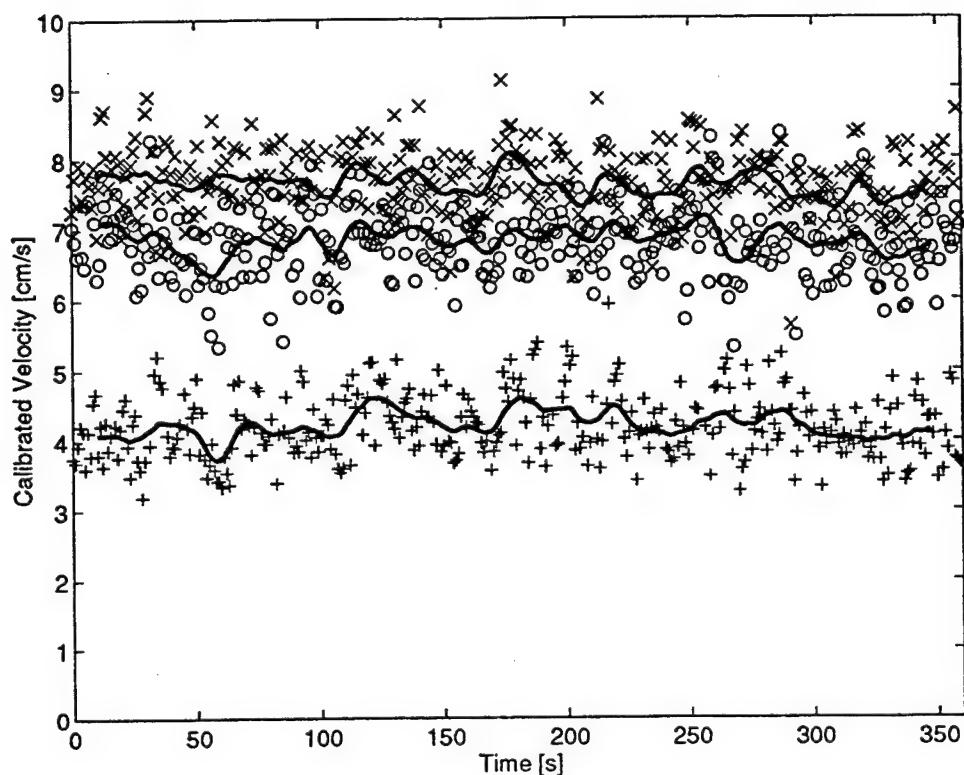


Figure 5.26: FLUME SPEED FLUCTUATIONS AT A NOMINAL VELOCITY OF  $8 \text{ cm} \cdot \text{s}^{-1}$  - Velocity measurements at  $0.45 \text{ cmab}$ ,  $2.4 \text{ cmab}$ , and  $4.9 \text{ cmab}$  during the  $8 \text{ cm} \cdot \text{s}^{-1}$  trial are denoted by +, o, and x. The heavy solid lines are running averages over 20 measurements for each acoustic axis. The initial and final portions of the running averages exhibit end effects caused by the filtering process and have been removed. The running averages show fluctuations in the speed of the flume on 10 s and longer scales. These are the fluctuations the 6 minute averaging period is intended to suppress. These correlated measurements resolve the dynamic behavior of the boundary layer on both short and long time scales and permit greater variation in the averaging period.

are shown in Figure 5.26. Fluctuations that are coherent across the boundary layer are visible near 50 s, 100 s, and 175 s in the record. These are the fluctuations the 6 minute averaging period is intended to suppress. Note that by measuring complete profiles, rather than by constructing profiles over time, greater variation in the choice of averaging periods is possible. Correlated measurements, such as these, resolve the dynamic behavior of the boundary layer on both short and long time scales.

A detail from the velocity records in Figure 5.26 is shown in Figure 5.27. The turbulent fluctuations evident in the figure occur on time scales of 3 s to 5 s and faster,

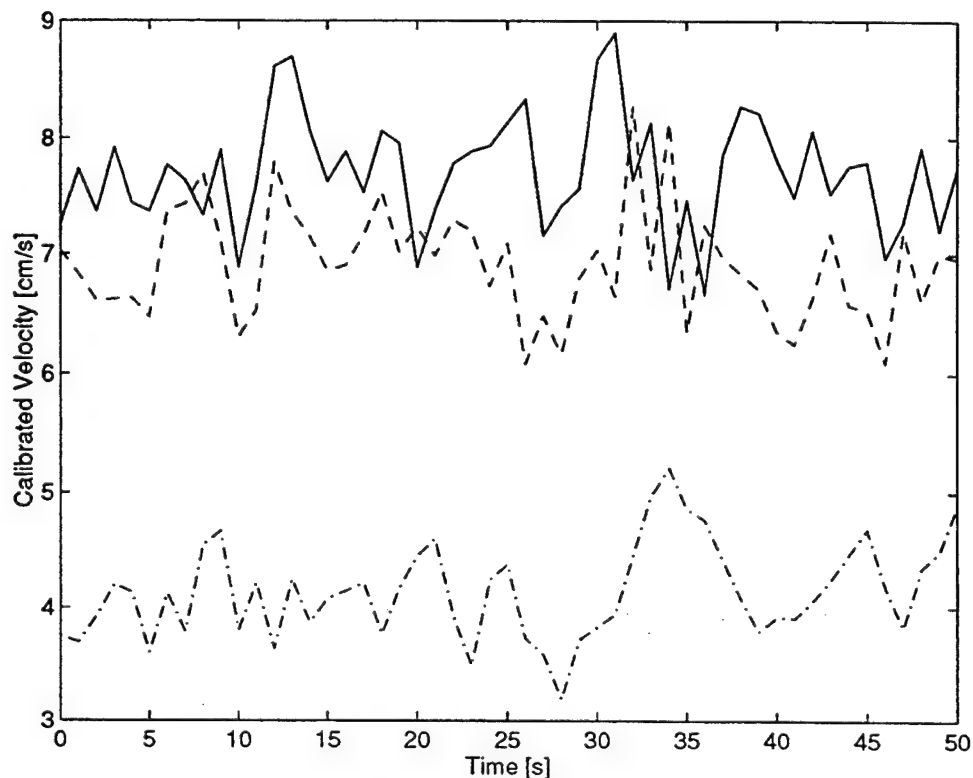


Figure 5.27: DETAIL FROM  $8 \text{ cm} \cdot \text{s}^{-1}$  VELOCITY RECORDS - The velocity measurements at  $0.45 \text{ cmab}$ ,  $2.4 \text{ cmab}$ , and  $4.9 \text{ cmab}$  are denoted by  $- \cdot -$ ,  $---$ , and  $—$ . The concurrent velocity records at three heights in the boundary layer are able to resolve coherent turbulent structures and turbulent instabilities on short time scales. Several examples from the traces shown here are described in the text. Information about the dynamic behavior of the boundary layer can only be obtained by making essentially instantaneous profile measurements.

with typical magnitudes of  $1 \text{ cm} \cdot \text{s}^{-1}$  to  $2 \text{ cm} \cdot \text{s}^{-1}$ . Figure 5.27 again demonstrates the advantage of multiple sample volumes and essentially instantaneous profiles by resolving the dynamic behavior of the boundary layer on these short time scales. A multi-peaked structure with both above and below average velocities and vertical coherence from  $2.4 \text{ cmab}$  to  $4.9 \text{ cmab}$  is visible centered at  $15 \text{ s}$ . The structure is preceded and followed by possible examples of bursting and sweeping behavior. These turbulent instabilities, discussed in Chapter 2, are mechanisms for the vertical exchange of momentum in the boundary layer (see for example Head and Bandyopadhyay [32] or Robinson [65]). The transport of relatively slow fluid away from the boundary is a burst. A sweep is the injection of relatively fast fluid towards the

boundary. An apparent sweep, with vertical coherence from 0.45 *cmab* to 2.4 *cmab*, can be seen between 8 s and 10 s in the velocity records. The magnitude of the sweep is large enough that the velocity at 2.4 *cmab* briefly exceeds the 4.9 *cmab* velocity. A possible burst at 20 s occurs in the 4.9 *cmab* velocity.

A more complicated interaction is visible from 30 s to 40 s, with a prolonged sweep in the 0.45 *cmab* and 2.4 *cmab* velocities and a concurrent burst in the 4.9 *cmab* velocity. Alternatively, the record at 28 s could be interpreted as a coherent burst across all three measurement levels followed by a sweep from 30 s to 36 s that exhibits a transport lag as it approaches the bottom. Other examples of coherent turbulent structures and turbulent instabilities can be found in Figure 5.27 and, indeed, anywhere in the BASS Rake data from the 17 m flume.

The importance of boundary layer flows in many contexts is well established and the dynamic behavior and structure of these flows is known to be rich and varied over a broad range of spatial and temporal scales. Making measurements of that structure is, in general, difficult. These characteristics of the flow are invisible to the single sample volume of the LDV, for example. However, the figures presented in this section demonstrate that the BASS Rake, using multiple sample volumes, is capable of observing and imaging these phenomena in the flow immediately adjacent to a natural bottom. The research described in earlier chapters shows that this technique is capable of resolving the scales of interest in the continental shelf wave bottom boundary layer.

## 5.6 Conclusions

The work with the laboratory prototype has established an important direction for future investigation. The flow distortion caused by the tines currently sets the limiting noise floor of the instrument. In the fully turbulent flow of the flume experiments the effects of this noise floor were small because the ambient fluctuations of the flow were uniformly larger than  $0.3 \text{ cm} \cdot \text{s}^{-1}$ . In other steady flows and in the WBBL this will not always be true and it will be desirable to reduce the disturbance. Several options

and their possible consequences were discussed in Section 5.4.

The laboratory prototype was constructed to evaluate and prove various aspects of the BASS Rake design. This is a normal part of the development process for any new instrument. The demonstration has been quite successful in this case. The performance of the integrated electrical and mechanical design of the tines has been thoroughly tested and shown to work well. The same can be said of the low impedance multiplexer that connects the T/R circuit to the transducers. The theoretical description of the sample volume also appears to be accurate. In all cases the empirically verified performance is in close agreement with calculations based on predictive models.

The dependence of the measurement on the flow has been accurately modeled and well determined by experiment. The mapping from measured to actual velocity is simple and single valued. The applicability of the mapping to oscillatory flows has been empirically established and that result is consistent with the flow distortion model and with the literature. Importantly, the laboratory prototype has demonstrated that a BASS DTT acoustic axis will reliably, accurately, and robustly operate within millimeters of a natural sand boundary. Finally, the prototype has shown the advantage of multiple sample volumes by imaging vertically coherent turbulent structures and turbulent instabilities in a steady boundary layer.

## Chapter 6

# Calibration and Deployment of the Field Prototype

### 6.1 Introduction

The BASS Rake was envisioned from the earliest phase of the design process as a field instrument. The laboratory evaluation of Chapter 5 demonstrated the viability of the mechanical and electrical designs and showed that an accurate BASS DTT measurement could be made parallel to and immediately above a sand bottom. This work was accomplished under controlled conditions with unconstrained access to the instrument. For example, positioning the tines above the sand bed in the flume with millimeter accuracy could be accomplished without great difficulty. That accuracy depended on the ease with which the instrument height could be adjusted in the open flume, the unobstructed view of the tines through clear water, and the relatively well defined location of a manually smoothed and leveled fluid-sediment interface. Such comfortable and benign working conditions simply do not occur on the continental shelf.

The field prototype documented in this chapter uses neither the integrated tine design nor the multiplexer interface. It is fabricated from stock BASS components and differs from that instrument only in using the acoustic axes geometry of the BASS Rake. The prototype is the precursor to a field instrument based on the more

ambitious design developed in the previous chapters. The field instrument was built to accomplish several well defined tasks. In this it has been largely successful. First, the prototype has demonstrated the operation of the BASS Rake technique in the field. The vertical resolution, because of the size of the standard BASS transducer assemblies [90], is insufficient to image the wave boundary layer. However, it can profile the lower 30 *cm* of the boundary layer at multiple levels and could, if certain conditions were met, detect the presence of a wave boundary layer based on the phase of the near-bottom velocity. These capabilities alone are nearly unique among currently available sensors.

The necessary conditions for a detection based on the phase lead are straightforward. First, the bottom roughness elements must be small compared to the thickness of the wave boundary layer so that the boundary layer can actually form. Second, the thickness must be at least 1 *cm* so that there is a measurable phase shift more than 0.5 *cmab*, the nearest approach for the 1 *cm* diameter standard BASS transducers. Finally, the lowermost measurement level must be within the wave boundary layer. The improved vertical resolution of the final instrument will make satisfying the latter conditions considerably less problematic.

Of equal importance to the demonstration of field operation, the prototype has afforded an opportunity to evaluate anchoring and other stabilizing techniques for deployments of several weeks duration in the energetic near-shore zone. It also permitted a practical test of the support frame design for deployment and access by divers. Diver access to the instrument, particularly the height adjustment of the tines, is a necessary feature. The design must allow for the sharply limited ability of divers to make fine adjustments in the field. Reduced performance is a function of ambient conditions in the form of wave and current forcing, limited visibility, and a poorly defined fluid-sediment interface. It is also a result of the reduced dexterity and visual field of a fully suited diver and the inability to communicate and coordinate easily and quickly with other divers. The author and the quadrapod designer are both divers with considerable professional experience in the practical realities of working underwater. As part of the design process, they were the lead divers for all

deployments and recoveries of the field prototype. The author was also the lead diver during all inspection and observation dives. With some modifications, determined from use, the support frame of the prototype will be used with the final instrument.

Finally, the processing and examination of the data from the field prototype have tested the sensor response function, a calibrated mapping depending on the magnitude and angle of the velocity, with real data. The demonstrated complexity of the near-shore wave flow when it is resolved with vertical coherence provides a useful input to both the mechanical design and the selection of measurement suites. It has also shown some of the environmental conditions for which it will be most important to control in future deployments.

The support frame, tines, and electronics package of the field prototype are described in Section 6.2. An initial deployment of several hours duration was conducted in the harbor adjacent to the Woods Hole Oceanographic Institution (WHOI) dock to evaluate the operation of the newly assembled support frame and to test sensor operation. Some of the harbor measurements are presented in Section 6.3. After the harbor test, the Reynolds number dependence and azimuthal cosine response of the sensor were empirically determined in the WHOI tow tank. These results and a mapping from the measured to the undisturbed velocity are reported in Section 6.4. The instrument was then twice deployed immediately outside the surf zone of a local beach. During the second beach deployment, profile measurements were made at 1 Hz over an uninterrupted period of three weeks in December of 1996. Some of the data acquired during that experiment are presented and analyzed in Section 6.5. Finally, in Section 6.6, the results of the field prototype evaluation are summarized.

## 6.2 The Field Prototype

The BASS Rake field prototype consists of a rigid outer frame constructed of aluminum tubing. The outer frame supports an inner frame, mounted on vertical sliders. The electronics housing, the coaxial transmission lines, and the tine assemblies of the BASS Rake are mounted on the inner frame. This construction permits vertical ad-



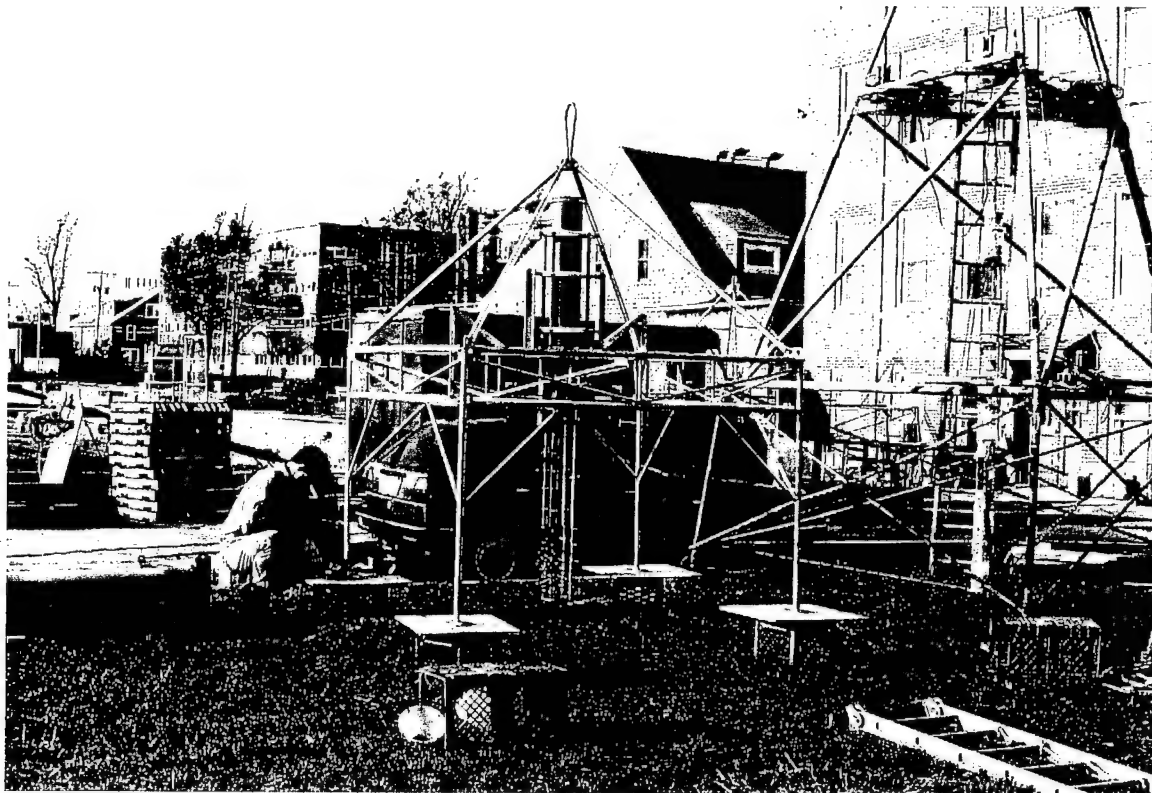


Figure 6.1: THE ASSEMBLED BASS RAKE FIELD PROTOTYPE - The rigid outer frame is constructed of aluminum tubing. The legs are arranged in a square with  $2\text{ m}$  sides. The height at the top of the box frame is  $1.4\text{ m}$  and the height at the lift point is  $2.75\text{ m}$ . The pyramidal members above the box frame support the lift point and protect the pressure housing. The housing, mounted vertically in the center of the frame, contains the BASS electronics package, the data logger, and batteries. The tine assemblies extend down from the pressure housing with the sensing volumes at the lower end. The quadrapod designer has been included for scale. The harbor deployment described in Section 6.3 took place from the edge of the dock immediately beyond the loading pallets on the left. Photograph by the author.

justment of the sensor head without loss of the calibrated zero offsets due to relative motions of the electronics housing, transmission line harness, and transducers [53, 90]. The inner assembly and the sliders can be cleanly separated as a rigid unit from the outer frame without disrupting the harness. This feature was necessary for the empirical tow tank determination of the sensor response. Two views of the assembled field prototype are shown in Figures 6.1 and 6.2.

The outer frame is light, but quite rigid because of the cross-braced box frame construction securing the tops of the four legs. The legs were each bent outwards and

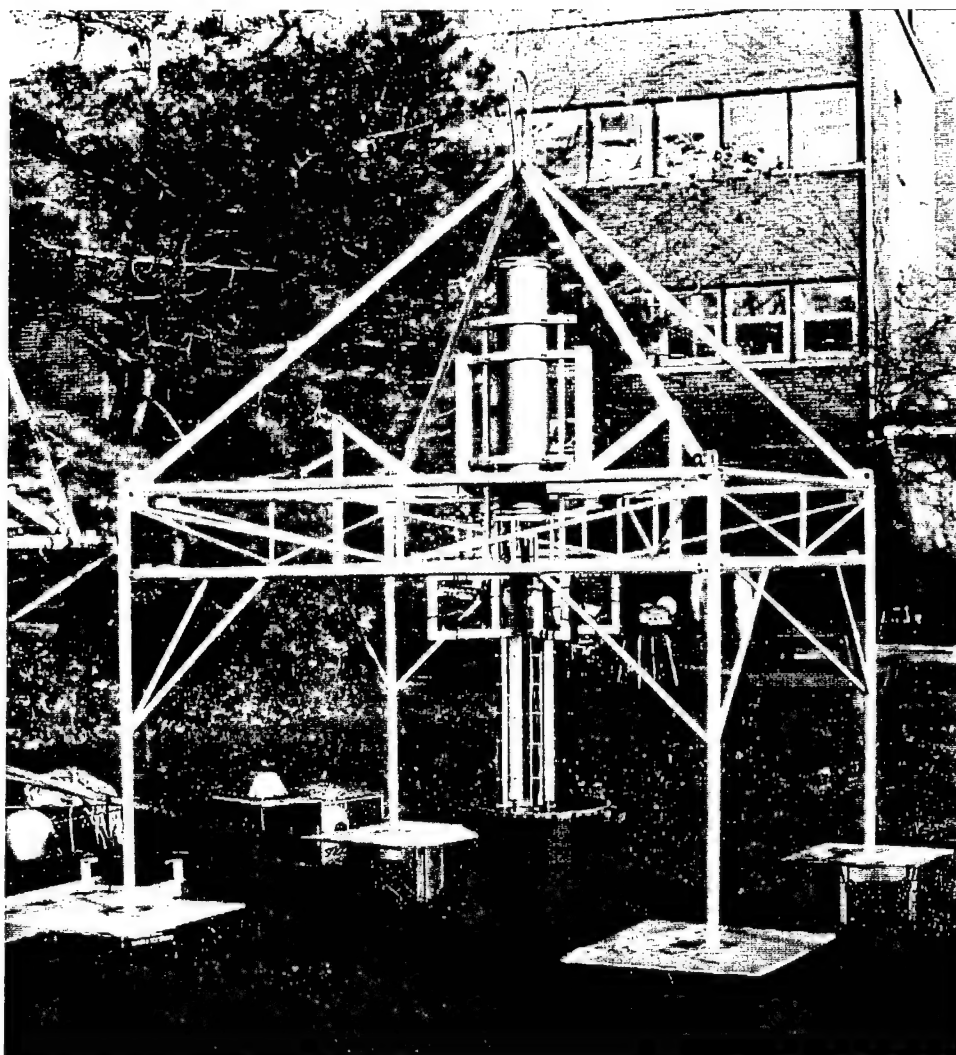


Figure 6.2: ZERO CALIBRATION OF THE FIELD PROTOTYPE - The field prototype is shown during the calibration of zero offsets for the first beach deployment. The inner frame has been lowered on the sliders so that the crossing ladders to which the tines are mounted are visible below the box frame. The ladders scissor around a central, vertical pivot so that the tine pattern can be changed from square to rectangular. The ladders have also been machined to accommodate greater tine separations. The large bucket contains water or gelatin for testing and zero calibration of the acoustic axes. Photograph by the author.

then pulled back so that the angled members below the box frame are under tension. This technique further increases rigidity. Once fully assembled, the frame is free of large, low frequency oscillations. Strouhal vibrations did not appear to be a problem during the beach deployments. Attachment points are provided at the top of each leg for anchor lines. The open design of the frame, the long tines, and the vertical

orientation of the single pressure housing are all intended to decrease the flow disturbance in the wave boundary layer and to permit clear access to divers. The pattern of horizontal cross-bracing within the box frame connects the "forward" corners to the midpoint of the "back" side. This V brace is not visible in the photograph. The brace securely supports the sliders and the inner frame while allowing access on the forward side to the slider blocks and the locking bolts used to hold the inner assembly in place after the height is set (see Figure 6.4).

The overall assembly has been kept small and light enough for deployment from small boats or by divers. The legs are arranged in a square with  $2\text{ m}$  sides. The height at the top of the box frame is  $1.4\text{ m}$  and the height at the lift point is  $2.75\text{ m}$ . The pyramidal members above the box frame support the lift point and protect the pressure housing. The overall weight in air, inclusive of the electronics package, is  $300\text{ lbs}$  to  $350\text{ lbs}$ . The in-water weight is  $150\text{ lbs}$  to  $200\text{ lbs}$ . Four divers were sufficient to load the instrument on and off a flatbed truck and to deploy and recover it from a beach. The winch and boom of a small boat would also be sufficient.

The inner frame supports the tine assemblies and the comparatively heavy pressure housing and electronics package. The tops of the tines are attached to two crossing ladders. This assembly is visible below the box frame in Figure 6.2. The ladders scissor around a central, vertical pivot so that the tine pattern can be changed from square to rectangular. The ladders have also been machined to accommodate greater tine separations. The adjustments make it possible to reduce the relative flow disturbance and modify the cosine response. The potential need for these features was discussed in Chapter 2.

The tine members are  $\frac{3}{8}$ " square stainless steel solid rod stock. Their overall length below the ladders is  $1\text{ m}$ . The tines are stiffened with  $1\frac{1}{4}$ " aluminum angle stock between the ladder assemblies and the sensing volumes. The tines extend  $5\text{ cm}$  below the lowermost measurement level and are secured at that point to a ring. The ring suppresses relative motions of the tines and maintains the  $15\text{ cm}$  path length separation of the transducers. Figure 6.3 is a close-up photograph of the transducers mounted along the ends of the tines.

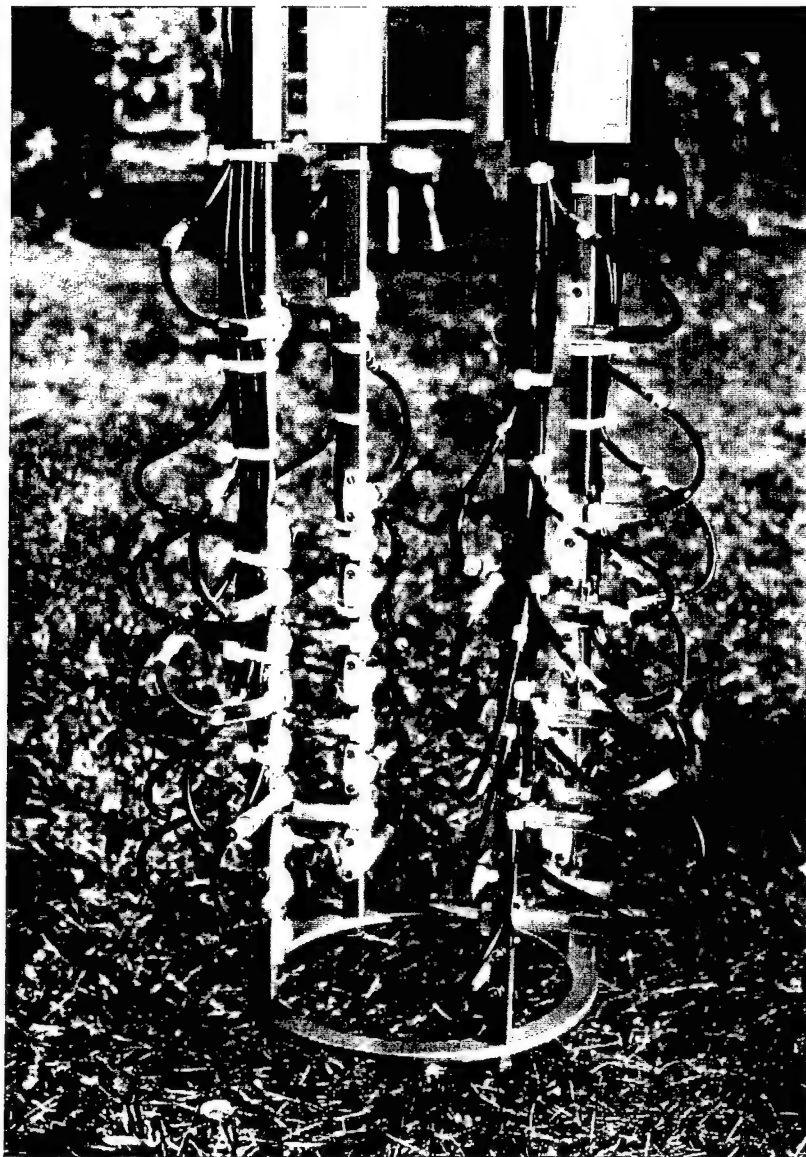


Figure 6.3: FIELD PROTOTYPE TRANSDUCER ARRAY - The molded polyurethane BASS transducer assemblies are bolted to the stainless steel tine members. There are ten measurement levels. The lower nine levels are linearly spaced with a vertical separation of 2.5 cm. The coaxial transmission lines are run along the tines and the angle stock stiffeners and secured with tie-wraps. The stems of the transducer assemblies are easily damaged by bending moments, lateral shear, and longitudinal stress. The loops of the coaxial cable visible in the photograph were not sufficiently wide to prevent damage to three of the transducer assemblies. This is not a particularly robust design. The structural ring is visible, bolted to the ends of the tines. Photograph by the author.

There are ten measurement levels. Following the tine and transducer designations defined in Chapter 3, the tines are denoted A, B, C, and D and the acoustic axes are numbered 0 to 9 from the bottom. Level 0 is defined to be the nominal bottom. Levels 0 to 8 are linearly spaced with a vertical separation of 2.5 cm. The physical size and shape of the standard BASS transducer assemblies prevents finer vertical resolution. Level 9 is located 30 cm above the nominal bottom and 10 cm above Level 8. The coarseness of the vertical spacing prevents accurate determination of the location of the fluid-sediment interface. Recall the influence this question had on the designed distribution of transducers along the tines as described in Chapter 2. The along-axis velocities are defined to be positive from tine A to tine C and from tine B to tine D. In the tow tank, where the relative angle of flow is known in advance, these measurements are mapped to along-tank and cross-tank velocities. This is the most convenient frame of reference for the determination of the flow speed and flow angle dependence of the sensor. The raw measurements from the second beach deployment are rotated into an instrument coordinate system that was manually aligned with the shore during deployment. The instrument coordinate system (*ics*) is defined in Figure 6.4.

The stems of the BASS transducer assemblies are easily damaged by bending moments, lateral shear, and longitudinal stress. The normal BASS mounting cage is designed to support and immobilize the stems and thus prevent damage [90]. However, in the configuration necessarily used for the field prototype, the transducers are uncomfortably exposed. Their susceptibility to damage is clearly evident in Figure 6.3. The mortality rate during the second field deployment, due to wave induced slamming after the anchors were pulled free of the bottom, was quite high. Additionally, axes A4-C4 and B9-D9 failed before the deployment. These failures were attributed to a history of fatigue in the stems and the bending moment applied by looping the coaxial cables back to the tines. Axis B6-D6 failed a few days into the second deployment, apparently for the same reason. Note that the integrated tine design described in Chapter 2 has no exposed protrusions and connections and will not be subject to failure during assembly. It has already proven to be reliable and

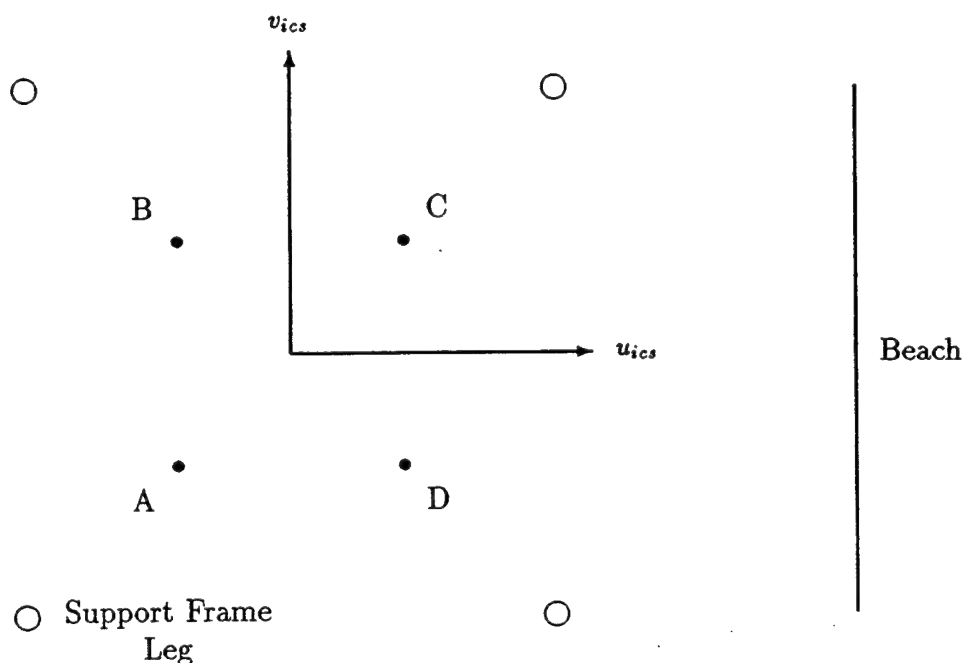


Figure 6.4: DEFINITION SKETCH FOR THE INSTRUMENT COORDINATE SYSTEM - The four tines, in plan view as seen from above, are shown as filled circles with their letter designations. The open circles represent the legs of the outer support frame. Tines A and B are on the "forward" side of the frame, which offers the best diver access to the slider blocks and locking bolts of the height adjustment. The  $u_{ics}$  and  $v_{ics}$  velocities of a right-handed, instrument-relative, coordinate system are positive as shown. The instantaneous angle of the velocity in the instrument coordinate system,  $\theta$ , is defined to be zero along the positive  $u_{ics}$ -axis.  $\theta$  is positive measured counter-clockwise from the positive  $u_{ics}$ -axis. During the field deployments the frame of the prototype was manually aligned to the shore as shown by the beach line on the right side of the figure. In the data analysis,  $u_{ics}$  and  $v_{ics}$  are equated with the on-shore and along-shore velocities. The elements of the figure are not drawn to a common scale.

physically robust when subjected to continuous use and occasional rough handling. The potential for column buckling caused by longitudinal compression is addressed, as described in Chapter 2, by adding stiffeners to the tines above the sample volumes and by improving the stability of the support frame through improved anchoring.

The transducer assembly stems and the loops of the cable harness also cause a wide flow disturbance compared to the slender tines described in Chapter 2. The wider disturbance narrows the angular window of relatively undisturbed flow, degrading the azimuthal cosine response of the sensor head compared to the slender tine design. It will be seen in Section 6.4 that the angular dependence of the gain correction rises

sharply when the wake of the loops falls along the acoustic axes. The slender tines will provide a wider window of acceptable flow angles. The protruding elements do shorten the along tine correlation length for shed vortices. The surface distortions in the wake of the field prototype tines, observed during the tow tank calibration, were noticeably less pronounced than the distortions in the wake of the laboratory prototype tines for the same tow speeds. The wake behind the field prototype also appeared to be less organized. These phenomena may also be effects of the additional pair of tines.

The response of a single axis sample volume of the field prototype can be estimated by applying the parametric model of the Fresnel averaging process developed in Chapter 4 to the standard transducers. The diameter of the transducers is 1 *cm*. At 1.75 *MHz* the mainlobe beam angle (first null) in the far field is  $\approx 6^\circ$ . Calculation shows that the averaging will produce no significant error down to 0.5 *cmab*, the closest approach to the bottom for these transducers. This result should be treated with some caution because the Rayleigh length of these transducers is nearly 12 *cm* and the far field approximation is not valid. However, the simple model does accurately characterize the response of the P2 transducers,  $L_{Rayleigh} = 4.2$  *cm*. Recall as well that the detailed derivation of the Fresnel averaging integral, to which the simple parametric model is matched, does not restrict application to the far field. The integral is valid at significantly shorter ranges. Empirically, no effects attributable to Fresnel averaging are apparent in the data.

The BASS electronics and data logger were assembled on a single backplane. The loaded chassis and two battery packs fit comfortably inside a 33" long, 6" *ID*, pressure housing. Two battery packs are sufficient for a 70 to 80 day deployment. Using a single, vertically mounted pressure housing simplifies deployment, particularly the height adjustment of the acoustic axes. The orientation and the absence of additional housings also reduce the flow disturbance near the sample volumes. There is sufficient room at the top of the housing for battery connections and a communication port, permitting control of program initiation and a convenient monitoring point to verify program operation before sealing the housing. A complete profile is acquired inside



a 6.4 ms window. The sample rate was 1 Hz for all measurements described in this chapter. Faster rates could be used, but 1 Hz is sufficient for the tasks defined for the field prototype. Data are accumulated in a RAM buffer on the logger and written to the logger hard disk when the buffer is full. Filling the buffer requires approximately 75 minutes for ten level profiles taken at 1 Hz. Data acquisition is disabled for 10 s during the disk write. The capacity of the disk is sufficient for a deployment of approximately 60 days at 1 Hz.

Experience with the quadrapod has shown that it does not significantly obstruct near-bottom flow. The instrument can be deployed by divers or small boats and access for inspection and adjustment by divers is excellent. Improved anchoring is clearly required for the near-shore zone if storm conditions are anticipated or the deployment is scheduled to last longer than a week. The height adjustment of the tines currently requires the participation and coordination of two divers. For future deployments, the slider block and locking bolt assemblies will be modified for one-handed operation, allowing the height to be adjusted by a single person. A scale will also be added to increase the accuracy and ease of vertically positioning the tines. With relatively minor modifications the frame will be completely suitable for use with the final field instrument described in previous chapters.

### 6.3 Harbor Deployment

Construction of the BASS Rake field prototype was completed in early November of 1996. The instrument was assembled on the WHOI dock as shown in Figures 6.1 and 6.2. Before calibrating the Reynolds number dependence and azimuthal cosine response of the sensor head, the instrument was deployed for several hours in Great Harbor, immediately adjacent to the dock. The deployment and recovery were accomplished using a crane, a "pillow" lift bag, and four divers. The short deployment, without calibration, was undertaken to evaluate the operation of the support frame. It was anticipated that the tow tank calibration would afford a one week window for any necessary changes to the outer support frame. As noted in the previous



section, only the inner assembly, necessary to the calibration, appeared to require modifications. The deployment also provided an opportunity to verify operation of the software and the electronics package. The measurements demonstrate the clean operation of an acoustic DTT axis parallel to and a few millimeters above a natural bottom.

Before deploying the instrument in the harbor, the sensor head was placed in a bucket, which was then filled with water from a hose (Figure 6.2). This was done to obtain approximate zero offsets. The sensor remained in the bucket for less than 30 minutes, a period of time insufficient for organized motions in the bucket to attenuate below the level of thermal convection. However, it was sufficient for the purposes of this test. The section of Great Harbor used for the deployment is a small embayment. It is bordered on three sides by the WHOI dock, a seawall, and the shallows around the pilings of a pier. The seawall and part of the harbor are visible in the background of Figure 6.1. The surface wave field at the time of the deployment consisted of short period chop propagating in several directions due to reflection and refraction within the embayment. The trough to crest height differential averaged 0.5 *m*. Sustained winds with regular gusts persisted throughout the day. Tidal currents also looped through the harbor and the embayment.

The instrument was placed on a sloping and irregular bottom at a depth of 5 *m* to 7 *m*. The bottom slope was estimated to be between 20° and 30°. The tines were approximately perpendicular to the local bottom. Visibility was as low as 15 *cm* because of fine silt resuspended from the bottom by the currents and the divers. At no time did the visibility exceed 2 *m*. In addition to the silt, the bottom is composed of sand and scattered cobbles. A shallow hole was dug below the sensor head for the structural ring and the extensions of the tines below the sample volumes. After the inner frame was lowered and the hole refilled, measurement Level 0 was observed to be approximately 1 *cm* above the bottom. Velocity measurements were made at seven of the ten levels. Assuming the estimate for Level 0 is accurate, the heights were 1 *cmab*, 6 *cmab*, 8.5 *cmab*, 11 *cmab*, 16 *cmab*, 18.5 *cmab*, and 31 *cmab*. The measurements reported in this section have been rotated into the instrument coordinate

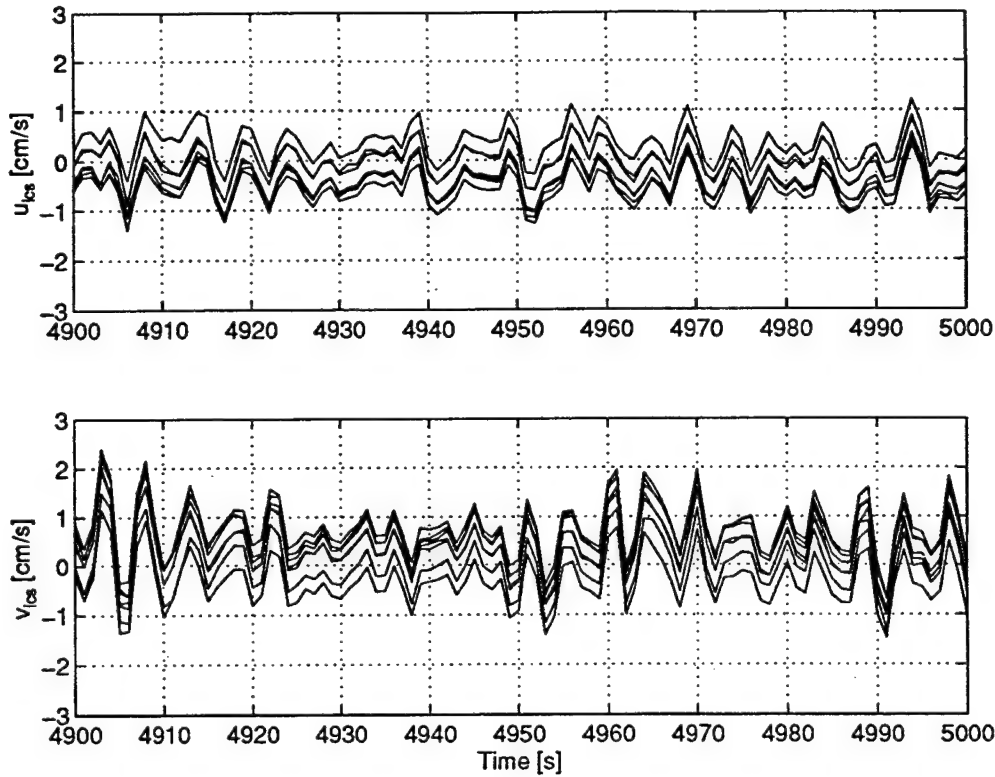


Figure 6.5: BOTTOM VELOCITY MEASUREMENTS IN GREAT HARBOR - The two panels show a 100 s time series of the velocities, in the instrument coordinate system, from seven measurement levels. The velocities were measured at nominal heights of 1 *cmab*, 6 *cmab*, 8.5 *cmab*, 11 *cmab*, 16 *cmab*, 18.5 *cmab*, and 31 *cmab*. The fixed velocity differences between measurement levels are caused by residual zero offsets, not by vertical structure in the bottom boundary layer. Temporal coherence between levels is clearly quite high.

system.  $u_{ics}$  is oriented roughly up the slope of the bottom and  $v_{ics}$  roughly follows the local isobath. The sensor response correction developed in Section 6.4 has not been applied to the Great Harbor measurements.

Figure 6.5 shows a 100 s time series of the measurements from all seven levels. The peak velocities are small because of the short period and wavelength of the surface chop. The measurements exhibit a high degree of temporal coherence. The fixed velocity differences between measurement levels are caused by residual zero offsets, not by vertical structure in the bottom boundary layer. Note that the measurements are quite clean, clearly showing a wave signal with a  $1 \text{ cm} \cdot \text{s}^{-1}$  amplitude and a period of  $\approx 4 \text{ s}$  immediately above the bottom.

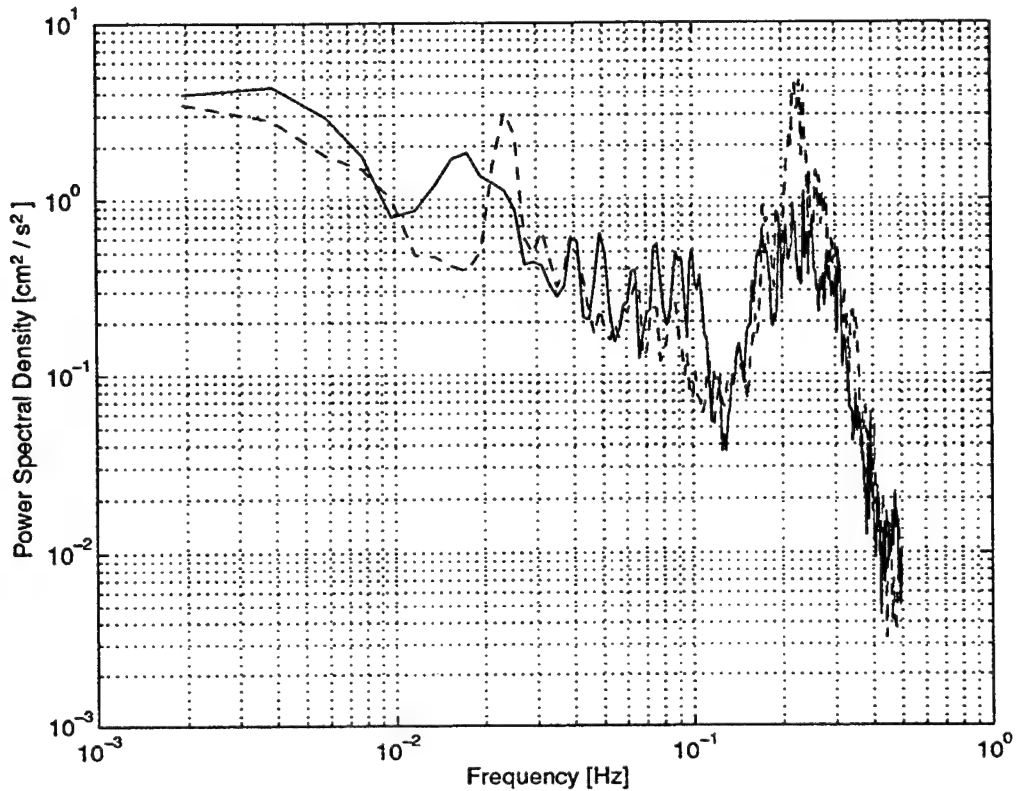


Figure 6.6: SPECTRA OF THE VELOCITY MEASURED 1 *cmab* - The solid line is the spectrum of  $u_{ics}$  and the dashed line is the spectrum of  $v_{ics}$ . The velocities were measured 1 *cmab* and the spectra were calculated from a 2.2 hour (8000 s) section of the data. The bottom velocities generated by the surface chop are clearly evident as a broad peak extending from 8 s down to 2.5 s. A few small peaks can be seen with periods from 25 s down to 10 s. The spectrum of  $v_{ics}$  shows a strong, relatively narrow, peak at 45 s and there is a broader peak at 1 minute in the  $u_{ics}$  spectrum. The slowly varying tidal current is responsible for the signal strength at the lowest frequencies. The data were detrended before calculating the spectra. This operation reduced the spectral density only in the lowest frequency bin.

The spectra for  $u_{ics}$  and  $v_{ics}$ , measured 1 *cmab* and calculated from a 2.2 hour (8000 s) section of the data, are shown in Figure 6.6. The bottom velocities generated by the surface chop are clearly evident as a broad peak extending from 8 s down to 2.5 s. A few small peaks can be seen with periods from 25 s down to 10 s. The spectrum of  $v_{ics}$  shows a strong, relatively narrow, peak at 45 s and a broader peak at 1 minute in the  $u_{ics}$  spectrum. The slowly varying tidal current is responsible for the signal strength at the lowest frequencies. The complexity of the surface wave field is apparent from the spectral structure and the differences between the two spectra.

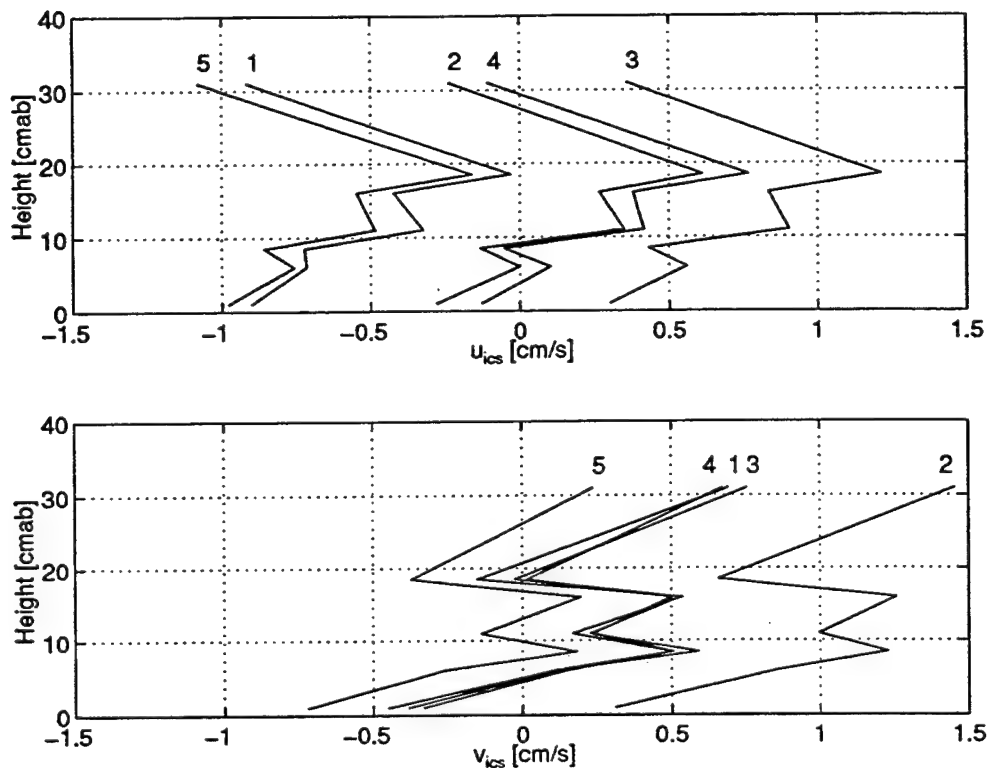


Figure 6.7: VELOCITY PROFILES OVER A SINGLE WAVE CYCLE - The two panels show  $u_{ics}$  and  $v_{ics}$  profiles recorded during a single wave cycle. The profiles were taken at 1 s intervals and are numbered in sequence. The vertical variation is caused by the residual zero offsets and the actual vertical structure, if any, cannot be determined. The record shows that whatever structure exists is cyclically advected with very little change over the period of the wave.

Profiles from a single wave cycle are shown in Figure 6.7. The particular cycle occurs from 4492 s to 4496 s in the time series of Figure 6.5. The vertical variation is caused by the residual zero offsets and the actual vertical structure, if any, cannot be determined. The record shows that whatever structure exists is cyclically advected with very little change over the period of the wave.

The brief evaluation of the field prototype identified the needed modifications to the slider blocks and locking bolts previously mentioned. It also gave the divers some experience positioning and adjusting the instrument. The measurements are imprecise because of residual zero offsets; however, they clearly resolve a  $1 \text{ cm} \cdot \text{s}^{-1}$  wave signal only 1 cm above a natural bottom and record near-bottom velocity profiles. Having

performed satisfactorily, the inner assembly was removed from the support frame so that the Reynolds number dependence and the azimuthal cosine response of the sensor head could be determined empirically.

## 6.4 Tow Tank Calibration

Based on the discussions and results presented in previous chapters, it can be asserted with confidence that the response of the sensor depends on both the magnitude and the angle of the flow in the instrument coordinate system. It can also be anticipated that the correction at small values of  $\theta$ , the flow angle, is smaller for the four tine field prototype than for the two tine laboratory prototype. The reorientation of the potential flow distortion by the second pair of tines was discussed in Chapter 5. The flow dependence of the sensor response was empirically determined in the WHOI tow tank. This facility and the general experimental procedures that were followed to insure the reliability and quality of the data were described in Chapter 5. The discussion here will focus on aspects of the calibration that are specific to the field prototype.

The instrument was towed at six speeds for each of four angles. The speeds were  $1.2 \text{ cm} \cdot \text{s}^{-1}$ ,  $5 \text{ cm} \cdot \text{s}^{-1}$ ,  $10 \text{ cm} \cdot \text{s}^{-1}$ ,  $20 \text{ cm} \cdot \text{s}^{-1}$ ,  $35 \text{ cm} \cdot \text{s}^{-1}$ , and  $50 \text{ cm} \cdot \text{s}^{-1}$ . This range is adequate for the anticipated magnitude of near-bottom flow at the beach selected for the field deployments. The angles, measured in the instrument coordinate system, were  $0^\circ$ ,  $15^\circ$ ,  $30^\circ$ , and  $45^\circ$ . Spanning one octant is sufficient because of symmetry. The twist angle of the sensor relative to the tow cart was measured with a solid pattern and monitored for movement while the clamps securing the sensor were tightened. The tines were observed to be free of vibration at all tow speeds. All tows were made in both the forward and reverse directions and no large or systematic differences were observed in the response. The length of the field prototype tines placed the sample volumes well below the surface of the water. As noted earlier, the distortion of the surface in the wake of the tines was small and disorganized compared to wake observations made while towing the laboratory prototype. Froude number effects are

therefore assumed to be negligible.

During processing, the zero offsets for each run are determined from the velocity measurements taken before cart motion was initiated. Residual and thermal currents in the tank were always determined to be slow compared to the tow speed before starting the cart. After the offsets are applied, the measurements are rotated into along-tank and cross-tank velocities. The rotation is based on the known angle, established by the solid pattern, between the sensor and tank coordinate systems. In general, the standard deviation of the cross-tank velocity depends on both the tow speed and the rotation angle. Values up to  $\approx 2.5 \text{ cm} \cdot \text{s}^{-1}$  are observed for fast tows with large rotation angles. However, the standard deviations are always less than 5% of the cart speed. Interestingly, the mean values of the cross-tank velocities are invariably near zero. There is some variation with measurement level, but it is neither systematic nor repeatable. The angle of the measured velocity can be calculated from the measured along-tank and cross-tank velocities and is always within a few degrees of the along-tank direction. Physically this means that the sensor head does not twist the flow. The constant angle simplifies the mapping from the measured velocity to the undisturbed velocity.

To determine the response of the sensor, the gain correction is defined by

$$G_{corr} = \frac{u_{cart}}{u_{mat}} \quad (6.1)$$

where  $u_{cart}$  is the cart speed and  $u_{mat}$  is the measured along-tank velocity.  $u_{mat}$ , and therefore  $G_{corr}$ , depends, in general, on both the magnitude and the angle of the flow. Equation 6.1 should be compared with Equation 5.4. In the case of actual field measurements,  $G_{corr}$  would be applied to the measured magnitude of the velocity and the angle would remain unchanged. The irregular cross-section of the tines makes it difficult to define a tine Reynolds number for the flow as was done in the case of the laboratory prototype. Because the relationship of interest is the mapping from the measured velocity to the undisturbed velocity, the equations are formulated in terms of the magnitudes and the angles of the velocities. The response of the sensor

Tow Speed [ $cm \cdot s^{-1}$ ]	Rotation Angle			
	0°	15°	30°	45°
1.2	1.12	1.23	1.56	4.33
5	1.07	1.15	1.44	3.69
10	1.06	1.12	1.41	3.29
20	1.04	1.09	1.36	3.04
35	1.04	1.09	1.35	3.02
50	1.04	1.09	1.36	3.02

Table 6.1: GAIN CORRECTION AS A FUNCTION OF TOW SPEED AND ROTATION ANGLE - The value of the gain correction is defined by Equation 6.1. The dependence on the magnitude of the velocity is essentially flat beyond  $10 \text{ cm} \cdot \text{s}^{-1}$ . The angular dependence is strong at all speeds. The response of the sensor for angles below  $30^\circ$  is relatively flat and the required correction is not excessive. For angles near  $45^\circ$  the correction is repeatable, but too large to preserve great measurement accuracy. As predicted, the correction at small rotation angles for the four tine prototype is smaller than the correction for the two tine prototype. Also in agreement with prediction, the measured velocity at small angles is low by less than 10 %.

clearly depends on the Reynolds number, but the dependence is not made explicit in this discussion. The gain corrections determined from the tow tank measurements are listed in Table 6.1 and plotted in Figure 6.8. The gain correction surface for the field prototype should be compared to the gain correction curve for the laboratory prototype (Figure 5.8).

The response is well behaved and relatively flat out to an angle of at least  $30^\circ$ . The magnitude of the correction in this region is not excessive. As predicted in Chapter 5, the correction at small rotation angles for the four tine prototype is smaller than the correction for the two tine prototype. The prediction that the measured velocity would be low by less than 10 % is also shown to be accurate. Curves drawn along the gain correction surface for a constant value of the rotation angle are qualitatively similar to the two tine gain correction curve in Figure 5.8. For angles near  $45^\circ$  the correction is repeatable, but the level of wake noise is high and the correction is too large to preserve great measurement accuracy. It is, of course, possible to remove or ignore velocities with angles near  $45^\circ$ , and the symmetrically equivalent angles, from the data set during processing. This did not prove necessary in the analysis of the field data described in Section 6.5. The gain correction surface is shown in polar form

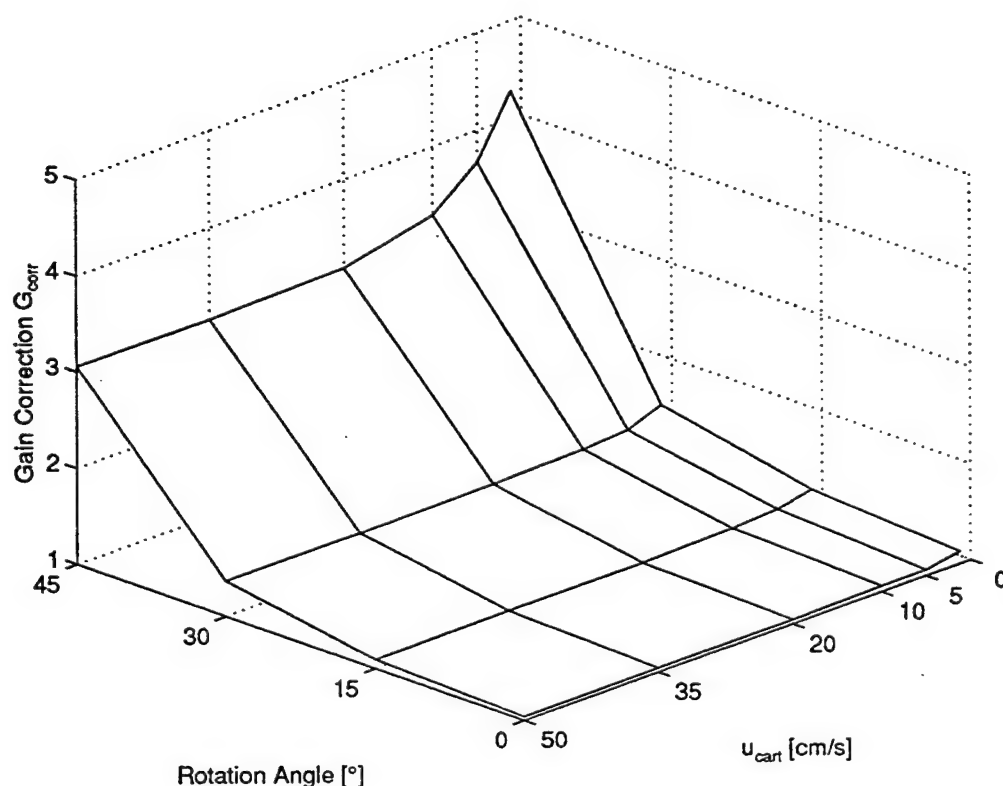


Figure 6.8: GAIN CORRECTION SURFACE AS A FUNCTION OF TOW SPEED AND ROTATION ANGLE - The gain correction at each point of the grid is calculated using Equation 6.1. Note the similarity of fixed angle curves on the surface to the two tine gain correction curve in Figure 5.8. As predicted, the four tine gain correction at small values of the rotation angle is smaller than the two tine gain correction and falls in the predicted range. The response of the sensor for angles below  $30^\circ$  is relatively flat and the required correction is not excessive. For angles near  $45^\circ$  the correction is repeatable, but too large to preserve great measurement accuracy. The surface is used to define a single-valued mapping from the measured velocity to the undisturbed velocity.

in Figure 6.9. This presentation fully characterizes the response of the field prototype sensor head.

The gain correction can now be formulated as a mapping from  $u_m$ , the measured velocity, to  $u_{gc}$ , the corrected velocity. The mapping can eventually be incorporated into the calibrated response of the sensor. The shape of the gain correction surface suggests a mapping that is exponential in the velocity angle,  $\theta$ . The relationship of the measured and undisturbed velocity magnitudes for fixed velocity angle is nearly linear, as in the case of the laboratory prototype. However, a best fit mapping that is



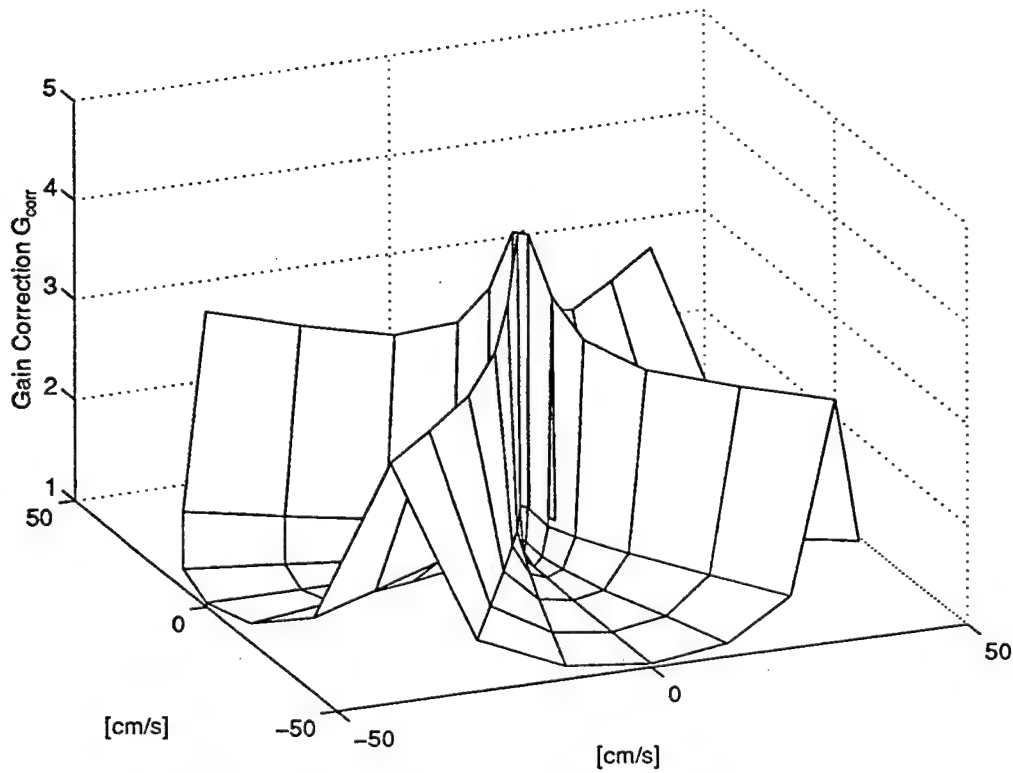


Figure 6.9: POLAR PRESENTATION OF THE GAIN CORRECTION SURFACE - The single octant of the gain correction surface shown in Figure 6.8 has been mapped to the eight octants of the polar velocity plane. Distance from the origin indicates the magnitude of the velocity. Angle about the origin indicates the angle of the velocity. The height of the surface is the gain correction. The angular locations of the four tines are clearly evident. The well behaved characteristic of the response for low angles, in the symmetrically equivalent sense, is also clearly apparent.

also exponential in the velocity magnitude produces an error surface,  $u_{cart} - u_{gc}$ , with a lower standard deviation than the best fit mapping that is linear in the velocity magnitude. The doubly exponential mapping, given in Equation 6.2, is therefore used here.

$$|u_{gc}| = (a_1 + a_2 e^{a_3 |u_m|}) (a_4 + a_5 e^{a_6 \theta}) \quad (6.2)$$

The six parameters,  $a_i$ , that minimize the least square error between the cart velocity

and the corrected velocity are

$$\begin{aligned} a_1 &= -9.60745 \cdot 10^{+1} & a_2 &= +9.60794 \cdot 10^{+1} & a_3 &= +2.20358 \cdot 10^{-4} \\ a_4 &= +4.83161 \cdot 10^{+1} & a_5 &= +4.06169 \cdot 10^{-1} & a_6 &= +1.20506 \cdot 10^{-1} \end{aligned}$$

These values assume that  $\theta$  is given in degrees, not radians, and that it falls in the range  $0 \leq \theta \leq 45$ . The error surface is shown in Figure 6.10. The standard deviation of the error surface is less than  $0.2 \text{ cm} \cdot \text{s}^{-1}$ . This mapping accuracy is better than the  $0.3 \text{ cm} \cdot \text{s}^{-1}$  accuracy level of the laboratory prototype mapping and well below the observed levels of wake noise. Like the laboratory prototype, the accuracy of the field prototype is limited by the flow disturbance of the intrusive sensor head and not by the electronics nor by the accuracy of the instrument calibration model.

Application of the mapping to a data set requires several processing steps. The velocity magnitudes and angles are determined from the measured velocity components in the instrument coordinate system. The angles are then folded, in the symmetrically equivalent sense, onto the first octant so that they fall in the appropriate range. The corrected velocity magnitude is then calculated with Equation 6.2 and the corrected velocity components are determined from the original angles. In the case of the beach measurements, the  $u_{ics}$  and  $v_{ics}$  velocity components in the instrument frame are equated with the on-shore and along-shore velocities. The gain corrected on-shore and along-shore velocities are denoted  $u_{ogc}$  and  $u_{agc}$ .

The field prototype was not calibrated in oscillatory flow. The decision to forgo these tests was based on the tight time constraint, the defined tasks that were to be accomplished with the field prototype, and the level of wake noise caused by the transducer stems and the loops of the coaxial harness wire. The characteristic length of the irregular tine cross-section is on the order of a centimeter and the tines are sharp edged. Therefore the sensor head flow distortion model, the literature, and the results of the Keulegan-Carpenter number tests with the laboratory prototype all support the decision. However, it will be necessary to calibrate the response of the integrated tine design in oscillatory flow as a function of  $KC$  and  $\theta$  once a complete

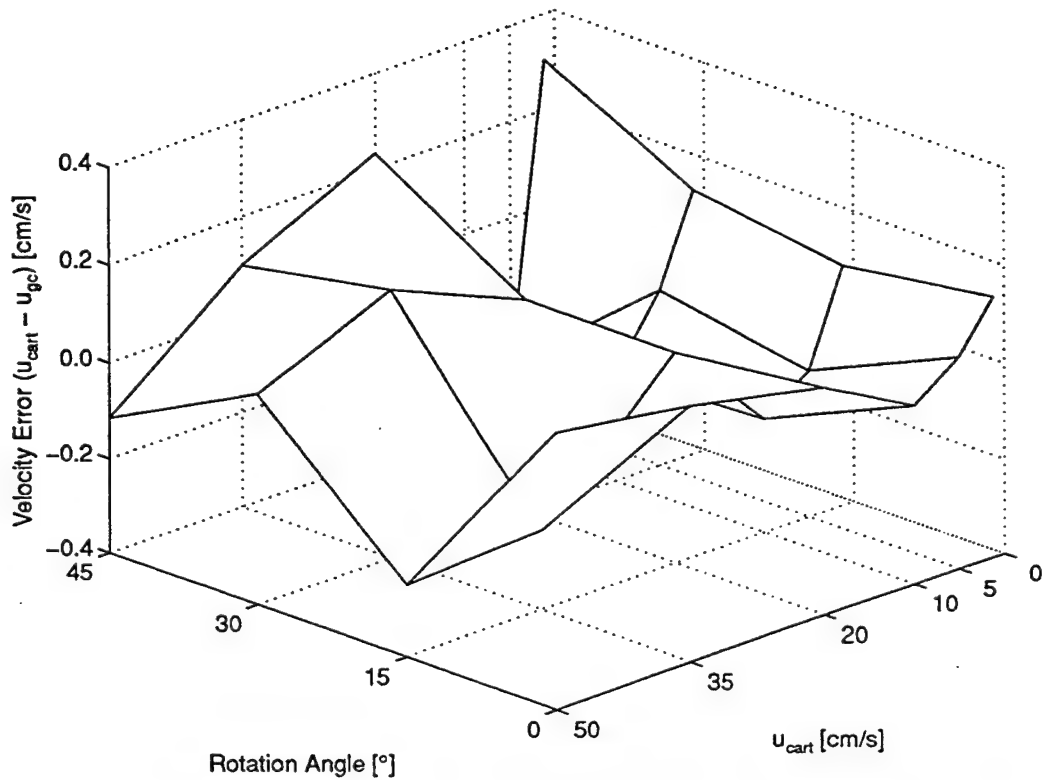


Figure 6.10: CALIBRATED MEASUREMENT ACCURACY OF THE FIELD PROTOTYPE - The plotted surface shows the error,  $u_{cart} - u_{gc}$ , of the gain correction mapping as a function of the magnitude and angle of the velocity. The standard deviation of the surface is less than  $0.2 \text{ cm} \cdot \text{s}^{-1}$ . The accuracy of the field prototype is limited by the flow disturbance of the intrusive sensor head and not by the electronics nor by the accuracy of the instrument calibration model.

set of tines is fabricated.

The cosine response of the field prototype degrades sharply only as the wake of the stems and the coaxial loops fully shadows the acoustic axes. This suggests that a sensor head built with the slender tines described in Chapter 2 will have a range of relatively flat, small gain correction that closely approaches  $45^\circ$  in each symmetrically equivalent octant. It may also be anticipated that the level of wake noise will be reduced in the final design by the regular cross-section of the tines. The accuracy of the mapping and the general performance of the field prototype, inclusive of the large distortion of the flow by the irregular tines, promise a smooth and well behaved response for the final design of the BASS Rake sensor head.

## 6.5 Near-Shore Field Deployments

The field prototype was twice deployed outside the surf zone of Nobska Beach, located approximately 1 *Km* from WHOI. The site is shown at two scales in Figures 6.11 and 6.12. The first deployment, on a mixed sand and cobble bottom designated Site 1, did not return any velocity measurements.<sup>1</sup> However, the author was able to closely observe and photograph the site and the instrument on several occasions while diving. These observations are important to the interpretation of the data from the second beach deployment and are reported very briefly in Section 6.5.1. A large sand patch was also located and photographed during the observation dives. This location, designated Site 2, was subsequently chosen for the second deployment, described in Section 6.5.2. The second deployment returned several weeks of velocity profiles, but no concurrent visual observations of the bottom were made.

### 6.5.1 Bottom Observations During the First Deployment

The instrument was deployed from Nobska Beach by four divers on November 20, 1996 and recovered by the same means on December 4, 1996, 14 days later. There were no large wind or storm events during that period. Irregular visual observations of the waves were made from the beach throughout the deployment. Significant wave heights varied from zero to 40 *cm* or 50 *cm* with periods from 4 *s* to 7 *s*.

The approximate location of Site 1 is marked on the chart in Figure 6.12. The depth is 3 *m* to 4 *m*. The bottom at Site 1 is relatively flat on meter length scales and covered by cobbles intermixed with small, amorphous, patches of sand. Characteristic horizontal dimensions for the sand patches vary up to 50 *cm*. Thick seaweed reaching 75 *cm* to 100 *cm* covers the bottom in patches. Seaweed was removed from the immediate vicinity of the frame during the deployment. The frame and sensor head remained free of drifting organic matter throughout the deployment. All rocks larger

---

<sup>1</sup>The data line to the logger was manually disabled after the tow tank calibration so that several transducer tests could be performed. The control switch was, unfortunately, not returned to the operational position after testing and, to the author's great annoyance and embarrassment, the logger files contained only null values when the instrument was recovered.

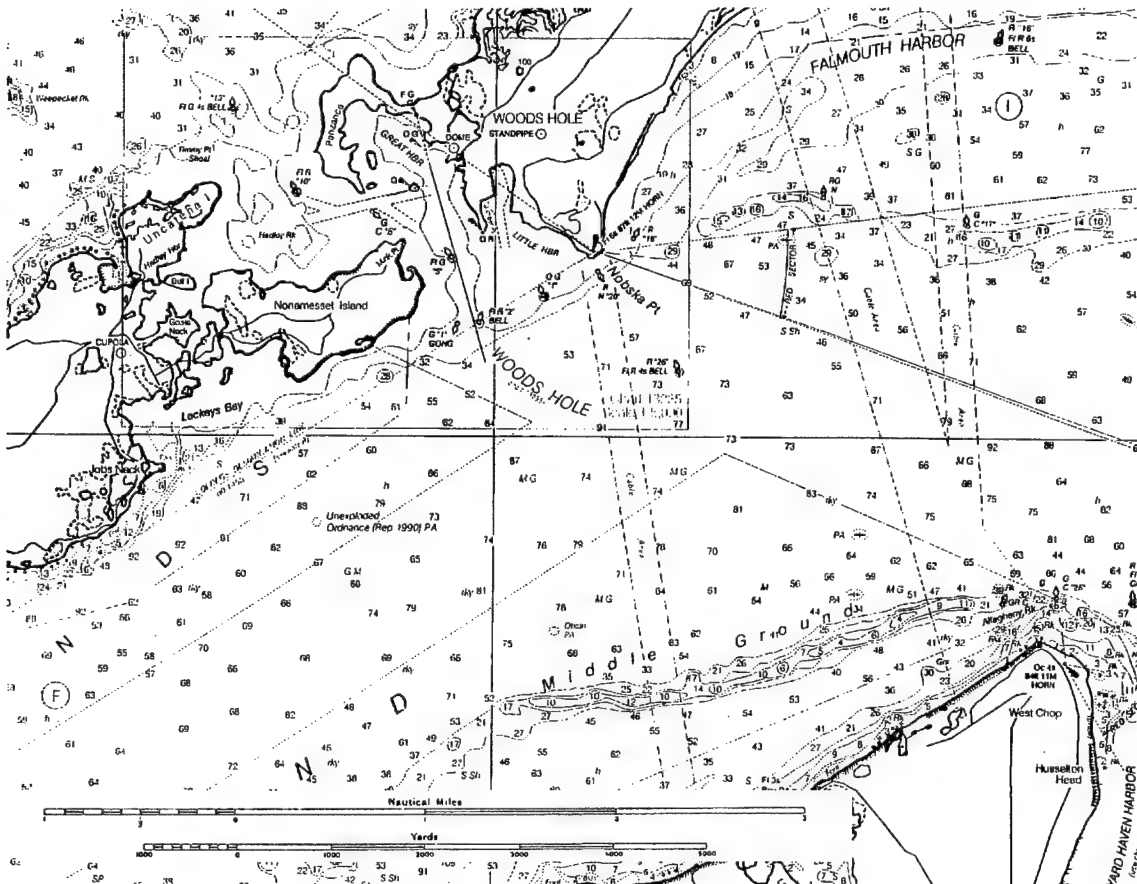


Figure 6.11: COASTAL CHART AND BATHYMETRY FOR THE WOODS HOLE AREA - North is towards the top of the chart, all soundings are in feet. WHOI is located at the DOME (⊙) on Great Harbor in the upper center. Nobska beach is to the east between Little Harbor and Nobska Point. The beach faces south-southwest along the broad channel of Vineyard Sound. The land mass to the south is Martha's Vineyard. The body of water northwest of Woods Hole Passage is Buzzard's Bay. Strong tidal currents flow through the passage from the Bay to the Sound during the flood tide. The flow is reversed during ebb tide. Strong tidal currents also flow around Nobska Point. The shallow bay of Nobska Beach is sheltered and the ebb and flood currents looping through the bay and along the beach are comparatively weak.

than the cobbles were cleared from the area within the legs of the outer support frame. A survey showed that none of the meter scale and larger rocks marked on the chart in Figure 6.12 were within 3 m to 5 m of the frame. In particular, there were no large obstructions either landward or seaward of the instrument, the expected axis of wave propagation.

The prototype was secured in place with eight heavy load, screw-in anchors and  $\frac{3}{8}$ " nylon line. Two anchors were used at each corner of the frame. Each is placed

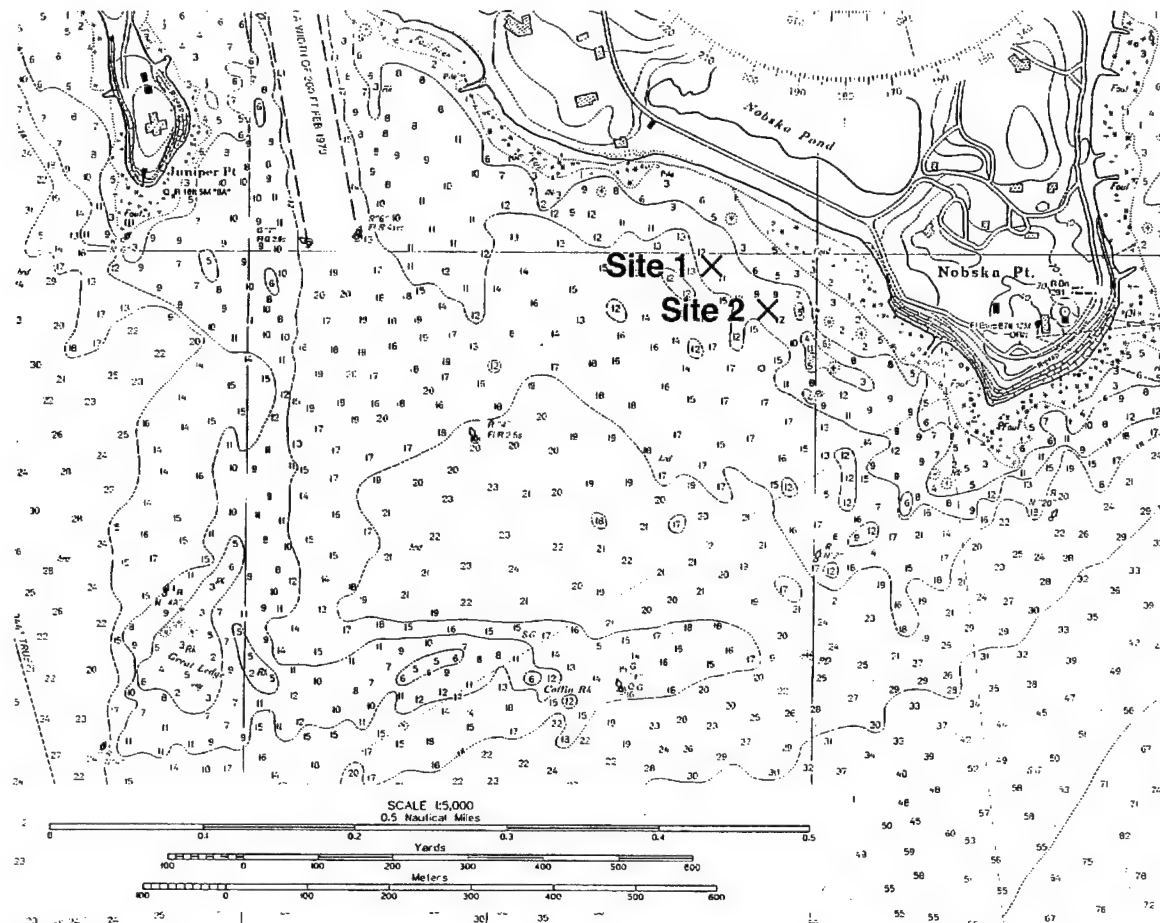


Figure 6.12: COASTAL CHART AND BATHYMETRY FOR NOBSKA BEACH - North is towards the top of the chart, all soundings are in feet. Nobska Beach faces south-southwest in the upper center. Woods Hole Passage is to the west. The approximate locations of the two field deployments are marked Site 1 and Site 2. The shallows of Great Ledge southwest of Nobska Beach attenuate waves propagating northeast up Vineyard Sound. The longest fetch for the beach is in this direction. Some phases of the tidal currents may refract waves around Great Ledge and onto the beach with less attenuation. The BASS Rake measurements consistently show increased wave velocities during the flood tide.

approximately 0.5 m from the foot of the adjacent support frame leg with a 90° angular separation. The lines were hand tightened and provided some compliance in the mount. There is no evidence that the frame shifted laterally at any time during this deployment. Similarly, there is no evidence of slamming and none of the transducers were damaged. Figure 6.13 shows one of the anchors in place in the bottom with the anchor line running up to the top corner of the box frame.

After the instrument was secured, a shallow hole was dug for the ring and tine extensions and the inner frame was lowered. Cobbles and rocks were removed for

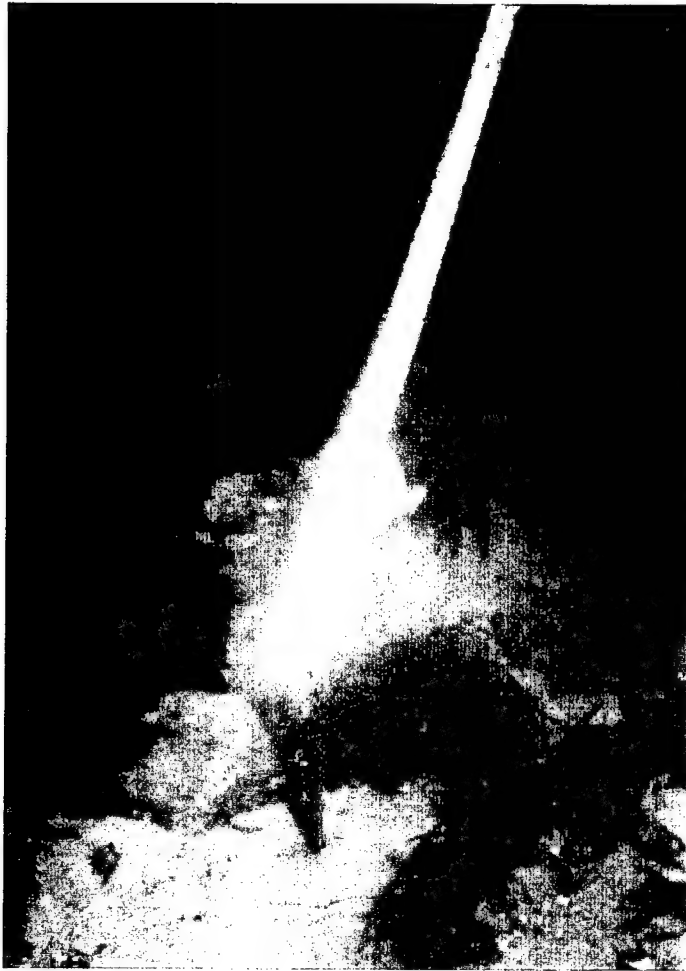


Figure 6.13: ANCHOR AND ANCHOR LINE SECURING THE FIELD PROTOTYPE TO THE BOTTOM - The protruding top of the anchor shaft, approximately 10 *cm*, is visible in the center of the photograph. The 10 *cm* diameter slotted twist plate welded to the shaft near the bottom of the anchor is approximately 30 *cm* below the fluid-sediment interface. The nylon line is clearly visible running up towards the attachment point at the top corner of the box frame. A sand patch, rocks, and some of the seaweed are visible around the anchor shaft. The photograph was taken on November 30, ten days into the deployment. Photograph by the author.

a radius of 50 *cm* around the sensor head and sand was manually transported from outside the frame to fill the hole and to cover and level the area cleared of cobbles. The constructed sand patch around the sensor head was roughly smoothed by hand before the divers left the site. Dives were made on November 22 and November 30 to inspect the instrument and observe the bottom near the tines. The divers visited both Site 1 and Site 2 on these occasions. Underwater photographs were taken during the dive on



Figure 6.14: NOBSKA BEACH AND THE DEPLOYMENT AREA - The photograph shows the view to the west from Nobska Point. Nobska beach is visible on the right. Conditions are calm and the tide is low, exposing several of the rocks marked on the chart in Figure 6.12. The deployment sites are both in the left third of the photograph and well outside the line of rocks. Photograph by the author.

November 30. The beach and deployment area were photographed on November 23. Figure 6.14 is the view looking west from Nobska Point (see Figure 6.12). The bottom near the tines was observed one final time on December 4, immediately prior to recovery.

On each occasion of observation, the constructed sand patch around the tines supported three sand ripples with the geometry shown in Figure 6.15. The ripple wavelength,  $\lambda_b$ , was 25 cm to 30 cm and approximately constant, with the center ripple fixed midway between the tines. The ripple height,  $\eta_b$ , varied dynamically from 5 cm to 8 cm. Figure 6.16 is a photograph of the tines and ripples.

The ripples were manually smoothed away during the first observation dive and



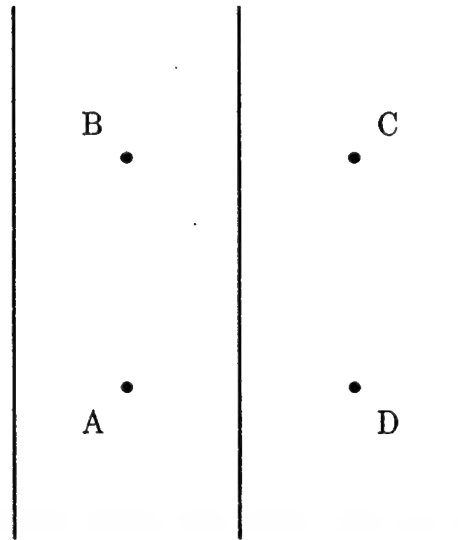


Figure 6.15: RIPPLE GEOMETRY NEAR THE TINES - The four tines, in plan view as seen from above, are shown as filled circles with their letter designations. The three vertical lines mark the persistent locations of the ripple crests. The elements of the figure are drawn to a common scale.

had reformed by the time of the second dive, demonstrating that the geometry is persistent. The presence of the ripples during the first observation dive indicates a generation time of no more than two days. The ripple crests were not perfectly straight, but exhibit shallow curves, deforming somewhat around the tines and the protruding stems and loops. The curve in the crest of the foreground ripple is visible in Figure 6.16. It is possible that the ripples were generated by the flow around the tines and would not have existed, or would have been markedly different, if the instrument had been absent. This is a disturbing possibility. Unfortunately, the shallow curves of the ripple crests suggest some influence on the formation process. However, the constructed sand patch supporting the ripples was symmetric about the tines and both the sensor head and the wave forcing were oriented to the shore line. It is, therefore, also possible that the ripples were locked to the constructed sand patch. The observed values of  $\lambda_b$  and  $\eta_b$  on the constructed sand patch are consistent with the values observed on sand patches of comparable size during the general diving surveys of the area. Thus, it appears likely that the ripples were "normal" for that location and that the presence of the tines simply modulated the generation process.

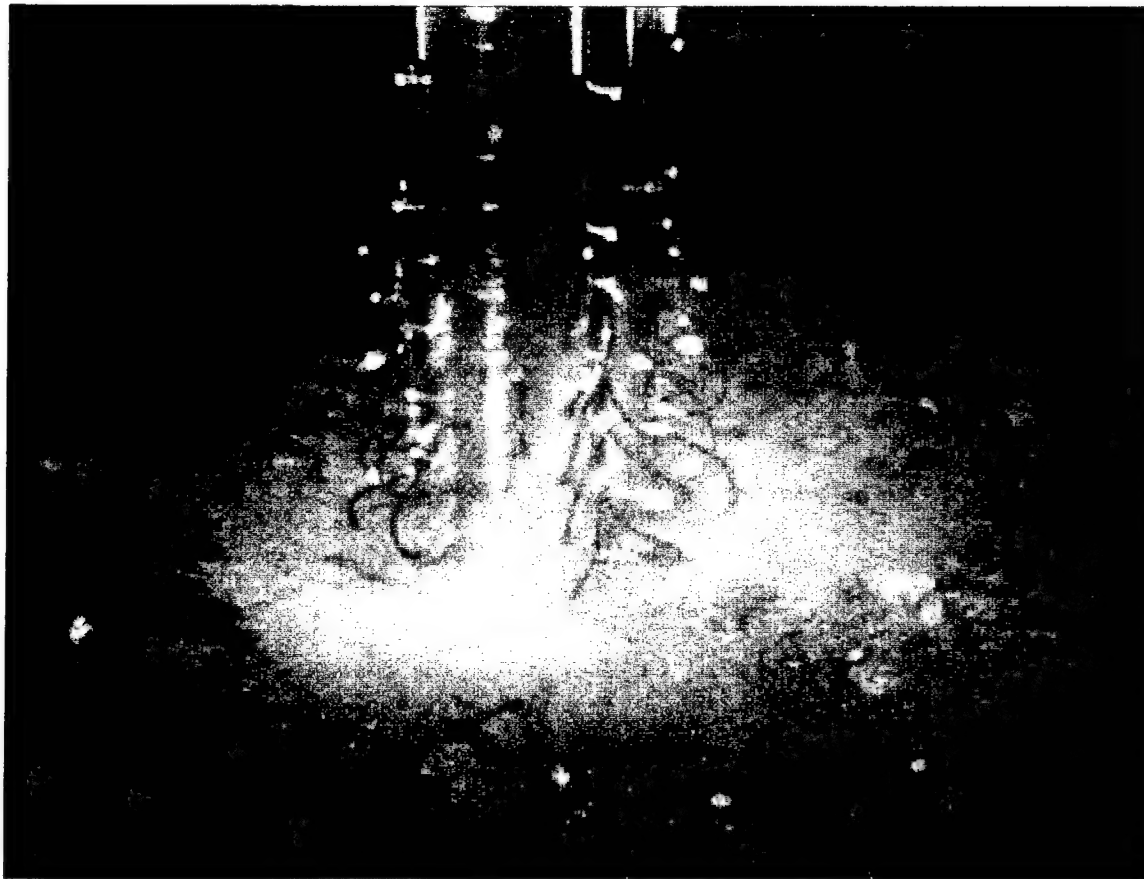


Figure 6.16: SAND RIPPLES NEAR THE TINES - The sensor head is visible in the center of the photograph and one of the three ripples is visible in the foreground. A shallow curve is visible in the crest. The curve is mirrored by the crest of the far ripple. The view is seawards and the near tine on the right is C. Photograph by the author.

It is reasonable to assume that the influence of slender tines will be less in either ripple formation scenario. No final conclusion can be reached without further use and observation.

## 6.5.2 Near-Bottom Velocity Measurements During the Second Deployment

### 6.5.2.1 General Observations and Measurements and the Evolution of the Bottom at Site 2

The field prototype was restarted on December 5, 1996 and left with the sensor head in a bucket of standing water for a period of approximately 20 hours (see Figure 6.2). The velocity record from this period shows the decay of organized flow down to the level of thermal convection. It also indicates the depth dependent effects of winds which blew across the open mouth of the bucket during the last few hours of the record. The field prototype was deployed at Site 2 by four divers at approximately 1200 hours on December 7, 1996. The location is marked on the chart in Figure 6.12.

Site 2 is an open sand patch 5 *m* to 8 *m* across in all directions. The water depth is approximately 3 *m*. A regular pattern of sand ripples was observed on each of the four occasions that the site was visited by divers in November and December of 1996. Those observations bracket the experiment. The BASS Rake measurements show that the bed was reworked over the course of the experiment and are consistent with the persistent presence of dynamically changing sand ripples. This appears to be the normal condition of Site 2. Figure 6.17 is a photograph of Site 2 taken on November 30, one week before the second deployment. The ripples are symmetric, indicating generation by waves rather than currents. The wavelength is 25 *cm* to 30 *cm* and the height is 5 *cm* to 8 *cm*. Wave forcing during late November and early December was fairly mild. The velocity measurements indicate greater ripple height during storm events in mid and late December.

The instrument was secured in place with screw-in anchors, as described in Section 6.5.1. While inserting the anchors, it was discovered that the sand at Site 2 is only 15 *cm* to 20 *cm* deep and covers a layer of packed cobbles. One anchor was damaged in attempting to penetrate the cobble layer and could not be used. The remaining seven secured the frame, but were not uniformly well seated. One area of future work with the BASS Rake will be investigation into more reliable anchoring

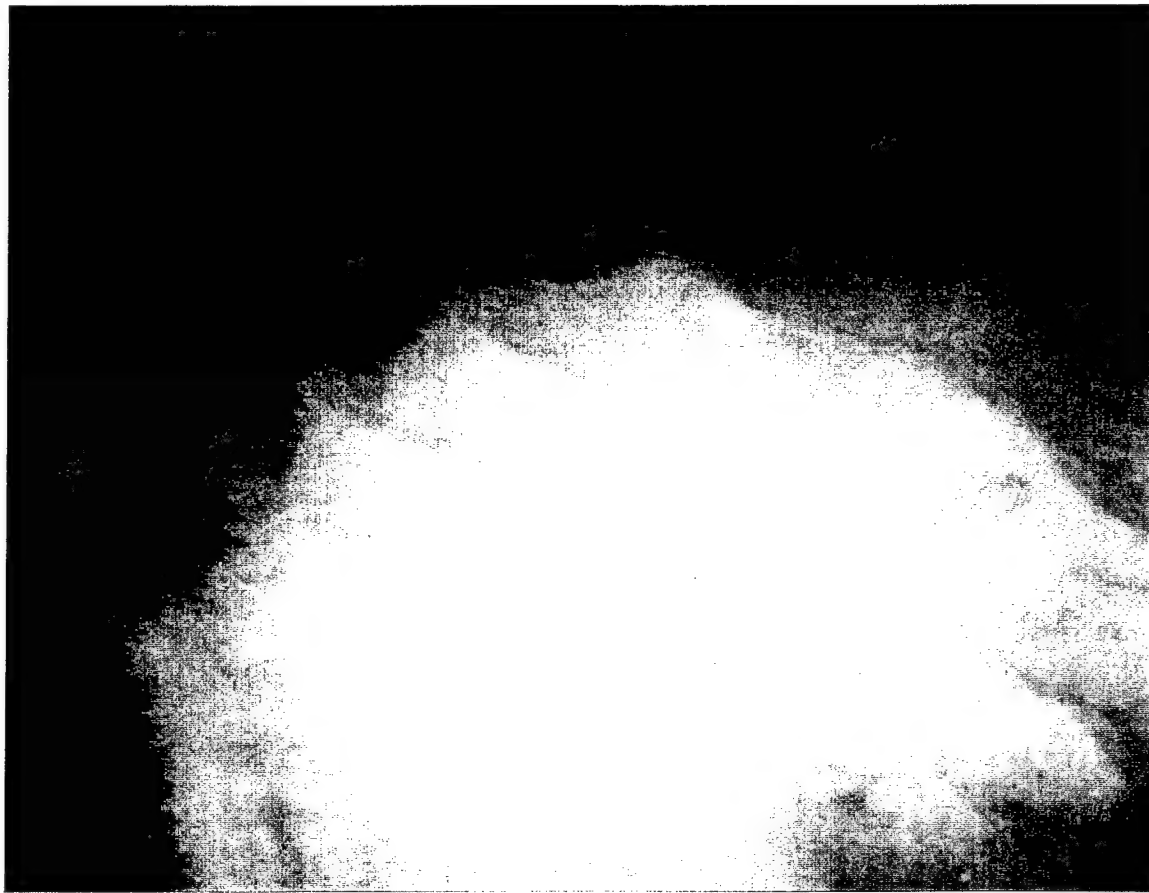


Figure 6.17: REGULAR SAND RIPPLES AT SITE 2 - The photograph shows the regular pattern of sand ripples observed on four occasions at Site 2. The wavelength is 25 cm to 30 cm and the height is 5 cm to 8 cm. The symmetric shape indicates generation by waves rather than currents. The photograph was taken on November 30, 1996, one week before the second deployment. Photograph by the author.

techniques. As before, a shallow hole was dug in the sand below the sensor head and the inner frame was lowered. The hole was filled in with sand and the area around and between the tines was manually smoothed before leaving the site. The instrument was not revisited until the recovery on December 31.

The evolution of the bottom and changes in the instrument during the deployment can be reconstructed from the velocity measurements. The sensor response mapping described in Section 6.4 has been applied to all of the measurements reported here. The on-shore and along-shore velocities are denoted  $u_{ogc}$  and  $u_{agc}$ . Consistent with the instrument coordinate system,  $u_{ogc}$  is positive towards the beach, roughly north-

ward, and  $u_{agc}$  is positive from Nobska Point towards Woods Hole Passage, roughly westward. It was noted in Section 6.2 that acoustic axes A4-C4 and B9-D9 failed during assembly. Clean velocity records were recorded by the remaining eight measurement levels on December 7, the day of the deployment. Beginning at 2100 hours on that day, near-bottom wave velocities began to increase. By 2230 hours the velocities had more than doubled, with sustained amplitudes of  $30 \text{ cm} \cdot \text{s}^{-1}$  to  $40 \text{ cm} \cdot \text{s}^{-1}$ . Isolated peaks reached  $60 \text{ cm} \cdot \text{s}^{-1}$ . Approaching midnight, the lower three measurement levels began intermittently returning null values. The velocity records show this behavior advancing in fairly rapid sequence from Level 0 to Level 2. Levels 1 and 2 returned intermittent velocities during both flood tides on December 8. The first of the December 8 flood tides began at 0100 hours as the storm waves decayed. In both instances Level 2 began operating sooner and ceased operating later. Level 0 returned only nulls during this period. All three levels returned only nulls for more than a week following December 8. Later in the record the pattern of intermittent velocities during the flood tide is repeated.

This early portion of the data set shows reworking of the bottom and the growth of a sand ripple to a height of  $5 \text{ cm}$  or more between the tines.  $5 \text{ cm}$  is the minimum height necessary to block acoustic transmission at Levels 0, 1, and 2. Continued modification of the bottom ripples occurs during some periods of flood tide. This interpretation is supported by the measured general characteristics of the near-bottom flow and by estimates of the Shields parameter for selected times on December 7. The Shields parameter,  $\psi_s$ , is a normalized measure of the bottom stress applied to the particles comprising the sediment bed. The normalization includes size, density, and specific gravity information about the particles and the fluid. A critical level of the parameter,  $\psi_{crit}$ , above which sediment motion will occur, has been established empirically. However, the experimental work was generally performed for steady flow using non-cohesive grains of uniform size and density. Even under these idealized conditions, the results have varied significantly. Published curves of  $\psi_{crit}$  can be applied to naturally occurring sediment beds using qualitative rules based on experience. An appreciation for the ranges of applicability and error is necessary. A more detailed

discussion of the Shields diagram and the modified Shields diagram can be found in Madsen [46]. Some experimental results for oscillatory flow are included. For non-uniform, non-cohesive, beds, Madsen suggests that sediment motion will begin when  $\psi_s$  is approximately half of  $\psi_{crit}$ . The calculation of both quantities is to be based on the size and density characteristics of the median grains.

Examination of the data from Levels 3 and above reveals a clear tidal signature throughout the experiment. Wave velocities are consistently higher during the flood tide while a strong current,  $> 3 \text{ kt}$ , comes through Woods Hole Passage from Buzzard's Bay and into Vineyard Sound (refer to Figure 6.11). It is possible that flood tides refract waves around Great Ledge (see Figure 6.12) and onto the beach with less than normal attenuation, but no mechanism has been firmly established. The eastward flow crosses the mouth of the shallow bay of Nobska Beach. Well off-shore of Nobska beach the peak flood tide velocity exceeds  $1.5 \text{ kt}$ . Within the bay, the along-shore current at Site 2 is eastward through the first half of the flood. It then reverses direction over a period of 15 to 20 minutes and flows westward for the remainder of the flood tide and the first half of the westward flowing ebb. This suggests the formation of vortical motion on the scale of Nobska Beach and the shallow bay. A clear semi-diurnal inequality is also evident in the data. These characteristics of the near-bottom flow are shown in Figures 6.18, 6.19, and 6.20 for December 11. This day is qualitatively typical; however, it coincides with the peak of the early December spring tide and the strength of the tidal signature is significantly greater than average. Wave velocities during the flood tide are comparable to those experienced during the storm on December 7.

Higher wave velocities and shorter wave periods both increase the bottom stress and rework the bed, potentially forming or modifying a pattern of sand ripples. The particularly high wave velocities that began at 2100 hours on December 7 were associated with a storm. They began to rise several hours in advance of the flood tide and the spectral content indicates local wind generation. The wave velocities were 30 % to 40 % higher than the average enhancement associated with the flood tide. The storm event was immediately followed by a period of flood tide, which began at

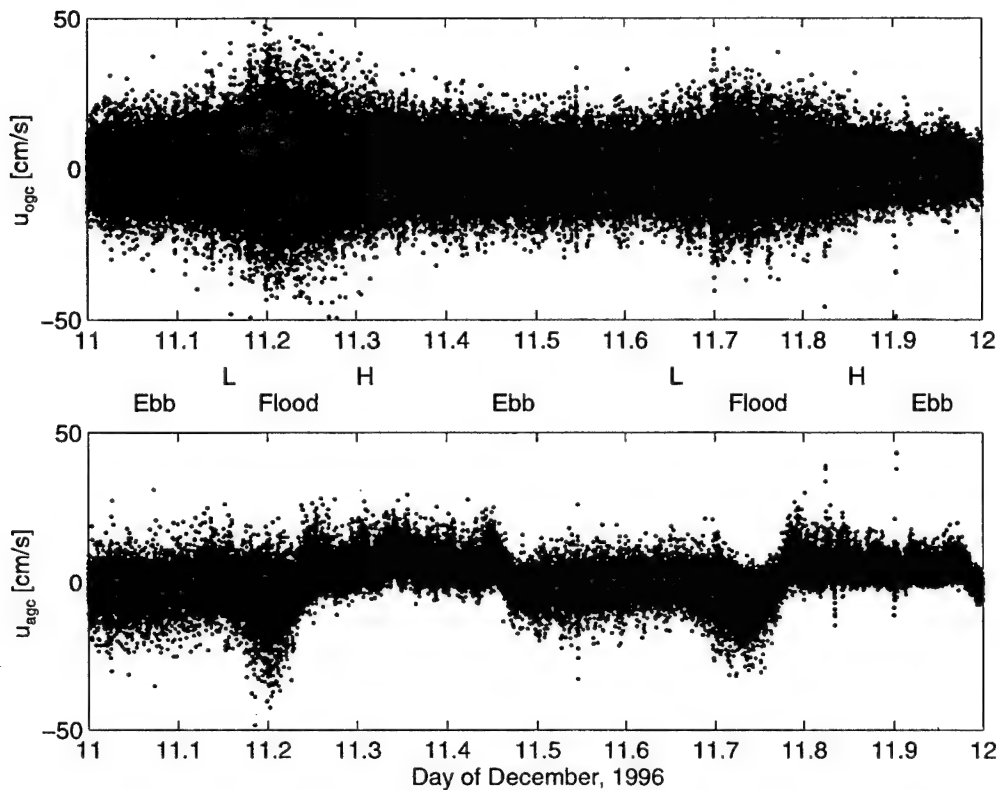


Figure 6.18: VELOCITY MEASUREMENTS AT LEVEL 3 FOR DECEMBER 11, 1996 - The two panels show the on-shore and along-shore velocities sampled at  $1\text{ Hz}$  approximately  $8.5\text{ cmab}$ . The horizontal scale extends for 24 hours, from midnight to midnight. 11.5 on the scale is noon of December 11, 1996. The state of the tide is marked on the strip between the panels. “H” and “L” mark the approximate times of high and low water at Little Harbor, adjacent to Nobska Beach. The periods of flood and ebb are also marked. Clearly the on-shore wave velocities increase during the flood tide and a semi-diurnal variation of this characteristic is evident. The along-shore record shows a repeating and asymmetric pattern of currents synchronized with the tides.

0100 hours on December 8. The waves early in the afternoon of December 7 had a relatively broad spectrum with two distinct peaks and periods from  $6\text{ s}$  to  $10\text{ s}$ . By 1900 hours the spectrum had narrowed, with a single peak in spectral density at  $10\text{ s}$ . The storm shifted the spectral peak down to  $4\text{ s}$  and raised the spectral density by an order of magnitude. Velocity standard deviations and means for December 7 are shown in Figure 6.21 and the three wave spectra are shown in Figure 6.22.

The bed at Site 2 is composed of quartz sand grains with a characteristic dimension of  $0.25\text{ mm}$  ( $250\text{ }\mu\text{m}$ ). The critical value of the Shields parameter for Site 2 is  $\psi_{crit} =$

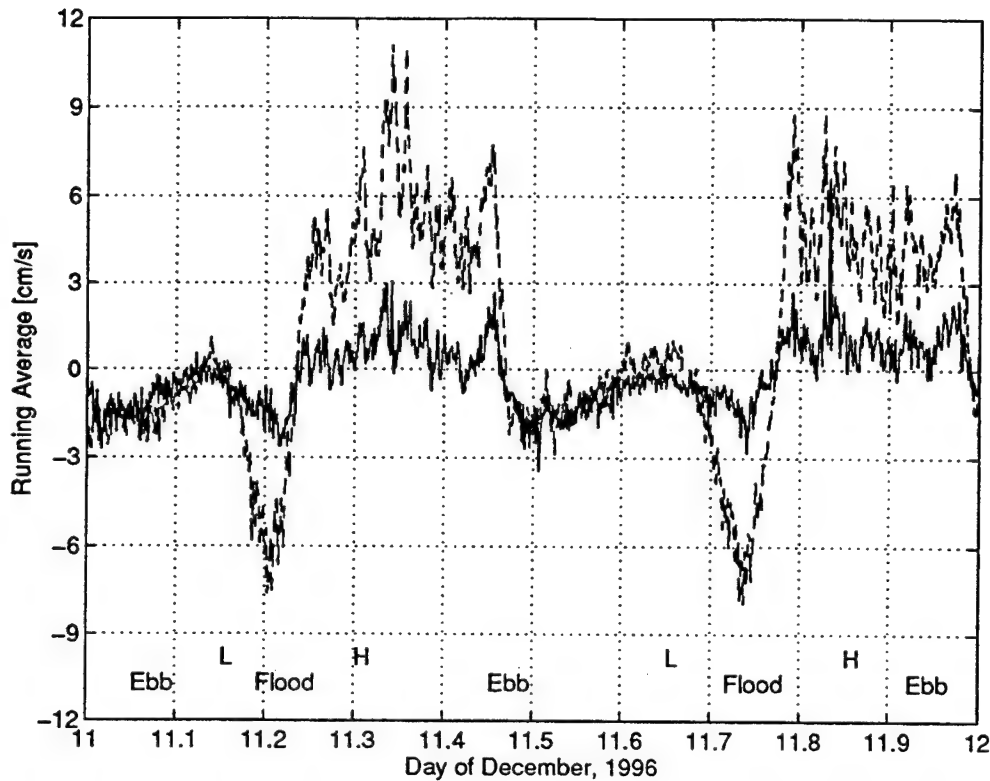


Figure 6.19: RUNNING AVERAGES OF THE LEVEL 3 VELOCITY COMPONENTS FOR DECEMBER 11, 1996 - The solid (—) and dashed (---) traces show running averages of the on-shore and along-shore velocities presented in Figure 6.18. The average is taken over 100 measurements in each direction of a bi-directional pass through the filter. The effective average is over 200 measurements. The average removes the wave signal and the bi-directional passes bring the phase shift of the filter to zero. Time and tide marks are described in the caption of Figure 6.18. The behavior of the along-shore tidal current, particularly the rapid reversal of direction during the flood, is more clearly apparent in this presentation than in the unaveraged velocity record.

$4.5 \times 10^{-2}$ . On the afternoon of December 7, before the storm event,  $\psi_s$  was  $\approx 1.6 \times 10^{-2}$ , well below the  $\frac{\psi_{crit}}{2}$  criterion of Madsen.<sup>2</sup> It is reasonable to conclude that the bed was not being reworked at this time. In the hours approaching midnight, the storm winds steadily increased the Shields parameter through the range  $4.4 \times 10^{-2} < \psi_s < 6.6 \times 10^{-2}$ , well above the level indicating sediment motion. The first intermittent measurements at Level 0 began at this point, indicating ongoing growth

<sup>2</sup>The bottom stress was calculated from the BASS Rake measurements using the wave-current boundary layer of Grant and Madsen [46].



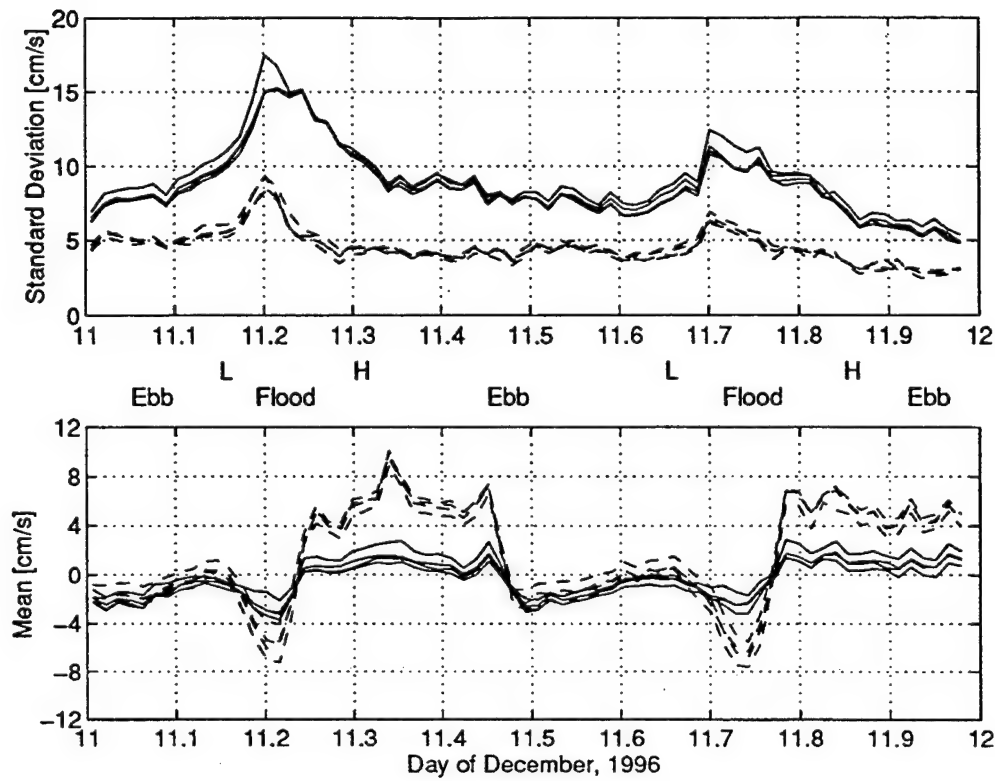


Figure 6.20: 20 MINUTE STANDARD DEVIATIONS AND MEANS FOR DECEMBER 11, 1996 - The two panels show the standard deviations and the means of the on-shore (—) and along-shore (---) velocities at Levels 3, 5, 7, and 8. The nominal heights are 8.5 *cmab*, 13.5 *cmab*, 18.5 *cmab*, and 21 *cmab*. The calculations were performed on sequential 20 minute sections of the measurements. The state of the tide is marked in the strip between the two panels. Time and tide marks are described in the caption of Figure 6.18. The standard deviations show the sharp increase in wave velocities associated with the flood tide and also the semi-diurnal inequality of this characteristic. The means show the asymmetric along-shore flow. The combination of the on-shore and along-shore means, the known location of the measurement, and the bathymetry support the idea that vortical motion on the scale of the beach begins midway through the period of flood and persists until the midpoint of the ebb tide. Note again the rapidity of the along-shore flow reversal during the flood tide.

of bedforms. Wave velocities, recorded higher above the bottom, continued to increase through midnight, and the Shields parameter reached a sustained level of  $1.3 \times 10^{-1}$ . The highest values of  $\psi_s$ , determined from velocity measurements recorded near the peak of the storm, exceeded  $2.0 \times 10^{-1}$ . These values suggest heavy transport of sand grains over the bed. These calculations strongly support the interpretation that the bed was rapidly reworked at this time, forming sand ripples on the portion of the sand

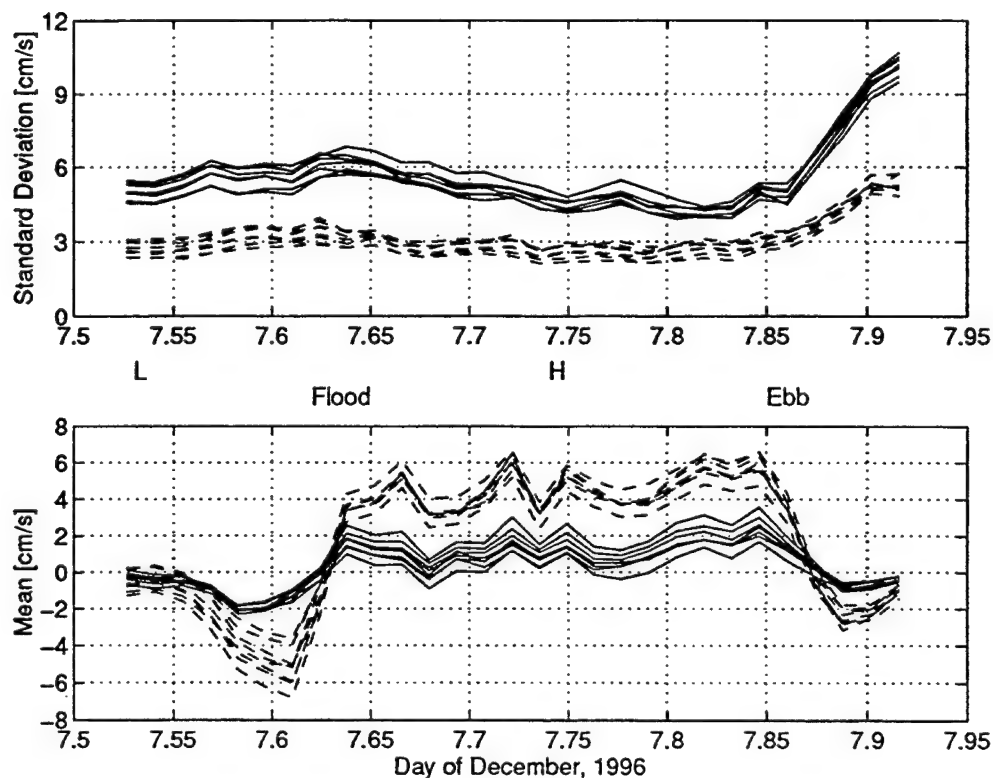


Figure 6.21: 20 MINUTE STANDARD DEVIATIONS AND MEANS FOR DECEMBER 7, 1996 - The two panels show the standard deviations and the means of the on-shore (—) and along-shore (---) velocities at Levels 0, 1, 2, 3, 5, 6, 7, and 8. The nominal heights are 1.0 *cmab*, 3.5 *cmab*, 6.0 *cmab*, 8.5 *cmab*, 13.5 *cmab*, 16.0 *cmab*, 18.5 *cmab*, and 21 *cmab*. The calculations were performed on sequential 20 minute sections of the measurements. The horizontal scale extends for less than 12 hours, from noon, 7.5, on December 7, 1996 until nearly midnight, 8.0, on December 8. The data cover the period from the time the divers left the site until the lowest measurement levels began to return intermittent nulls. The state of the tide is marked in the strip between the two panels. "H" and "L" mark the approximate times of high and low water at Little Harbor, adjacent to Nobska Beach. The periods of flood and ebb are also marked. The the along-shore flow reversal and a weak increase in wave velocity is apparent during the early afternoon flood tide. The weak enhancement coincides with the early December neap tides. The strong and rapid increase in wave velocities that began at 2100 hours (7.87) is clearly evident in the standard deviation traces. Note that the increase occurred during the ebb tide. These waves were generated by local wind forcing. The next flood tide did not begin until 0100 hours on December 8 as the waves began to decay. Comparison to Figure 6.20 shows that many features of the average wave behavior and of the mean flow are present during both the spring and neap phases of the tidal cycle. However, the strength of these features, particularly the wave velocities, appears to vary with the strength of the tidal currents. Wave velocities are modulated over semi-diurnal, diurnal, and spring/neap time scales.

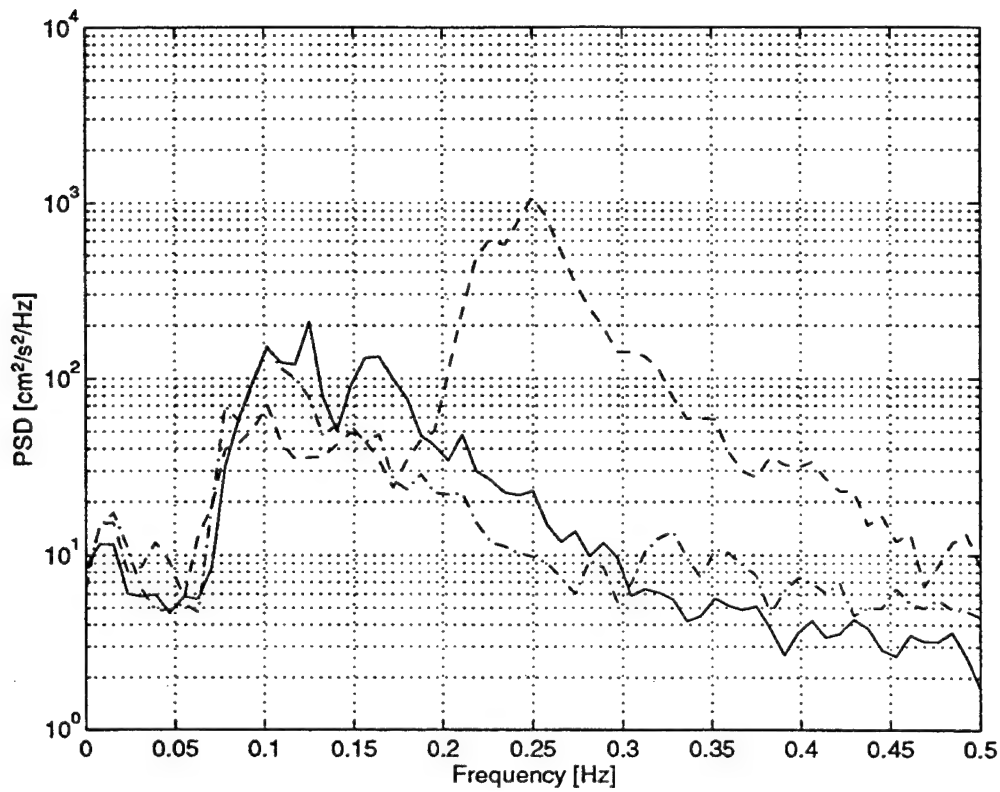


Figure 6.22: WAVE SPECTRA FOR DECEMBER 7, 1996 - The three traces show wave spectra for 1600 hours (—), 1900 hours (---), and 2200 hours (-.-) on December 7. These times correspond to 7.67, 7.77, and 7.91 on the time axis of Figure 6.21. The spectra were calculated from the on-shore velocity component of Level 8, nominally 21 *cmab*. The short period waves present in the early afternoon are absent in the early evening, leaving 10 *s* waves, presumably generated some distance away. The strong, late evening, increase in wave velocities and the increase in wave energy at 4 *s* is readily apparent. Note that the 10 *s* waves, somewhat reduced in magnitude, were still present.

patch around the sensor head that had been smoothed. The observations of Site 1 show that a persistent sand ripple can form between the tines and the observations of Site 2 show that ripples with a height of 5 *cm* or more are normally present. This is also consistent with the interpretation. Finally, experimentation with the laboratory prototype showed that a sand ripple that physically obstructs the acoustic axis will prevent any measurement and cause a null value to be returned. The conclusion that a sand ripple obscured the lowest measurement levels is reasonable and well supported.

The subsequent intermittent velocity measurements, made during periods of flood tide, show continued modification of the bed at the times of greater bottom stress.

The velocity measurements made further above the bed clearly show the increase in near-bottom wave velocities. Values of the Shields parameter during representative flood tides fall in a wide range from  $\psi_s < 2 \times 10^{-2}$ , which is less than  $\frac{\psi_{crit}}{2}$ , to  $\psi_s > 5 \times 10^{-2}$ , which is greater than  $\psi_{crit}$ . It is reasonable to conclude that, during some occurrences of flood tide, the bottom remains stable. A stable bed is also normal during ebb tide. At other times, sediment motion does occur during the flood tide, either strongly or weakly, and the height or position of the obscuring ripple or ripples is occasionally altered sufficiently to permit acoustic propagation along the lower axes. This interpretation of the measurements is both consistent and reasonable. Note that the asymmetric correlation of sediment resuspension with the phase of the tide can support net advective transport. Fine sediment, in varying concentration and possibly organic in origin, was observed in suspension during all of the inspection dives and a thick coating of fine sediment aggregates was visible on rocks and seaweed after one storm. This material is easily resuspended and settles slowly, readily providing mass for net transport.

The possibility exists that the measurement intermittence of Levels 0, 1, and 2 is caused by vertical movement of the sensor head rather than reworking of the bed. This would occur if the frame rocked back and forth on the footpads under the influence of wave forcing on the pressure housing and the structural elements. Like reworking of the bed, this would be associated with periods of increased wave orbital velocities. Slamming did occur on December 24, caused by strong wave forcing during a storm, and the quality of the records deteriorates after December 20. The deterioration may be caused by dynamic flexure of the exposed loops of the coaxial harness. The electronics package did not include tilt sensors, so the possibility of instrument movement cannot be disproved by a direct measurement. Consider, however, that each time the sensor head moved upwards, sand would fill the volume vacated by the tines and the structural ring. This would prevent the sensor from returning to the original height above the nominal bottom when the rocking ceased. Rocking would tend to expose the lower acoustic axes and not rebury them. Measurements taken before December 24 show no evidence of this tendency. Additionally, unless the foot-

pads of the support frame sank several centimeters into the bottom, the intermittence recorded at Level 3 on December 20 (described below) can only be explained by ripple growth. The data and observations are more consistent with ripple formation and episodic reworking of the bed. The model based calculations support this interpretation, as do the profile measurements presented in Section 6.5.2.2. Movement of the frame before December 20 is therefore assumed to be negligible.

The evolution of the bottom during the remainder of the deployment includes several similar episodes of bed and ripple modification. Levels 0, 1, and 2 returned only null values for eight days following the initial occurrences of intermittent velocity measurements during the flood tides on December 8. Axis B6-D6 failed early on December 8. The loss was caused by the bending moment applied to the stem of the transducer assembly by the harness loop. The four functioning measurement levels, Levels 3, 5, 7, and 8, recorded without interruption during that period and throughout the deployment. The measurements from December 11, shown earlier, are representative. Velocity profiles taken during this period will be presented below. Reworking of the bed may have occurred, since the value of the Shields parameter during flood tides is consistent with sediment motion, but the three lowest acoustic axes remained fully obscured.

A series of storm events with more energetic wind forcing began on December 16. The neap phase of the tidal cycle reached a low on December 17, so the early storm events occurred during relatively weak flood tides. The strongest wave forcing occurred at the peak of the late December spring tides. Measurement Level 2 was intermittently exposed during flood tides on December 16 and 17, indicating some reworking of the bed. The two acoustic axes, A2-C2 and B2-D2, were obscured unevenly, suggesting asymmetries in the location and height of the intervening bedform in relation to the tines. A storm late on December 19 exhibited a rapid rise in the measured wave velocities, similar to the December 7 storm; however, the standard deviation of the on-shore velocities was more than three times greater. The magnitude of the wave forcing may have been sufficient to affect the anchors. This is only speculation. The velocity records show no indication that the frame moved during

this event. In the wake of this storm, Level 3 was intermittently obscured during flood tides on December 20, fully obscured throughout December 21, and intermittently obscured again on December 22. Ripple growth to a height of 7.5 *cm* or more is required to obscure measurement Level 3. Ripple heights up to 8 *cm* were observed at Site 2 before the deployment and an 8 *cm* ripple was observed between the tines during one of the dives at Site 1. The velocity record and the observations are consistent with ripple growth. As noted above, the quality of measurements at higher levels began to deteriorate at this time. The velocity record is not consistent with vertical movement of the sensor head and some form of dynamic flexure of the exposed harness is assumed.

The strongest wave forcing of the deployment occurred on December 24. Late in the afternoon the seaward anchors were pulled free of the bottom. Several were later discovered to be plastically deformed from the stress. After repeated slamming of the sensor head into the bed, the entire instrument rolled towards the beach and onto the pyramidal frame protecting the pressure housing. A number of the transducer assemblies were broken by the slamming, which sheared several of the exposed stems from the tines. The structural ring at the end of the tines was severely deformed. It was evident from the deformation that at least one rock had been present in the sand beneath the sensor head. The pattern and location of scratch marks on the outer support frame indicated that the instrument rolled laterally on the pyramidal members. It may have been this motion that pulled the shoreward anchors free of the bottom. Alternatively, they may have come free during the initial rocking. One leg of the support frame was slightly bent, but the box frame, the inner frame, the pressure housing, and the electronics were undamaged.

The field prototype was recovered during a windless snow fall on December 31. The structural ring was flattened and a full zero calibration using gelatin was performed on January 7 and 8, 1997 [53]. Only Level 8 retained two functioning acoustic axes. For this reason the cleanest portion of the bucket velocities obtained on December 5 and 6 is used to calculate the zero offsets for the second field deployment. Specifically, the offsets are calculated from the period after organized motion in the bucket decayed

to the level of thermal convection and before strong winds started to blow across the mouth of the bucket. The obtained offsets are consistent and reasonable.

#### 6.5.2.2 Selected Velocity Measurements

The known vertical spacing of the acoustic axes, the velocity record as interpreted in Section 6.5.2.1, and the visual observations of Sites 1 and 2 provide some information about the actual height above bottom of acoustic axes in the array. Level 0 is no less than 0.5 *cm* above the initially smoothed bottom on which the ripples formed or the first measurements would have been adversely affected. The measurements presented in this section suggest that the height is at least 0.8 *cm* to 1 *cm* above the smoothed bottom. It is unlikely that Level 0 is more than 1.5 *cm* to 2 *cm*, because the history of obscured and intermittent measurements would require persistent sand ripples of considerably greater height than were commonly observed. A comparable or greater degree of uncertainty exists in simply defining what the reference location is, independent of the sensor head, because of the bottom roughness height associated with the ripples and because the bottom, however defined, may have moved locally due to the erosional and depositional events that took place during the deployment. As a convenience, a nominal height above bottom for Level 0 of 1 *cm* will be assumed. The assumed height above bottom for Level  $k$  is, therefore,  $2.5k + 1$  *cm*.

Selected data from December 7 and December 11 are presented here. December 7 was chosen because it is the only day on which velocities from eight measurement levels were returned. The day is also interesting because of the rapid onset and strength of the storm and the resulting changes to the bottom at Site 2. December 11 is qualitatively representative of the deployment before December 20, the period when movement of the instrument frame is most confidently assumed to be negligible. These measurements show the behavior of the flow above sand ripples. December 11 also coincides with the height of the spring tide and the wave velocities during flood tides are well above average. During the more energetic of the two flood tides on December 11, wave velocities are comparable to those reached at the height of the December 7 storm. The peak of the spectral density curve is actually greater during

that flood tide than during the storm. The figures presented in Section 6.5.2.1 provide summary information about the general wave and current conditions that prevailed when each of the isolated data sets presented below were recorded.

Figures 6.23, 6.24, and 6.25 each show three brief time series from the on-shore velocities measured at Levels 0, 1, 2, 3, 5, 6, 7, and 8 on December 7. Each selection is part of one of the larger time series from which the three spectra in Figure 6.22 were calculated. The records are included to provide qualitative visual information about the characteristics and the complexity of the flow. All three figures are plotted with the same vertical and horizontal scales to facilitate visual comparison. Several features of the records are noted in the captions.

The Grant-Madsen (GM) model [46] can be used to calculate many characteristics of the wave-current boundary layer, including the thickness of the wave bottom boundary layer and the maximum bottom stress. The GM model requires, as inputs, the near-bottom wave amplitude, the wave period, the mean current at some reference height, and the angle between the current and the direction of wave propagation. All of these quantities are provided by the velocity measurements of the BASS Rake. The wave amplitude is measured directly and can be averaged over a suitable number of wave cycles. The angle of wave propagation in the instrument coordinate system can be estimated from a histogram of the velocity angles measured during the same averaging period. The angle of the velocity is not well resolved when the magnitude is close to zero, so the accuracy of the histogram method can be improved by using a threshold to select less ambiguous data for the plot. The wave period is determined by calculating the spectrum and selecting a representative frequency. "Representative" has been defined by Madsen to be the monochromatic wave which would produce the same bottom boundary layer characteristics as the spectral waves [46]. The procedure followed here was selection of a frequency near the peak of narrow spectra or selection of a frequency near the median of relatively broad or multi-peaked spectra. The steady current is simply the vector sum of the mean on-shore and along-shore currents, measured at one of the nominally known heights, and the angle of the current, in the instrument coordinate system, is simply the arctangent of their ratio.



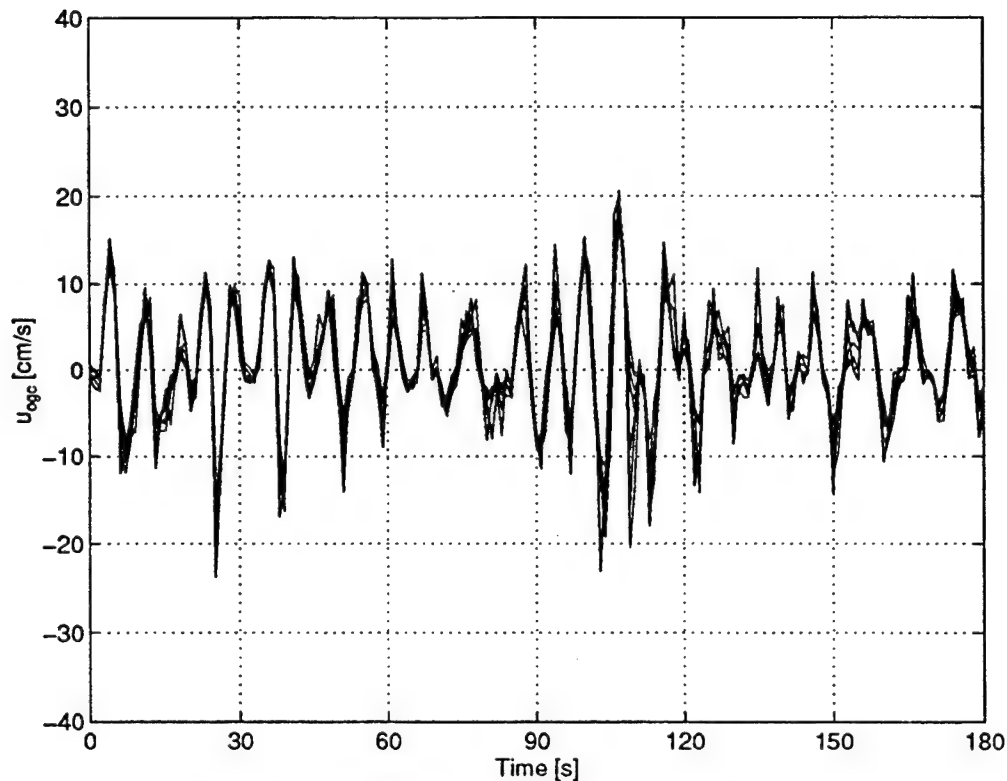


Figure 6.23: 3 MINUTE TIME SERIES, 1600 HOURS ON DECEMBER 7, 1996 - This is a 3 minute record of the on-shore velocity,  $u_{ogc}$ , measured at Levels 0, 1, 2, 3, 5, 6, 7, and 8. The nominal heights are 1.0 *cmab*, 3.5 *cmab*, 6.0 *cmab*, 8.5 *cmab*, 13.5 *cmab*, 16.0 *cmab*, 18.5 *cmab*, and 21 *cmab*. The time series begins at 7.670 on the time axis of Figure 6.21 and is part of the larger time series from which the first spectrum in Figure 6.22 was calculated. The measurements were made shortly after the peak of a weak flood tide. The spectrum is relatively broad and shows two peaks with periods of 6 s and 9 s. The record between 80 s and 130 s shows the passage of a wave group. Some on-shore/off-shore asymmetry is apparent in the first third of the record.

The GM model also requires the bottom roughness,  $k_n$ , as an input. As used here, bottom roughness refers to the equivalent Nikuradse sand grain roughness. This subject is discussed at length in Chapter 2 and in Appendix A. For a fixed, flat bed,  $k_n$  is the characteristic diameter of the grains. Under those conditions  $k_n = 0.25 \text{ mm}$  at Site 2. During bedload transport and once bedforms have been generated, the bottom roughness is not well characterized. Madsen has, tentatively and with several cautions, proposed means of estimating  $k_n$  under these conditions [46]. The methodology is straightforward, though somewhat involved, and is based on separating the

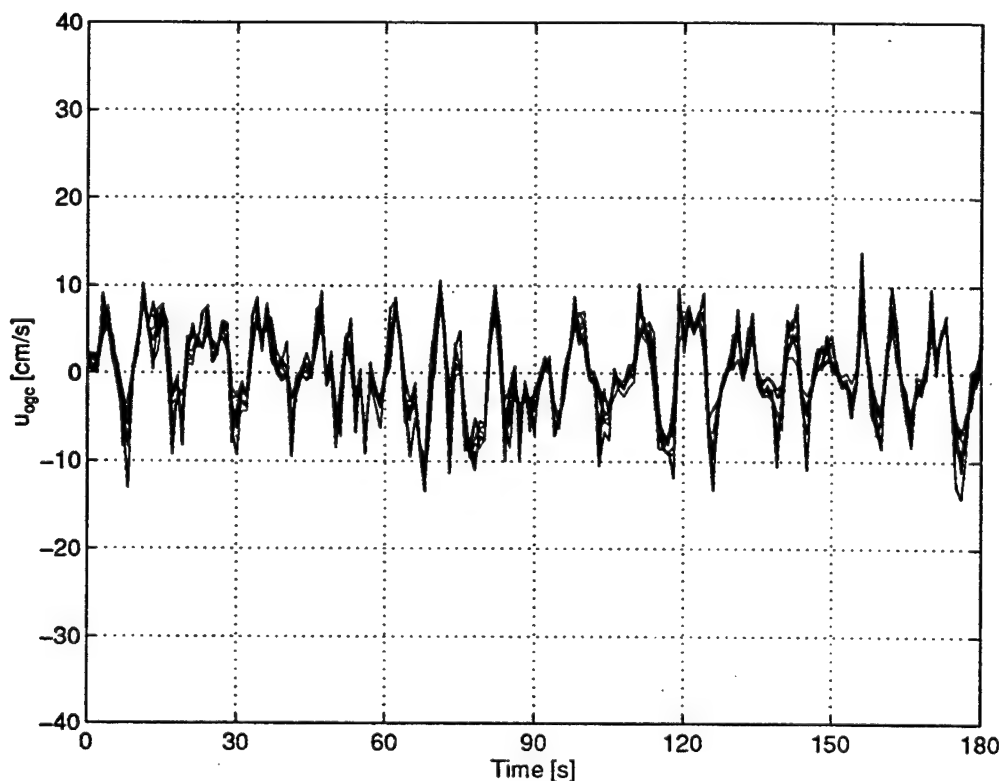


Figure 6.24: 3 MINUTE TIME SERIES, 1900 HOURS ON DECEMBER 7, 1996 - This is a 3 minute record of the on-shore velocity,  $u_{ogc}$ , measured at Levels 0, 1, 2, 3, 5, 6, 7, and 8. The nominal heights are 1.0 *cmab*, 3.5 *cmab*, 6.0 *cmab*, 8.5 *cmab*, 13.5 *cmab*, 16.0 *cmab*, 18.5 *cmab*, and 21 *cmab*. The time series begins at 7.772 on the time axis of Figure 6.21 and is part of the larger time series from which the second spectrum in Figure 6.22 was calculated. The measurements were made during the beginning of the ebb tide. On-shore wave velocities are low and the steady, along-shore current is relatively strong, approximately twice the wave amplitude. The spectrum shows a single peak with a period of 10 s.

bottom stress into skin friction and form drag components. The skin friction component is supported by the sand grains and is responsible for sediment motion. The form drag component is supported by the bedforms and can be much larger than the skin friction. The values of the constants scaling the expressions were determined from laboratory results using monochromatic waves, not from field conditions. Those results show considerable scatter and no distinct trends. The approach has been used here, tentatively and with caution. The results for the three periods of December 7 shown in Figures 6.23, 6.24, and 6.25 are summarized in Table 6.2.

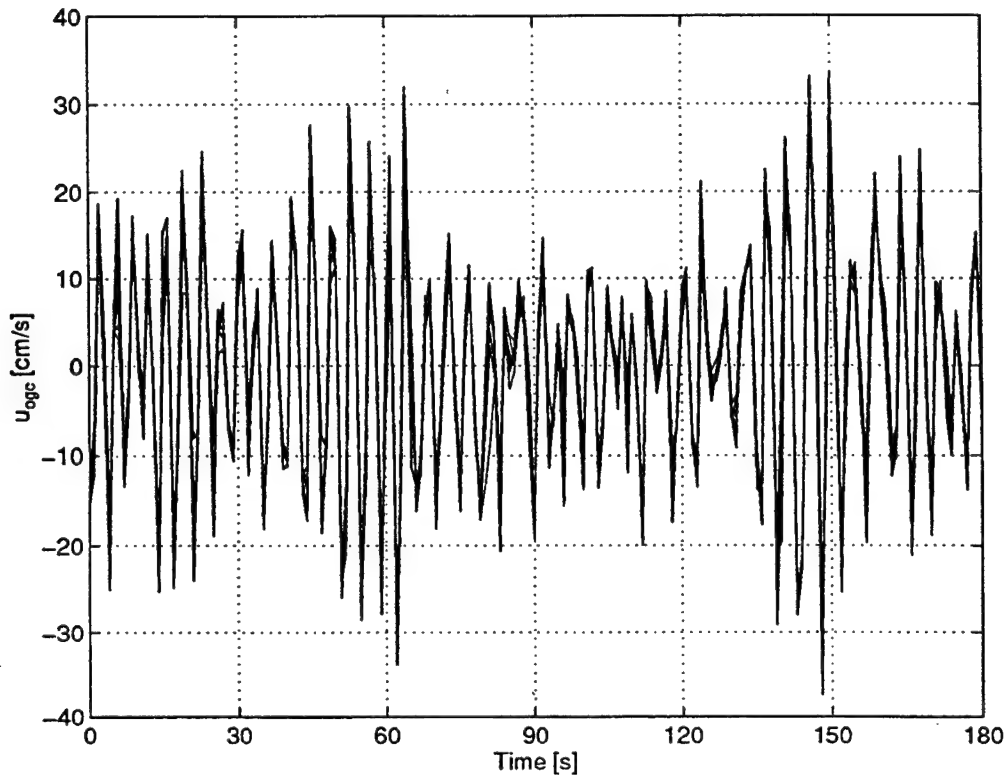


Figure 6.25: 3 MINUTE TIME SERIES, 2200 HOURS ON DECEMBER 7, 1996 - This is a 3 minute record of the on-shore velocity,  $u_{ogc}$ , measured at Levels 0, 1, 2, 3, 5, 6, 7, and 8. The nominal heights are 1.0 *cmab*, 3.5 *cmab*, 6.0 *cmab*, 8.5 *cmab*, 13.5 *cmab*, 16.0 *cmab*, 18.5 *cmab*, and 21 *cmab*. The time series begins at 7.925 on the time axis of Figure 6.21 and is part of the larger time series from which the third spectrum in Figure 6.22 was calculated. The measurements were made approaching the peak of the storm and shortly before Level 0 began to return intermittent nulls. 10 *s* waves are still present, but the spectrum is strongly dominated by 4 *s* waves generated locally by the wind. Wave velocities are up to three times larger and have less than half the period of velocities measured during the ebb tide. This combination increases the bottom stress by a factor of 5.

The calculation shows, not unexpectedly, that the wave boundary layer does not satisfy the necessary conditions, stated at the beginning of the chapter, for a detection based on the phase lead of the velocity in the boundary layer. Only the final entry in the table is thick enough, and then only if the lowest measurement level had been located 0.5 *cmab*. The data indicate Level 0 was higher than this. Additionally, the probable physical height of the bedforms would have inhibited the formation of a wave bottom boundary layer. The need for greater vertical resolution is obvious.

Despite the absence of a detectable wave boundary layer, it is instructive to plot

Day of December	General Conditions	$k_n$ [cm]	Character of Flow	$\tau_m$ [dyn · cm <sup>-2</sup> ]	$\psi_s$ [×10 <sup>-2</sup> ]	$\delta_{cw}$ [cm]
7.670	Flood	0.025	STF	0.6	1.5	0.3
7.772	Ebb	0.025	STF	0.9	2.3	0.5
7.925	Storm	0.025	STF	2.6	6.6	0.4
		1	RTF	10.5	6.6	0.8
		2	RTF	15.0	6.6	1.0

Table 6.2: WAVE BOUNDARY LAYER CHARACTERISTICS ON DECEMBER 7, 1996 - The first three lines of the table describe the wave boundary layer assuming the bottom remains flat and stationary. The bottom roughness is the known size of the sand grains and the flow in the boundary layer is characterized as smooth turbulent (STF, see Madsen [46]). The maximum bottom stress,  $\tau_m$ , depends on the amplitude and period of the waves, the magnitude of the steady flow, and the angle between the direction of wave and the steady velocity. The Shields parameter is calculated from the bottom stress associated with the sand grains (skin friction), not the stress associated with the bedforms, if present. The calculated thickness of the wave boundary layer in a wave-current flow,  $\delta_{cw}$ , is shown in the last column. During the storm the bottom was neither flat nor stationary. Sand ripples were forming, but had not yet obscured Level 0. This suggests a physical height of 3 mm to 5 mm and an equivalent Nikuradse sand grain roughness of 1 cm to 2 cm [46]. This range is considered in the last two lines of the table. The boundary layer flow is fully rough turbulent (RTF) and the bottom stress, which now includes form drag, has increased significantly. The Shields parameter is determined by the skin friction and does not increase. Finally, the calculated thickness of the boundary layer has risen, but is still quite small.  $\delta_{cw}$  is comparable to the height of the bedforms.

two examples of oscillatory velocity profiles. Figure 6.26 shows a single wave cycle taken from the time series in Figure 6.25. The profiles from this cycle are shown in Figure 6.27. Figures 6.28 and 6.29 present the equivalent information for a wave cycle taken from the time series in Figure 6.23.

The changing shapes of the velocity profiles demonstrate the presence of turbulent eddies in the near-bottom flow. The steady and wave components of the current advect these structures through the sample volume where they produce the measured velocity fluctuations. It is the multiple sample volume design of the BASS Rake that allows these features to be imaged. This could not be done with a single sample volume. As predicted by the earlier calculations, the profiles show no evidence of the structure associated with a turbulent wave bottom boundary layer. Of course, even with vertical resolution sufficient for these thin wave boundary layers, the model

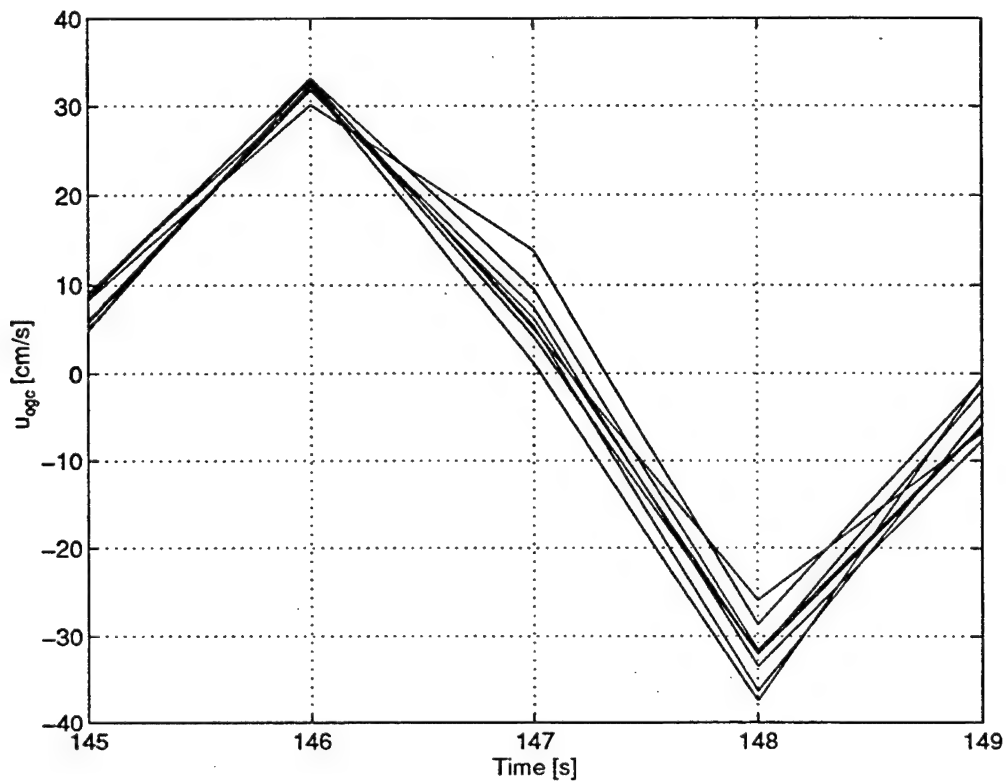


Figure 6.26: A SINGLE WAVE CYCLE FROM THE DECEMBER 7 STORM - Time is measured from the beginning of the 3 minute record in Figure 6.25. The on-shore velocities from all eight measurement levels are shown. Actual wave velocities were less than  $20^\circ$  from the on-shore axis. There is no strong dependence of phase on the height above bottom. The magnitude is also fairly constant with height, particularly early in the wave.

solutions would only fit a measured profile in a rough sense. This is discussed in Appendix A and is due to the turbulent nature of the flow. The profiles graphically demonstrate this characteristic.

The profiles, the longer time series, and the spectra presented earlier show the complexity of the flow over a range of time and length scales. The spectral nature of the waves in particular, even during periods of stochastic stationarity, makes the process of determining the average properties of the wave boundary layer quite difficult. It is the average properties, without the turbulent features, that are described by models of the boundary layer. One possible approach is the calculation of a transfer function from  $u_\infty$ , the measured velocity above the wave boundary layer, to the

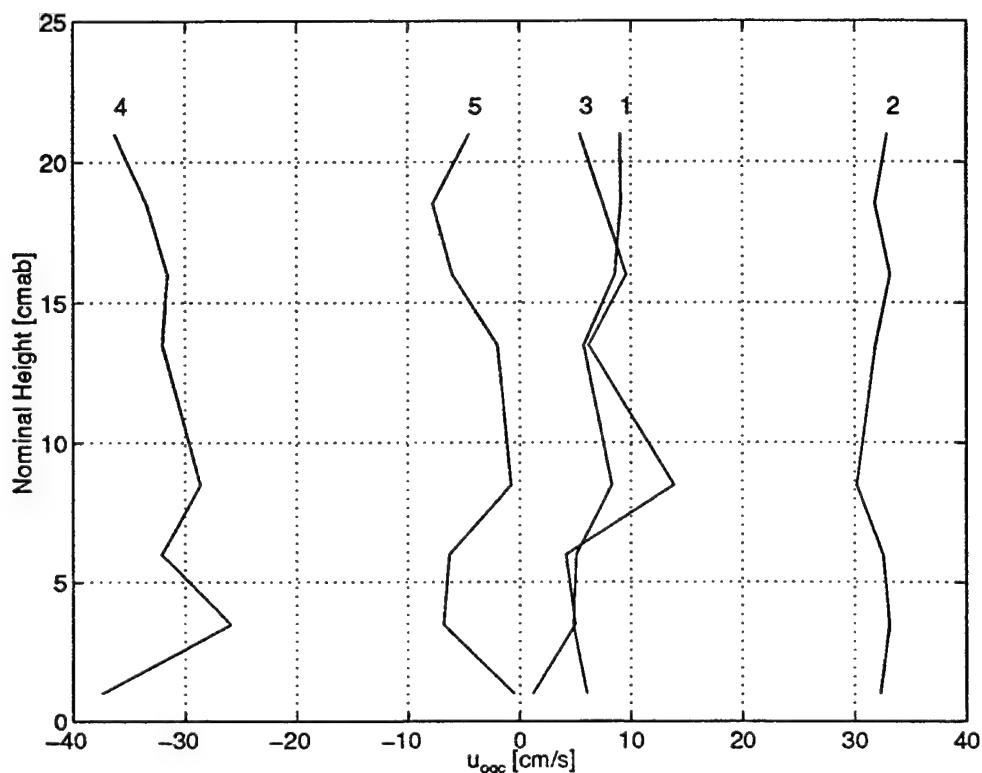


Figure 6.27: VELOCITY PROFILES FOR THE DECEMBER 7 STORM WAVE - The profiles are numbered in chronological sequence near the top of the figure. Note the changes in the shape of the on-shore velocity profiles over time. Actual wave velocities were less than  $20^\circ$  from the on-shore axis. The response of the sensor is well characterized in this range and the noise level caused by flow distortion is at least an order of magnitude below the velocity changes being measured. The changes in shape are caused by turbulent eddies as they are advected through the sample volume by the flow. The advection mechanism is invoked because the near-bottom velocity changes in profile 4 suggest an eddy scale of 3 cm to 5 cm. The excursion amplitude is approximately 20 cm. These rapidly changing profiles should be compared to the nearly stable profiles measured in Great Harbor under considerably less energetic conditions (Figure 6.7).

velocities measured closer to the bed. The transfer function is the complex valued cross-spectral density of the two velocity time series normalized by the power spectral density of  $u_\infty$ . The spectral calculations provide the needed average over a large number of cycles without requiring a monochromatic signal. The magnitude and phase of the transfer function, at any frequency within the spectral distribution of the waves, describe the average structural characteristics of the wave boundary layer for that frequency, near-bottom orbital velocity, steady current, and bottom rough-

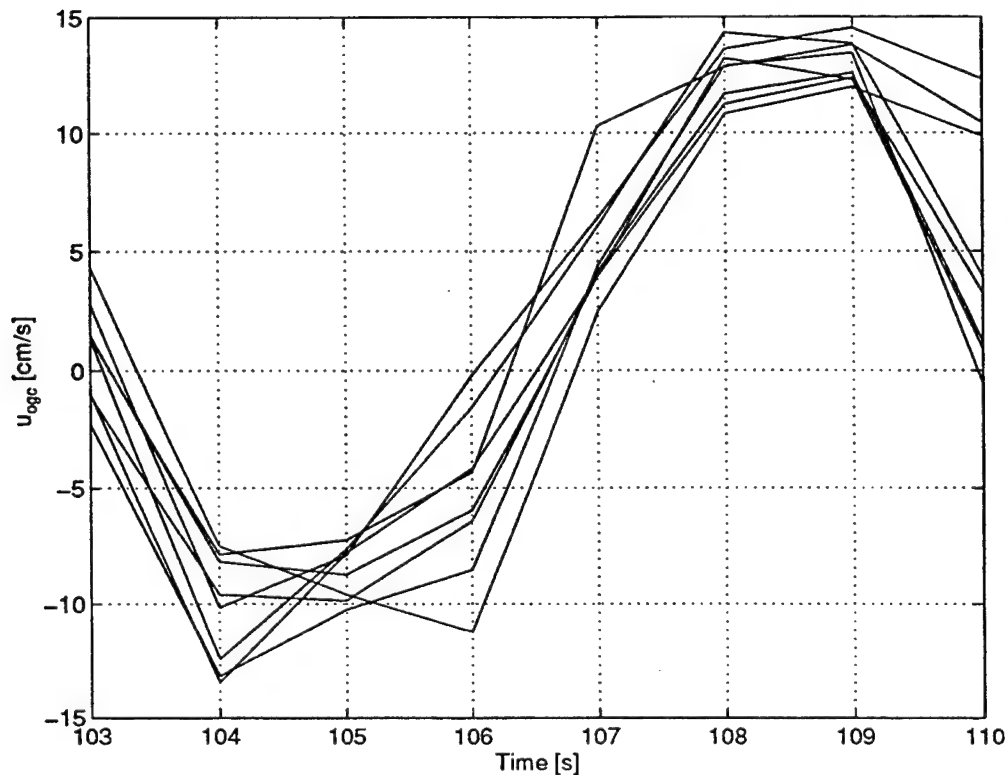


Figure 6.28: A SINGLE WAVE CYCLE FROM THE DECEMBER 7 FLOOD TIDE - Time is measured from the beginning of the 3 minute record in Figure 6.23. The on-shore velocities from all eight measurement levels are shown. Actual wave velocities were less than  $10^\circ$  from the on-shore axis. Note that the extent of the vertical scale has been reduced compared to the vertical scale in Figure 6.26. The variation of magnitude with height above bottom is comparable to the variation in the storm wave. Some phase variation is present, but it does not appear to be organized.

ness. Note that this approach requires concurrent time series and is only possible with an instrument that has multiple sample volumes.

The transfer function technique was applied to field prototype measurements acquired throughout the deployment during periods of widely varying flow and bottom conditions. There was no evidence of a resolved wave boundary layer nor a detection based on the phase lead of the near-bottom velocity. In all cases, calculation of  $\delta_{cw}$  predicted a boundary layer too thin to be resolved or too thin to form in the presence of the physical roughness elements. One commonly, but not universally, observed feature was a phase lag of  $10^\circ$  to  $20^\circ$  at the lowest active measurement level. The lag decreased to near zero over several centimeters vertically and remained near zero to

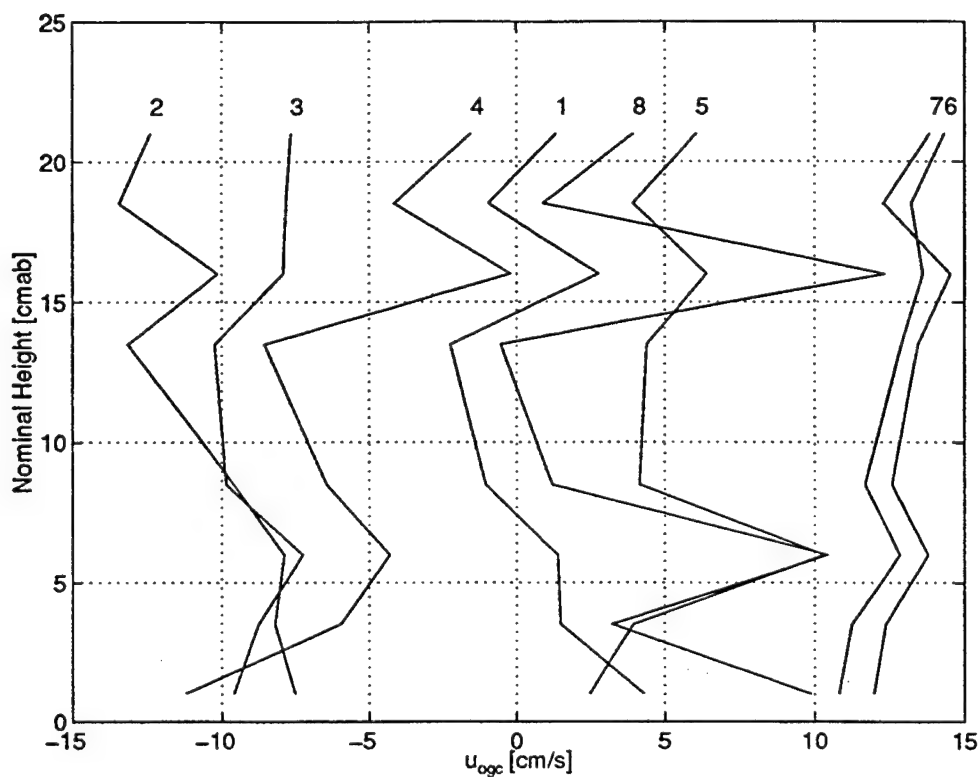


Figure 6.29: VELOCITY PROFILES FOR THE DECEMBER 7 FLOOD TIDE WAVE - The profiles are numbered in chronological sequence near the top of the figure. Shape changes indicating the presence of turbulent eddies are again present. Some of the more dramatic fluctuations are comparable to the maximum wave velocity. The steady along-shore current was  $4 \text{ cm} \cdot \text{s}^{-1}$  to  $6 \text{ cm} \cdot \text{s}^{-1}$  at this time. The large signal  $16 \text{ cmab}$  may result from the interaction of steady along-shore and oscillatory on-shore advection. The near-bottom excursion amplitude is approximately  $13 \text{ cm}$ .

the highest measurement level. The cause of the lag is unknown, but may be related to the distortion of the near-bottom flow around and over the bedforms.

The velocity records, as interpreted above, suggest that in the days following the December 7 storm a persistent sand ripple lay between the tines of the sensor head. The height of the ripple, to be consistent with the interpretation, must have been at least  $6 \text{ cm}$ . Estimates of the equivalent Nikuradse sand grain roughness are large enough to prevent convergence of the GM model, however, a wave boundary layer is not expected to form in the presence of bedforms this high. The measurements made on December 11 show the behavior of the oscillatory flow over the rippled bed. Spectra for two selected periods are shown in Figure 6.30.



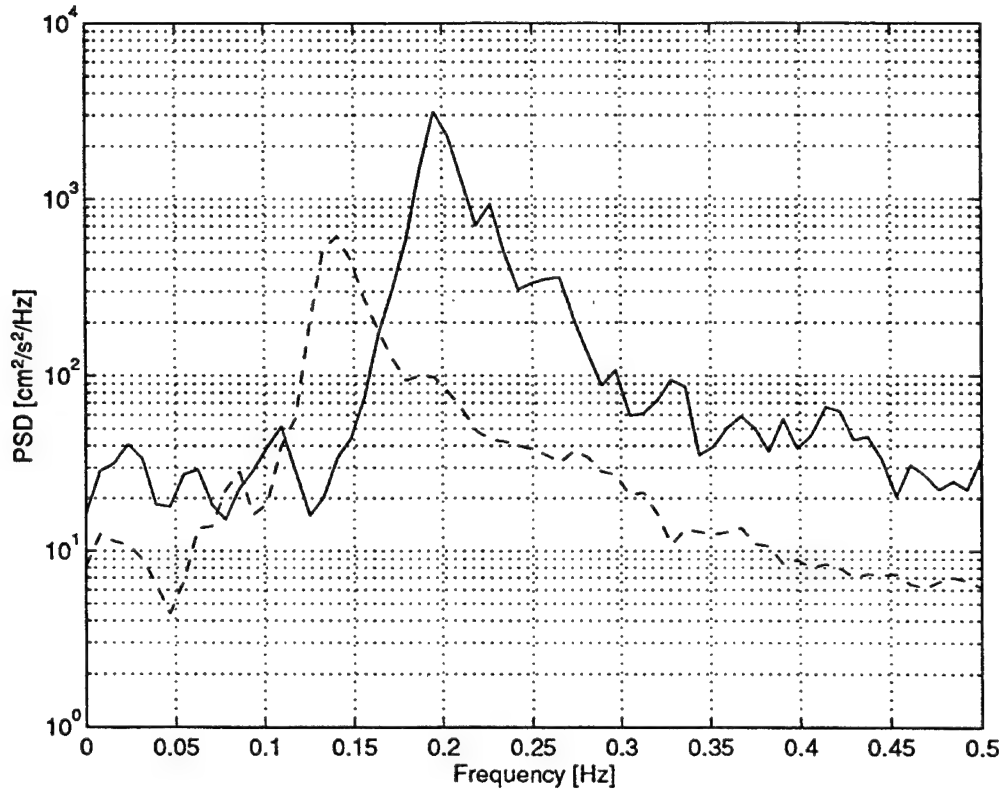


Figure 6.30: WAVE SPECTRA FOR DECEMBER 11, 1996 - The dashed trace (---) shows the wave spectrum for the period from 1200 hours to 1440 hours. This corresponds to 11.5 – 11.6 on the time axis of Figure 6.20, the latter half of the ebb tide. The solid trace (—) shows the wave spectrum for the comparatively brief period from 0445 hours to 0515 hours (11.20 – 11.22). This corresponds to the peak of the flood tide enhanced wave velocities and occurs immediately before the along-shore flow reversal. The spectra show the increase in wave velocities associated with the flood phase of the tidal cycle. A reduction in the prevailing wave period during the flood tide is commonly observed in the data, but has not been confirmed for all occurrences.

The selected periods are the latter half of the early afternoon ebb tide and the peak of the early morning flood tide, immediately before the along-shore flow reversal. The spectra show the increase in wave velocities associated with the flood phase of the tidal cycle. The reduction in the prevailing wave period during the flood tide exhibited by the two spectra is commonly observed in the data, but has not been confirmed for all occurrences. Short time series from these two periods are shown in Figures 6.31 and 6.32.

The two time series show the passage of organized wave groups past the sensor.

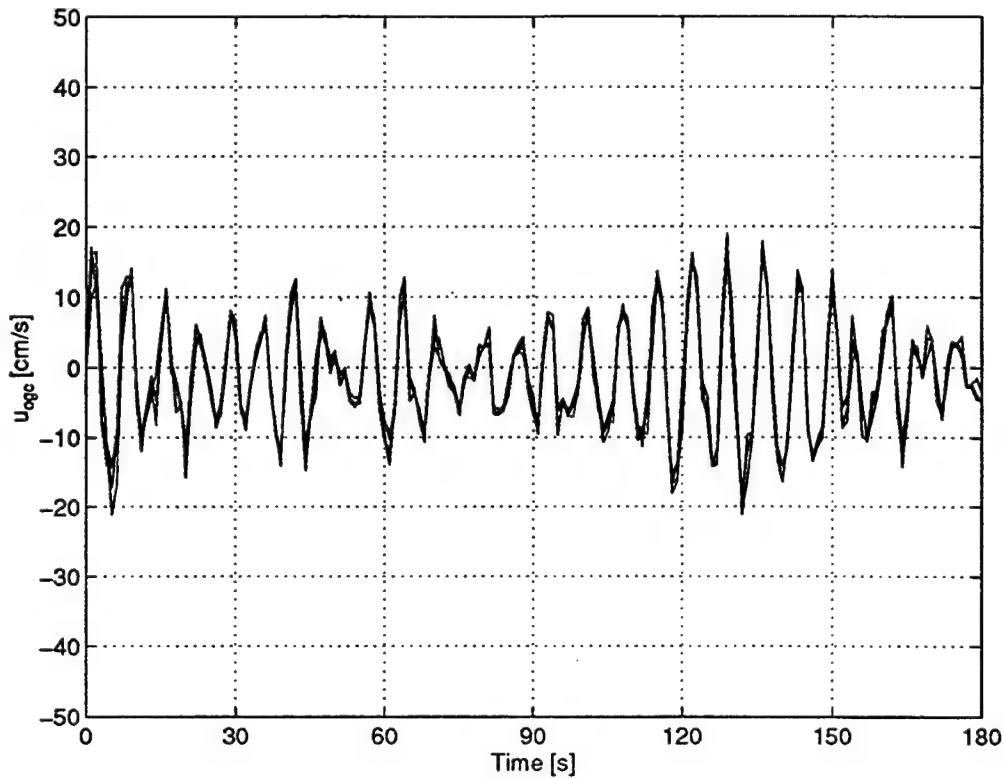


Figure 6.31: 3 MINUTE TIME SERIES, 1400 HOURS ON DECEMBER 11, 1996 - This is a 3 minute record of the on-shore velocity,  $u_{ogc}$ , measured at Levels 3, 5, 7, and 8. The nominal heights are 8.5 *cmab*, 13.5 *cmab*, 18.5 *cmab*, and 21 *cmab*. The time series begins at 11.58 on the time axis of Figure 6.20. The dominant wave period is 7 s. The passage of a wave group is apparent in the second half of the record.

The same vertical and horizontal scales have been used for both plots to facilitate visual comparison. The Shields parameter during the ebb tide is  $2 \times 10^{-2}$ , indicating no motion of the sand grains. The larger wave velocities and shorter period during the flood tide raise  $\psi_s$  to more than  $1.2 \times 10^{-1}$ . This is more than twice the critical value for the sand at Site 2. In combination with the velocity records, this suggests oscillatory bedload transport in approximate equilibrium with the bedforms. Finally, Figures 6.33 and 6.34 show velocity profiles acquired over single wave cycles during each of the selected periods on December 11.

The profiles show some evidence of turbulent eddies in the flow. More interestingly, both sets of profiles exhibit a consistent outward slant with the highest velocities

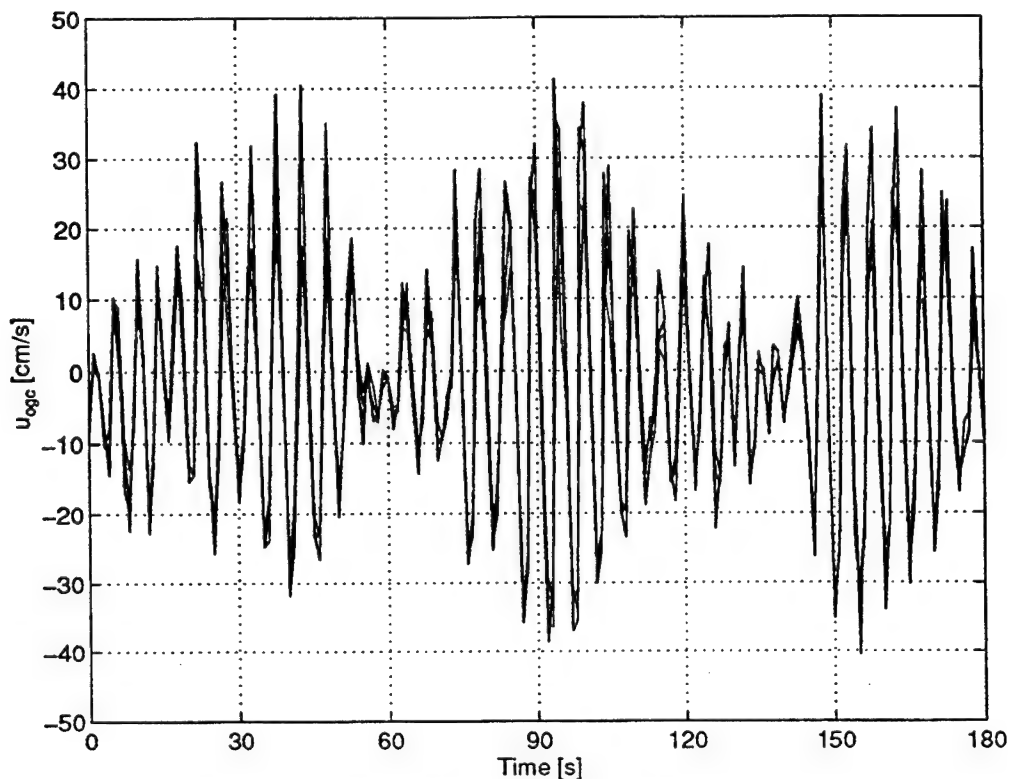


Figure 6.32: 3 MINUTE TIME SERIES, 0445 HOURS ON DECEMBER 11, 1996 - This is a 3 minute record of the on-shore velocity,  $u_{ogc}$ , measured at Levels 3, 5, 7, and 8. The nominal heights are 8.5 *cmab*, 13.5 *cmab*, 18.5 *cmab*, and 21 *cmab*. The time series begins at 11.20 on the time axis of Figure 6.20. The dominant wave period is 5 s. The passage of several organized wave groups is apparent.

closest to the bottom. Higher velocities could be caused by the acceleration of the flow over the ripple. This characteristic was previously observed by Agrawal and Aubrey [2] over a sand ripple under waves in the near-shore zone. Thus the slanting profiles provide additional support for the sand ripple interpretation of the field prototype measurements.

## 6.6 Conclusions

During the beach deployment, accurate profile measurements were made reliably and autonomously in the field over a period of several weeks. Vertically coherent velocities,

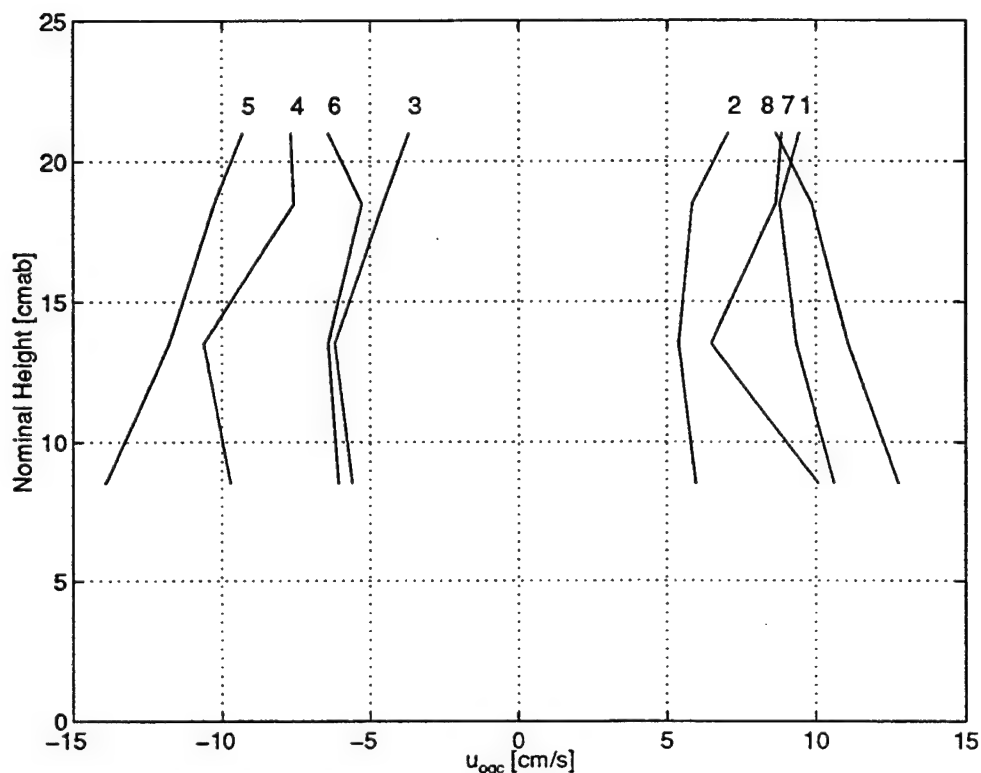


Figure 6.33: VELOCITY PROFILES DURING THE DECEMBER 11 EBB TIDE - The profiles are numbered in chronological sequence near the top of the figure and span approximately one wave cycle. Some effects of turbulence in the flow are visible. Note the outward slant of the profiles with the highest velocities closest to the bottom. This indicates acceleration of the flow over the sand ripple.

recurring structures, and turbulent features in the oscillatory bottom boundary layer were imaged by the prototype. Information of this nature is only available from an instrument with multiple sample volumes. In addition, even with its coarse vertical resolution, and with no concurrent visual observations, the field prototype provided a considerable quantity of information about the morphology and evolution of the bed at Site 2.

It is clear from the data that the bed was reworked many times during the experiment. Ripple growth was occasionally rapid and height changes of 3 cm to 5 cm were observed during periods of strong wave forcing. Semi-diurnal, diurnal, and spring/neap tidal cycles modulate both the currents and the waves in the near-shore

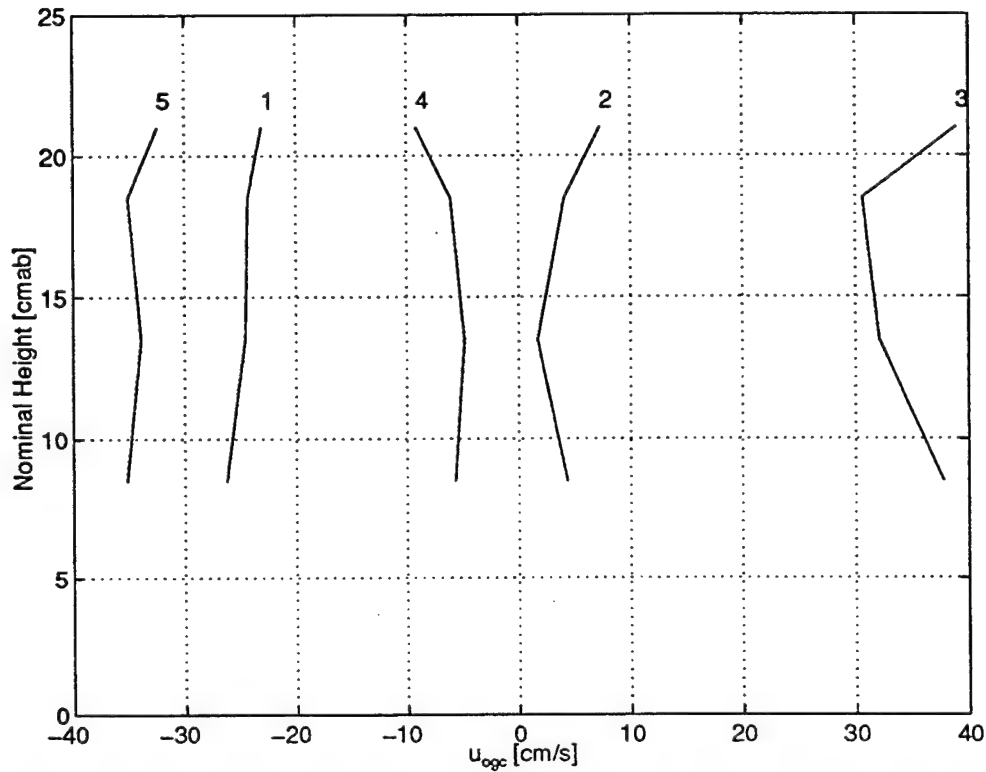


Figure 6.34: VELOCITY PROFILES DURING THE DECEMBER 11 FLOOD TIDE - The profiles are numbered in chronological sequence near the top of the figure and span approximately one wave cycle. Some effects of turbulence in the flow are visible. The outward slant of the profiles, indicating acceleration of the flow over the sand ripple, is again evident.

zone of Nobska Beach. While storms have a strong influence on the movement of sand, the tidal modulations of the waves regularly increase the bottom stress sufficiently to rework the sand bottom.

The tow tank tests and field deployments have accomplished all of the defined tasks set out in Section 6.1. The measurements demonstrate both the capabilities and the benefits of the BASS Rake design. The results presented in this chapter validate this approach towards instrumenting the continental shelf wave bottom boundary layer.

# Chapter 7

## Conclusion

### 7.1 General Summary

The BASS Rake has the ability to accurately and reliably measure temporally coherent, near-bottom, velocity profiles, in the laboratory and in the field. Measurement levels can be positioned within millimeters of the bed with dense vertical spacing through the wave boundary layer and into the forcing flow above it. The technique is insensitive to fouling and suspended sediment concentration and performs well in the energetic environments found on the continental shelf. A detailed comparison made to existing instrumentation showed that these abilities are currently unique to the BASS Rake.

The four tines of the sensor head support an array of acoustic transducers in a geometry tailored to dynamically image flow in the continental shelf wave bottom boundary layer. The sensor head design includes a number of mechanical and electrical features that improve transducer performance and signal quality while the layered multiplexer provides a flexible interface from the transmit/receive circuits to the transducer array. This system permits a full suite of horizontal and vertical velocity measurements without compromising the electrical characteristics necessary to measurement accuracy. It also provides cross-channel signal isolation in the absence of shielded transmission lines, relieving constraints on the diameter of the tine and the number of measurement levels. The overall performance of the sensor depends

heavily on the integrated nature of the mechanical and electrical designs.

The vertical resolution of the BASS Rake is a function of both the geometry of the transducer array and the sample volume of a single acoustic axis. A model of acoustic propagation in a scattering medium, appropriate for a BASS Rake differential travel time axis, was developed. The model includes the interaction of the sample volume with the bottom and was used to understand and predict the effects of Fresnel averaging on near-bottom velocity measurement. Averaging error was shown to be insignificant more than a few millimeters from the bed for continental shelf boundary layers. The error can become significant closer to the bed, but it can be controlled by adjusting the frequency and diameter of the transducers. A fast parametric model was used to determine, within constraints, the transducer characteristics necessary to image the continental shelf wave bottom boundary layer with 1 *mm* vertical resolution and negligible sample bias. These transducers are within the performance envelope of the mechanical and electrical designs. Used in this way, the Fresnel averaging model is a valuable design tool.

Understanding and characterizing the response of a sensor is a critical part of the development process. The intrusion of the tines into the flow causes distortion and generates wakes. The effect of these disturbances on the velocity measurement was first modeled and then determined empirically for both prototypes. The determination for the field prototype was, of course, somewhat more involved because of the angular dependence. The tow tank tests demonstrated a non-linear Reynolds number dependence, a new finding for BASS instruments. The model readily explains the dependence, relating it to the location and angle of flow separation from the tines. The result is consistent with the literature for flow around bluff bodies. The flat response of the laboratory prototype to changes in the Keulegan-Carpenter number is also consistent. It was shown that the measured response of either instrument could be incorporated into the calibration with a single valued mapping and that the accuracy of the mapping does not limit the accuracy of the instrument. For both instruments, the noise floor is established by turbulence in the wakes of the tines, not by the electronics or the calibrated response.

The measurements performed with the laboratory prototype thoroughly tested the integrated mechanical and electrical designs. The tines, transmission lines, MUX, and sequencer meet the design specifications cleanly. Accurate measurements were made a few millimeters above a natural sand bottom in a range of flow conditions. Heavy bedload transport did not degrade the response and the theoretical description of the sample volume was verified. The flume measurements demonstrated the importance and worth of multiple sample volumes by recording vertically coherent velocity structures and turbulent instabilities.

The BASS Rake has always been intended for field use. The field prototype was built to place the BASS Rake geometry on the continental shelf and demonstrate that it could operate there, accurately and reliably, immediately above the bed. The instrument returned several weeks of  $1\text{ Hz}$  velocity profiles. Measurements were acquired less than one centimeter above a sand bed, over sand ripples, during storms, and during periods of heavy bedload transport. The record shows regular reworking of the sand bed, tidal modulation of both currents and waves, and the presence of turbulent eddies in the flow. The pattern of returned velocities provided information about bottom morphology and the location of the fluid-sediment interface. This was all accomplished with very coarse vertical resolution. With improved vertical resolution, the quality of the information, particularly information about bedform generation and modulation, will improve. The observed evolution of the bottom may usefully influence the distribution of transducers in future versions of the instrument.

## 7.2 Directions for Future Development

Any effort to improve accuracy and reduce measurement noise must first focus on reducing the flow disturbance caused by the sensor head. In the field, where the relative direction of flow is changing and uncertain, there is no clear alternative to halfround or fully round tines. Increasing the path length will decrease the relative disturbance, but introduce other problems that make this an undesirable option. A better choice is a reduction in the diameter of the tines. A  $7\text{ mm}$ , halfround



tine could accommodate a single column of the 6 mm P2 transducers. The vertical resolution of these tines would be sufficient for wave boundary layer detection under some conditions. In general, the value of profiles with 6 mm resolution from the bottom to 30 cmab, particularly coupled with measurements taken higher in the water column, would be enormous. This is a particularly attractive approach because the laboratory prototype has already proven the design. A field capable P2 instrument should be developed.

A similar variation, with better vertical resolution, would be a 3 mm to 4 mm tine supporting a single column of 2.5 mm transducers. A necessary first step for these narrow tines, and for the dense, three column array designed to image the wave bottom boundary layer, is a laboratory evaluation of 2.5 mm, 5 MHz transducers. The prediction that these transducers will operate next to a boundary must be verified. Operating the electronics at 5 MHz may present some difficulties and these should be addressed and solved immediately. This project could easily be pursued in parallel with the construction of a field capable P2 design. A 5 MHz, WBL instrument could follow, with the new design benefitting from the information obtained deploying the P2 instrument.

The gain correction for a sensor head with four regulation tines needs to be established as a function of Reynolds number, Keulegan-Carpenter number, and rotation angle. Again, the field capable P2 design could be used for this purpose. Improvements in the cosine response, in particular, are expected. Additionally, recall that it is the wake noise associated with the irregular shape of the tines and transducer assemblies that sets the limit on measurement accuracy for the field prototype. While the wake noise is expected to be lower for the smooth, slender shape of the integrated tine design, it is nonetheless important to determine what that level is.

A multiple sample volume instrument would also have great utility in the laboratory. Consider, for example, the abilities and advantages demonstrated by the laboratory prototype during the flume tests. Not only did the BASS Rake record characteristics of the flow invisible to the LDV, but it determined a complete profile in only one flume averaging period. In the laboratory, the direction of flow is generally

known and reshaping the tines to decrease flow noise is feasible. Simply fairing the tines on a laboratory instrument is one option. The resulting attenuation and refraction of the acoustic signal could probably be corrected. Consider, however, another possibility. A non-intrusive, multiple sample volume sensor could be constructed by mounting the transducers in the walls of a flume or wave tank. The sample volumes could be flexibly positioned along a tank by using sectional walls, similar to the modular false bottoms used in some flumes. Alternatively, thin panels with faired edges could be placed against the walls, creating a minimal disturbance. An instrument of this nature could provide full profiles of flow in a flume or wave tank in real time. Fabricating a laboratory instrument of this nature should be undertaken.

The BASS Rake is well suited to the general study of boundary layer flow, both in the laboratory and on the continental shelf. Multiple sample volumes permit the imaging of vertically coherent velocity structures that are invisible to instruments with a single measurement volume. The wave boundary layer is of particular interest because of the strong effect it has on the mean flow and because of the important role it plays in the processes of sediment entrainment and transport. The short periods of wave oscillation sharply limit the vertical extent of the WBBL and make it a technically challenging region to instrument. The BASS Rake has the unique ability to image the dynamic behavior of the wave bottom boundary layer and can now be applied to the continuing study of boundary layer flow on the continental shelf.



## Appendix A

# Derivation and Solution of the Equation of Motion for a Wall Boundary Layer

The mechanical design of the BASS Rake was largely dictated by the expected time and length scales of the wave bottom boundary layer over the continental shelf. This appendix summarizes the background information from which those scales were determined. The wave-current boundary layer model of Grant and Madsen, which was used in the measurement analysis, is also discussed. Source material for this summary may be found in several of the references listed in the bibliography, most notably Batchelor [5], Grant and Madsen [24, 27], Kundu [39], Lamb [40], Madsen and Wikramanayake [45], Madsen [46], and Trowbridge and Madsen [80, 81].

A linear equation of motion for a wall boundary layer is derived in Section A.1 by applying a scaling argument to the Navier-Stokes and continuity equations. Emphasis is placed on characteristic time and length scales for the continental shelf. The equation is solved for both steady and oscillatory flows in Section A.2. Laminar wave boundary layers can occur on the shelf and are the norm in laboratory wave tanks where considerable effort is needed to produce a fully turbulent flow. The laminar oscillatory solution, first published by Stokes in 1851 [40], is therefore included. However, the wave boundary layer in the ocean is also commonly turbulent and steady free

surface flows in both the laboratory and the ocean are almost invariably turbulent. The simple turbulent closure formula used in the Grant-Madsen (GM) wave-current boundary layer model [24, 27, 45, 46] is used here. While other models of the wave-current boundary layer exist, the GM model is the most flexible in application to field and laboratory data and it enjoys a wide, if not universal, degree of acceptance. The GM and other models of the boundary layer are briefly discussed in Chapter 2. A more detailed comparison and evaluation of several of these models can be found in Madsen and Wikramanayake [45]. Entries in the bibliography describing other models include Kajiura [38], Smith [73], and Davies, Soulsby, and King [13].

## A.1 Derivation of the Governing Equation

Derivations of the Navier-Stokes equations, which express the momentum balance, and of the continuity relation, which expresses mass conservation, can be found in any standard textbook of fluid mechanics [5, 39, 40]. For the case of a homogeneous and incompressible two dimensional flow these equations can be written

$$\frac{\partial u}{\partial t} + u \frac{\partial u}{\partial x} + w \frac{\partial u}{\partial z} = -\frac{1}{\rho} \frac{\partial p}{\partial x} + \frac{\partial(\tau_{xx}/\rho)}{\partial x} + \frac{\partial(\tau_{zx}/\rho)}{\partial z} \quad (\text{A.1})$$

$$\frac{\partial w}{\partial t} + u \frac{\partial w}{\partial x} + w \frac{\partial w}{\partial z} = -\frac{1}{\rho} \frac{\partial p}{\partial z} - g + \frac{\partial(\tau_{xz}/\rho)}{\partial x} + \frac{\partial(\tau_{zz}/\rho)}{\partial z} \quad (\text{A.2})$$

$$\frac{\partial u}{\partial x} + \frac{\partial w}{\partial z} = 0 \quad (\text{A.3})$$

where  $t$  is time,  $p$  is pressure, and  $\rho$  is density. The other quantities are defined in Figure A.1. The assumption of incompressibility is warranted in the ocean where fluid velocities are at least two orders of magnitude less than the speed of sound. Homogeneity is a reasonable assumption for a thin and well mixed boundary layer [24, 27, 45]. The notable consequence of these assumptions is that the density,  $\rho$ , can be treated as a constant, independent of  $x$ ,  $z$ , and  $t$ . For this reason it has been moved from the LHS of the momentum equations to a position inside the stress derivatives on the right hand, or forcing, side. The quantity  $\sqrt{\frac{\tau}{\rho}}$ , commonly referred to as the shear or friction velocity, is the characteristic turbulent velocity scale for the boundary

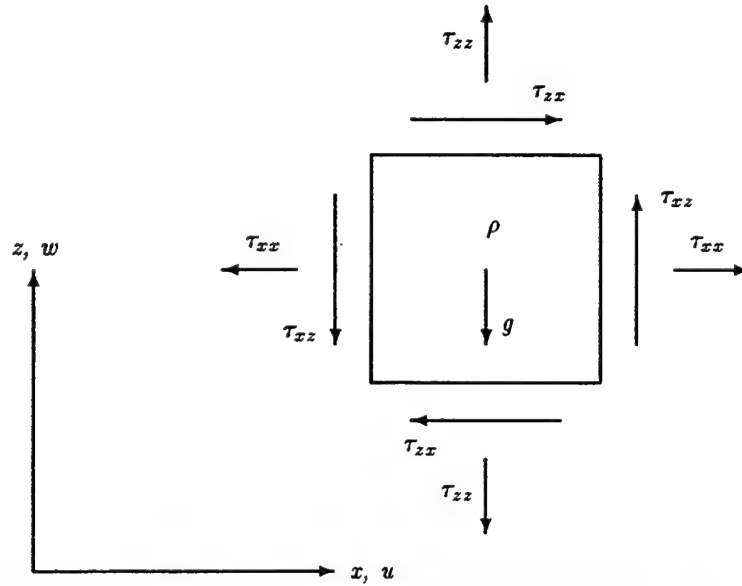


Figure A.1: DEFINITION OF TERMS FOR THE GOVERNING EQUATIONS -  $x$  and  $z$  are the horizontal and vertical spatial coordinates.  $u$  and  $w$  are the horizontal and vertical velocities. The various quantities denoted by  $\tau$ s are normal and tangential (viscous) stress terms acting on the fluid element pictured.  $g$  is the gravitational acceleration. Vectors indicate the positive direction for the associated variable.

layer.

Let the characteristic scales of the terms in Equations A.1 - A.3 be denoted by

$$u = O(U) \quad w = O(W) \quad \frac{\tau_{ij}}{\rho} = O(U_*^2) \quad (\text{A.4})$$

$$\frac{\partial}{\partial x} = O(k) \quad \frac{\partial}{\partial z} = O\left(\frac{1}{\delta}\right) \quad \frac{\partial}{\partial t} = O(\omega) \quad (\text{A.5})$$

$U$  and  $W$  are the horizontal and vertical velocity scales.  $k$  and  $\omega$  are the wave number and radian frequency for oscillatory motions and tend to zero in the limiting case of a steady current.  $\frac{1}{k}$  provides a horizontal length scale and  $\frac{1}{\omega}$  provides a time scale.  $\delta$  is the vertical length scale of the boundary layer. Applying these scales to the continuity relation (Equation A.3) yields  $W = (k\delta)U$ . Wavelengths on the continental shelf are typically hundreds of meters while the thickness of the WBBL is on the order of one centimeter. Therefore  $k\delta \approx 10^{-4} \ll 1$  and  $W \ll U$ , as expected in the region of a solid boundary. For a steady current boundary layer  $\delta$  may be on the order of meters

to tens of meters, however,  $k$  is zero in this limit and the conclusion  $W \ll U$  remains valid. Similar arguments can be applied for the steady case in the discussion below, but, for reasons of brevity, explicit mention will not be made.

On the LHS of the momentum equations (Equations A.1 and A.2) the nonlinear convective acceleration terms are of order  $\frac{U}{c_p}$  compared to the leading order term,  $\frac{\partial u}{\partial t}$ , where  $c_p = \frac{\omega}{k}$  is the phase velocity of the waves. This is clear from

$$O \left[ u \frac{\partial u / \partial x}{\partial u / \partial t} \right] = \frac{kU^2}{\omega U} = \frac{kU}{\omega} = \frac{U}{c_p} \quad (\text{A.6})$$

For the continental shelf typical values are

$$c = \frac{\omega}{k} = \frac{\lambda_w}{T} \approx \frac{10^4}{10} \text{ cm} \cdot \text{s}^{-1} = 10^3 \text{ cm} \cdot \text{s}^{-1} \quad (\text{A.7})$$

and

$$U \approx 10^1 \text{ cm} \cdot \text{s}^{-1} \quad (\text{A.8})$$

Thus

$$\frac{U}{c_p} \approx 10^{-2} \ll 1 \quad (\text{A.9})$$

Similarly, for the other convective acceleration terms in the momentum equations,

$$O \left[ w \frac{\partial u / \partial z}{\partial u / \partial t} \right] = \frac{UW}{\delta} \frac{1}{\omega U} = \frac{kU}{\omega} = \frac{U}{c_p} \ll 1 \quad (\text{A.10})$$

$$O \left[ u \frac{\partial w / \partial x}{\partial w / \partial t} \right] = \frac{kUW}{\omega W} = \frac{kU}{\omega} = \frac{U}{c_p} \ll 1 \quad (\text{A.11})$$

$$O \left[ w \frac{\partial w / \partial z}{\partial w / \partial t} \right] = \frac{W^2}{\delta \omega W} = \frac{kU}{\omega} = \frac{U}{c_p} \ll 1 \quad (\text{A.12})$$

Neglecting the convective acceleration terms, the vertical momentum equation may now be written

$$\frac{\partial(p/\rho + gz - \tau_{zz}/\rho)}{\partial z} = -\frac{\partial w}{\partial t} + \frac{\partial \tau_{xz}/\rho}{\partial x} = O(\omega W + kU^2) \quad (\text{A.13})$$

Integrating this expression from some  $z$  inside the boundary layer to  $\delta$ , where  $p = p_\infty$

and  $\tau_{zz} \rightarrow 0$ , yields

$$\frac{p}{\rho} = \frac{p_{\infty}}{\rho} + g(\delta - z) - \frac{\tau_{zz}}{\rho} + O[(\omega W + kU_*^2)(\delta - z)] \quad (\text{A.14})$$

Then differentiating with respect to  $x$  produces

$$\frac{1}{\rho} \frac{\partial p}{\partial x} = \frac{1}{\rho} \frac{\partial(p_{\infty} + \tau_{zz})}{\partial x} + O[(\omega W + kU_*^2)k\delta] \quad (\text{A.15})$$

or, using the result from the continuity equation and reorganizing the terms,

$$\frac{1}{\rho} \frac{\partial p}{\partial x} = \frac{1}{\rho} \frac{\partial(p_{\infty} + \tau_{zz})}{\partial x} + \underbrace{O[\omega U(k\delta)^2]} + \underbrace{O\left[\omega U_* \frac{U_*}{c_p}(k\delta)\right]} \quad (\text{A.16})$$

It was determined above that the leading order term in the horizontal momentum equation,  $\frac{\partial u}{\partial t}$ , is  $O(\omega U)$ , and that the horizontal convective acceleration terms,  $u \frac{\partial u}{\partial x}$  and  $w \frac{\partial u}{\partial z}$ , are  $O(kU^2) = O\left(\omega U \frac{U}{c_p}\right)$ . Therefore the first underlined term on the RHS of Equation A.16 is  $O[(k\delta)^2]$  compared to  $\frac{\partial u}{\partial t}$ , the leading order term. Typically,  $U_*$  is an order of magnitude smaller than  $U$  and  $k\delta$  is two orders of magnitude smaller than  $\frac{U}{c_p}$ .<sup>1</sup> Conservatively then, the second underlined term on the RHS of Equation A.16 is also  $O[(k\delta)^2]$  compared to  $\frac{\partial u}{\partial t}$ . Thus, with accuracy to  $O[(k\delta)^2]$ , the horizontal momentum equation can be written

$$\frac{\partial u}{\partial t} + u \frac{\partial u}{\partial x} + w \frac{\partial u}{\partial z} = -\frac{1}{\rho} \frac{\partial p_{\infty}}{\partial x} + \frac{1}{\rho} \frac{\partial \tau_{zx}}{\partial z} + \frac{1}{\rho} \frac{\partial(\tau_{xx} - \tau_{zz})}{\partial x} \quad (\text{A.17})$$

Note that

$$O\left[\frac{\frac{1}{\rho} \frac{\partial(\tau_{xx} - \tau_{zz})}{\partial x}}{\frac{1}{\rho} \frac{\partial \tau_{zx}}{\partial z}}\right] = \frac{kU_*^2}{U_*^2/\delta} = k\delta. \quad (\text{A.18})$$

In linear wave theory terms of  $O\left(\frac{U}{c_p}\right)$ ,  $O(k\delta)$ ,  $O[(k\delta)^2]$ , and smaller compared to

<sup>1</sup>For a 10 s wave of 2 m amplitude,  $k\delta$  is  $O(10^{-4})$  in 50 m depth and  $O(10^{-3})$  in 5 m depth.  $\frac{U}{c_p}$  changes from  $O(10^{-2})$  to  $O(10^{-1})$  for the same conditions. Note that the ratio,  $\frac{k\delta}{U/c_p}$ , remains nearly constant as the two quantities change through an order of magnitude. Note also that in shallower water, approaching the surf zone,  $\frac{U}{c_p} \ll 1$  ceases to be valid. The linear boundary layer equation will break down here, just as the linear model of surface gravity waves breaks down and the surface gravity waves simply break.



the leading order terms are neglected [5, 39, 61]. Therefore, with accuracy to  $O\left(\frac{U}{c_p}\right)$ , the linear governing equation for the boundary layer is

$$\frac{\partial u}{\partial t} = -\frac{1}{\rho} \frac{\partial p_\infty}{\partial x} + \frac{\partial(\tau/\rho)}{\partial z} \quad (\text{A.19})$$

The subscript on the viscous stress term,  $\tau_{zx}$  is not longer needed and has been dropped.

Above the boundary layer the shear stress goes to zero and

$$\frac{\partial u_\infty}{\partial t} = -\frac{1}{\rho} \frac{\partial p_\infty}{\partial x} \quad (\text{A.20})$$

Substituting, the linear governing equation can also be written

$$\frac{\partial u}{\partial t} = \frac{\partial u_\infty}{\partial t} + \frac{\partial(\tau/\rho)}{\partial z} \quad (\text{A.21})$$

The dependence of  $\tau$  on  $\frac{\partial u}{\partial z}$  will be discussed in Section A.2.1. The importance here is simply that two, rather than one, spatial boundary conditions on  $u$  are required for solution of Equation A.21. Physically,  $u$  must satisfy a “no-slip” condition at the bottom of the boundary layer and it must match  $u_\infty$ , the external forcing velocity, above the boundary layer. These boundary conditions may be expressed as

$$u = 0 \quad \text{at} \quad z = z_o \quad (\text{A.22})$$

$$u \rightarrow u_\infty \quad \text{as} \quad z \rightarrow \infty \quad (\text{A.23})$$

$z_o$  is the “level of zero flow” and not necessarily equal to zero. Consider particularly that, on the scale of the bottom roughness elements,  $z = 0$  is not a well defined quantity.  $z \rightarrow \infty$  simply means for  $z$  sufficiently large to be “outside” the boundary layer, but not so far away that it may no longer be considered the forcing flow. A direct measure of  $u_\infty$  would be a highly desirable part of a WBBL data set.

The common practice when investigating the wave boundary layer has been to use pressure, measured well above the boundary layer, as a surrogate for the velocity

outside the boundary layer. Alternatively,  $u_\infty$  has been determined by applying linear wave theory to surface wave measurements or to velocity measurements taken well above the boundary layer.  $u_\infty$  is given in Equation A.24 for the case of surface wave measurements.

$$\begin{aligned} u_\infty &= a\omega \frac{\cosh(k\delta)}{\sinh(kh)} \cos(\omega t - kx) \\ &= \frac{a\omega}{\sinh(kh)} \cos(\omega t - kx) \\ &= u_{bm} \cos(\omega t - kx) \end{aligned} \tag{A.24}$$

The surface wave amplitude is  $a$  and the water depth is  $h$ . The Taylor expansion about zero of  $\cosh(k\delta)$  shows that this expression is accurate to  $O[(k\delta)^2]$ .  $u_{bm}$ , the maximum wave orbital velocity just outside the boundary layer, should be identified as the scaling velocity,  $U$ . All of these methods determine  $u_\infty$ , the forcing input to the boundary layer governing equation, indirectly. The design of the BASS Rake permits a direct, simultaneous, measurement of the velocity just above the thin boundary layer being profiled. The importance of this capability will be clear in the next section where the flow dependent phase relationship between the oscillatory velocities inside and outside of a wave boundary layer will be determined.

## A.2 Solutions of the Governing Equation

### A.2.1 The Eddy Viscosity

When solving the linearized governing equation, the forcing term,  $\frac{\partial u_\infty}{\partial t}$  or  $\frac{\partial p_\infty}{\partial x}$ , is assumed to be known. It is also implicitly independent of  $z$  because the pressure across the "thin" boundary layer was assumed constant in the scaling argument of Section A.1. It remains then to determine an expression for  $\tau$  in terms of the flow variable,  $u$ , to close the system of equations. For a laminar flow this relationship is

$$\tau = \rho\nu \frac{\partial u}{\partial z} \tag{A.25}$$

where  $\nu$ , the kinematic viscosity, is a material property of the water and therefore independent of both  $z$  and  $t$  [5, 39, 40, 46]. The shear stress in a turbulent boundary layer is not so easily specified. Turbulent closure schemes range from elaborate numerical models to a constant eddy viscosity,  $\nu_t$ . Values of  $\nu_t$  are much larger than the material value of  $\nu$ , reflecting the greatly enhanced rate of mixing by eddies in a turbulent flow compared to mixing by molecular diffusion. In the Grant-Madsen wave-current boundary layer model  $\tau$  is given by

$$\tau = \rho \nu_t \frac{\partial u}{\partial z} \quad (\text{A.26})$$

where

$$\nu_t = \kappa u_* z \quad (\text{A.27})$$

is the turbulent eddy viscosity.  $\kappa$  is von Karman's constant, empirically determined to be approximately 0.4 [5, 39, 40, 46]. As before,  $u_*$  is the shear velocity and equal to  $\sqrt{\frac{\tau}{\rho}}$ . The shear velocity and the eddy viscosity depend on the flow. In a steady current  $u_{*c} = \sqrt{\frac{\tau_c}{\rho}}$ , where  $\tau_c$  is the bottom stress. In a purely oscillatory flow the GM model stipulates  $u_{*w} = \sqrt{\frac{\tau_{wm}}{\rho}}$ , where  $\tau_{wm}$  is the maximum bottom stress during a wave cycle. The assumption of time independence is valid for a first order description of the flow. A time dependent eddy viscosity is important when modeling second order effects such as mass transport [46, 80, 81]. In a combined wave-current flow, with some angle between the waves and the current,  $u_{*w} = \sqrt{\frac{\tau_m}{\rho}}$ , where  $\tau_m = |\vec{\tau}_{wm} + \vec{\tau}_c|$  and the addition is in the vector sense. Then

$$\nu_t = \begin{cases} \kappa u_{*m} z & z < \delta_{cw} \\ \kappa u_{*c} z & z > \delta_{cw} \end{cases} \quad (\text{A.28})$$

where  $\delta_{cw}$  is the height at which the two portions of the steady solution are matched. The combined solution is a superposition of the pure wave and current solutions with the stipulated choices of eddy viscosity and shear velocity in each layer. Only the pure cases will be solved in this appendix. Note that in all cases the eddy viscosity and the shear velocity are explicitly independent of time; the wave and current problems

can be solved separately within the assumptions of the GM model. A more detailed discussion of the model can be found in [24, 27, 45, 46].

Several comments should be made here. First, in the GM model,  $\delta_{cw}$  is at first only a convenient label for the height at which the two portions of the steady solution are equal. It is taken by assumption, and with the support of some data, to be the height of the wave boundary layer. Physically, this is the height at which wave generated turbulence vanishes, or at least diminishes greatly in importance. The value of  $\delta_{cw}$ , by analogy to the pure wave case, is scaled by  $\frac{\kappa u_{*wm}}{\omega}$ , with a multiplier variously given in the range 1 to 2 [24, 27, 45, 46]. Some recent work suggests that the multiplier may actually be larger, however, those experimental conditions were outside the range of validity for the model [47, 48].

Second, this definition of the shear stress is circular without additional relationships between the unknowns. For this reason, solution using the GM model is often iterative, depending on the conditions and the measurements obtained. A direct determination of the shear velocity and of the hydrodynamic bottom roughness in the field, in unsteady flow, is highly desirable. A velocity profile through the boundary layer would yield this information, precisely the task for which the BASS Rake is designed. Measurement of the Reynolds stress,  $-\overline{u'w'}$ , and the mean profile would also yield the eddy viscosity. The BASS Rake may eventually be able to do this as well (see Chapter 2).

Third, this is not an unreasonably simple model of the shear stress near the bottom. More elaborate closure schemes commonly require the eddy viscosity to be linear in  $z$  near the wall, as in Equation A.27, as a boundary condition [45, 46]. Additionally, Prandtl's mixing length hypothesis, a simple conceptual model of turbulent mixing, leads directly to this form for the shear stress [45, 46]. And while the physical basis for the mixing length hypothesis is now considered incorrect in principle, the same logarithmic profile that Equations A.26 and A.27 lead to in steady flow can be derived entirely from dimensional considerations [39]. Finally, the deviation of this simple approach from measurements and from the more elaborate numerical models of wave and current boundary layers is quite small compared to the

actual velocities [24, 27, 45, 46, 80, 81].

### A.2.2 Solution for a Steady Current

The steady solution is straightforward and will be familiar to most readers. With the time derivative necessarily zero and recalling that  $p_\infty$  does not depend on  $z$ , Equation A.19 may be integrated from the “bottom” to a height  $z$ , yielding

$$\tau(z) = \tau_c + \frac{\partial p_\infty}{\partial x} z \quad (\text{A.29})$$

$\tau_c$  is the bottom shear stress due to the current. For small values of  $z$ ,  $\frac{\partial p_\infty}{\partial x} z \ll \tau_c$  and  $\tau(z) = \tau_c$ . The statement of constant stress across the boundary layer is commonly referred to as the “law of the wall” [39, 46]. Substituting the turbulent eddy viscosity model for the stress produces

$$\frac{\tau_c}{\rho} = \kappa u_{*c} z \frac{\partial u_c}{\partial z} \quad (\text{A.30})$$

where  $u_c$  is the steady current velocity in the boundary layer. Equation A.30 is easily integrated to reach the familiar logarithmic velocity profile

$$u_c = \frac{u_{*c}}{\kappa} \ln \frac{z}{z_o} \quad (\text{A.31})$$

with

$$u_c = 0 \text{ at } z = z_o \quad (\text{A.32})$$

The constant of integration is incorporated as a length scale,  $z_o$ , the hydrodynamic roughness. As noted at the end of Section A.2.1, this form of the solution can also be derived purely on dimensional grounds [39]. Empirically, the solution is still accurate for relatively large values of  $z$  [45, 46].

### A.2.3 The Hydrodynamic Roughness

The bottom roughness is often specified in terms of the equivalent Nikuradse sand grain roughness,  $k_n$ , based on the pipe flow measurements made by Nikuradse during

the 1930s [5, 39, 40, 46]. Equivalence, as used here, refers to closely packed, stationary grains scaled to match the apparent roughness experienced by the flow. Empirically, and as used in the GM model,

$$z_o = \begin{cases} \frac{\nu}{9u_*} & \frac{k_n u_*}{\nu} \leq 3.3 \\ \frac{k_n}{30} & \frac{k_n u_*}{\nu} \geq 3.3 \end{cases} \quad (\text{A.33})$$

The two regimes are smooth and rough turbulent flow. For smooth turbulent flow (STF) the physical roughness height is small compared to the developed thickness of the viscous sublayer and  $k_n$  is not physically relevant. The flow is hydrodynamically smooth. This is also true for laminar flow. In fully rough turbulent flow (RTF), however, the roughness elements are large enough to disrupt and prevent the formation of the sublayer. A transition range of the boundary Reynolds number,  $Re_* = \frac{k_n u_*}{\nu}$ , is neglected for simplicity [45, 46]. This distinction between turbulent regimes is made for steady, oscillating, and combined flows in the GM model with  $u_* = u_{*c}$ ,  $u_{*w}$ , or  $u_{*cw}$  as appropriate. One of the important predictions of the model is the observed increase in apparent bottom roughness experienced by the steady current above a wave boundary layer.

The value of  $k_n$ , the equivalent roughness experienced by the flow, is an input to the GM model and must be estimated from the geometry, physical scale, and active motion of the roughness elements and bedforms. The estimate is not refined by the iterative loops of the model. The equivalent roughness for a given geometry is assumed by all wave-current boundary layer models to be a function of the boundary, with dependence on the flow characteristics only in the sense that the flow may have shaped the boundary. Recent experiments appear to support this assumption for the GM model [47, 48]. For a stationary, flat sand bed,  $k_n$  is normally taken to be the diameter of the sand grains [45, 46]. However, there is no predictive relationship linking  $k_n$  to bedform geometry and scale or to sediment motion, all of which are known to affect the effective roughness [25, 46, 88]. Existing data are very limited. Laboratory experiments in steady and oscillatory flows show that the hydrodynamic roughness is strongly sensitive to both the geometry and the scale of the bedforms.

For example, the equivalent roughness of two dimensional bedforms may be an order of magnitude larger than their height [46, 47, 48]. Experimental data from the field are generally for steady boundary layers of several meters thickness and begin 30 *cm* or more above the bottom. Field measurements nearer to the bed and in waves are rare. Most used mechanically scanned sensors during stationary conditions and do not include detailed observations of the bottom (see Chapter 2). Laboratory measurements in waves exist only for periodic conditions with mechanically scanned sensors and do not exhibit a well defined dependence [46, 47, 48, 88]. An estimate of  $k_n$  for typical field conditions is, at best, an approximation based on experience and intuition.

Clearly, an accurately measured and densely spaced velocity profile, if it was available, could be fitted to the logarithmic profile to determine  $z_o$ .  $k_n$  would follow from Equation A.33; in the presence of bedforms the boundary Reynolds number will necessarily be larger than the transition value and the flow will be fully rough turbulent. Recall that  $z = 0$  is poorly defined at the scale of the physical roughness elements, particularly when the bed is in motion, so the nominal height above bottom of the measurements should be an adjustable parameter during the fitting process. The best fit, in the least squares sense, would determine both  $u_{*c}$  and  $k_n$ . An analogous procedure can be performed for the wave boundary layer. The difficulty, of course, is reliably obtaining a profile in the field across a boundary layer that may only be a few centimeters thick. That scale is the norm for the wave boundary layer. It may also be the pertinent scale for a current boundary layer which is limited in extent by stratification and interior flow. Determination of the hydrodynamic roughness under a variety of conditions, including non-stationary spectral waves, is an important task, and one to which the BASS Rake is well suited.

#### A.2.4 Solution for a Laminar Wave Boundary Layer

For a laminar wave boundary layer, the viscosity is a material property of the fluid and Equation A.21 may be rewritten as

$$\frac{\partial u_w}{\partial t} = \frac{\partial u_{\infty w}}{\partial t} + \nu \frac{\partial^2 u_w}{\partial z^2} \quad (\text{A.34})$$

where  $u_w$  is the velocity within the wave boundary layer and  $u_{\infty w}$  is a purely oscillatory forcing flow,  $u_{\infty w} = \Re \{u_{bm} e^{i\omega t}\}$ . Under these conditions a solution to Equation A.34 of the form

$$u_w = \Re \{f(z) e^{i\omega t}\} \quad (\text{A.35})$$

may be assumed [33]. Substitution shows that the function  $f(z)$  must satisfy

$$f'' - \frac{i\omega}{\nu} f = -\frac{i\omega}{\nu} u_{bm} \quad (\text{A.36})$$

with boundary conditions

$$f = 0 \quad \text{at} \quad z = 0 \quad (\text{A.37})$$

$$f = u_{bm} \quad \text{as} \quad z \rightarrow \infty \quad (\text{A.38})$$

The homogeneous solution of Equation A.36 is a complex exponential in  $z$  and a suitable forced solution is simply a constant. Applying the boundary conditions yields

$$f(z) = u_{bm} \left[ 1 - e^{-(1+i)\frac{z}{\delta_w}} \right] \quad (\text{A.39})$$

$\delta_w = \sqrt{\frac{2\nu}{\omega}}$  is the characteristic length scale for the thickness of a laminar wave boundary layer. Substitution into Equation A.35 gives the velocity distribution within the boundary layer.

$$u_w(z, t) = \Re \left\{ u_{bm} \left[ 1 - e^{-(1+i)\frac{z}{\delta_w}} \right] e^{i\omega t} \right\} \quad (\text{A.40})$$



$\tau$  may be determined by differentiating  $u_w$  with respect to  $z$

$$\tau_w(z, t) = \Re \left\{ u_{bm} \rho \nu \frac{1+i}{\delta_w} e^{-(1+i)\frac{z}{\delta_w}} e^{i\omega t} \right\} \quad (\text{A.41})$$

Table A.1 presents two sets of conditions for a region outside the surf zone of a straight beach with a gently sloping sand bottom free of bedforms. The first scenario represents typical conditions for locally generated surface waves. The GM model as described in [46] predicts a thin, laminar wave boundary layer for these conditions. The prediction is supported by the laboratory study of Jensen, *et al.* [35], which indicates the boundary layer will be laminar throughout the wave cycle. The second scenario is more typical of swell generated in a distant storm. The surface amplitude is larger and the period has lengthened. The GM model predicts a thicker, fully rough turbulent wave boundary layer in this case. The work of Jensen, *et al.* suggests the wave boundary layer will be both transitionally and fully turbulent as a function of  $\omega t \pm kx$ , the local phase of the wave cycle. The GM model changes state, from laminar to turbulent, at a single representative value of the wave Reynolds number,  $RE = \frac{u_{bm} A_{bm}}{\nu} = 10^5$ . As with the boundary Reynolds number,  $Re_*$ , a transition range is neglected for simplicity [45, 46].  $A_{bm} = \frac{u_{bm}}{\omega}$  is the bottom excursion amplitude. No STF regime is predicted because the sand grains are sufficiently large to cause the boundary Reynolds number transition before the wave Reynolds number threshold is reached.

The laminar velocity and stress distributions, Equations A.40 and A.41, for the first set of conditions listed in Table A.1, are plotted in Figure A.2. Velocity and stress profiles spanning half of a wave cycle are shown. The characteristic scale height of the boundary layer,  $\delta_w = \sqrt{\frac{2\nu}{\omega}}$ , is indicated on both plots. The flow exhibits noticeable structure up to nearly  $4\delta_w$ . The phase lead of the boundary layer velocity relative to  $u_{\infty w}$  increases as the boundary is approached. The maximum value is approximately  $45^\circ$ . The phase behavior is more clearly evident in Figure A.3 where the magnitude and phase of the complex valued velocity and stress have been plotted.  $u_w$  and  $\tau_w$  are the real parts of the complex velocity and stress.

Wave Condition		Local Wind	Distant Storm
Surface Wave Amplitude	[m]	0.5	1.0
Depth	[m]	10	10
Wave Period	[s]	6	8
Sand Grain Diameter	[ $\mu m$ ]	250	250

Table A.1: WAVE CONDITIONS FOR LAMINAR AND TURBULENT WAVE BOUNDARY LAYERS - The values in the first column are typical for locally forced, near shore waves. In the absence of bedforms they produce a laminar wave boundary layer. The values in the second column assume incoming swell from a distant storm. Wave amplitude and period have both increased and, in the absence of bedforms, the GM model predicts a fully rough turbulent wave boundary layer. For finer sediment, e.g., 100  $\mu m$ , a smooth turbulent wave boundary layer is predicted.

The obvious thinness of this laminar wave boundary layer makes the inherent difficulty of wave boundary layer measurements clear. The actual volume of water sampled by an acoustic path of the BASS Rake depends on the frequency of the acoustic signal. Resolving the structure of flow in the wave boundary layer depends on the vertical extent of that volume compared to  $\delta_w$  and the vertical spacing of the sample volumes. These issues are discussed in Chapter 4. Some of the transducer arrays discussed in that chapter lack the spatial density needed to image the different shapes of laminar and turbulent flows. However, the flow conditions might still be differentiated by accurate, near-bottom, velocity measurements. The phase lead of the turbulent case is only 10°, significantly less than the laminar phase lead. The phase lead change is quite sudden and dramatic, occurring over much less than an order of magnitude change in  $RE$  [35]. For a sample volume sufficiently narrow and close to the bottom, the velocity phase lead is a relatively simple target, even during weak forcing, yet it provides a great deal of information about the condition of the wave boundary layer.

### A.2.5 Solution for a Turbulent Wave Boundary Layer

In a turbulent wave boundary layer the shear stress is a result of the vertical exchange of momentum by turbulent eddies. Above the sublayer,  $\tau$  is due to the Reynolds stress,

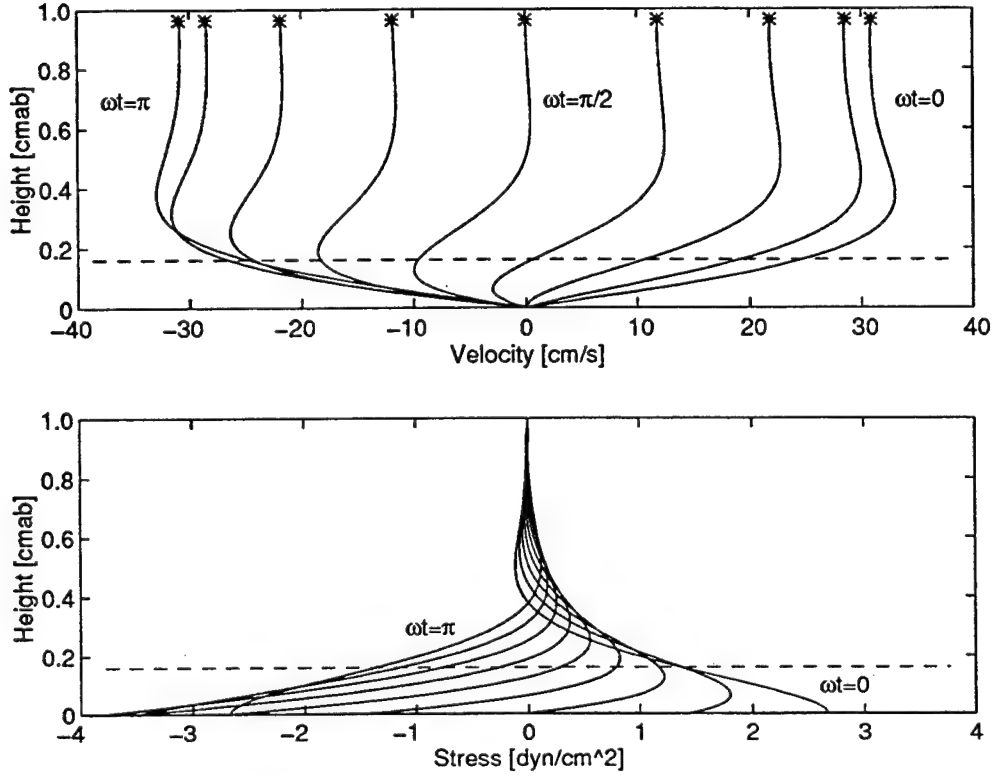


Figure A.2: VELOCITY AND STRESS PROFILES FOR A LAMINAR WAVE BOUNDARY LAYER - Velocity and stress profiles are shown for evenly spaced values of the phase,  $\omega t$ , between 0 and  $\pi$ . The phase increments are  $\frac{\pi}{8}$ . The dashed lines mark the characteristic scale height of the boundary layer,  $\delta_w = \sqrt{\frac{2\nu}{\omega}}$ . The \*s mark the value of  $u_{\infty w}$  for each value of the phase. Both the velocity and the stress exhibit structure well above the scale height.

$-\rho \overline{u'w'}$ . As such, it is entirely a function of the flow and a closure model is needed to express the governing equation in solvable form. Using the turbulent closure defined in Equations A.26 and A.27, Equation A.21 may be rewritten as

$$\frac{\partial u_w}{\partial t} = \frac{\partial u_{\infty w}}{\partial t} + \frac{\partial}{\partial z} \left[ \kappa u_{*w} z \frac{\partial u_w}{\partial z} \right] \quad (\text{A.42})$$

Proceeding as in Section A.2.4, the spatial dependence of the solution,  $f(z)$ , must satisfy

$$z f'' + f' - \frac{i\omega}{\kappa u_{*w}} f = -\frac{i\omega}{\kappa u_{*w}} u_{bm} \quad (\text{A.43})$$

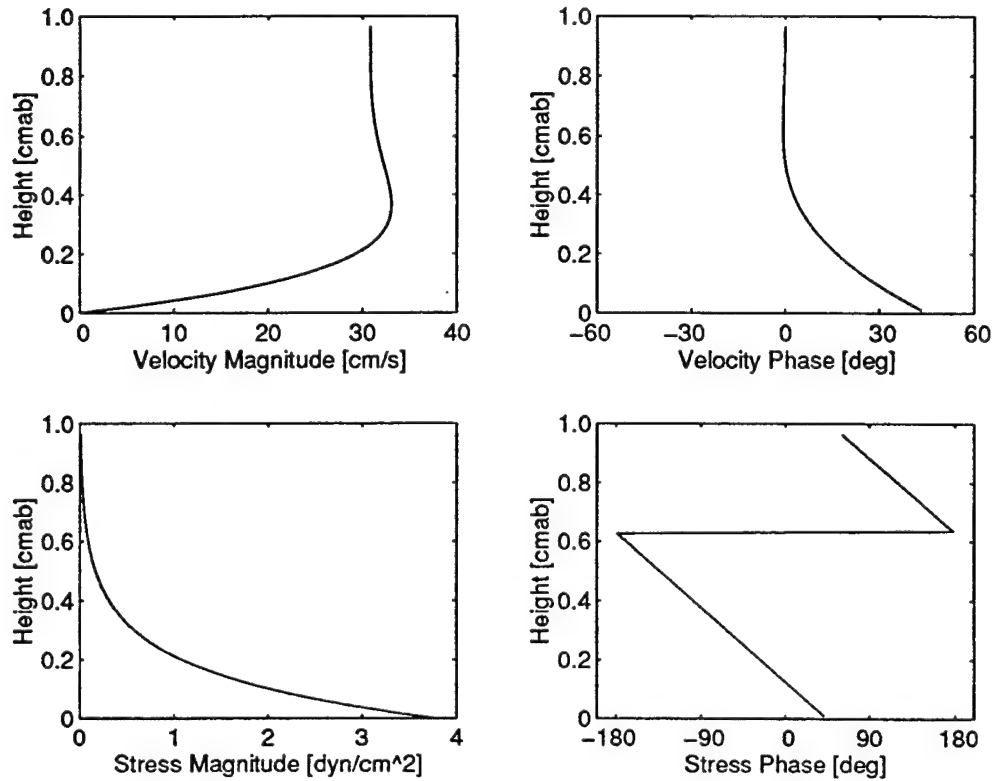


Figure A.3: MAGNITUDE AND PHASE OF VELOCITY AND STRESS FOR A LAMINAR WAVE BOUNDARY LAYER - The magnitude and phase of the complex valued functions on the RHSs of Equations A.40 and A.41 are shown.  $u_w$  and  $\tau_w$  are the real parts of the complex velocity and stress. Phase increases as the boundary is approached. The velocity phase lead reaches a maximum of approximately  $45^\circ$ .

with boundary conditions

$$f = 0 \quad \text{at} \quad z = z_o \quad (\text{A.44})$$

$$f = u_{bm} \quad \text{as} \quad z \rightarrow \infty \quad (\text{A.45})$$

The solution to Equations A.43–A.45 can be expressed in terms of  $\ker$  and  $\kei$  functions, the real and imaginary parts of  $K$ , the modified Bessel function of the second kind. The relation is defined by  $i^{-p}K\left(i^{\frac{1}{2}}\beta x\right) = \ker_p(\beta x) + i\kei_p(\beta x)$  [1, 33, 45, 80, 81]. The resulting velocity distribution within the turbulent wave boundary layer is given

by

$$u_w(z, t) = \Re \left\{ u_{bm} \left[ 1 - \frac{K_0 \left( i^{\frac{1}{2}} 2 \sqrt{\frac{z}{\delta_w}} \right)}{K_0 \left( i^{\frac{1}{2}} 2 \sqrt{\frac{z_o}{\delta_w}} \right)} \right] e^{i\omega t} \right\} \quad (\text{A.46})$$

As before,  $\tau$  may be determined by differentiating  $u_w$  with respect to  $z$ .

$$\tau_w(z, t) = \Re \left\{ u_{bm} \rho \kappa u_{*w} z^{\frac{1}{2}} \frac{K_{-1} \left( i^{\frac{1}{2}} 2 \sqrt{\frac{z}{\delta_w}} \right)}{\sqrt{z \delta_w} K_0 \left( i^{\frac{1}{2}} 2 \sqrt{\frac{z_o}{\delta_w}} \right)} e^{i\omega t} \right\} \quad (\text{A.47})$$

The turbulent velocity and stress distributions, for the second set of conditions listed in Table A.1, are plotted in Figure A.4. As in Figure A.2, profiles covering half of a wave cycle are shown and the characteristic scale height,  $\delta_w = \frac{\kappa u_{*w}}{\omega}$ , is indicated. Note the change of scale for both axes when comparing the laminar and turbulent profiles. The vertical axis spans six scale heights in both cases.

$u_\infty$ , the forcing velocity, is more than twice as large in this case simply due to the doubling of the surface wave amplitude and the increase in wave period. Maximum stress levels have increased by approximately the square of the velocity increase. The turbulent velocity profiles do not exhibit strong structure above the scale height, but the vertical exchange of momentum by turbulent eddies generated at the boundary sustains relatively high levels of stress well above the bottom [32, 59, 65]. At  $4 \delta_w$  the stress is as large as the maximum laminar bottom stress. Stress levels of several  $\text{dyn} \cdot \text{cm}^{-2}$  are still present more than  $10 \delta_w$  above the bottom (Figure A.5).

The magnitude and phase of the complex valued turbulent velocity and stress are shown in Figure A.6. As discussed in Section A.2.4, the maximum turbulent phase lead is only  $10^\circ$ . Interestingly, the turbulent stress "at the bottom",  $z \approx z_o$ , appears to be nearly in phase with  $u_\infty$ , the velocity above the wave boundary layer. This suggests that bedload movement will be in phase with  $u_\infty$  rather than  $u_w$ . The turbulent stress and boundary layer velocity do have the same phase when extrapolated to  $z = 0$ . The laminar stress at the bottom is in phase with  $u_w$ , the boundary layer velocity at the bottom,  $45^\circ$  ahead of  $u_\infty$ .

One further comment should be made about the velocity and stress profiles dis-

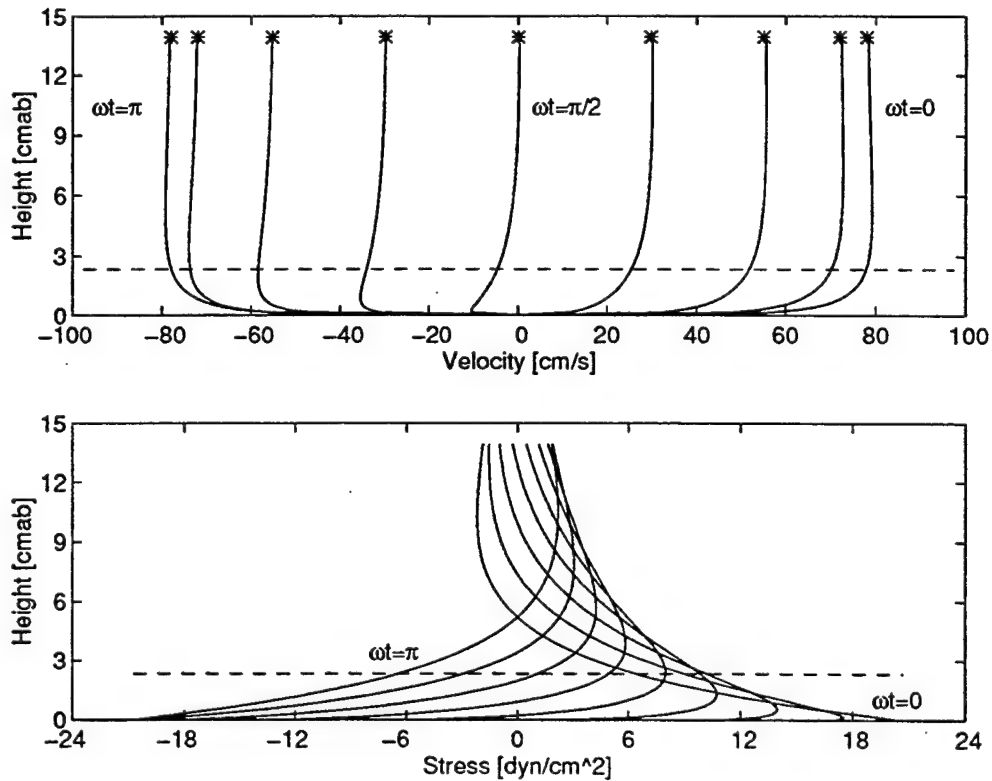


Figure A.4: VELOCITY AND STRESS PROFILES FOR A TURBULENT WAVE BOUNDARY LAYER - Velocity and stress profiles are shown for evenly spaced values of the phase,  $\omega t$ , between 0 and  $\pi$ . The phase increments are  $\frac{\pi}{8}$ . The dashed lines mark the characteristic scale height of the boundary layer,  $\delta_w = \frac{\kappa u_{*w}}{\omega}$ . The \*s mark the value of  $u_{\infty w}$  for each value of the phase. Unlike the laminar case, the velocity profiles do not exhibit strong structure above the scale height. However, the magnitude of the stress more than  $6\delta_w$  above the bottom is still comparable to the maximum laminar bottom stress.

played in this appendix. They should be viewed as the averages over time of multiple realizations of actual velocity and stress distributions. This is particularly true in the turbulent case. A set of single measurement profiles for a single wave would not be this smooth. Contributions from  $u'$  and  $w'$ , the unsteady, non-periodic components of the flow, can add a noise level of 5% to 10% of  $u_{bm}$ , the maximum value of  $u_{\infty}$ , to the flow. Although turbulent flows are generally recognized to have some structure [32, 44, 60, 65], these contributions are generally assumed to be zero mean stochastic processes. Profiles taken with the multiple measurement volume BASS Rake will have to be averaged over time, just as those taken by single measurement

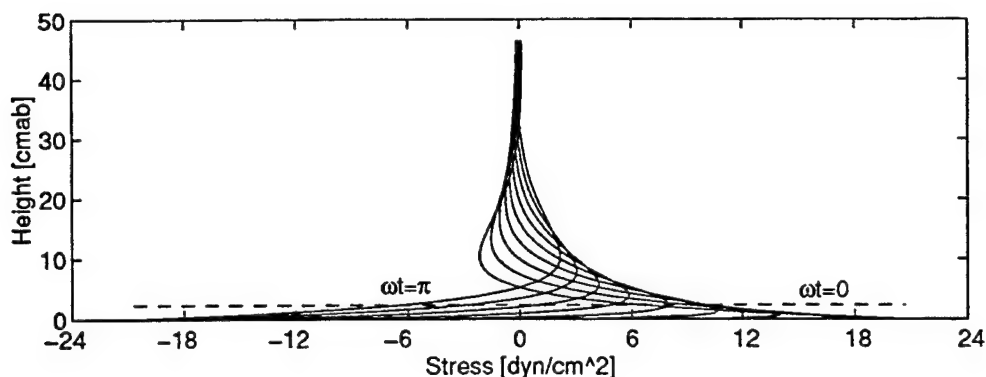


Figure A.5: TURBULENT STRESS PROFILES OVER AN EXTENDED VERTICAL RANGE - The stress profiles of Figure A.4 are shown over a vertical range extended to 20 scale heights. Several  $\text{dyn} \cdot \text{cm}^{-2}$  of stress are still present more than  $10 \delta_w$  above the bottom.

volume instruments are, to show the steady and wave components of the flow as described by boundary layer models. However, the BASS Rake does not require long periods of stationary conditions to achieve this end because each measurement includes all levels of a profile. For example, clean averages over a single wave group are possible. Additionally, sampling at multiple levels over a time window that is short compared to both wave and turbulent time scales makes it possible to image turbulent instabilities and turbulent correlations across the boundary layer. At the present time, only the BASS Rake has these capabilities.

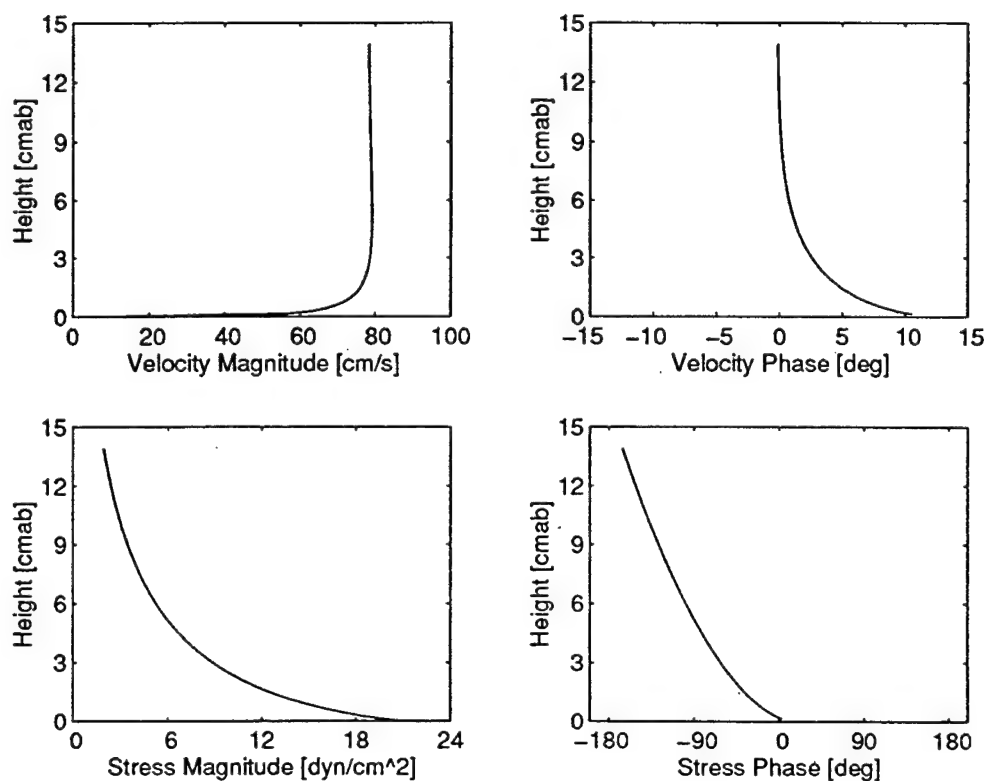


Figure A.6: MAGNITUDE AND PHASE OF VELOCITY AND STRESS FOR A TURBULENT WAVE BOUNDARY LAYER - The magnitude and phase of the complex valued functions on the RHSs of Equations A.46 and A.47 are shown.  $u_w$  and  $\tau_w$  are the real parts of the complex velocity and stress. Phase increases as the boundary is approached. The velocity phase lead reaches a maximum of approximately  $10^\circ$ , significantly less than the laminar phase lead.





## Appendix B

# Schematic Wiring Diagrams for the BASS Rake Laboratory Prototype

The BASS Rake schematics in this appendix are intended for reference purposes only. The drawings document the wiring and the circuit boards of the laboratory prototype. A table of contents, with brief functional descriptions, appears below. Detailed discussions of circuit operation can be found in Chapters 3 and 5. The BASS T/R board was developed prior to and independently of this project by A. J. Williams 3rd and R. L. Koehler [90]. However, the T/R circuit had a strong influence on the design of the BASS Rake MUX. A schematic of the BASS T/R board has, therefore, been added to this appendix. Drawings of the BASS backplane and of other BASS circuit boards are not included.

The BASS Rake cards are mounted on their own backplane and chassis. This assembly is connected to and controlled from a BASS backplane. The TattleTale V (TTV, Onset Computer Corporation©) microprocessor, the signal source and timing board, and the signal detection and differential travel time board are all mounted on the BASS backplane. The connection between the backplanes is made through a jumper of multiple twisted pairs. The jumper replaces a T/R board on the BASS backplane and connects to J1 (see Figure B.1) on the BASS Rake backplane. The

T/R board is mounted on the BASS Rake backplane. The jumper carries analog and logic signals, power supply connections, and power and signal grounds. The dual chassis construction of the prototype was necessary to minimize alterations to existing, standard BASS backplanes. The BASS chassis are active spares and may be called into service on short notice to support changes in the deployment and recovery schedule. Fortunately, only one exchange of BASS backplanes was required during the laboratory prototype phase of the investigation. The two chassis are ohmically connected by a heavy, braided ground strap to provide a low resistance ground path. This reduces high frequency differences in the electric potential between the two chassis that are otherwise coupled to the signal path. Both chassis are locally connected to signal and power grounds. In the future, it will be possible to assemble the BASS Rake on a single backplane and chassis and this problem will be eliminated.

### Schematics

**Figure B.1 BACKPLANE** - Revision 4 of the backplane is wired for both P2 and P3 operation. The selected tine board/tine assemblies connect to J9 and J10. {4,6} Multiplexer Boards appropriate to the tines used connect to J5 through J8. For P3 operation a COSAC card is connected to J11. For P2 operation a simple jumper replaces the COSAC board in J11.

**Figure B.2 P2 {4,6} MULTIPLEXER BOARD** - One of four identical boards connected to J5 through J8. Each board contains a single Layer 1 L-section, the six Layer 2 L-sections of that branch, and the hardware OR of the Layer 2 SELECT lines that is fed to the Layer 1 SELECT line. The L-section blocks in Layer 2 are wired for P2 transducers.

**Figure B.3 MUX SEQUENCER BOARD** - The MUX address sequence is coded as firmware in the two EPROMs. SELECT signals are generated from the 12 bit address by the commercial MUX ICs. The four control bits connect to the T/R board and the TattleTale V (Onset Computer Corporation©) microprocessor. The sequencer board is the same for both P2 and P3 operation.

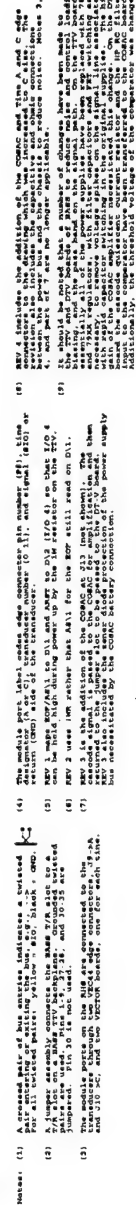
**Figure B.4 DUMMY LOAD** - Each P3 tine contains only 12 transducers, rather than the 48 transducers for which the multiplexer is optimized. The dummy load contains the balance of the VN3205 L-sections in {4,6} trees with 130 pF capacitors simulating the transmission lines and the transducers. Each L-section is hardwired in the deselected state. The dummy load was used to demonstrate that the calculated loading of the signal line by the MUX was accurate.

**Figure B.5 TINE BOARD** - The P2 and P3 tines were each hardwired to circuit boards so that they could easily be connected to or disconnected from the backplane. The high voltage test slot, no longer included on the backplane, was used to bypass the MUX and work directly with the tine and transducers during testing and troubleshooting.

**Figure B.6 P3 {4,6} MULTIPLEXER BOARD** - One of four identical boards connected to J5 through J8. Each board contains a single Layer 1 L-section, the six Layer 2 L-sections of that branch, and the hardware OR of the Layer 2 SELECT lines that is fed to the Layer 1 SELECT line. The L-section blocks in Layer 2 are wired for P3 transducers.

**Figure B.7 P3 CASCODE OUTPUT SIGNAL AMPLIFIER CIRCUIT (COSAC)** - The COSAC is a two stage, high gain, low noise amplifier with a narrow pass band. It is used only with the P3 transducers. The COSAC provides an overall gain of approximately 50 dB from the cascode receiver output to the signal detection and differential travel time circuits.

**Figure B.8 BASS TRANSMIT/RECEIVE BOARD** - The T/R board contains four independent T/R circuits. Only one of these is used in the laboratory prototype. The transmitter consists of a toroidal transformer driven through a pair of FETs. The receiver is a cascode circuit with the N/R switching incorporated in the design. The board and circuit were developed by A. J. Williams 3rd and R. L. Koehler [90].



MOORE HOLE OCEANOGRAPHIC INSTITUTION	
Title	
BACKPLANE	PROTOTYPE BASS BASE
Issue	Document Number
C	ATN 112 12-01-95
	REV
	4



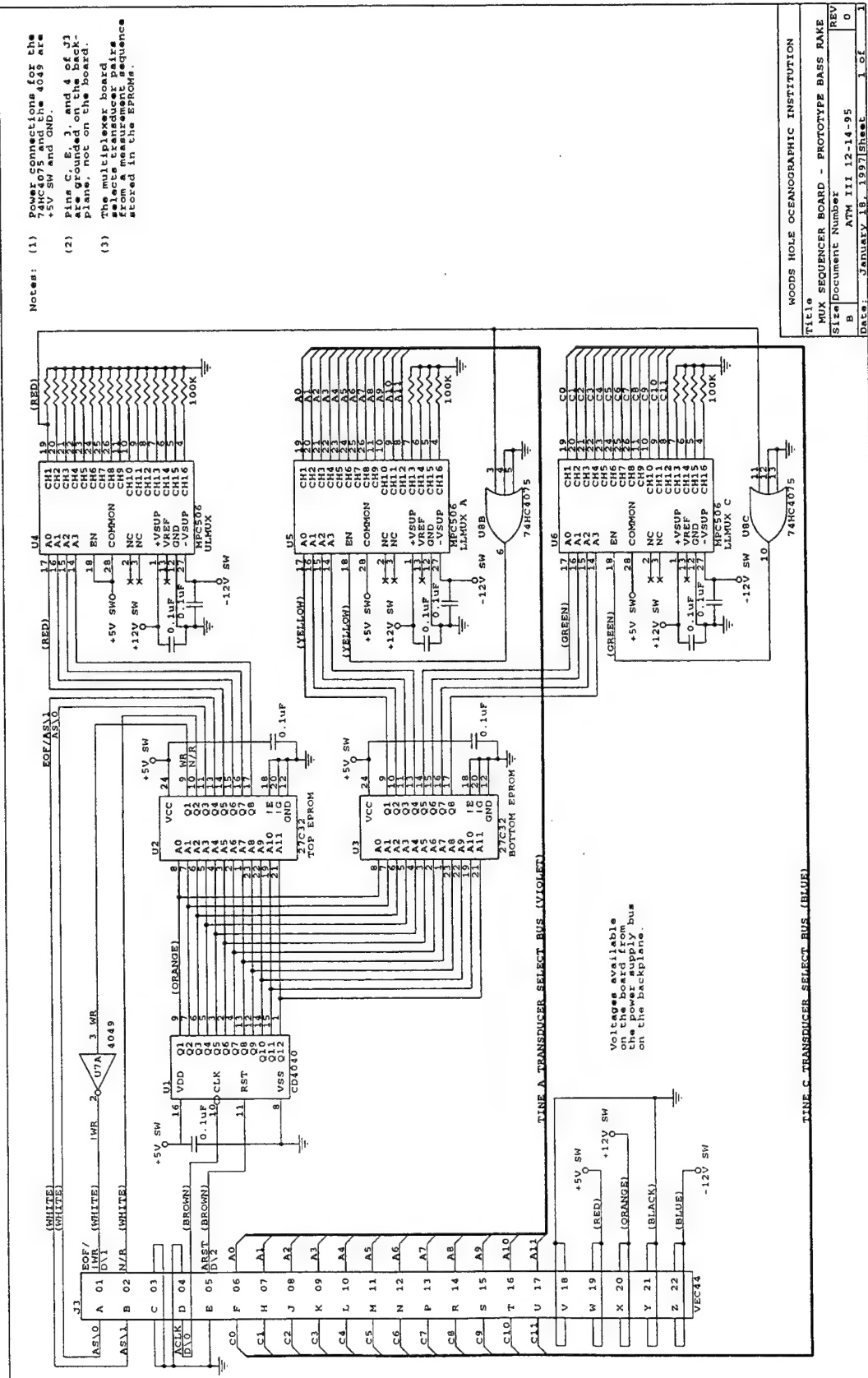


Figure B.3: MUX Sequencer Board

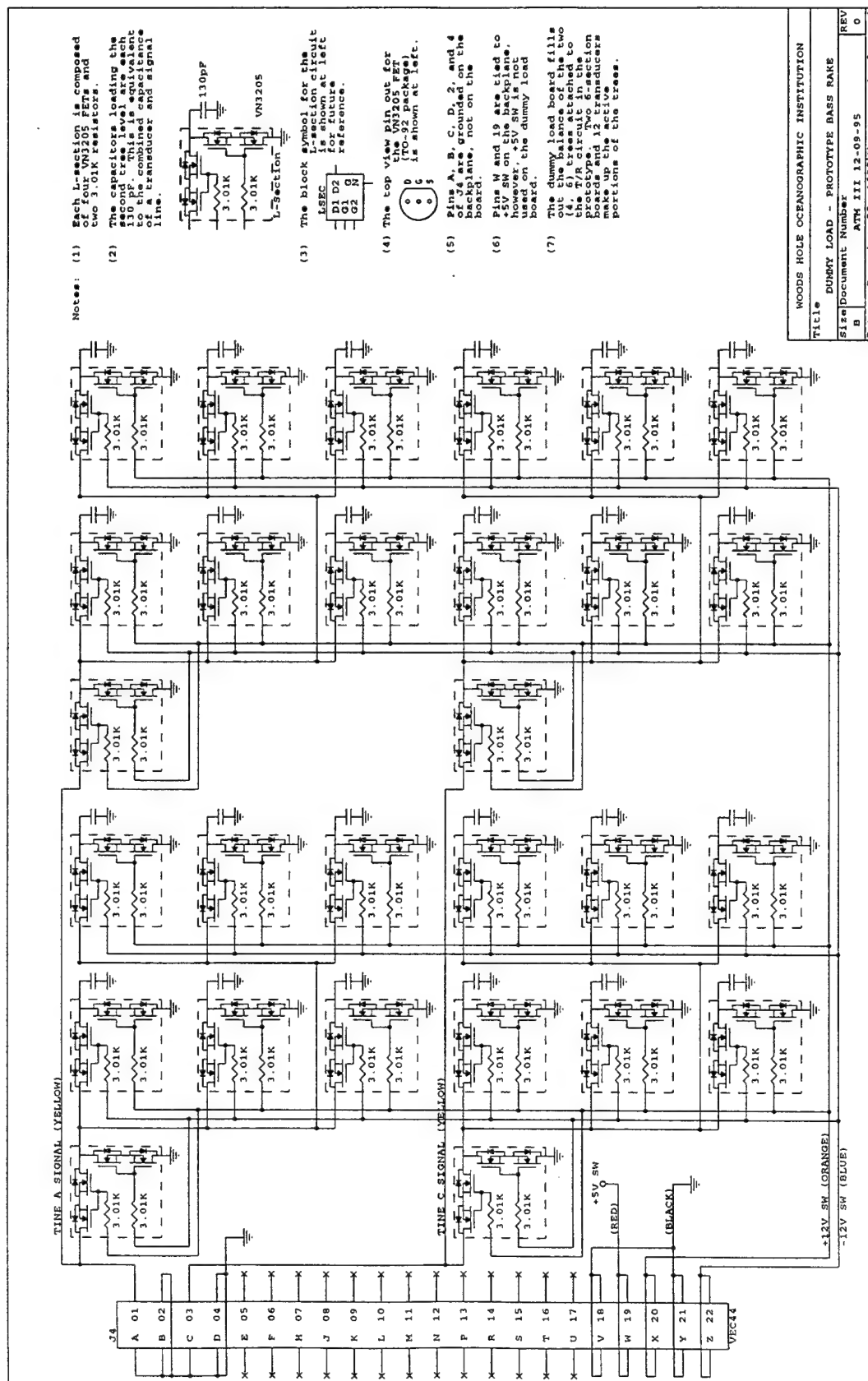


Figure B.4: DUMMY LOAD



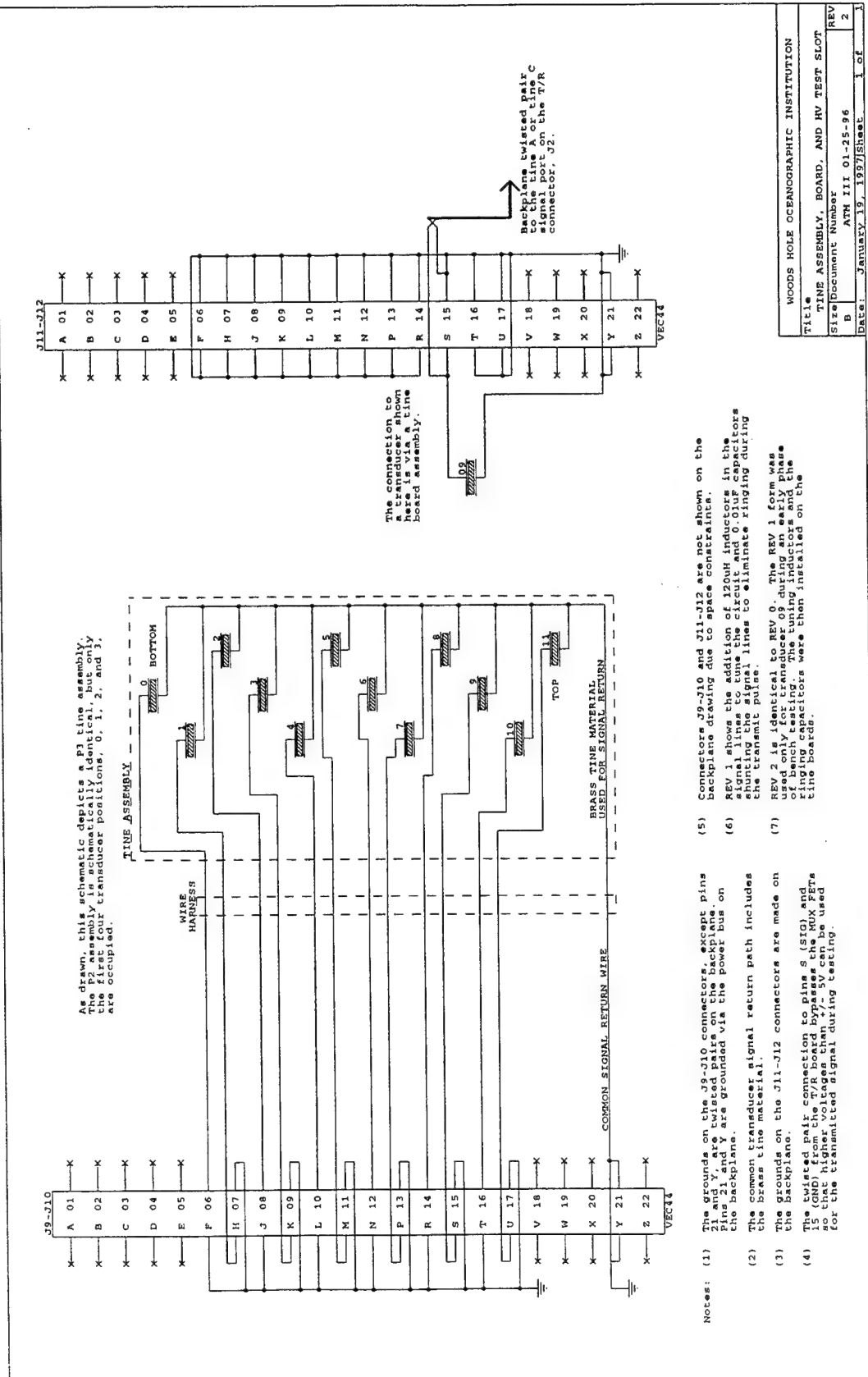


Figure B.5: TINE BOARD

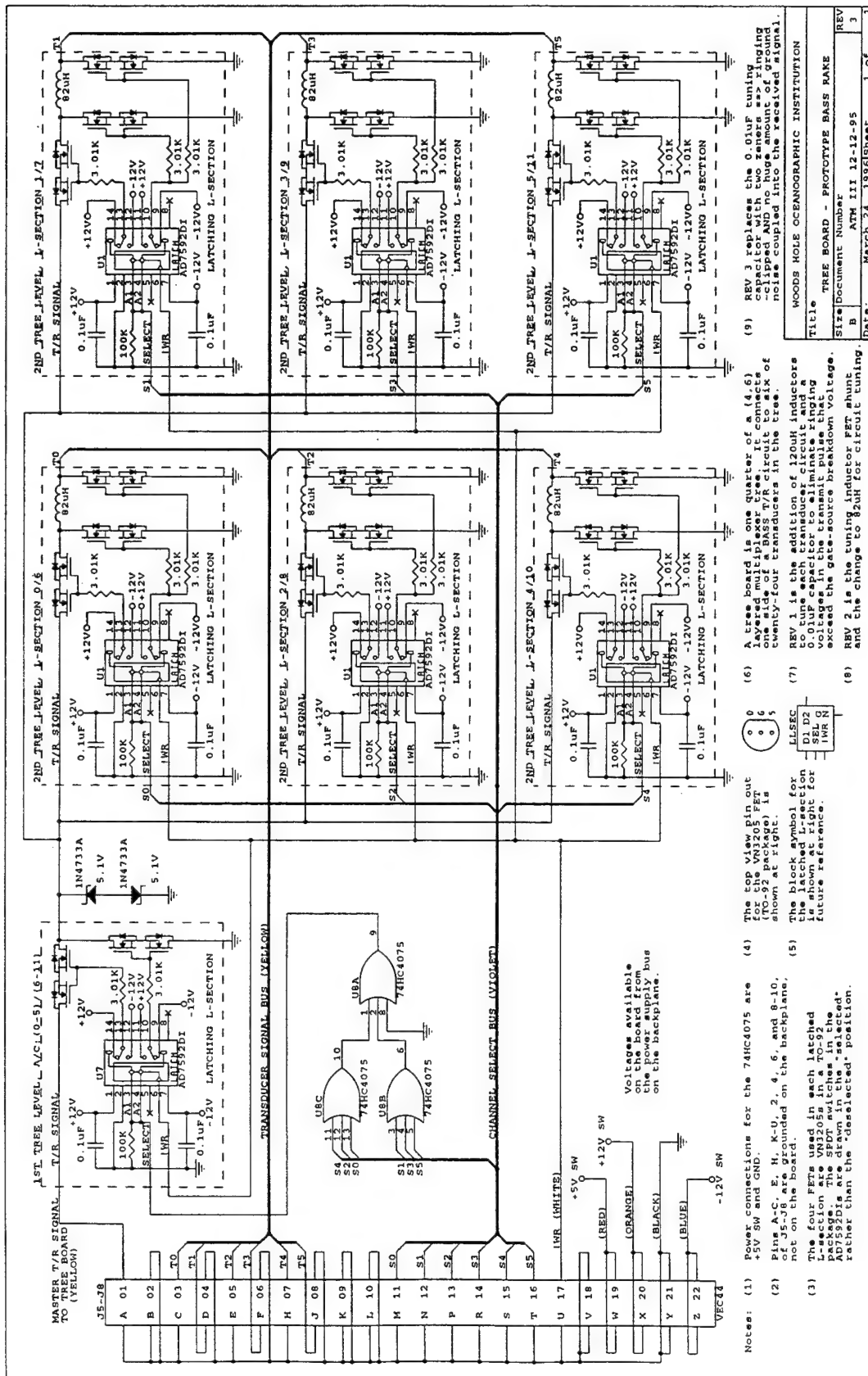


Figure B.6: P3 {4,6} MULTIPLEXER BOARD

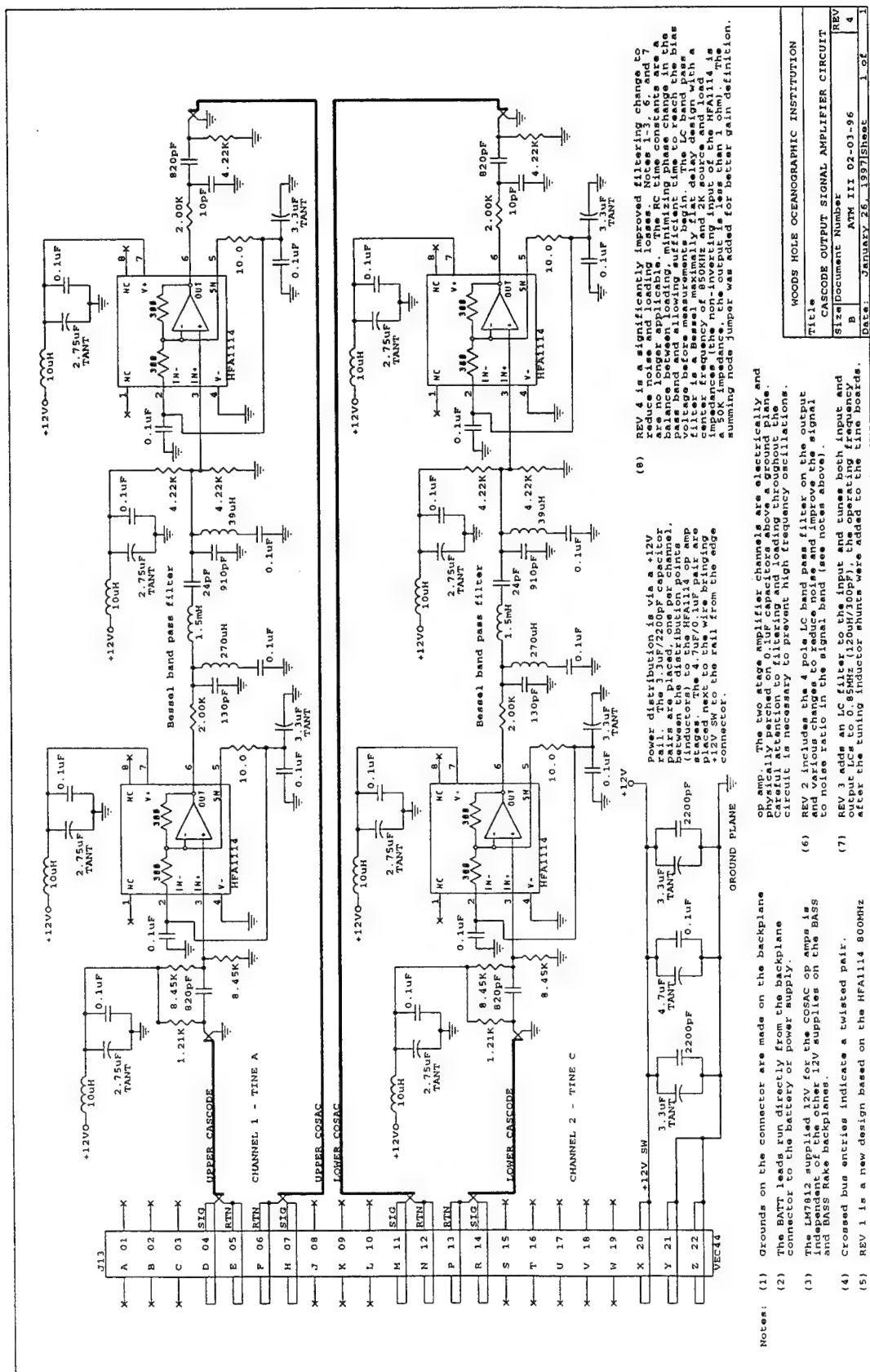


Figure B.7: P3 Cascode Output Signal Amplifier Circuit (COSAC)

WOODS HOLE OCEANOGRAPHIC INSTITUTION	
TITLE	
CASCODE OUTPUT SIGNAL AMPLIFIER CIRCUIT	
SIZE/Document Number	
B	APM 111 02-03-96
REV	4
Date: JANUARY 26, 1997 Sheet 1 of 1	





# Bibliography

- [1] Abramowitz, M., Stegun, I. A., Handbook of Mathematical Functions, National Bureau of Standards, Washington, DC, 1964.
- [2] Agrawal, Y. C., Aubrey, D. G., "Velocity Observations Above a Rippled Bed Using Laser-Doppler Velocimetry", *Journal of Geophysical Research* (1992), Vol. 97, No. C12, pp. 20249-20260.
- [3] Anderson, S., Lohrmann, A., "Open Water Test of the SonTek Acoustic Doppler Velocimeter", *Proceedings of the IEEE Fifth Working Conference on Current Measurement*, IEEE/OES, February 1995, pp. 188-192.
- [4] Bartee, T. C., Digital Computer Fundamentals, 4<sup>th</sup> Edition, McGraw-Hill Book Company, Inc., New York, 1977.
- [5] Batchelor, G. K., An Introduction to Fluid Dynamics, Cambridge University Press, Cambridge, 1967.
- [6] Bearman, P. W., Downie, M. J., Graham, J. M. R., Obasaju, E. D., "Forces On Cylinders in Viscous Oscillatory Flow at Low Keulegan-Carpenter Numbers", *Journal of Fluid Mechanics* (1985), Vol. 154, pp. 337-356.
- [7] Cabrera, R., Lohrmann, A., "Small Scale Laboratory Flow Measurements with the ADV-1", *Proceedings OCEANS '93*, IEEE/OES, October 1993, Vol. II, pp. 404-407.
- [8] Caldwell, D. R., Chriss, T. M., "The Viscous Sublayer at the Sea Floor", *Science* (1979), Vol. 205, No. 4411, pp. 1131-1132.

- [9] Chriss, T. M., Caldwell, D. R., "Evidence for the Influence of Form Drag on Bottom Boundary Layer Flow", *Journal of Geophysical Research* (1982), Vol. 87, No. C6, pp. 4148-4154.
- [10] Conley, D. C., Inman, D. L., "Field Observations of the Fluid-Granular Boundary Layer Under Near-Breaking Waves", *Journal of Geophysical Research* (1992), Vol. 97, No. C6, pp. 9631-9643.
- [11] Cowen, E. A., Monismith, S. G., "A Hybrid Digital Particle Tracking Velocimetry Technique", *Experiments in Fluids*, in press, January 1996.
- [12] Crawford, F. S., Jr., Waves, Berkeley Physics Course, Volume 3, McGraw-Hill Book Company, Inc., New York, 1965.
- [13] Davies, A. G., Soulsby, R. L., King, H. L., "A Numerical Model of the Combined Wave and Current Bottom Boundary Layer", *Journal of Geophysical Research* (1988), Vol. 93, No. C1, pp. 491-508.
- [14] Dyer, I., "Fundamentals and Applications of Underwater Sound", Class notes provided for 13.851 - Fundamentals and Applications of Underwater Sound, Department of Ocean Engineering, Massachusetts Institute of Technology, Cambridge, Massachusetts, 1992.
- [15] Faltinsen, O. M., Sea Loads on Ships and Offshore Structures, Ocean Technology Series, Cambridge University Press, Cambridge, 1990.
- [16] Flick, R. E., George, R. A., "Turbulence Scales in the Surf and Swash", *Proceedings of the International Conference on Coastal Engineering*, 22<sup>nd</sup> Edition, July 1990, Vol. 1, pp. 557-569.
- [17] Foster, D. L., Dynamics of the Nearshore Wave Bottom Boundary Layer, Ph. D. Thesis, Oregon State University, June 1996.
- [18] Fowles, G. R., Introduction to Modern Optics Holt, Rinehart and Winston, Inc., New York, 1968.

- [19] Fredericks, J. J., Trowbridge, J. H., Williams, A. J., 3rd, Lentz, S. J., Butman, B., Gross, T. F., "Fluid Mechanical Measurements Within the Bottom Boundary Layer Over the Northern California Continental Shelf During STRESS", Woods Hole Oceanographic Institution Technical Report No. WHOI-93-32, September 1993.
- [20] Fries, J. S., Chan, L. H., Woods Hole Oceanographic Institution, Woods Hole, MA, personal communication, September 5, 1996.
- [21] Fries, J. S., Woods Hole Oceanographic Institution, Woods Hole, MA, personal communication, December 23, 1996.
- [22] Gartner, J. W., Cheng, R. T., "Near Bottom Velocity Measurements in San Francisco Bay, California", *Proceedings OCEANS '96*, MTS/IEEE/OES, September 1996, Vol. I, pp. 457-462.
- [23] Graham, J. M. R., "The Forces on Sharp-edged Cylinders in Oscillatory Flow at Low Keulegan-Carpenter Numbers", *Journal of Fluid Mechanics* (1980), Vol. 97, pp. 331-346.
- [24] Grant, W. D., Madsen, O. S., "Combined Wave and Current Interaction With a Rough Bottom", *Journal of Geophysical Research* (1979), Vol. 84, No. C4, pp. 1797-1808.
- [25] Grant, W. D., Madsen, O. S., "Movable Bed Roughness in Unsteady Oscillatory Flow", *Journal of Geophysical Research* (1982), Vol. 87, No. C1, pp. 469-481.
- [26] Grant, W. D., Williams, A. J., 3rd, Glenn, S. M., "Bottom Stress Estimates and Their Prediction On the Northern California Continental Shelf During CODE-1: The Importance of Wave-Current Interaction", *Journal of Physical Oceanography* (1984), Vol. 14, No. 3, pp. 506-527.
- [27] Grant, W. D., Madsen, O. S., "The Continental-Shelf Bottom Boundary Layer", *Annual Review of Fluid Mechanics* (1986), Vol. 18, pp. 265-305.



- [28] Gust, G., "Tools for Oceanic Small-Scale, High Frequency Flows: Metal-Clad Hot Wires", *Journal of Geophysical Research* (1982), Vol. 87, No. C1, pp. 447-455.
- [29] Gytte, T., Nilsen, J. E. O., Stiansen, J. E., Sundby, S., "Resolving Small Scale Turbulence with Acoustic Doppler and Acoustic Travel Time Difference Current Meters from an Underwater Tower", *Proceedings OCEANS '96*, MTS/IEEE/OES, September 1996, Vol. I, pp. 442-450.
- [30] Hart, D. D., Clark, B. D., Jasentuliyana, A., "Fine-scale Field Measurement of Benthic Flow Environments Inhabited by Stream Invertebrates", *Limnology and Oceanography* (1996), Vol. 41, No. 2, pp. 297-308.
- [31] Hay, A. E., Memorial University of Newfoundland, St. John's, NF, Canada, personal communication, December 1996.
- [32] Head, M. R., Bandyopadhyay, P., "New Aspects of Turbulent Boundary-Layer Structure", *Journal of Fluid Mechanics* (1981), Vol. 107, pp. 297-338.
- [33] Hildebrand, F. B., Advanced Calculus for Applications, 2<sup>nd</sup> Edition, Prentice-Hall, Inc., Englewood Cliffs, New Jersey, 1976.
- [34] Horowitz, P., Hill, W., The Art of Electronics, 2<sup>nd</sup> Edition, Cambridge University Press, Cambridge, 1989.
- [35] Jensen, B. L., Sumer, B. M., Fredsøe, J., "Turbulent Oscillatory Boundary Layers at High Reynolds Numbers", *Journal of Fluid Mechanics* (1989), Vol. 206, pp. 265-297.
- [36] Jonsson, I. G., "Measurements in the Turbulent Wave Boundary Layer", *Proceedings of the 10<sup>th</sup> Congress of the International Association for Hydraulic Research*, IAHR, London, September 1963, Vol. 1, Paper 1.12, pp. 85-92.
- [37] Jonsson, I. G., Carlsen, N. A., "Experimental and Theoretical Investigations In an Oscillatory Turbulent Boundary Layer", *Journal of Hydraulic Research* (1976), Vol. 14, No. 1, pp. 45-60.

- [38] Kajiura, K., "A Model of the Bottom Boundary Layer In Water Waves", *Bulletin of the Earthquake Research Institute* (1968), Vol. 46, pp. 75-122.
- [39] Kundu, P. K., Fluid Mechanics, Academic Press, Inc., Harcourt Brace Jovanovich, Publishers, San Diego, 1990.
- [40] Lamb, H., Hydrodynamics, 6<sup>th</sup> Edition, Dover Publications, New York, 1932.
- [41] Liu, Z.-C., Landreth, C. C., Adrian, R. J., Hanratty, T. J., "High Resolution Measurement of Turbulent Structure in a Channel with Particle Image Velocimetry", *Experiments in Fluids* (1991), Vol. 10, pp. 301-312.
- [42] Lukasik, S. J, Grosch, C. E., "Pressure-Velocity Correlations in Ocean Swell", *Journal of Geophysical Research* (1963), Vol. 68, No. 20, pp. 5689-5699.
- [43] MacKenzie, K. V., "Nine-Term Equation for Sound Speed in the Oceans", *Journal of the Acoustical Society of America* (September 1981), Vol. 70, No. 3, pp. 807-812.
- [44] McLean, S. R., Nelson, J. M., Wolfe, S. R., "Turbulence Structure Over Two-Dimensional Bed Forms: Implications for Sediment Transport", *Journal of Geophysical Research* (1994), Vol. 99, No. C6, pp. 12,729-12,747.
- [45] Madsen, O. S., Wikramanayake, P. N., "Simple Models for Turbulent Wave-Current Bottom Boundary Layer Flow", Dredging Research Program, Final Report, Contract Report No. DRP-91-1, U. S. Army Corps of Engineers, Waterways Experiment Station, Coastal Engineering Research Center, December 1991.
- [46] Madsen, O. S., "Sediment Transport on the Shelf", Final Draft of Chapter III.6 of The Coastal Engineering Manual, to be published by the U. S. Army Corps of Engineers, Waterways Experiment Station, Coastal Engineering Research Center, December 30, 1993.

- [47] Mathisen, P. P., Madsen, O. S., "Waves and Currents Over a Fixed Rippled Bed, 1, Bottom Roughness Experienced by Waves in the Presence and Absence of Currents", *Journal of Geophysical Research* (1996), Vol. 101, No. C7, pp. 16,533-16,542.
- [48] Mathisen, P. P., Madsen, O. S., "Waves and Currents Over a Fixed Rippled Bed, 2, Bottom and Apparent Roughness Experienced by Currents in the Presence of Waves", *Journal of Geophysical Research* (1996), Vol. 101, No. C7, pp. 16,543-16,550.
- [49] Monin, A. S., Yaglom, A. M., Statistical Fluid Mechanics: Mechanics of Turbulence, Volume 2, The MIT Press, Cambridge, Massachusetts, 1975.
- [50] Monk, G. S., Light: Principles and Experiments, 2<sup>nd</sup> Edition, Dover Publications, Inc., New York, 1963.
- [51] Morgan, J., Introduction to Geometrical and Physical Optics, McGraw-Hill Book Company, Inc., New York, 1953.
- [52] Morrison, A. T., III, Yoerger, D. R., "Determination of the Hydrodynamic Parameters of an Underwater Vehicle During Small Scale, Nonuniform, 1-Dimensional Translation", *Proceedings OCEANS '93*, IEEE/OES, October 1993, Vol. II, pp. 277-282.
- [53] Morrison, A. T., III, Williams, A. J., 3rd, Martini, M., "Calibration of the BASS Acoustic Current Meter With Carrageenan Agar", *Proceedings OCEANS '93*, IEEE/OES, October 1993, Vol. III, pp. 143-148.
- [54] Morrison, A. T., III, Williams, A. J., 3rd, "STRESS II BASS Data Archive", Anonymous ftp site: sharatz.whoi.edu (128.128.92.20), NetCDF binary and ASCII files: /pub/STRESS\_II/netcdf/\*.nc and \*.cdl, MATLAB binary and ASCII files: /pub/STRESS\_II/matlab/\*.mat and \*.RME, December 1994.

- [55] Morrison, A. T., III, "A New Technique for Detailed Acoustic Current Profiles in the Continental Shelf Wave Bottom Boundary Layer", *Proceedings of the IEEE Fifth Working Conference on Current Measurement*, IEEE/OES, February 1995, pp. 220-225.
- [56] Morrison, A. T., III, "Multiplexer Design for the BASS Rake Acoustic Transducer Array", *Proceedings OCEANS '95*, MTS/IEEE/OES, October 1995, Vol. III, pp. 1528-1532.
- [57] Morrison, A. T., III, "Low Impedance Multiplexer for BASS Rake Transducer Array", *Sea Technology*, May 1996, Vol. 37, No. 5, pp. 15-21.
- [58] Morrison, A. T., III, Williams, A. J., 3rd, "Preliminary Tow Tank and Flume Tests of a Prototype BASS Rake Wave Bottom Boundary Layer Sensor", *Proceedings OCEANS '96*, MTS/IEEE/OES, September 1996, Vol. I, pp. 451-456.
- [59] Morton, B. R., "The Generation and Decay of Vorticity", *Geophysical and Astrophysical Fluid Dynamics* (1984), Vol. 28, pp. 277-308.
- [60] Nikolaides, C., Lau, K. K., Hanratty, T. J., "A Study of the Spanwise Structure of Coherent Eddies in the Viscous Wall Region", *Journal of Fluid Mechanics* (1983), Vol. 130, pp. 91-108.
- [61] Newman, J. N., Marine Hydrodynamics, The MIT Press, Cambridge, Massachusetts, 1977.
- [62] Ogata, K., Modern Control Engineering, Prentice-Hall, Englewood Cliffs, New Jersey, 1970.
- [63] Pierce, A. D., Acoustics, An Introduction to Its Physical Principles and Applications, 2<sup>nd</sup> Edition, Acoustical Society of America (American Institute of Physics), Woodbury, New York, 1989.
- [64] Rayleigh, J. W. S., The Theory of Sound, Volumes I and II, Dover Publications, New York, 1896.

- [65] Robinson, S. K., "Coherent Motions in the Turbulent Boundary Layer", *Annual Review of Fluid Mechanics* (1991), Vol. 23, pp. 601-639.
- [66] Sarpkaya, T., Isaacson, M., Mechanics of Wave Forces On Offshore Structures, Van Nostrand Reinhold Company, New York, 1981.
- [67] Sarpkaya, T., "Force On a Circular Cylinder in Viscous Oscillatory Flow at Low Keulegan-Carpenter Numbers", *Journal of Fluid Mechanics* (1986), Vol. 165, pp. 61-71.
- [68] Shaw, W. J., Williams, A. J., 3rd, Trowbridge, J. H., "Measurement of Turbulent Sound Speed Fluctuations with an Acoustic Travel-Time Meter", *Proceedings OCEANS '96, MTS/IEEE/OES*, September 1996, Supplementary Volume, pp. 105-110.
- [69] Skilling, H. H., Electric Networks, John Wiley and Sons, New York, 1974.
- [70] Sherwin, J., "Noise Specs Confusing?", Application Note 104 (AN-104), National Semiconductor Corporation, May 1974.
- [71] Sleath, J. F. A., "A Device for Velocity Measurement in Oscillatory Boundary Layers in Water", *Journal of Scientific Instruments (Journal of Physics E)* (1969), Series 2, Vol. 2, No. 2, pp. 446-448.
- [72] Sleath, J. F. A., "Velocity Measurements Close to the Bed in a Wave Tank", *Journal of Fluid Mechanics* (1970), Vol. 42, pp. 111-123.
- [73] Smith, J. D., "Modeling of Sediment Transport On Continental Shelves", in The Sea, Vol. 6, Chap. 13, pp. 539-577, Interscience, New York, 1977.
- [74] Stanton, T. P., "Probing Ocean Wave Boundary Layers with a Hybrid Bistatic/Monostatic Coherent Acoustic Doppler Profiler", *Proceedings of the Microstructure Sensors in the Ocean Workshop*, ONR, October 1996, pp. 76-84.
- [75] Terray, E. A., Woods Hole Oceanographic Institution, Woods Hole, MA, personal communications, 1996, 1997.

- [76] Thompson, C., Transducer Products, Inc., Goshen, CT, personal communications, May 1995.
- [77] Trivett, D. A., Diffuse Flow From Hydrothermal Vents, Ph. D. Thesis, Massachusetts Institute of Technology/Woods Hole Oceanographic Institution, August 1991.
- [78] Trivett, D. A., Terray, E. A., Williams, A. J., 3rd, "Error Analysis of an Acoustic Current Meter", *IEEE Journal of Oceanic Engineering* (1991), Vol. 16, No. 4, pp. 329-337.
- [79] Trivett, D. A., Bowers, C., Bowen, A., Snow, J., Skafel, M., "The Combined Velocity-Density-Vorticity (VDV) Sensor: A Report on its First Use", *Proceedings of the IEEE Fifth Working Conference on Current Measurement*, IEEE/OES, February 1995, pp. 183-187.
- [80] Trowbridge, J. H., Madsen, O. S., "Turbulent Wave Boundary Layers, 1, Model Formulation and First-Order Solution", *Journal of Geophysical Research* (1984), Vol. 89, No. C5, pp. 7989-7997.
- [81] Trowbridge, J. H., Madsen, O. S., "Turbulent Wave Boundary Layers, 2, Second-Order Theory and Mass Transport", *Journal of Geophysical Research* (1984), Vol. 89, No. C5, pp. 7999-8007.
- [82] Trowbridge, J. H., Geyer, W. R., Butman, C. A., Chapman, R. J., "The 17-Meter Flume at the Coastal Research Laboratory, Part II: Flow Characteristics", Woods Hole Oceanographic Institution Technical Report WHOI-89-11, May 1989.
- [83] Trowbridge, J. H., Agrawal, Y. C., "Glimpses of a Wave Boundary Layer", *Journal of Geophysical Research* (1995), Vol. 100, No. C10, pp. 20,729-20,743.
- [84] Trowbridge, J. H., "Note on a Technique for Measurement of Turbulent Shear Stress in the Presence of Surface Waves", *Journal of Atmospheric and Oceanic Technology*, in press, February 1997.

- [85] Veron, F., Melville, W. K., "Pulse-to-Pulse Coherent Doppler Measurements of Waves and Turbulence: Laboratory and Field Testing", *Proceedings of the Microstructure Sensors in the Ocean Workshop*, ONR, October 1996, part of an unnumbered set of papers included in a supplement.
- [86] Voulgaris, G., Trowbridge, J. H., "Evaluation of the Acoustic Doppler Velocimeter (ADV) for Turbulence Measurements", submitted to *Journal of Atmospheric and Oceanic Technology*, August 1996.
- [87] Wiberg, P. L., Harris, C. K., "Ripple Geometry in Wave-dominated Environments", *Journal of Geophysical Research* (1994), Vol. 99, No. C1, pp. 775-789.
- [88] Wikramanayake, P. N., Madsen, O. S., "Calculation of Movable Bed Friction Factors", Dredging Research Program, Technical Progress Report No. 2, U. S. Army Corps of Engineers, Waterways Experiment Station, Coastal Engineering Research Center, December 1990.
- [89] Willert, C. E., Gharib, M., "Digital Particle Image Velocimetry", *Experiments in Fluids* (1991), Vol. 10, pp. 181-193.
- [90] Williams, A. J., 3rd, Tochko, J. S., Koehler, R. L., Grant, W. D., Gross, T. F., Dunn, C. V. R., "Measurement of Turbulence in the Oceanic Bottom Boundary Layer with an Acoustic Current Meter Array", *Journal of Atmospheric and Oceanic Technology*, Vol. 4, No. 2, June 1987.
- [91] Williams, A. J., 3rd, Gross, T. F., "In Situ Processing of Boundary layer Flow Measurements For Data Compression", *Proceedings OCEANS '91*, IEEE/OES, October 1991, Vol. II, pp. 973-976.
- [92] Williams, A. J., 3rd, "Linearity and Noise in Differential Travel Time and Acoustic Velocity Measurement", *Proceedings of the IEEE Fifth Working Conference on Current Measurement*, IEEE/OES, February 1995, pp. 216-219.

- [93] Williams, A. J., 3rd, Morrison, A. T., III, "Shallow-Water Messenger-Line Recovery System", *Proceedings OCEANS '96*, IEEE/OES, September 1996, Vol. II, pp. 646-649.
- [94] Williams, A. B., Taylor, F. J., Electronic Filter Design Handbook, 3<sup>rd</sup> Edition, McGraw-Hill, Inc., New York, 1995.
- [95] Williams, J., "High Speed Amplifier Techniques: A Designer's Companion for Wideband Circuitry", Application Note 47 (AN47), Linear Technology Corporation, August 1991.
- [96] Wright, C., Thermo Systems, Incorporated, personal communication, December 1996.



The End

## DOCUMENT LIBRARY

*Distribution List for Technical Report Exchange – February 1996*

University of California, San Diego  
SIO Library 0175C  
9500 Gilman Drive  
La Jolla, CA 92093-0175

Hancock Library of Biology & Oceanography  
Alan Hancock Laboratory  
University of Southern California  
University Park  
Los Angeles, CA 90089-0371

Gifts & Exchanges  
Library  
Bedford Institute of Oceanography  
P.O. Box 1006  
Dartmouth, NS, B2Y 4A2, CANADA

Commander  
International Ice Patrol  
1082 Shennecossett Road  
Groton, CT 06340-6095

NOAA/EDIS Miami Library Center  
4301 Rickenbacker Causeway  
Miami, FL 33149

Research Library  
U.S. Army Corps of Engineers  
Waterways Experiment Station  
3909 Halls Ferry Road  
Vicksburg, MS 39180-6199

Institute of Geophysics  
University of Hawaii  
Library Room 252  
2525 Correa Road  
Honolulu, HI 96822

Marine Resources Information Center  
Building E38-320  
MIT  
Cambridge, MA 02139

Library  
Lamont-Doherty Geological Observatory  
Columbia University  
Palisades, NY 10964

Library  
Serials Department  
Oregon State University  
Corvallis, OR 97331

Pell Marine Science Library  
University of Rhode Island  
Narragansett Bay Campus  
Narragansett, RI 02882

Working Collection  
Texas A&M University  
Dept. of Oceanography  
College Station, TX 77843

Fisheries-Oceanography Library  
151 Oceanography Teaching Bldg.  
University of Washington  
Seattle, WA 98195

Library  
R.S.M.A.S.  
University of Miami  
4600 Rickenbacker Causeway  
Miami, FL 33149

Maury Oceanographic Library  
Naval Oceanographic Office  
Building 1003 South  
1002 Balch Blvd.  
Stennis Space Center, MS, 39522-5001

Library  
Institute of Ocean Sciences  
P.O. Box 6000  
Sidney, B.C. V8L 4B2  
CANADA

National Oceanographic Library  
Southampton Oceanography Centre  
European Way  
Southampton SO14 3ZH  
UK

The Librarian  
CSIRO Marine Laboratories  
G.P.O. Box 1538  
Hobart, Tasmania  
AUSTRALIA 7001

Library  
Proudman Oceanographic Laboratory  
Bidston Observatory  
Birkenhead  
Merseyside L43 7 RA  
UNITED KINGDOM

IFREMER  
Centre de Brest  
Service Documentation - Publications  
BP 70 29280 PLOUZANE  
FRANCE

<b>REPORT DOCUMENTATION PAGE</b>	<b>1. REPORT NO.</b> MIT/WHOI 97-20	<b>2.</b>	<b>3. Recipient's Accession No.</b>
<b>4. Title and Subtitle</b> Development of the BASS Rake Acoustic Current Sensor: Measuring Velocity in the Continental Shelf Wave Bottom Boundary Layer			<b>5. Report Date</b> June 1997
			<b>6.</b>
<b>7. Author(s)</b> Archie Todd Morrison III			<b>8. Performing Organization Rept. No.</b>
<b>9. Performing Organization Name and Address</b>  MIT/WHOI Joint Program in Oceanography/Applied Ocean Science & Engineering			<b>10. Project/Task/Work Unit No.</b> MIT/WHOI 97-20
			<b>11. Contract(C) or Grant(G) No.</b> (C) N00014-93-1-1140 (G) OCE-9314357
<b>12. Sponsoring Organization Name and Address</b>  The Office of Naval Research and the National Science Foundation			<b>13. Type of Report &amp; Period Covered</b> Ph.D. Thesis
			<b>14.</b>
<b>15. Supplementary Notes</b> This thesis should be cited as: Archie Todd Morrison III, 1997. Development of the BASS Rake Acoustic Current Sensor: Measuring Velocity in the Continental Shelf Wave Bottom Boundary Layer. Ph.D. Thesis. MIT/WHOI, 97-20.			
<b>16. Abstract (Limit: 200 words)</b>  This thesis documents the development, testing, and field use of the BASS Rake, an instrument designed to measure velocity profiles in the continental shelf wave bottom boundary layer. The mechanical design supports multiple measurement levels with millimeter vertical spacing and is integrated to an electronic interface that permits flexible acquisition of horizontal and vertical velocity measurements. The effects of the sample volume are calculated with a model of acoustic propagation in a scattering medium and used to specify the transducer characteristics necessary to image the wave boundary layer. A flow distortion model and empirical determinations of the Reynolds number, Keulegan-Carpenter number, and angular dependencies of the sensor response are presented. The calibrated response is tested against concurrent LDV measurements over a natural sand bed in a flume. The single measurement accuracy of the BASS Rake is higher than that of the LDV and the multiple sample volumes allow measurement of vertically coherent turbulent instabilities. Selected data from a twenty-four day field deployment are presented and analyzed, revealing regular movement of the sand bed, generation and modification of sand ripples, and strong tidal modulation of the current and wave velocities. The data set is unique in containing concurrent velocity time series, of several weeks duration, with coverage from 1 cm to 20 cm above the bottom.			
<b>17. Document Analysis</b> <b>a. Descriptors</b>  instrumentation velocity measurement boundary layer  <b>b. Identifiers/Open-Ended Terms</b>     <b>c. COSATI Field/Group</b>			
<b>18. Availability Statement</b>  Approved for publication; distribution unlimited.	<b>19. Security Class (This Report)</b> UNCLASSIFIED	<b>21. No. of Pages</b> 360	
	<b>20. Security Class (This Page)</b>	<b>22. Price</b>	